IPP-Report

Max-Planck-Institut
für Plasmaphysik

Ulrike Plank

The Effect of the Radial Electric Field around the Separatrix on the Access to the High Confinement Mode at ASDEX Upgrade

IPP 2022-03
März 2022

The Effect of the Radial Electric Field around the Separatrix on the Access to the High Confinement Mode at ASDEX Upgrade

Ulrike Plank

München 2021

SIGILL·UNIVERSITAT·LUDOVIC·MAXIM·

The Effect of the Radial Electric Field around the Separatrix on the Access to the High Confinement Mode at ASDEX Upgrade

Dissertation zur Erlangung des akademischen Grades eines
Doktors der Naturwissenschaften (Dr. rer. nat.)
an der Fakultät für Physik der Ludwig-Maximilians-Universität München

durchgeführt am
Max-Planck-Institut für Plasmaphysik in Garching bei München

vorgelegt von
Ulrike Plank
geboren am 27. April 1991 in Straubing

München, den 13. Oktober 2021

Erstgutachter: PD Dr. Thomas Pütterich
Zweitgutachter: Prof. Dr. Harald Lesch
Tag der mündlichen Prüfung: 23. Februar 2022

Zusammenfassung

In magnetisch eingeschlossenen Fusionsplasmen im Typ Tokamak existiert das H-mode-Regime mit erhöhtem Teilchen- und Energieeinschluss. Es zeichnet sich durch eine Transportbarriere aus, die sich über die äußersten 5 % des eingeschlossenen Plasmabereichs erstreckt. Es ist jedoch noch nicht vollständig verstanden, wie genau der Übergang von der L-mode ohne Transportbarriere in die H-Mode stattfindet. Dies geschieht beim sogenannten L-H-Übergang. Das radiale elektrische Feld E_r könnte eine entscheidendende Rolle bei der Ausbildung der Transportbarriere am Plasmarand und damit zum L-H-Übergang spielen. E_r hat am Plasmarand eine Senke mit zwei starken Gradienten, einem inneren und einem äußeren E_r-Gradienten. Diese Gradienten führen zu einer Scherströmung der $E \times B$-Geschwindigkeit, welche eine Unterdrückung des turbulenten Randtransports bewirkt. Im Experiment wird die H-Mode erreicht, sobald die Heizleistung die sognenannte H-Modenschwelle (P_{LH}) überschreitet. Es zeigt sich aber, dass P_{LH} von Veränderungen in der sogenannten Abschälschicht (SOL) abhängig ist, einem dünnen Plasmabereich, der das heiße, gut eingeschlossene Hauptplasma von der Gefäßwand trennt. Eine mögliche Erklärung ist, dass sich E_r in der SOL ändert und somit der äußere E_r-Gradient modifiziert wird, d.h. jener Gradient, welcher die SOL und das eingeschlossene Plasma verbindet.

Am Tokamak ASDEX Upgrade in Garching wurden Experimente zum L-H-Übergang durchgeführt, um zu klären, welche Rolle E_r in der SOL am L-H-Übergang spielt. Es wurde untersucht ob sich das SOL-E_r unter den Bedingungen ändert, unter denen eine erhöhte H-Modenschwelle beobachtet worden war. Zu den Experimenten gehören Vergleiche in zwei magnetischen Konfigurationen, der sogenannten günstigen und der ungünstigen Driftkonfiguration, und Vergleiche von Wasserstoff- mit Deuteriumplasmen. Um den äußeren E_r-Gradienten zu messen, wurde eine neue Messmethode entwickelt, die auf der aktiven Spektroskopie von einfach ionisiertem Helium basiert (HES). Mit diesem neuen System ist es möglich, E_r in unterschiedlichen Plasmaregimen (L- und H-Mode) mit einer Zeitauflösung von 2,45 ms zu messen. Für eine verbesserte Interpretation der Messdaten wurde eine synthetische Messdiagnostik entwickelt. Auch wurden neben den E_r-Profilen die experimentellen Messungen kinetischer Elektronen- und Ionenrandprofile sowie Rotationsprofile der Verunreinigungen für die unterschiedlichen Plasmabedingungen untersucht. Ebenso wurden Berechnungen der Leistungsbilanz durchgeführt, um zu erfassen, welche Leistung im Ionen- und welche im Elektronenkanal steckt. Außerdem wurden die experimentellen Daten mit Berechnungen aus der lokalen neoklassischen Theorie verglichen.

Es stellt sich heraus, dass der äußere E_r-Gradient vor dem L-H-Übergang meistens relativ konstant ist und er erst steiler wird, sobald der L-H-Übergang stattgefunden hat. Die Entwicklung des E_r-Randprofils folgt der des Hauptionendruckgradienten. In der L-mode hat jedoch auch die toroidale Plasmarotation einen nicht vernachlässigbaren Einfluss auf das E_r-Profil. Insbesondere zeigt sich, dass die intrinsische Hauptionenrotation, die in Richtung des Plasmastroms zeigt, mit zunehmender Randkollisionalität betragsmäßig abnimmt, was folglich das E_r-Profil im eingeschlossenen Plasma absenkt. Jedoch verän-

dert sich gleichzeitig auch das E_r-Profil in der SOL um den gleichen Betrag, was auf eine starke Wechselwirkung zwischen SOL-Flüssen und der toroidalen Randrotation hindeutet. Die Richtung der intrinsischen Randrotation folgt der der Pfirsch-Schlüter-Flüsse. Ein Vergleich mit der neoklassischen Theorie legt nahe, dass die poloidale Rotation der Hauptionen, wie erwartet, klein ist, wenn auch im Detail Abweichungen von der neoklassischen Theorie beobachtet werden. Insbesondere kann sie nicht das im Vergleich zur günstigen Driftkonfiguration flachere E_r-Profil erklären, welches in der ungünstigen Driftkonfiguration experimentell gefunden wird.

Messungen in Plasmen mit Ionenmischungen aus Wasserstoff (H) und Helium (He) zeigen einen konstanten Gesamtwärmefluss am L-H-Übergang, welcher unabhängig von der verwendeten Heizmethode ist. In Experimenten mit Mischungen aus Wasserstoff und Deuterium (D) von 5 – 95 % H-Gehalt zeigt P_{LH} eine nichtlineare Abhängigkeit vom relativen Wasserstoffgehalt, was mit einem im Vergleich zu reinem D erhöhten Wärme- und Teilchentransport in H zusammenhängt. Vergleiche von L-H- und H-L-Übergängen (der Übergang von der H-Mode zurück in die L-Mode) zeigen, dass das Minimum im E_r direkt vor dem jeweiligen Übergang den gleichen Wert hat. Diese Ergebnisse lassen für ITER den Schluss zu, dass der Ionenwärmefluss eine entscheidende Rolle für den L-H-Übergang spielt und somit Skalierungen, die auf der Annahme eines konstanten Wärmeflusses basieren, korrekte Vorhersagen liefern werden.

Frühere Ergebnisse von AUG zu den Abhängigkeiten von E_r in H-Mode und in L-Moden, die unter Standardbedingungen ausgeführt wurden, konnten bestätigt werden. Die neuen Messungen zeigen aber auch, dass die experimentell bestimmte Rotation am Plasmarand in L-Moden mit modifizierter magnetischer Konfiguration von der neoklassischen Theorie abweicht und dass E_r durch eine komplexe Wechselwirkung zwischen SOL-Strömungen, toroidaler Rotation und kinetischen Profilen bestimmt wird. Die experimentellen Daten können die Vorhersagen einer Änderung des E_r in der SOL durch Einflüsse der magnetischen Konfiguration oder des Wasserstoffisotops nicht bestätigen. Außerdem gibt es keine Indizien für eine vorherrschende Rolle des inneren oder äußeren E_r-Gradienten, um den L-H-Übergang herbeizuführen. Diese Ergebnisse sind ein wichtiger Beitrag für die Fusionsforschung, da die erlangten Erkenntnisse eine bessere Vorhersage des Plasmaverhaltens am L-H-Übergang in zukünftigen Fusionsreaktoren ermöglichen können, im Speziellen für die nicht-nukleare Phase des Testfusionsreaktors ITER.

Abstract

The high-confinement mode (H-mode) is a plasma regime in tokamak type fusion devices of improved energy and particle confinement. It exhibits a transport barrier at the outermost 5 % of the confined plasma region. The underlying mechanism leading to the transition from the low confinement mode (L-mode) to the H-mode, the so called L-H transition, is not fully understood, but the radial electric field E_r is considered to be responsible for the formation of the edge transport barrier. E_r exhibits a well with two strong gradients at the very edge of the confined plasma. These gradients produce a shear in the $E \times B$-velocity flow, which causes suppression of turbulent edge transport. The H-mode is accessed by surpassing a threshold in heating power (P_{LH}). P_{LH} shows some dependencies on changes in the scrape-off layer (SOL), a thin plasma region which separates the hot, confined fusion plasma from the first wall. A possible explanation is that E_r in the SOL is modified and, thus, is the outer E_r gradient, i.e. the gradient connecting the SOL and the confined plasma.

L-H transition experiments have been conducted at the ASDEX Upgrade tokamak in Garching to elucidate the role of the SOL-E_r for the access condition to H-mode. It was addressed whether the SOL-E_r shows changes in conditions for which P_{LH} is strongly increased, i.e. in unfavourable versus favourable magnetic drift configuration and in hydrogen versus deuterium plasmas. To measure the outer E_r gradient, a new diagnostic has been developed, which is based on the active spectroscopy of singly ionized helium (HES). With this new system it is possible to monitor E_r in all confinement regimes (L- and H-mode) with a time resolution of 2.45 ms. For a systematic interpretation of the measurements a synthetic diagnostics has been developed. Besides the E_r profiles, experimental edge kinetic electron and ion profiles, as well as impurity rotation profiles were examined and compared with their respective counterparts. Furthermore, power balance calculations were conducted to determine the energy separation in the ion and the electron channel and the experimental data were compared to predictions from local neoclassical theory.

It is found that prior to the L-H transition the outer E_r gradient shows little variation in most investigated cases and only steepens once the L-H transition has occurred. To first order the evolution of the edge E_r profile follows the main ion pressure gradient, but in L-mode the toroidal plasma rotation can have a non-negligible impact on the E_r profile. In particular it is found that the intrinsic main ion rotation becomes less co-current with increasing edge collisionality, leading to a decrease of E_r in the confined plasma. The SOL-E_r profile decreases concomitantly by about the same amount, which indicates a strong interaction between SOL flows and the edge toroidal rotation. The direction of the intrinsic edge rotation follows the Pfirsch-Schlüter flows. A comparison with neoclassical theory suggests that the main ion poloidal rotation is on the neoclassical level, although in detail deviations are observed. In particular, the experimentally observed differences, a shallower E_r well is found in unfavourable compared to favourable drift configuration, are not reproduced by neoclassical theory.

Measurements in hydrogen plasmas with helium doping show a constant edge ion heat flux at the L-H transition, which holds independently of the externally applied heating scheme. In mixed hydrogen-deuterium plasmas P_{LH} exhibits a non-linear dependence on the relative hydrogen content ($0 - 95\,\%$), which can be related to an increased heat and particle transport in hydrogen compared to deuterium L-modes. Comparisons of L-H and H-L transitions (the transition from H-mode back into L-mode) show that the minimum of the E_r well is the same at the respective transition. These observations can help to improve predictions for next-step fusion devices like ITER.

In this thesis I show that previous experimental findings from AUG on the dependencies of E_r in H-mode and in L-modes under standard conditions can be confirmed. With the new E_r measurements I document that the edge flows can deviate from neoclassical theory in L-modes with modified magnetic configuration and that E_r is formed by a complex interaction between SOL flows, toroidal edge rotation and edge kinetic profiles. The predicted effects of changes in the magnetic configuration or the hydrogen isotope on the SOL-E_r are not confirmed by the experiments. Furthermore, I find no evidence for a dominant role of the inner or the outer E_r gradient in the L-H transition. These results are an important contribution to the better understanding of the plasma behaviour at the L-H transition and, thus, help the fusion community to improve the predictions for future fusion reactors.

« *The truth is rarely pure and never simple.* »
– Oscar Wilde in ’The Importance of Being Earnest’ , 1895

Contents

1 Introduction **1**
- 1.1 Thermonuclear Fusion . . . 1
- 1.2 Tokamak Principle . . . 3
- 1.3 Diverted Plasmas . . . 5
- 1.4 ASDEX Upgrade . . . 5
- 1.5 The L-H Transition . . . 7
- 1.6 Thesis Scope . . . 8

2 Theoretical Background **9**
- 2.1 Particle Motion and Transport Processes in a Tokamak . . . 9
  - 2.1.1 Particle Motion . . . 9
    - 2.1.1.1 Guiding Centre Approximation . . . 9
    - 2.1.1.2 Particle Drifts . . . 10
  - 2.1.2 Collisional and Turbulent Transport . . . 11
    - 2.1.2.1 Classical Transport . . . 11
    - 2.1.2.2 Neoclassical Transport . . . 12
    - 2.1.2.3 Turbulent Transport . . . 14
- 2.2 Plasma Flows and the Radial Electric Field . . . 15
  - 2.2.1 Kinetic Equation and Fluid Description . . . 15
  - 2.2.2 Radial Force Balance . . . 16
  - 2.2.3 Generation of the Radial Electric Field . . . 17
  - 2.2.4 Neoclassical Plasma Flows . . . 18
    - 2.2.4.1 Structure of the Total Flow . . . 18
    - 2.2.4.2 Calculation of the Banana-Plateau Contribution . . . 18
    - 2.2.4.3 Neoclassical Poloidal and Toroidal Flows . . . 19
  - 2.2.5 E_r in the Scrape-off Layer . . . 20
- 2.3 Plasma Quantities . . . 21
  - 2.3.1 Confinement and Heating Power . . . 21
  - 2.3.2 Magnetic Equilibrium . . . 21
- 2.4 Background on the L-H Transition . . . 22
  - 2.4.1 Confinement Regimes . . . 23
    - 2.4.1.1 L-mode and H-mode . . . 23
    - 2.4.1.2 I-mode . . . 25
  - 2.4.2 The H-mode Power Threshold . . . 27
    - 2.4.2.1 Edge Ion Heat Flux . . . 27
    - 2.4.2.2 Dependence of P_{LH} on the Magnetic Configuration . . . 28
    - 2.4.2.3 Isotope Effect . . . 29
  - 2.4.3 The Role of the Radial Electric Field in the L-H Transition . . . 30
- 2.5 Coordinate System and Magnetic Configurations . . . 31
  - 2.5.1 Sign conventions . . . 31
  - 2.5.2 Favourable and Unfavourable Drift Configuration . . . 31

3 Methodology **35**
3.1 Plasma Diagnostics . . . 35
3.1.1 Integrated Data Analysis . . . 35
3.1.2 Beam-based Charge Exchange Recombination Spectroscopy . . . 35
3.1.3 Doppler Reflectometry . . . 36
3.1.4 Langmuir Probes . . . 37
3.1.5 Equilibrium Reconstruction . . . 37
3.2 Discharge Design . . . 38
3.3 Determination of the L-H Transition Time and Power . . . 39
3.4 Analysis Methods . . . 40
3.4.1 Power Balance Analysis . . . 40
3.4.2 Kinetic Profile Alignment . . . 41

4 Experimental Set-up **43**
4.1 Components . . . 43
4.2 Gas Inlet System . . . 43
4.2.1 Design of the Gas Valve . . . 45
4.2.2 Design of the Gas Supply and Pump System . . . 46
4.2.3 Calibration and Characterization of the Gas Valve . . . 46
4.2.3.1 Flow Rate . . . 47
4.2.3.2 Gas Cloud Shape . . . 48
4.2.3.3 Performance . . . 49
4.3 Spectroscopic System . . . 50
4.3.1 Components . . . 50
4.3.1.1 In-vessel Optics . . . 50
4.3.1.2 Spectrometer . . . 51
4.3.2 Calibration of the Spectroscopic System . . . 52
4.3.2.1 Geometry Calibration . . . 52
4.3.2.2 Radiance Calibration . . . 55
4.3.2.3 Wavelength Calibration . . . 56
4.3.2.4 Instrument Function . . . 59
4.3.2.5 Further Calibrations . . . 59
4.4 Operation . . . 60

5 Spectroscopic Methods **63**
5.1 Charge Exchange Recombination Spectroscopy . . . 63
5.1.1 Atomic Processes . . . 63
5.1.2 Deduction of Plasma Quantities . . . 64
5.1.2.1 Active Signal . . . 64
5.1.2.2 Passive Signal . . . 66
5.1.2.3 Corrections to the Measured Signal . . . 67
5.1.3 Derivation of the Radial Electric Field . . . 69
5.1.4 Comparison with Beam-based CXRS . . . 69
5.1.5 Limitations . . . 71
5.2 He II Spectroscopy . . . 74
5.2.1 Atomic Processes . . . 75
5.2.2 Deduction of Measured Quantities . . . 76
5.2.2.1 Active Signal . . . 76
5.2.2.2 Passive Signal . . . 77

5.2.2.3 Corrections to the Active Signal 78
5.2.2.4 Example Profiles and Limitations of the Measurement . 79
5.2.3 Derivation of the Radial Electric Field 81
5.2.4 Characterisation 82
5.2.5 Synthetic Diagnostics 85
5.2.5.1 Model 86
5.2.5.2 Results 87
5.2.6 Comparison with other E_r Diagnostics 90
5.2.6.1 Comparison with Beam-based CXRS 90
5.2.6.2 Comparison with Doppler Reflectometry 91
5.2.6.3 Comparison with Langmuir Probe Data 91

6 Diagnostic Effects on Radial Electric Field Measurements 95
6.1 Loss of LoS Alignment During Experimental Campaign 2019/2020 95
6.2 Diagnostic Comparison in Different Drift Configurations 96
6.2.1 Comparison in LSN Plasmas 97
6.2.1.1 Favourable Drift Configuration 97
6.2.1.2 Unfavourable Drift Configuration 99
6.2.2 Comparison in USN Plasmas 99
6.3 Consequences for Further Comparisons 101

7 H-mode Access in Different Drift Configurations 105
7.1 Density Dependence of P_{LH} and P_{IH} 105
7.2 Evolution of E_r in the Transition from L- to H-mode 107
7.2.1 Favourable Drift Configuration 107
7.2.2 Unfavourable Drift Configuration 112
7.3 Comparison of L-modes in Different Drift Configurations 114
7.3.1 LSN Plasmas 114
7.3.1.1 Discharges 114
7.3.1.2 Same Heating Power and Same Plasma Density 116
7.3.1.3 Different Heating Power and Same Plasma Density . . . 123
7.3.1.4 Same Heating Power and Different Plasma Density . . . 126
7.3.2 USN Plasmas 129
7.3.2.1 Same ECRH Power and Same Plasma Density 129
7.3.2.2 Different ECRH Power and Same Plasma Density 131
7.3.2.3 Different NBI Power and Same Plasma Density 132
7.3.3 LSN versus USN Plasmas 134
7.4 Comparison to Neoclassical Theory 135
7.4.1 LSN Plasmas 136
7.4.1.1 Same Heating Power and Same Plasma Density 136
7.4.1.2 Discussion of Uncertainties 138
7.4.1.3 Different Heating Power and Same Plasma Density . . . 141
7.4.1.4 Same Heating Power and Different Plasma Density . . . 144
7.4.2 USN Plasmas 146
7.4.2.1 Same Heating Power and Same Plasma Density 146
7.4.2.2 Different ECRH Power and Same Plasma Density 149
7.4.2.3 Different NBI Power and Same Plasma Density 150
7.4.3 Validity of Local Neoclassical Theory 151

7.5 E_r Profiles at the Confinement Transition . . . 153
  7.5.1 Favourable Drift Configuration at Different Densities . . . 153
  7.5.2 Favourable versus Unfavourable Drift Configuration . . . 155
    7.5.2.1 Low Density Branch . . . 155
    7.5.2.2 High Density Branch . . . 156
7.6 Discussion of Experimental Results . . . 157
  7.6.1 Power Threshold . . . 157
  7.6.2 Plasma Behaviour . . . 157
  7.6.3 E_r in L-mode . . . 157
    7.6.3.1 Evolution . . . 157
    7.6.3.2 Collisionality Dependence and Relation to SOL Flows . 158
    7.6.3.3 Favourable and Unfavourable Drift Configuration . . . 160
    7.6.3.4 Comparison to Theory . . . 161

8 The Isotope Effect of the L-H Transition 163
8.1 Investigations in Pure D, H and He Plasmas . . . 163
  8.1.1 Power Threshold . . . 164
  8.1.2 Edge Radial Electric Field . . . 165
8.2 Investigations in Mixed Main Ion Species Plasmas . . . 169
  8.2.1 H Plasmas with He Doping . . . 169
    8.2.1.1 Power Threshold and Edge Ion Heat Flux . . . 169
  8.2.2 Hydrogen-Deuterium Plasmas . . . 173
    8.2.2.1 High-Density Branch . . . 173
    8.2.2.2 Low-Density Branch . . . 184

9 Summary and Outlook 187
9.1 Summary . . . 187
9.2 Outlook . . . 190

Acknowledgements 203

1 Introduction

The first plasma operation of ITER (acronym for 'International Thermonuclear Experimental Reactor' or 'the way' in Latin) is scheduled for December 2025 and by now about 75 % of the entire work on this project has been accomplished to fulfil this goal [1]. ITER is a fusion research reactor of the tokamak type, which is currently built in Cadarache, France, to show the feasibility of a thermonuclear fusion power plant. This international project on the exploration of thermonuclear fusion is often strongly criticized, since it is one of the most expensive research projects in the history of mankind. At the same time it is highly demanded as it may pave the way for one promising future power supply. Controlled nuclear fusion is a cleaner and more sustainable energy source than coal or fossil fuels, more efficient and safer than other nuclear energy sources like nuclear fission and more reliable than state-of-the-art renewable power supplies like solar or wind energy. This would make nuclear fusion a provider of cheap and abundant electric energy in the long term. Although the basic principle of thermonuclear fusion is conceptually simple and similar processes take also place in the core of stars, like our Sun, the realization of controlled nuclear fusion faces some challenging problems. One of them is the demand for large devices which is mainly related to high turbulent transport and low energy confinement of the fusion plasma. The following considerations on controlled nuclear fusion for energy production are summarized from references [2–4].

1.1 Thermonuclear Fusion

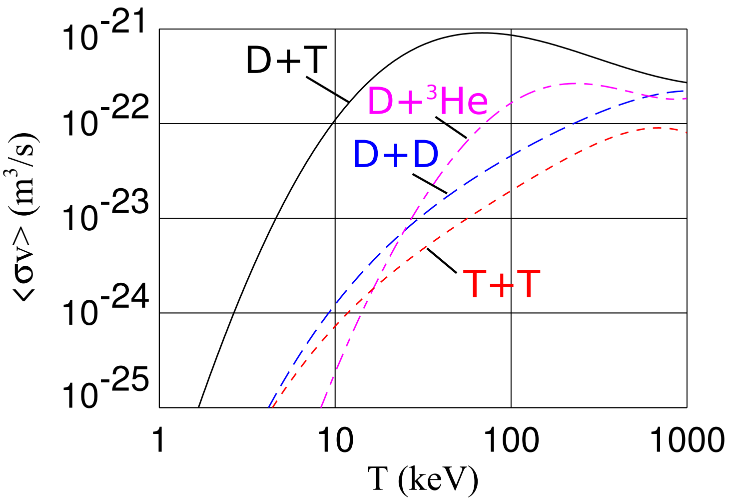

Figure 1.1: *Reaction processes for thermonuclear fusion on Earth.* Reaction rate coefficient of different fusion reactions against temperature. The DT reaction (black solid line) has the highest reaction rate and peaks at the lowest temperature, making it the most promising candidate for thermonuclear fusion reactions on Earth. Figure from [2].

The most important fusion processes used in thermonuclear fusion are shown in Figure 1.1. The process with the highest reaction rate coefficient $\langle \sigma v \rangle$ is the most attractive, also because it releases one of the highest amounts of energy per reaction. It employs as reactants the nuclei of the two heavier isotopes of hydrogen, deuterium (D) and tritium (T). The hydrogen isotope D is largely abundant in form of heavy water and the radioactive T with a half-life period of about 12 years can be produced from lithium (Li) by neutron capture. Li is also naturally abundant. The fusion of the D and T nuclei produces an alpha-particle (He) and a neutron (n) under the release of 17.6 MeV per reaction:

$$^{2}_{1}\mathrm{D} + ^{3}_{1}\mathrm{T} \rightarrow ^{5}_{2}\mathrm{He}^{*} \rightarrow ^{4}_{2}\mathrm{He} + ^{1}_{0}\mathrm{n} + 17.6\,\mathrm{MeV}. \tag{1.1}$$

Approximately 4/5 of the released energy is carried by the neutron. In a fusion reactor the neutron will be used to produce electric energy and to breed the T fuel from a Li blanket, while the energy of the alpha particle (3.52 MeV) will be used to heat the DT fuel.

For the nuclear fusion process to start the reactants have to be close enough for the strong interaction to act. For this the positively charged nuclei have to overcome the repelling Coulomb force. A temperature T of $T \geq 10\,\mathrm{keV} \approx 11.6 \times 10^{7}\,\mathrm{K}$ is required[1]. At such a high temperature the DT fuel is fully ionized and forms a plasma.

To reach ignition, which means a self-sustaining nuclear fusion reaction without the need of external heating, the fusion plasma has to fulfil the Lawson criterion [5], which gives constraints on the total plasma density n and the energy confinement time, τ_{E} :

$$nT\tau_{\mathrm{E}} \geq 3 \times 10^{21}\,\mathrm{m}^{-3}\,\mathrm{keV\,s} \tag{1.2}$$

τ_{E} is a figure of merit for the plasma energy isolation and is defined in Equation 2.49. In reality, power losses are present in a fusion reactor in form of plasma instabilities and turbulent outward transport. To make a fusion reactor economically efficient for energy production, τ_{E} has to be in the order of a few seconds.

A figure of merit for the efficiency of a fusion reactor is the fusion gain, Q, defined as:

$$Q = \frac{P_{\mathrm{fus}}}{P_{\mathrm{aux}}}. \tag{1.3}$$

P_{fus} is hereby the total fusion power, while P_{aux} is the total externally applied heating power. Thus, self-sustaining burning plasmas with $P_{\mathrm{aux}} = 0$ have $Q = \infty$. At $Q = 5$ the auxiliary heating power equals the internal heating by alpha-particles. The highest Q achieved so far was by DT operation in the JET (acronym for 'Joint European Torus') tokamak in 1997, which had $Q = 0.67$ [6]. In ITER $Q = 10$ is foreseen during its first phase of operation [1].

The above presented considerations are valid to a large extent for all types of thermonuclear fusion approaches, may it be for nuclear fusion via inertial confinement or via magnetic confinement. The presented work focuses on the latter one, which aims to confine the charged plasma particles by strong magnetic fields.

---

[1] In thermonuclear fusion it is the convention to give T in units of energy. This convention is also applied in this work. The Boltzmann constant k_{B} relates the thermal energy E_{therm} to T via $E_{\mathrm{therm}} = k_{\mathrm{B}}T$. Hence, $1\,\mathrm{eV} \approx 11\,600\,\mathrm{K}$.

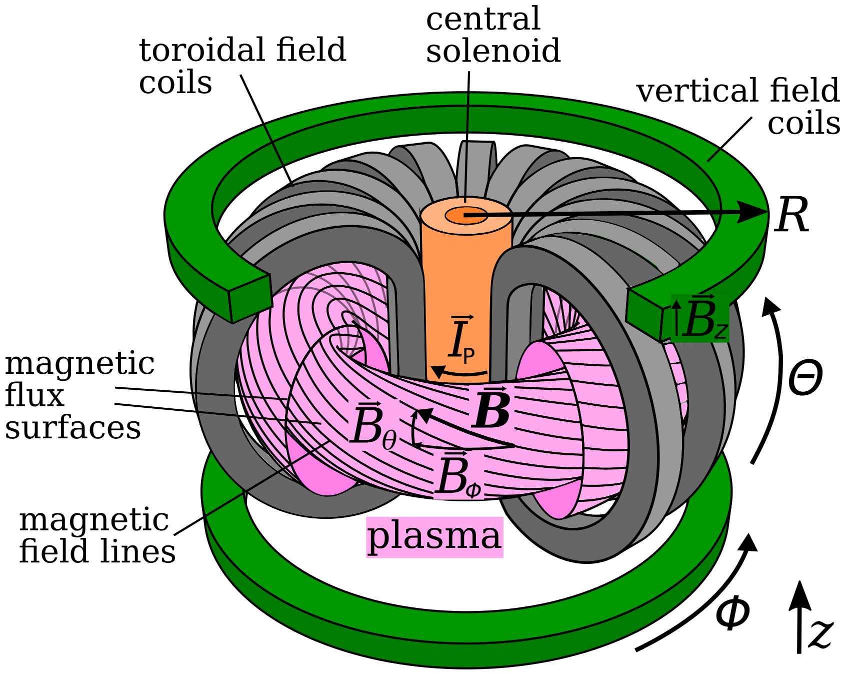

Figure 1.2: *Schematic of a tokamak.* The fusion plasma (pink) is confined by helical magnetic field lines in an axis-symmetric torus. The magnetic structure is produced by toroidal field coils (grey), creating a homogeneous toroidal magnetic field B_ϕ and a central solenoid (orange) which induces a toroidal plasma current I_p, leading to a poloidal magnetic field B_θ. The vertical field coils (green) are employed for stability. The vacuum vessel which surrounds the plasma would be located between the plasma and the magnetic field coils, but it is not shown in the schematic. Figure adapted from [2].

1.2 Tokamak Principle

The tokamak is the most established magnetic configuration type in magnetic confinement fusion. The name tokamak is an acronym of the Russian words 'toroidal chamber with magnetic coil'. The tokamak consists of an axis-symmetric torus of toroidal magnetic field coils (grey in Figure 1.2), producing a toroidal (ϕ) magnetic field $\boldsymbol{B}_\phi$, and a central solenoid (orange), which induces a toroidal current in the plasma (pink), $\boldsymbol{I}_\mathrm{p}$. According to Lenz's law this produces a poloidal (θ) magnetic field $\boldsymbol{B}_\theta$. $\boldsymbol{B}_\theta$ is needed to compensate particle drifts due to the intrinsic gradient of $\boldsymbol{B}_\phi$ along the radial coordinate of the torus (R). This drift would ultimately lead to a loss of confinement. As a result, the field lines of the total magnetic field $\boldsymbol{B}$ are still closed, but twist helically from the side of low magnetic field (low-field side or LFS) to the high-(magnetic-)field side (HFS). In this way, the charged plasma particles (ions and electrons), which gyrate along the magnetic field lines, are well confined and the outward drift can be compensated.

In the magnetic confinement approach a gradient in the plasma pressure ∇p is compensated by the magnetic force. In equilibrium no net force acts and, thus,

$$\nabla p = \boldsymbol{j} \times \boldsymbol{B}, \tag{1.4}$$

with $\boldsymbol{j}$ being the plasma current density. Applying this equation for the tokamak geometry leads to the Grad-Shafranov equation [7]. The equality of the two terms in Equation 1.4

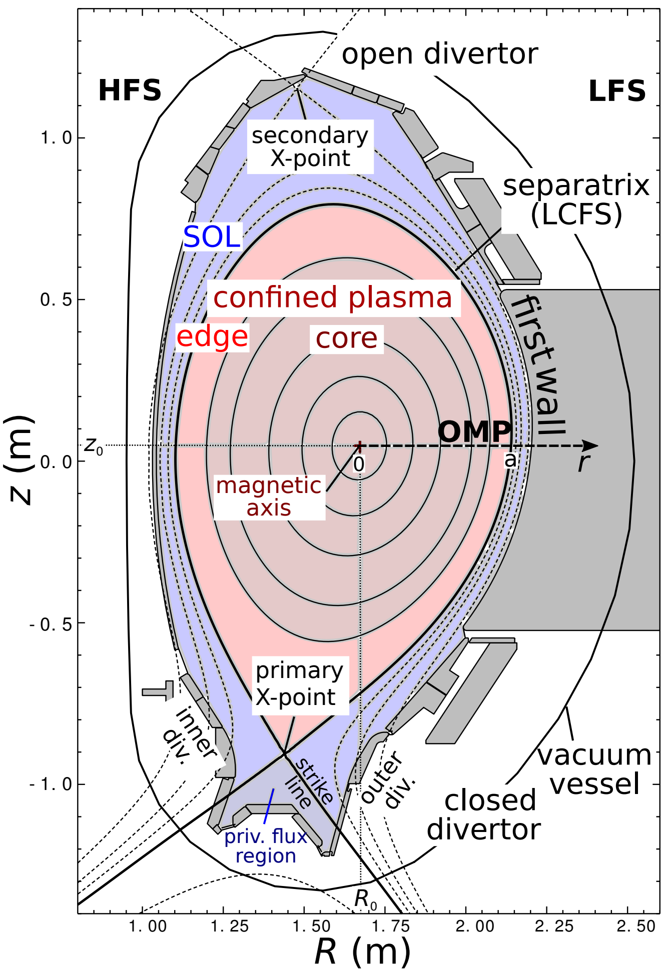

Figure 1.3: *Poloidal cross section of the ASDEX Upgrade tokamak.* In the divertor configuration the outermost magnetic field lines are intentionally led on target plates located in the divertor, a region of the wall remote from the confined plasma. In this way the interaction between the hot confined fusion plasma (red) and the first wall (grey) is reduced. Atomic processes mainly take place in the thin plasma region between the wall and the last closed flux surface of the confined plasma, which is called the scrape-off layer (SOL, blue).

implies that there is no pressure gradient along the magnetic field lines ($\boldsymbol{B} \cdot \nabla p = 0$). This produces concentric magnetic flux surfaces of constant plasma pressure.

The circular poloidal cross section of the magnetic flux surfaces can be modified, e.g. to form a diverted plasma (see Figure 1.3), by additional field coils, which are not shown in Figure 1.2. This is referred to as plasma shaping.

Due to the need of inducing a current in the plasma to produce $\boldsymbol{B}_\theta$, the plasma can only be confined over a limited time in a tokamak. Thus, a fusion reactor of the tokamak type has to rely on self-induced currents as well as the support of external current-drive (e.g. via the heating systems) to extend its plasma operation to a pulse length of several minutes.

1.3 Diverted Plasmas

In the early tokamak experiments the main plasma had a circular cross section and was limited by several points on the first wall, the limiters. At these limiters the interaction between plasma particles and wall material is strong. The impinging plasma particles erode the surface of the wall material, which also has to withstand high temperatures. The hereby arising impurity particles can easily enter the fusion plasma and decrease its fusion performance. To reduce the interaction between the hot, confined fusion plasma and the surrounding wall, the so called divertor configuration (see Figure 1.3) is realized in current research and future fusion reactors.

In the divertor configuration the outermost field lines are intentionally guided onto target plates, remote from the confined plasma. The whole volume around the target plates is called the divertor, whereas the entire plasma volume with field lines connecting to the divertor plates is called the scrape-off layer (SOL). The SOL separates the confined plasma from the plasma-facing components (PFCs) of the first wall (see Figure 1.3). The magnetic field lines in the SOL expand radially towards the divertor target plates. In this way the particle and heat flux density onto the target plates is decreased. If plasma particles escape the confined plasma, they enter the SOL, where they undergo ionization and recombination processes with colder parts of the plasma, consisting of impurities, ionized and recombined plasma particles and neutral gas particles. These different atomic interaction processes moderate the previously highly energetic particles from the main plasma on their way into the divertor. After neutralization in the divertor they are removed by cryogenic and other high-performance vacuum pumps. Also the He ash of a fusion reactor will be removed via the divertor.

The last closed flux surface (LCFS) of the confined plasma in the divertor configuration is called separatrix (see Figure 1.3). The diverted plasma features a primary and, for reasons of symmetry, a secondary X-point which is located on the other side of the equatorial axis. At the X-point the separatrix field line crosses (see Figure 1.3). The volume enclosed by the X-point and the divertor targets is called the private flux region. The part of the separatrix from the X-point to the divertor plates is called strike line and the crossing-point with the target plates strike point (SP).

The radial coordinate from the center of the magnetic flux surfaces, the magnetic axis, towards the first wall is denoted as r. Radial profiles of plasma quantities like p are given in terms of the normalized poloidal and toroidal flux coordinates ρ_{pol} and ρ_{tor}, respectively (see Equations 2.53 and 2.54). The radial profiles over the full plasma range are to first order symmetric with respect to these two radial coordinates.

If plasma quantities at the divertor are considered they are referred to as downstream, while plasma profiles at the mid-plane are referred to as upstream. Quantities regarding the plasma half located on the LFS are referred to as outer, e.g. outer mid-plane (OMP), and for the ones located on the HFS as inner, e.g. inner divertor.

1.4 ASDEX Upgrade

The experiments for the present work were conducted at the fusion research device ASDEX Upgrade (AUG), a tokamak operated since 1991 by the Max Planck Institute for Plasma Physics in Garching, Germany [8]. Its name is composed from the acronym 'axial symmetric divertor experiment' (ASDEX) and the word 'upgrade', as AUG it is the follow-up experiment of ASDEX. The characteristic parameters of AUG are given in Table 1.1. At AUG $B_\theta \ll B_\phi$, thus the inclination angle of the field lines is small, of the order of a few degree.

plasma parameter	symbol	value
major plasma radius	R_0	1.65 m
minor plasma radius	a	0.5 m
toroidal magnetic field at the magnetic axis	B_ϕ	1.8 – 3.2 T
plasma current at the magnetic axis	I_p	0.4 – 1.4 MA
discharge length	t	max. 10 s
installed auxiliary heating power	P_aux	36 MW
plasma volume	V	$13\,\mathrm{m}^3$
plasma mass		3 – 5 mg
plasma species		D, (H, He)

Table 1.1: Typical parameters of the medium-sized tokamak ASDEX Upgrade [8].

AUG is equipped with three different heating systems, two wave heating systems for electrons and ions and neutral beam injection (NBI), which together deliver a power of up to 36 MW. The wave heating systems transfer their energy onto the plasma particles by exciting resonances in the plasma. The electron cyclotron resonance heating (ECRH) transmits electromagnetic radiation in the frequency range of the electron gyration frequency (100 – 140 GHz), whereas ion cyclotron resonance heating (ICRH) employs electromagnetic radiation at the frequency of the ion gyration frequency (30 – 40 MHz). The energy deposition of the ECRH can be well localized and this method heats the electrons exclusively, whereas ICRH heats both plasma species. Each of the wave heating systems has a nominal heating power of about 8 MW.

The two neutral beam injectors are the most powerful heating system at AUG, with a nominal heating power of 10 MW each. In the beam lines hydrogen ions (D or H) are accelerated to kinetic energies of up to 60 and 93 keV, respectively. This energy is higher than the thermal energy of the plasma particles. The beam ions get neutralized before entering the plasma in order to be able to penetrate through the magnetic field up to the central part (plasma core) of the confined plasma. The beam neutrals get ionized and then transfer their kinetic energy onto the plasma particles by collisions. NBI is a heating method which heats both electrons and ions, where the ratio of electron to ion heating depends on the beam energy and the temperature of the plasma particles. The NBI exhibits a relatively broad heat deposition profile. Furthermore, the NBI system is a particle source and, due to its tangential injection geometry, transfers momentum onto the plasma.

As can be seen in Figure 1.3, AUG features two divertors, with the lower one being a closed divertor and the upper one an open divertor. The terms open and closed are connected to the recycling behaviour of neutrals at the strike line. Similar designs of closed divertors as the one of AUG are also planned for future fusion reactors [9]. The advantage of a closed divertor is that the confined, hot plasma and the interaction area of plasma particles with wall material are even better separated. The design of the closed divertor at AUG poses restrictions on the magnetic field configuration as is discussed in Section 2.5.2, but is considered to influence the access conditions to the high-confinement mode (H-mode) (see Section 2.4.2).

Since 2007 the first wall material of AUG is exclusively tungsten (W), which is a robust metal that also shows low erosion [10]. Only spurious amounts ($c_{\mathrm{W}} < 10^{-4}$) are allowed in the confined plasma, as higher concentrations lead to intolerable radiative cooling.

A coating of the first wall with a thin layer of boron (B) at regular intervals reduces the overall impurity content in the plasma and, thus, also controls the W-content. The coating process is called boronisation, where the reactive B acts as a getter layer [11–13].

Mainly deuterium (D) and occasionally hydrogen (H) or helium (He) are used as gas fuel at AUG. Together with a maximal central temperature of a few keV this implies that during a plasma discharge no substantial amount of fusion energy is produced.

One plasma pulse, also called plasma discharge, lasts up to 10 s and its duration is restricted by the Ohmic flux of the central solenoid and the heat up of the copper coils. The temporal development (time trace) of a plasma discharge at AUG can be split into three parts: the short ramp-up phase of the plasma current, the constant plasma current phase and the ramp-down phase of the plasma current. During one plasma discharge several plasma parameters can be influenced by many actuators including gas fuelling, the external heating power or the magnetic coils for the plasma shaping. The plasma performance can be studied with about 40 different diagnostics monitoring the various plasma parameters.

An experimental campaign lasts about 9 months, with 2 – 3 days of plasma operation per week and on average 20 successful discharges per operational day. During the venting of the plasma vessel, broken plasma-facing components (PFCs) and diagnostics are exchanged and exposed components are cleaned from coating, occurring due to plasma-material interaction. At the beginning and end of a vessel vent, the diagnostics are calibrated (post- and pre-calibration). In order to start a new experimental campaign, the plasma vessel has to reach ultra-high vacuum (UHV) conditions (10^{-8}mbar). For this, after closing the plasma vessel and pumping it with vacuum pumps (turbo-molecular pumps), the complete plasma vessel is heated to about 150 °C for about 72 h (the so called baking) in order to remove bound dust particles and water molecules from the PFCs [11].

1.5 The L-H Transition

The L-H transition is a plasma confinement transition in magnetically confined fusion plasmas from a state with low particle and energy confinement (L-mode) to a plasma state with improved particle and energy confinement (H-mode). The H-mode was discovered at ASDEX in 1982 and it is reached if a threshold in heating power (P_{LH}) is surpassed [14]. In H-mode the plasma exhibits a region of reduced turbulent transport, the edge transport barrier (ETB), in the outermost 5 % of the confined plasma. At the same time the edge gradients of the T- and n-profiles steepen in this radial region and form a pedestal, which leads to an elevation of the entire T- and n-profiles (see Figure 2.1). The higher reached values of T and n lead to an increased stored thermal plasma energy W_{th} (see Equation 2.48). According to Equation 2.49 this increases τ_{E}, since the increase in heating power to reach H-mode is only marginal. This improved confinement properties of the H-mode make it a desirable operational regime for future fusion reactors.

In tokamaks the H-mode is considered to be accessed if the shear rate of the $E \times B$-flow ($\gamma_{E \times B}$) is larger than the growth rate of the characteristic turbulence (γ_{turb}) [15], which means:

$$|\gamma_{E\times B}| > \gamma_{\mathrm{turb}}. \tag{1.5}$$

In this picture, referred to as the paradigm of a critical $\gamma_{E\times B}$ in the following, the shear of the poloidally directed $E\times B$-velocity ($v_{E\times B}$) decorrelates the turbulent structures and, thus, reduces radial turbulent transport. This implies that the radial electric field E_r at the plasma edge is the responsible quantity or at least an important parameter in the establishment of the H-mode. Although this mechanism of turbulence suppression by $E\times B$-shearing is widely accepted to be responsible for the L-H transition, it has not been proven unambiguously and other possible mechanisms leading to the L-H transition are conceivable [16].

The L-H transition is a highly reproducible phenomenon, observed at several tokamaks. Some dependencies of P_{LH} on changes in the SOL conditions or the used plasma species are common to the different tokamaks, others are not. The reasons for these differences are not fully understood as inter-machine comparisons are often difficult to achieve due to the different plasma specifications. However, dependencies like the increase of P_{LH} by a factor of two if the magnetic field configuration is changed from favourable to unfavourable drift configuration (see Section 2.5.2) and the inverse dependence of P_{LH} on the plasma isotope mass are common to all tokamaks, although the underlying reason for these changes in P_{LH} are not clear as of yet. In the paradigm of a critical $\gamma_{E\times B}$ needed for the L-H transition this implies that either the properties of the turbulent transport change or E_r at the plasma edge shows differences already in L-mode.

1.6 Thesis Scope

The present work aims to experimentally investigate the formation of E_r in L-mode around the separatrix and its development at the L-H transition. In this way it can be addressed whether E_r is responsible for the L-H transition and how SOL conditions influence both E_r and P_{LH}. For this purpose pairs of L-H transition experiments were conducted at AUG in plasma conditions for which it is known that P_{LH} differs. In particular, L-mode parameters and E_r profiles were compared in favourable versus unfavourable drift configuration and in H versus D plasmas. In order to monitor the E_r gradient across the separatrix in all confinement regimes, a new active spectroscopy diagnostics was developed, which detects the line emission of singly ionized helium (He II).

The thesis is ordered as follows: Chapter 2 provides the theoretical background on the formation of E_r and the current physics picture of the L-H transition. Chapter 3 describes the different measurement systems and methods and techniques used for the analysis and interpretation of the experimental data. In Chapter 4 the experimental set-up and the calibration of the new spectroscopic system are described. Chapter 5 investigates the two different approaches tested to spectroscopically detect the E_r gradient across the separatrix in L-mode and introduces the synthetic He II spectroscopy diagnostics. In Chapter 6 the measurements of the He II spectroscopy diagnostics are characterized by comparisons with other E_r measurement systems and the synthetic diagnostics. In Chapter 7 the results on the experiments of L-H transitions in different drift configurations and in Chapter 8 the results on the L-H transition experiments in different main ion species plasmas are presented. Chapter 9 finishes with conclusions drawn from these experiments and an outlook for the next steps regarding this study in understanding the role of E_r for the L-H transition.

2 Theoretical Background

2.1 Particle Motion and Transport Processes in a Tokamak

The idea of magnetic confinement fusion is to keep the charged plasma particles confined by strong magnetic fields. The typical topology is a torus to avoid losses of plasma at the end boundaries. Due to the toroidal geometry and external sources of particles and heat, spatial gradients exist. They lead to a collective movement of particles and energy, which is known as transport. The plasma transport along the magnetic field lines is fast, causing that plasma quantities like the plasma pressure p and the electrostatic plasma potential Φ_p are (almost) constant on a flux surface and only negligible gradients can develop in the direction parallel to the magnetic field. The transport perpendicular to the magnetic field is much slower, due to the existence of the magnetic flux surfaces (see Section 1.2). Since the perpendicular transport is directed radially outward, it is responsible for the decrease of the plasma confinement and, thus, reduces the fusion plasma performance [17]. After a general description of the particle motion, only perpendicular transport will be considered. As underlying transport mechanisms typically collisional and turbulent effects are distinguished.

2.1.1 Particle Motion

The equation of motion for a plasma particle α at time t and position $\boldsymbol{r}$ with mass m_α and electric charge q_α is given by [18]:

$$m_\alpha \frac{\mathrm{d}\boldsymbol{v}}{\mathrm{d}t} = \boldsymbol{F} + q_\alpha \boldsymbol{v} \times \boldsymbol{B}, \tag{2.1}$$

with $\boldsymbol{v} = \boldsymbol{v}(\boldsymbol{r}, t) = \mathrm{d}\boldsymbol{r}/\mathrm{d}t$ the velocity of α, $\boldsymbol{F} = \boldsymbol{F}(\boldsymbol{r}, t)$ a force acting on α and $\boldsymbol{B} = \boldsymbol{B}(\boldsymbol{r}, t)$ the magnetic field.

2.1.1.1 Guiding Centre Approximation

First it is assumed that no external force is present, i.e. $F = |\boldsymbol{F}| = 0$, and that the magnetic field is radially and temporally constant, i.e. $B = |\boldsymbol{B}| = \mathrm{const.}$. Then the particle experiences only the Lorentz force which is perpendicular to $\boldsymbol{v}$ and $\boldsymbol{B}$. The Lorentz force causes the particles to gyrate around the magnetic field lines with the gyration frequency (or cyclotron frequency) $\omega_{\mathrm{c},\alpha}$, which is defined as:

$$\omega_{\mathrm{c},\alpha} = \frac{|q_\alpha| B}{m_\alpha}. \tag{2.2}$$

The radius of the gyration motion (also called Larmor radius) of α, $r_{\mathrm{L},\alpha}$, is given as:

$$r_{\mathrm{L},\alpha} = \frac{v_{\perp,\alpha}}{\omega_{\mathrm{c},\alpha}} = \frac{m_\alpha v_{\perp,\alpha}}{|q_\alpha| B}, \tag{2.3}$$

with $v_{\perp,\alpha}$ being the absolute value of the velocity component perpendicular to $\boldsymbol{B}$. In a thermal plasma

$$r_{\mathrm{L},\alpha} = \frac{\sqrt{2 m_\alpha k_\mathrm{B} T_\alpha}}{|q_\alpha| B}, \tag{2.4}$$

with k_B the Boltzmann constant. Please note that $r_{\mathrm{L},\alpha}$ in Equation 2.3 is proportional to m_α and inversely proportional to B while the gyration frequency scales the other way round with these two quantities. Also, due to the different sign of charge, the helicity of the electron and the ion gyration is opposite.

$\boldsymbol{F}$ does not act on the particle's gyration motion, but leads to a movement of the gyration (or guiding) centre. Its motion can be considered separately from the gyration as long as it holds that $B/\nabla B \gg r_{\mathrm{L},\alpha}$ and $(\partial B/\partial t)/B \ll \omega_{\mathrm{c},\alpha}$ [3]. This so-called guiding centre approximation is valid in the here considered fusion plasmas.

2.1.1.2 Particle Drifts

The component of $\boldsymbol{F}$ parallel to $\boldsymbol{B}$ leads to an acceleration of the guiding centre, while the component perpendicular to $\boldsymbol{B}$ leads to a drift motion, $\boldsymbol{v}_\mathrm{D}$, of the guiding centre, given as:

$$\boldsymbol{v}_{\mathrm{D},\alpha} = \frac{\boldsymbol{F} \times \boldsymbol{B}}{q_\alpha B^2}. \tag{2.5}$$

$\boldsymbol{E}\times\boldsymbol{B}$ Drift The most important particle drift in this work is the $\boldsymbol{E}\times\boldsymbol{B}$ drift ($\boldsymbol{v}_{E\times B}$). It arises if an electric field, $\boldsymbol{E}$, is present, which is inherent to a tokamak plasma (see Section 2.2.3). Since $\boldsymbol{F} = q_\alpha \boldsymbol{E}$, $\boldsymbol{v}_{E\times B,\alpha}$ can be written as:

$$\boldsymbol{v}_{E\times B,\alpha} = \frac{\boldsymbol{E} \times \boldsymbol{B}}{B^2}. \tag{2.6}$$

This drift is independent of the charge and mass of the particle, i.e. its direction and value are the same for all plasma species.

$\nabla\boldsymbol{B}$ and Curvature Drift Two other drifts are very important in a tokamak since they arise due to the existence of a gradient in the absolute magnetic field (∇B-drift) and the curvature of the magnetic field lines (curvature drift). The magnetic force $\boldsymbol{F} = -\mu \nabla B$, with μ the magnetic moment, leads to a drift velocity, $\boldsymbol{v}_{\nabla B,\alpha}$, of:

$$\boldsymbol{v}_{\nabla B,\alpha} = -\frac{m_\alpha v_{\perp,\alpha}^2}{2 q_\alpha B^3} \nabla B \times \boldsymbol{B}. \tag{2.7}$$

The curvature of the magnetic field lines makes that the particles experience a centrifugal force while following them, which leads to a motion perpendicular to the field lines:

$$\boldsymbol{v}_{\mathrm{curv},\alpha} = -\frac{m_\alpha v_{\parallel,\alpha}^2}{q_\alpha B^3} \nabla B \times \boldsymbol{B}. \tag{2.8}$$

For these two drifts it holds that their sign depends on the particle charge. Moreover, these two drifts combined are almost proportional to the kinetic energy of the particle α.

Diamagnetic Drift Another drift occurring in a tokamak is the diamagnetic drift. It arises if a gradient ∇p_α is present in the pressure profile of all particles of the same species α. It leads to the following expression:

$$\boldsymbol{v}_{\mathrm{dia},\alpha} = -\frac{\nabla p_\alpha \times \boldsymbol{B}}{q_\alpha n_\alpha B^2}. \tag{2.9}$$

The diamagnetic drift does not, like the other particle drifts, cause a motion of the guiding centre and it can also not be understood as a single particle drift, but has to be considered in the fluid picture (see Section 2.2.1): The superimposition of ∇p_α on the gyration motion leads to an apparent drift motion of the plasma fluid. Since $\boldsymbol{v}_{\mathrm{dia},\alpha}$ is charge-dependent, it generates a current in the plasma, called the diamagnetic current $\boldsymbol{j}_{\mathrm{dia}}$.

2.1.2 Collisional and Turbulent Transport

In the following the different processes are reviewed which cause radial outward transport of particles and energy[1] in magnetically confined fusion plasmas. They can be categorized in two types, the collisional and the turbulent transport. Usually collisional transport is much smaller than turbulent transport, but collisional transport may become important in conditions in which turbulent transport is small, e.g. in the edge transport barrier (ETB) of the H-mode.

For diffusive transport radial gradients in the respective plasma quantities ($\nabla_r n$ for the particles and $\nabla_r T$ for the energy) lead, according to Fick's law of diffusion, to a particle and heat flux ($\mathit{\Gamma}$ and Q) which is directed opposite to the gradient:

$$\mathit{\Gamma} = -D\nabla_r n \tag{2.10}$$

and

$$Q = -\chi n \nabla_r T, \tag{2.11}$$

with D being the diffusion and χ the heat diffusion coefficient. Starting from these equations, the diffusivity coefficient will be determined depending on the considered transport mechanism. In the following the considerations are done for the particle transport but can be applied analogously to the heat transport [19]. First, the collisional transport is covered.

2.1.2.1 Classical Transport

Classical transport is the radial transport due to Coulomb collisions [2]. It can be treated as a stochastic movement of the particles (random walk) which is superimposed by the

---

[1] In this section the coefficients for the plasma species (electron, ion) at the respective quantities are omitted since the equations apply equally to each of the two plasma species. The transport in each plasma species can, thus, be considered separately.

density gradient. The characteristic scale length is the Larmor radius r_{L} of the particle, while the characteristic time τ is the inverse of the collision frequency, ν.

Thus, the diffusion coefficient of the classical transport is given by [20]:

$$D_{\mathrm{class}} = \frac{r_{\mathrm{L}}^2}{2\tau} = \frac{r_{\mathrm{L}}^2 \nu}{2}. \tag{2.12}$$

This equation shows that classical transport increases with increasing collision frequency. For Coulomb collisions between plasma species α and β the latter is given by [21]:

$$\nu_{\alpha,\beta} = \frac{4\sqrt{2\pi}}{3\,(4\pi\epsilon_0)^2} \frac{\sqrt{m_{\alpha,\beta}}}{m_j} \frac{q_\alpha^2 q_b^2 n_\alpha}{(k_{\mathrm{B}} T_\alpha)^{3/2}} \ln\mathit{\Lambda}_{\alpha,\beta}. \tag{2.13}$$

ϵ_0 is the dielectric constant, $m_{\alpha,\beta}$ the reduced mass of species α and β and $\ln\mathit{\Lambda}_{\alpha,\beta} \approx 15$ the Coulomb logarithm [18].

The classical transport is connected to the diamagnetic drift motion (see Equation 2.9) [20]. Since $\boldsymbol{v}_{\mathrm{dia}}$ depends on the charge of the particle it leads to $\boldsymbol{j}_{\mathrm{dia}}$. This, in turn, leads to a friction force $\boldsymbol{F}$ between the different plasma species, which is perpendicular to $\boldsymbol{B}$. According to Equation 2.5, a drift motion is produced which is directed radially outward for both plasma species. Thus, in a pure plasma, consisting of hydrogen ions and electrons only, classical transport is inherently ambipolar [22].

2.1.2.2 Neoclassical Transport

In neoclassical transport theory the toroidal geometry, i.e. the curvature of the magnetic field lines, is taken into account [23]. In such a geometry the parallel and the perpendicular motion of particles are coupled due to the mirror effect. The particles move along the field lines with their kinetic energy $E_{\mathrm{kin},\alpha} = 1/2 m_\alpha v_\alpha^2 = 1/2 m_\alpha (v_{\perp,\alpha}^2 + v_{\parallel,\alpha}^2)$. While moving towards higher B, their parallel velocity $v_{\parallel,\alpha}$ reduces and transforms into perpendicular velocity $v_{\perp,\alpha}$ due to the conservation of magnetic moment $\mu_\alpha = m_\alpha v_{\perp,\alpha}^2 / 2B$ and kinetic energy. This means if their kinetic energy is not high enough they can not pass to the HFS (as passing particles do), but will get trapped on the LFS (trapped particles). Due to the ∇B- drift motion, which displaces the particles from their original magnetic surfaces, the poloidal projection of the trapped particles' trajectory forms a banana-like shape, called banana-orbit. These trapped particles are a source of increased collisional perpendicular transport.

The excursion width w_{B} of the trapped particles is given by:

$$w_{\mathrm{B}} = \frac{q}{2} \frac{v_\perp}{v_\parallel} \Delta\mathit{\Theta} \approx \frac{r_{\mathrm{L}} q}{\epsilon} = \sqrt{\epsilon}\, r_{\mathrm{L,p}}, \tag{2.14}$$

with q being the safety factor (see Equation 2.55) and $\Delta\mathit{\Theta}$ the poloidal angle measured from the centre of the banana orbit to the turning point. $\epsilon = r/R$ is the inverse aspect ratio, which is much smaller than 1 in a non-spherical tokamak. The quantity $r_{\mathrm{L,p}}$ is the poloidal Larmor radius, for which B is replaced with B_θ in Equation 2.3, and, since usually $B_\theta \ll B_\phi$, $r_{\mathrm{L,p}} \gg r_{\mathrm{L}}$.

The effective collision frequency ν_{eff} making free particles trapped and vice versa is given by:

$$\nu_{\text{eff}} = \frac{\nu}{2\epsilon}. \tag{2.15}$$

Since the excursion width w_{B} is much larger than r_{L} and $\nu_{\text{eff}} > \nu$, collisions involving trapped particles increase the radial transport. In order to quantify the importance of trapped particles for the neoclassical transport coefficient D correctly, the ratio between the collision frequency and the trapped particle bounce frequency, ω_{B}, has to be considered. This dimensionless parameter is termed the collisionality, ν^*, and is defined as:

$$\nu^* = \frac{\nu}{2\epsilon\omega_{\text{B}}} = \frac{\nu q R}{\epsilon^{3/2} v_{\text{th}}}. \tag{2.16}$$

Hereby is q the safety factor, R the major radius, ϵ the inverse aspect ratio and v_{th} the thermal velocity of the trapped particle.

Banana Transport For low collisionality, i.e. $\nu^* \leq 1$ the trapped particles complete the banana orbit several times before they collide. This low-collisionality regime is known as banana regime and the diffusion coefficient, $D_{\text{neo,B}}$, is:

$$D_{\text{neo,B}} = \omega_{\text{B}}^2 \nu_{\text{eff}} f_{\text{t}} \approx \frac{q^2}{\epsilon^{3/2}} D_{\text{class}}, \tag{2.17}$$

with f_{t} the fraction of trapped particles, which increases with r [22]. The diffusion coefficient is larger than the classical diffusion coefficient by a large factor and it depends linearly on the collision frequency.

Plateau Transport For medium collisionality, i.e. $1 \leq \nu^* \leq \epsilon^{-3/2}$, the bounce frequency is about the collision frequency. Here, the diffusion coefficient, $D_{\text{neo,P}}$, is:

$$D_{\text{neo,P}} = \frac{v_{\text{th}} r_{\text{L}}^2 q}{R}. \tag{2.18}$$

Since $D_{\text{neo,P}}$ is independent of the collision frequency, this collisionality regime is called plateau regime.

Pfirsch-Schlüter Transport For high collisionality, i.e. $\nu^* \geq \epsilon^{-3/2}$, collisions occur before the particle finish the banana orbit. In this regime, the so-called Pfirsch-Schlüter regime, the diffusion coefficient, $D_{\text{neo,PS}}$, is:

$$D_{\text{neo,PS}} = q^2 r_{\text{L}}^2 \nu = q^2 D_{\text{class}}. \tag{2.19}$$

This means that transport is still increased due to the ∇B-drift compared to the classical transport but it is lower than in the banana regime.

The complete collisional transport is the sum of the transport originating from perpendicular friction, i.e. classical transport, and from parallel friction, i.e. neoclassical transport [22]. The obtained diffusion coefficients are, however, not large enough to explain the experimentally measured values of particle and heat diffusivity in a fusion plasma, which are caused by turbulent transport.

2.1.2.3 Turbulent Transport

The cause for turbulent transport is the destabilization of (electrostatic and electromagnetic) micro-instabilities which are present in a magnetically confined fusion plasma due to the magnetic geometry and the resulting kinetic plasma profiles. These micro-instabilities can be excited if critical values in the normalized gradients of the density $\nabla n/n$ or the temperature $\nabla T/T$ are exceeded. Depending on the actual driving mechanism and the type of transport they produce (heat or particle transport of ions or electrons), one can distinguish different types of micro-instabilities [20].

In the gyro-kinetic description, which is a special form of the kinetic description, starting also from the kinetic equation (Equation 2.26 or Equation 2.27) and assuming $(\partial B/\partial t)/B \ll \omega_{\mathrm{c},\alpha}$, the plasma quantities are normally decomposed in a fluctuating state (denoted with $\tilde{}$) and a background flow (denoted with $\hat{}$) [17]. The background flow is the average taken over the equilibrium distribution function f_α of the transported plasma quantity (n or T) for plasma species α (ions, electrons), whereas the fluctuating part occurs due to the disturbance of the distribution function from its equilibrium state [24]. For n this decomposition reads like:

$$n = n(\boldsymbol{r}, t) = \hat{n}(\boldsymbol{r}) + \tilde{n}(\boldsymbol{r}, t). \tag{2.20}$$

In the following we concentrate on the fluctuating part, $\tilde{n}$, since this is the driver of turbulent transport. The time average of the fluctuation $\tilde{n}$ is $\langle\tilde{n}\rangle = 0$.

The fluctuations can be considered as small irregular structures (turbulent eddies) with a correlation length (L_{c}) and a correlation time (τ_c). These quantities can be determined from the frequency spectrum of the Fourier-decomposition of the fluctuations. In the mixing-length model a turbulent structure flattens a gradient region equal to its correlation length [20]. This means for $\tilde{n}$:

$$\frac{\mathrm{d}n}{\mathrm{d}r} = \frac{\tilde{n}}{L_{\mathrm{c}}}. \tag{2.21}$$

Turbulent transport can only occur if the micro-instabilities can grow, i.e. they are destabilized. Therefore, the fluctuation in the transported quantity, here n, must be in the correct phase-relation to a fluctuation in the plasma potential, $\tilde{\Phi}_{\mathrm{p}}$ [17]. In this way locally an electric field perturbation, $\tilde{\boldsymbol{E}}$, builds up, which can, according to Equation 2.6, lead to a radial drift velocity $\tilde{v}_r$ [20]. This velocity is the characteristic velocity of the turbulence and can be also written in terms of the structure quantities, i.e. $\tilde{v}_r = L_{\mathrm{c}}/\tau_{\mathrm{c}}$.

The size of the turbulent particle transport is then calculated as:

$$\Gamma = \tilde{n}\tilde{v}_r. \tag{2.22}$$

This might look like a convective particle transport, but inserting Equation 2.21 into Equation 2.22 reveals the diffusive nature and delivers:

$$\Gamma = L_{\mathrm{c}}\tilde{v}_r\frac{\mathrm{d}n}{\mathrm{d}r} = \frac{L_{\mathrm{c}}^2}{\tau_{\mathrm{c}}}\frac{\mathrm{d}n}{\mathrm{d}r}. \tag{2.23}$$

Thus, the turbulent diffusivity D_{turb} is given by:

$$D_{\text{turb}} = \frac{L_{\text{c}}^2}{\tau_{\text{c}}}. \tag{2.24}$$

For typical values of the turbulent structures, diffusion coefficients in the order of m^2/s are obtained which is by 4 – 5 orders larger than typical classical diffusion coefficients [2].

2.2 Plasma Flows and the Radial Electric Field

In the following a theoretical description is given for the definition of a radial electric field E_r in a fusion plasma, starting from the equation of motion for a particle α in a magnetized plasma (see Equation 2.1).

2.2.1 Kinetic Equation and Fluid Description

In the particle picture each particle α is represented as a point in the six-dimensional space $(\boldsymbol{r}, \boldsymbol{v})$. Since a plasma consists of many particles of the same species α (electrons, ions, different impurities) and not each single trajectory of particle motion is of interest for the mean movement of α, the equations of motions of particles of the same species α can be simplified using the distribution function $f_\alpha(\boldsymbol{r}, \boldsymbol{v}, t)$ [18–20]. $f_\alpha(\boldsymbol{r}, \boldsymbol{v}, t)$ obeys the conservation equation, i.e.

$$\frac{\mathrm{d}f_\alpha}{\mathrm{d}t} = \frac{\partial f_\alpha}{\partial t} + \nabla f_\alpha \frac{\mathrm{d}\boldsymbol{r}}{\mathrm{d}t} + \nabla_v f_\alpha \frac{\mathrm{d}\boldsymbol{v}}{\mathrm{d}t} = 0. \tag{2.25}$$

Thus, in a plasma where no external forces are present the equation of motion reads:

$$\frac{\partial f_\alpha}{\partial t} + \boldsymbol{v}\nabla f_\alpha + \frac{q_\alpha}{m_\alpha}(\boldsymbol{E} + \boldsymbol{v} \times \boldsymbol{B}) \cdot \nabla_v f_\alpha = 0. \tag{2.26}$$

This is the Vlasov-equation, which neglects all forms of collisions. They can be implemented using the Fokker-Planck collision operator $C_\alpha(f_\alpha)$ [19], which leads to the kinetic equation:

$$\frac{\partial f_\alpha}{\partial t} + \boldsymbol{v}\nabla f_\alpha + \frac{q_\alpha}{m_\alpha}(\boldsymbol{E} + \boldsymbol{v} \times \boldsymbol{B}) \cdot \nabla_v f_\alpha = C_\alpha(f_\alpha). \tag{2.27}$$

In order to get a description of the average behaviour of all particles of plasma species α in real space (fluid motion), moments are taken of the kinetic equation, which are an integral of the distribution function f_α over the three-dimensional velocity space weighted with $\boldsymbol{v}^k$, where k is the order of the moment [18]. The motion of plasma species α is then described like a fluid. Hence, building different moments of the kinetic equation yields the magneto-hydrodynamic description of a magnetized plasma [19, 20].

The zeroth order moment leads to the continuity equation:

$$\frac{\mathrm{d}m_\alpha n_\alpha}{\mathrm{d}t} + m_\alpha n_\alpha \nabla \boldsymbol{u}_\alpha = 0, \tag{2.28}$$

with m_α being the mass of species α and $n_\alpha = \int f_\alpha \mathrm{d}^3\boldsymbol{v}$ the particle density. The total time derivative in the fluid description reads as $\mathrm{d}/\mathrm{d}t = \partial/\partial t + \boldsymbol{u}_\alpha \nabla$, with $\boldsymbol{u}_\alpha = 1/n_\alpha \int \boldsymbol{v} f_\alpha \mathrm{d}^3\boldsymbol{v}$.

To get the equation of motion for the fluid velocity $\boldsymbol{u}_\alpha$, the first order moment of Equation 2.27 is taken:

$$\underbrace{m_\alpha n_\alpha \frac{\mathrm{d}\boldsymbol{u}_\alpha}{\mathrm{d}t}}_{\text{inertia}} = \underbrace{q_\alpha n_\alpha (\boldsymbol{E} + \boldsymbol{u}_\alpha \times \boldsymbol{B})}_{\text{Lorentz force}} - \underbrace{\nabla p_\alpha}_{\text{pressure force}} - \underbrace{\nabla_\beta \boldsymbol{\Pi}_{\alpha,\beta}}_{\text{viscosity}} + \underbrace{\boldsymbol{R}_{\alpha,\beta}}_{\text{friction}}. \tag{2.29}$$

Here q_α is the charge, p_α the scalar pressure and $\boldsymbol{\Pi}_{\alpha,\beta}$ the viscous stress tensor[2], $\boldsymbol{R}_{\alpha,\beta}$ is the friction force between species α and β, respectively.

Equation 2.29 is known as the momentum conservation or force balance equation and in this form it is valid over the complete plasma range from the core to the SOL.

2.2.2 Radial Force Balance

For the following considerations a stationary plasma, i.e. $\mathrm{d}\boldsymbol{u}_\alpha/\mathrm{d}t = 0$, in thermodynamic equilibrium (i.e. the pressure is isotropic and the viscosity is zero) is considered [18]. If Equation 2.29 is developed in the Larmor radius $r_{\mathrm{L},\alpha}$ and friction forces are neglected then it simplifies in first order to [25]:

$$\nabla p_\alpha = \rho_\alpha (\boldsymbol{E} + \boldsymbol{u}_\alpha \times \boldsymbol{B}). \tag{2.30}$$

Taking the cross-product with $\boldsymbol{B}/B^2$ yields for the velocity perpendicular to $\boldsymbol{B}$, $\boldsymbol{u}_{\perp,\alpha}$:

$$\boldsymbol{u}_{\perp,\alpha} = -\frac{\nabla p_\alpha \times \boldsymbol{B}}{n_\alpha q_\alpha B^2} + \frac{\boldsymbol{E} \times \boldsymbol{B}}{B^2} = \boldsymbol{v}_{dia,\alpha} + \boldsymbol{v}_{E \times B}. \tag{2.31}$$

This means that in a magnetized plasma the perpendicular velocity of plasma species α is given by the sum of the diamagnetic and the $E \times B$ drift.

Since the pressure of species α, i.e. p_α, and the plasma potential $\varPhi_\mathrm{p}$ are flux functions, they show no gradients parallel to the magnetic field, i.e. $\nabla_\| p_\alpha = 0$ and $-\nabla_\| \varPhi_\mathrm{p} = \boldsymbol{E}_\| = 0$. In radial direction an electric field ($\boldsymbol{E}_r = E_r \boldsymbol{e}_r$)[3] can emerge, governed by the radial transport of electrons and ions. Using Equation 2.31 and an axis-symmetric coordinate system (R, ϕ, θ)[4] (see Figure 1.2), this leads to the radial force balance equation of species α :

$$E_r = \frac{\nabla_r p_\alpha}{n_\alpha q_\alpha} + v_{\perp,\alpha} B = \frac{\nabla_r p_\alpha}{n_\alpha Z_\alpha e} - v_{\theta,\alpha} B_\phi + v_{\phi,\alpha} B_\theta. \tag{2.32}$$

With $\nabla_r = \partial/\partial R$, $\boldsymbol{u}_{\perp,\alpha} = v_{\perp,\alpha} \boldsymbol{e}_\perp$ and $q_\alpha = Z_\alpha e$, where Z_α is the charge number of species α and e the electron charge. $v_{\phi,\alpha}$ and $v_{\theta,\alpha}$ are the toroidal and the poloidal velocity and B_ϕ and B_θ the toroidal and poloidal magnetic field components.

---

[2] The scalar pressure p_α and the viscous stress tensor $\boldsymbol{\Pi}_{\alpha,\beta}$ can be combined in the pressure tensor $\boldsymbol{P}_{\alpha,\beta}$, in which p_α are the diagonal and $\boldsymbol{\Pi}_{\alpha,\beta}$ the non-diagonal entries.

[3] In the running text of the following chapters the boldface typesetting of $\boldsymbol{E}_r$ and other vector quantities is omitted for better readability.

[4] AUG uses a left-handed (R, ϕ, θ) system (see Section 2.5.2). Therefore, in this work the following equality holds: $-\boldsymbol{e}_r = \boldsymbol{e}_\phi \times \boldsymbol{e}_\theta$, with $\boldsymbol{e}$ denoting the unit vector in the respective direction.

Every plasma species α is subject to the same E_r, although the relative importance of the pressure gradient term (or diamagnetic term), $(\nabla_r p_\alpha)/(n_\alpha Z_\alpha e)$, compared to the v×B-term, $v_{\perp,\alpha} B$, can vary for each plasma species α. For example, for impurities at the plasma edge it holds that $E_r \approx -v_{\theta,\mathrm{imp}} B_\phi$.

2.2.3 Generation of the Radial Electric Field

From the quasi-neutrality condition of a plasma, which requires that $n_e \approx n_i$, and the Poisson equation it follows that an electric potential will always be shielded on a scale given by the Debye-length:

$$\lambda_\mathrm{D} = \sqrt{\frac{\epsilon_0 k_\mathrm{B} T}{n e^2}}. \tag{2.33}$$

Due to this shielding mechanism the electric potential in the confined plasma, the plasma potential Φ_p, can be considered constant for scales larger than λ_D. However, $\boldsymbol{E}_\perp = -\nabla_\perp \Phi_\mathrm{p} \neq 0$ is found in a magnetized plasma even on a scale larger than λ_D. There, an electric field can form although the quasi-neutrality condition is fulfilled due to the gyro-motion [26].

λ_D is a few tenth of µm in a fusion plasma [18]. On the other hand the ions and electrons precess around their guiding centre, with their respective Larmor radius (see Equation 2.3). $r_\mathrm{L,e}$ is also in the range of a few tenth of µm, but the Larmor radius of the ions, $r_\mathrm{L,i}$ is, due to their higher mass, larger, in the range of a few mm. This radial displacement of electron and ion charge, called the polarisation density, leads to an electric field E. It can be shown in the gyro-kinetic framework that the equilibrium E-field fulfils Equation 2.30 [27].

This leads for E_r to its determining equation:

$$E_r = \frac{\nabla_r p_i}{n_i Z_i e} - v_{\theta,i} B_\phi + v_{\phi,i} B_\theta, \tag{2.34}$$

which is the radial force balance of the plasma main ions i.

A modification of the ion diamagnetic pressure gradient or the ion flow velocities lead to a modification of E_r. In toroidal geometry E_r is undetermined because the toroidal rotation is a free parameter [28]. Therefore, mechanisms are needed which set the toroidal velocity and, thus, E_r. Various mechanisms are known, amongst them neutral friction, turbulent Reynolds stress, fast-ion orbit width effects, ion orbit losses or toroidal torque input by the neutral beam injection (NBI) [29–32]. Some of these mechanism modify directly the toroidal rotation, like torque input by NBI, others lead to non-ambipolar particle transport, which has to be compensated by the radial electric. Especially at the plasma edge E_r exhibits comparably large values (see e.g. Figure 2.1).

Based on neoclassical theory an expression for the poloidal and toroidal ion velocities, $v_{\theta,i}$ and $v_{\phi,i}$, can be found if, for the latter, the impurity velocity $v_{\phi,\mathrm{imp}}$ is known. This is shown in the next section.

2.2.4 Neoclassical Plasma Flows

Due to the continuity equation (Equation 2.28) plasma flows are divergence free, i.e. $\nabla \cdot \boldsymbol{u}_\alpha = 0$. In a toroidal geometry the perpendicular flow velocity $\boldsymbol{u}_{\perp,\alpha}$ (see Equation 2.31) is not divergence-free at least in consequence of the diamagnetic drift velocity term. It has to be compensated by parallel flows, the so-called Pfirsch-Schlüter (PS) flows $\boldsymbol{u}_{\|,\alpha}^{\mathrm{PS}}$. In the following these flows will be deduced in the framework of neoclassical (NC) theory, leading to expressions for $v_{\phi,\alpha}$ and $v_{\theta,\alpha}$.

2.2.4.1 Structure of the Total Flow

Re-writing the perpendicular velocity results in:

$$\boldsymbol{u}_{\perp,\alpha} = -(\omega_{\mathrm{dia},\alpha} + \omega_{E\times B}) \frac{RB_\theta}{B} \boldsymbol{e}_\perp, \tag{2.35}$$

with the diamagnetic rotation frequency $\omega_{\mathrm{dia},\alpha}$ and the $E\times B$ rotation frequency $\omega_{E\times B}$. Assuming that the total flow is divergence free, the total parallel velocity reads as:

$$\boldsymbol{u}_{\|,\alpha} = \underbrace{\omega_{\mathrm{dia},\alpha} RB_\phi \left(\frac{1}{B} - \frac{B}{\langle B^2 \rangle} \right) \boldsymbol{e}_\|}_{=\boldsymbol{u}_\|^{\mathrm{PS}}} + \underbrace{\hat{u}_\alpha \frac{B}{\langle B^2 \rangle} \boldsymbol{e}_\|}_{=\boldsymbol{u}_\|^{\mathrm{BP}}} + \underbrace{\omega_{E\times B} RB_\phi \frac{1}{B} \boldsymbol{e}_\|}_{=\boldsymbol{u}_\|^{E\times B}} . \tag{2.36}$$

The first term is the PS velocity, $\boldsymbol{u}_\|^{\mathrm{PS}}$, which compensates the finite divergence of the diamagnetic term in $\boldsymbol{u}_\perp$. It shows a poloidal variation due to the variation of B and changes its direction at the top and the bottom of a flux surface. However, its flux surface-average $\langle \boldsymbol{u}_\|^{\mathrm{PS}} \boldsymbol{B} \rangle = 0$. The second term, $\boldsymbol{u}_\|^{\mathrm{BP}}$, is the banana-plateau velocity. It is divergence-free and arises due to collisions of trapped and passing particles. $\hat{u}_\alpha$ is the quantity which is calculated in neoclassical codes [22]. The last term, $\boldsymbol{u}_\|^{E\times B}$, compensates the divergence of the $E\times B$- drift. Thus, it allows for an additional degree of freedom via a stiff toroidal rotation. In this way the total plasma flow of each species α complies with the radial force balance [33]. $\langle \boldsymbol{u}_\|^{\mathrm{E\times B}} \boldsymbol{B} \rangle \neq 0$, but the same for all species α, and, thus, it does not produce any friction force between the particles. Therefore, it also does not add to $\hat{u}_\alpha$ [33].

Combining Equations 2.35 and 2.36 gives for the total flow velocity $\boldsymbol{u}_\alpha$ an expression of the following form:

$$\boldsymbol{u}_\alpha = (\omega_{\mathrm{dia},\alpha} + \omega_{E\times B}) R\boldsymbol{e}_\phi + k_\alpha \boldsymbol{B} = \omega_\alpha R\boldsymbol{e}_\phi + k_\alpha \boldsymbol{B}, \tag{2.37}$$

with $k_\alpha = (\hat{u}_\alpha - \omega_{\mathrm{dia},\alpha} RB_\phi)/\langle B^2 \rangle$. This equation shows that the total plasma flow of species α, $\boldsymbol{u}_\alpha$, can be expressed by a rigid body rotation of angular frequency ω_α, which is purely toroidal, and a component parallel to the magnetic field [34].

2.2.4.2 Calculation of the Banana-Plateau Contribution

According to [35] $\hat{u}_\alpha$ can be calculated from the flux-surface-averaged parallel momentum balance (see Equation 2.29):

$$\langle \boldsymbol{B} \cdot (\nabla \boldsymbol{P}_{\alpha,\beta})_\| \rangle = \langle \boldsymbol{B} \cdot (\boldsymbol{R}_{\alpha,\beta})_\| \rangle. \tag{2.38}$$

This leads to a set of coupled equations, where $\hat{u}_\alpha$ depends on the viscosity coefficients, the collision frequencies and the pressure gradient. The solution of this coupled equation system gives the banana-plateau contribution to the neoclassical perpendicular and toroidal flows.

2.2.4.3 Neoclassical Poloidal and Toroidal Flows

Taking the toroidal and poloidal projection of Equation 2.37 gives the following two equations for the size of the toroidal and poloidal flows:

$$v_{\theta,\alpha} = k_\alpha B_\theta \tag{2.39}$$

and

$$v_{\phi,\alpha} = \omega_\alpha R + k_\alpha B_\phi . \tag{2.40}$$

These equalities imply that the strength of the neoclassical poloidal flow and the neoclassical contribution to the toroidal flow scale with their respective poloidal and toroidal magnetic field components.

Neoclassical poloidal flows will always remain small, since the damping of the poloidal velocity is very high due to the collisions with the trapped particles. On the other hand a pure toroidal velocity will not experience any damping from trapped particles. There is no process in NC theory to set the toroidal rotation and with Equation 2.34 this is also true for E_r. However, NC theory can predict the differential parallel and, thus, the toroidal velocity between two species α and β if the velocity of one species is known. From this also E_r can be determined using the radial force balance.

According to [36] the neoclassical poloidal main ion (i) and impurity (A) rotations can be calculated as:

$$v_{\theta,i} = \frac{1}{2} v_{th,i} r_{\mathrm{L},i} \left(K_1 \frac{1}{L_{T_i}} \right) \frac{B B_\phi}{\langle B^2 \rangle} \tag{2.41}$$

and

$$v_{\theta,A} = \frac{1}{2} v_{th,i} r_{\mathrm{L},i} \left(\left(K_1 + \frac{3}{2} K_2 \right) \frac{1}{L_{T_i}} - \frac{1}{L_{p_i}} + \frac{Z_i T_A}{Z_A T_i} \frac{1}{L_{p_A}} \right) \frac{B B_\phi}{\langle B^2 \rangle} \tag{2.42}$$

Hereby are K_1 and K_2 the two viscosity-coefficients defined in [36], which are collisionality-dependent.

For a given toroidal impurity velocity $v_{\phi,A}$ the toroidal velocity of the main ions ($v_{\phi,i}$) is [36]:

$$v_{\phi,i} = v_{\phi,A} + \frac{v_{\mathrm{th},i} r_{\mathrm{L},i}}{2 B_\theta} \frac{3 K_2}{2} \frac{1}{L_{T_i}} . \tag{2.43}$$

It can be shown with Equations 2.41 – 2.43 that the neoclassical poloidal rotation flips sign with a sign change pf B_ϕ, whereas it does not change with a reversal of B_θ. For the toroidal rotation it is the other way round [36].

2.2.5 E_r in the Scrape-off Layer

Starting from the momentum conservation equation (Equation 2.29) an expression for the parallel electric field can be derived, assuming singly ionized plasma species [37,38]:

$$E_{\parallel} = \underbrace{\frac{j_{\parallel}}{\sigma_{\parallel}}}_{\text{from friction force}} - \underbrace{\frac{1}{en_e}\nabla_{\parallel}p_e}_{\text{from pressure gradient force}} - \underbrace{\frac{0.71}{e}\nabla_{\parallel}T_e}_{\text{from thermo-electric force}} . \tag{2.44}$$

Here $j_{\parallel} = en(v_i - v_e)$ is the parallel current density with the ion and electron velocities v_i, v_e. $\sigma_{\parallel} = (e^2 n)/(m_e \nu_{ei})$, is the parallel heat conductivity, where ν_{ei} is the collision frequency between electrons and ions [37]. This parallel force balance equation is also known as Ohm's law of the SOL since it connects the electric field with the current-density.

Integrating Equation 2.44 in the SOL from the divertor target plates (denoted with t) upstream to the outer mid-plane (denoted with OMP), assuming $j_{\parallel} = 0$ and some constraints on the shape of p_e along the field line [39], delivers an analytic expression for the electric potential at the outer mid-plane, V_{OMP} for each flux surface ψ :

$$V_{\text{OMP}} = \underbrace{\frac{2.8}{e}T_{e,\text{t}} + V_{\text{fl}}}_{=V_{\text{sh}}} + \underbrace{\frac{0.71 + a}{e}(T_{e,\text{OMP}} - T_{e,\text{t}})}_{\text{pre-sheath}}, \tag{2.45}$$

where V_{fl} is the potential of the electrically floating divertor target plates and $a = \ln 2/\ln(T_{e,\text{OMP}}/T_{e,\text{t}})$. E_r at the OMP is then calculated as $-\nabla_r V_{\text{OMP}}(r)$.

The two equations above show that the electric potential in the SOL, V, is not a flux function [5], but decreases towards the divertor to V_{fl}. To still sustain the ambipolarity condition, i.e. $\Gamma_e = \Gamma_i$ on the divertor target plates, an additional parallel electric field arises just in front of the wall which repels the electrons [18,37]. The sum of the first two terms on the right-hand side of Equation 2.45 is known as the Debye-sheath potential V_{sh}, which occurs in the region of a few Debye-length in front of the target due to violation of the quasi-neutrality. The second term on the right-hand side of Equation 2.45 shows that already in the SOL further upstream from the Debye-sheath a drop of the plasma potential occurs which is referred to as the pre-sheath potential drop.

In the sheath-limited or low-recycling regime, appearing at low collisionality, parallel gradients are small and, thus, $T_{e,\text{OMP}} \approx T_{e,\text{t}}$ [37]. The plasma potential drop is then given by the Debye-sheath potential drop V_{sh} and E_r at the OMP is:

$$E_r \approx -\nabla_r V_{\text{sh}} = -\frac{2.8}{e}\nabla_r T_{e,\text{t}}, \tag{2.46}$$

where $T_{e,\text{t}}$ is the electron temperature at the target mapped to the OMP.

In the conduction-limited or high-recycling regime ionization processes within the SOL become important, leading to $\nabla_{\parallel}T_e \neq 0$ [37]. Thus, $T_{e,\text{OMP}} \gg T_{e,\text{t}}$ and E_r reads:

$$E_r \approx -\frac{1}{e}\nabla_r T_{e,\text{OMP}}. \tag{2.47}$$

---

[5] As discussed before in the confined plasma it can be assumed that $V(\Psi) = \Phi_{\text{p}} = \text{const}$.

In both cases it is assumed that V_{fl} at the target plate is radially constant which is the case if no current flux is present in the divertor targets. The two equations also indicate that normally E_r is positive in the SOL, since $\nabla_r T_{e,\mathrm{t}}$ and $\nabla_r T_{e,\mathrm{OMP}}$ are negative in the SOL.

2.3 Plasma Quantities

In the following important plasma quantities are introduced in order to describe the plasma behaviour, plasma performance and the magnetic equilibrium.

2.3.1 Confinement and Heating Power

The confinement of a plasma is to first order characterized by two quantities. The thermal energy W_{th} stored in the plasma is given by [3]:

$$W_{\mathrm{th}} = \frac{3}{2}\int (p_i + p_e)\mathrm{d}V = \frac{3}{2}\int (n_i T_i + n_e T_e)\mathrm{d}V, \tag{2.48}$$

where p_i, T_i, n_i are the kinetic profiles (pressure, temperature, density) of the ions and p_e, T_e, n_e those of the electrons. V is the plasma volume.

The energy confinement time τ_{E} is defined as:

$$\tau_{\mathrm{E}} = \frac{W_{\mathrm{th}}}{P_{\mathrm{loss}}} = \frac{W_{\mathrm{th}}}{P_{\mathrm{net}} - P_{\mathrm{rad,main}}}, \tag{2.49}$$

where $P_{\mathrm{loss}} = P_{\mathrm{sep}}$ the power which crosses the separatrix, $P_{\mathrm{rad,main}}$ is the power loss due to radiation in the main chamber and P_{net} is the net input power defined as:

$$P_{\mathrm{net}} = P_{\mathrm{heat}} - \frac{\mathrm{d}W_{\mathrm{th}}}{\mathrm{d}t} = P_{\mathrm{OH}} + P_{\mathrm{aux}} - \frac{\mathrm{d}W_{\mathrm{th}}}{\mathrm{d}t}. \tag{2.50}$$

P_{heat} is hereby the absorbed heating power from all heating contributions, namely the Ohmic power P_{OH} introduced through the plasma current and all applied auxiliary heating contributions $P_{\mathrm{aux}} = P_{\mathrm{NBI}} + P_{\mathrm{ECRH}} + P_{\mathrm{ICRH}}$, corrected for their respective losses. P_{net} also includes a correction for changes of the plasma stored energy $\mathrm{d}W_{\mathrm{th}}/\mathrm{d}t$.

In equilibrium it is:

$$P_{\mathrm{net}} = P_{\mathrm{loss}} + P_{\mathrm{rad,main}} = Q_i + Q_e + P_{\mathrm{rad,main}}, \tag{2.51}$$

where $Q_{i,e}$ is the total integrated ion and electron heat flux, respectively. $P_{\mathrm{rad,main}}$ is often neglected in these definitions due to limited measurement capabilities.

2.3.2 Magnetic Equilibrium

As stated in Section 1.2 the magnetic equilibrium of a tokamak is given by the Grad-Shafranov Equation, which is a representation of the magnetic equilibrium equation

(Equation 1.4) for toroidal geometry [40, 41]:

$$-\left(\frac{\partial^2\psi}{\partial^2 R}-\frac{1}{R}\frac{\partial\psi}{\partial R}+\frac{\partial^2\psi}{\partial z^2}\right)=\mu_0 R^2\frac{\mathrm{d}p}{\mathrm{d}\psi}+f\frac{\mathrm{d}f}{\mathrm{d}\psi}=\mu_0 R j_\phi, \tag{2.52}$$

with μ_0 the permeability and ψ the poloidal magnetic flux. p and f are flux functions describing the plasma pressure and the poloidal current and j_ϕ is the toroidal current-density. The equation describes a set of nested surfaces with constant magnetic flux ψ, the magnetic flux surfaces (see Section 1.2). Equilibrium codes solve this equation in an iterative manner for ψ, with constraints on p and f by measurements (see Section 3.1.5).

From the magnetic equilibrium two radial coordinates can be defined. The poloidal normalized flux ρ_{pol} is given by:

$$\rho_{\mathrm{pol}}=\sqrt{\frac{\psi-\psi_{\mathrm{ax}}}{\psi_{\mathrm{sep}}-\psi_{\mathrm{ax}}}}, \tag{2.53}$$

with ψ_{ax} and ψ_{sep} the poloidal magnetic flux at the magnetic axis and the separatrix, respectively.

The toroidal normalized flux ρ_{tor} is given by:

$$\rho_{\mathrm{tor}}=\sqrt{\frac{\phi-\phi_{\mathrm{ax}}}{\phi_{\mathrm{sep}}-\phi_{\mathrm{ax}}}}, \tag{2.54}$$

where ϕ_{ax} and ϕ_{sep} are the toroidal magnetic flux at the magnetic axis and the separatrix, respectively.

For both normalized flux coordinates one has $\rho = 0$ at the magnetic axis and $\rho = 1$ at the separatrix. ρ_{tor} (as ϕ) is not defined outside the separatrix, whereas ρ_{pol} can also be larger than 1.

The two quantities are related via the safety factor q, given by:

$$q=\frac{\mathrm{d}\phi}{\mathrm{d}\psi}. \tag{2.55}$$

The safety factor expresses the helicity of the magnetic field lines and can be also written as $q = m/n$, with m the number of poloidal and n the number of toroidal turns. The sign of the safety factor indicates whether the field lines have a left-hand or a right-hand helicity.

2.4 Background on the L-H Transition

In the following information on the phenomenology of the transition from L-mode to H-mode (L-H transition) is given.

2.4.1 Confinement Regimes

The three confinement regimes investigated in this work are the L-, the I- and the H-mode. They are also the most common observed confinement regimes of a tokamak. The L-mode (low-confinement mode) can be considered the standard confinement regime, while the H-mode (high-confinement mode) is reached if sufficient heating power is supplied to the plasma. Compared to the L-mode, the H-mode exhibits improved particle and energy confinement. The I-mode is a regime which shows improved energy, but L-mode-like particle confinement.

2.4.1.1 L-mode and H-mode

Figure 2.1a shows a typical radial p_i-profile in L-mode (black) and H-mode (red) from the ASDEX Upgrade tokamak. Figure 2.1b depicts the respective L- and H-mode E_r profiles. As can be seen in the figure, H-mode features steep p_i and E_r gradients at the plasma edge (region from $\rho_{\mathrm{pol}} \approx 0.96 - 1$, marked in yellow), which are much stronger than in L-mode. The formation of the steep edge p_i gradient in H-mode implies a higher boundary condition for core transport effects, which take over inside of the transport barrier. Thus, the edge gradients act like a pedestal for the core gradients. The spatial extent of the pedestal is no wider than 2 cm. Since the pedestal structure is present in both, n- and T-profiles, H-mode features increased energy and particle confinement. Furthermore, the pedestal structure is present in the kinetic profiles of both plasma species, electrons and ions. The increased plasma pressure p leads, according to Equation 2.48 to a higher W_{th}. A multi-machine scaling law[6] on L-mode and H-mode confinement (employing data from several tokamaks) shows that for otherwise similar parameters (plasma current, magnetic field, plasma shape etc.) a well established H-mode has $\tau_{\mathrm{E}}^{H} \approx 2\,\tau_{\mathrm{E}}^{L}$ [42].

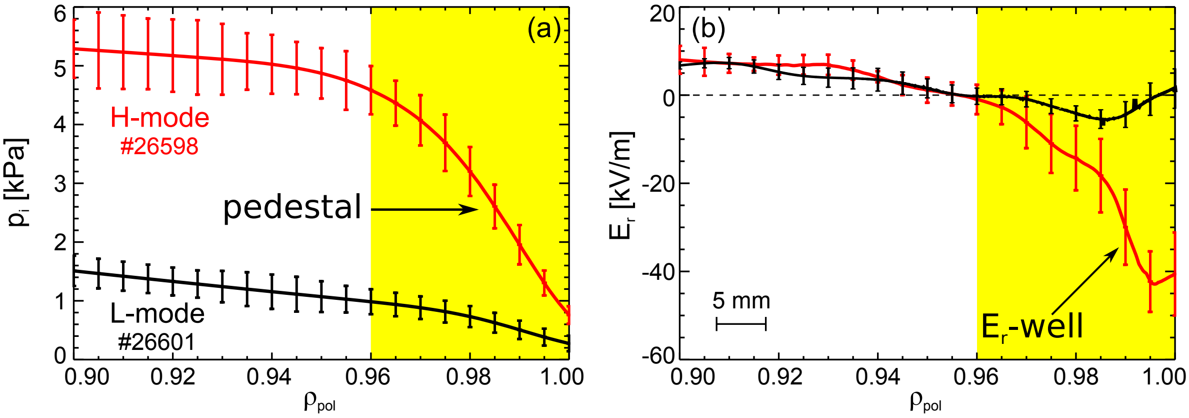

Figure 2.1: (a) Radial profile of the ion pressure of a typical L-mode (black) and H-mode (red) at AUG and corresponding radial electric field (b). The region marked in yellow is the plasma edge in which the H-mode pedestal and the edge transport barrier form. Figure adapted from [43].

The radial electric field E_r exhibits a negative well in the plasma edge of the confined region with a strong negative gradient, called the inner E_r gradient. The minimum

---

[6] Regression analysis of experimental data helps to find the main dependencies of one plasma quantity on other plasma quantities. Scaling laws, therefore, help to find common similarities on several fusion devices and can be used for predictions to future fusion devices.

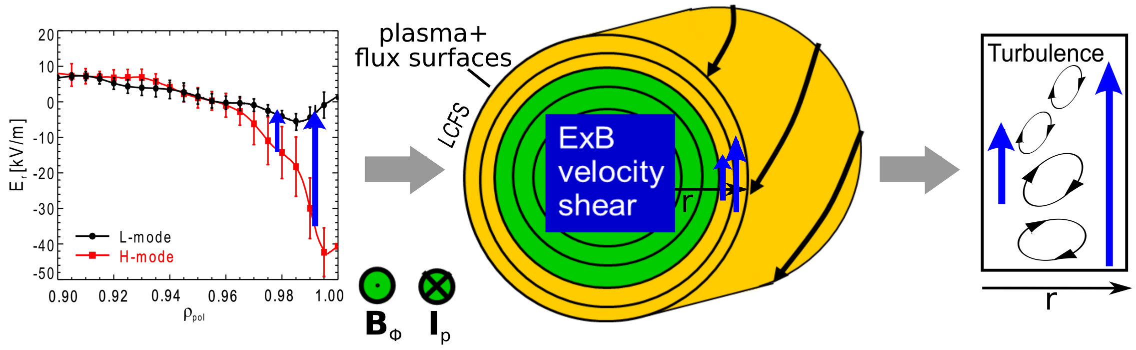

Figure 2.2: Schematic of the mechanism leading to the edge transport barrier. The shear in the perpendicular background flow ($E \times B$ flow) at the plasma edge leads to a de-correlation of turbulence structures and a suppression of turbulent transport at the plasma edge. Figures adapted from [20, 43].

of E_r, $E_{r,\mathrm{min}}$, is reached at $\rho_{\mathrm{pol}} \approx 0.99$ for both, L- and H-mode. E_r increases again towards the separatrix and reaches positive values in the SOL (not shown in Figure 2.1). The E_r gradient across the separatrix, connecting confined plasma and SOL, is named the outer E_r gradient. In an established H-mode, $E_{r,\mathrm{min}}$ reaches values between -30 and $-50\,\mathrm{kV/m}$, whereas in standard L-mode plasmas values of $E_{r,\mathrm{min}} \approx -10\,\mathrm{kV/m}$ are observed. Generally it is observed that in H-mode $E_r \approx \nabla_r p_i/(en_i)$, i.e. the contribution from $v_i \times B$ is negligible (see Equation 2.34). Thus, it is concluded that plasma flows in the edge region of H-mode are on the neoclassical level [44]. Since the width of the E_r well and E_r in the plasma core (i.e. $\rho_{\mathrm{pol}} < 0.95$) do not change significantly between L-mode and H-mode, the value of $E_{r,\mathrm{min}}$ is commonly used as a proxy for the E_r gradient [45].

Simultaneously with the steepening of the edge gradients a significant reduction of turbulent transport is found (edge transport barrier, ETB) [14]. The region of the ETB coincides with the edge pedestal and has a size of several tens of ion Larmor radii. Turbulence measurements show a reduced fluctuation level at the ETB. Therefore, an interplay between the perpendicular component of a sheared background flow ($E \times B$) and the radial transport due to plasma turbulence is assumed. The shear of the background flow tears apart turbulence structures (straining out mechanism), which leads to a de-correlation of turbulence and a reduction of turbulent transport (see Figure 2.2). The reduction of turbulent transport leads to a confinement improvement and allows for a further increase of the edge plasma gradients. These, in turn, are a drive for turbulence (see Equation 2.22). At the same time they lead to an increase of the shear of the background-flow (see Equation 2.31). This predator-prey mechanism is also assumed to be responsible for the transition from L- to H-mode (see Section 2.4.3).

On a macroscopic level, the H-mode is accessed from L-mode when a certain level of heating power is surpassed. This critical value is known as the H-mode power threshold (P_{LH}), and its dependencies are discussed in more detail in Section 2.4.2.

Another feature of the H-mode are edge-localized modes (ELMs). ELMs are magnetohydrodynamic edge instabilities occurring with a regular frequency as soon as the peeling-ballooning boundary is crossed [46]. The word ELM commonly refers to the type-I ELMs which are ideal peeling-ballooning instabilities, whose frequency increases with heating power. Type-III ELMs are considered to be resistive peeling-ballooning instabilities and their frequency decreases with heating power. Type-II ELMs are small and frequent ELMs which develop from type-I ELMs when the density in the SOL is sufficiently high [47].

ELMs are also known as short ($\approx 200 - 1000\,\mu\text{s}$)pedestal-relaxation events which produce an energy loss of 1 to 10 % of the total plasma energy. During an ELM crash the edge temperature- and density gradients collapse, what can be seen as wiggles on the time traces of the edge T- and n-signals. The particles and energy expelled during an ELM crash lead to high heat loads on the divertor targets. Therefore, ELMs can be also detected in the divertor signals, like the outer and inner divertor shunt current $I_{\text{SOL,a}}$ and $I_{\text{SOL,i}}$, or in some of the magnetic detection coils (Mirnov and ballooning coils). These signals are also used to determine the time point of the L-H transition (see Section 3.3).

2.4.1.2 I-mode

In the unfavourable drift configuration, a magnetic configuration in which the ∇B-drift of the ions points away from the primary X-point (see Figure 2.6b,c), it is found that P_{LH} is increased by about a factor of two (see also Section 2.4.2.2) compared to the favourable drift configuration ($v_{\nabla B \times B,i}$ towards primary X-point, see Figures 2.6a,d). In the unfavourable drift configuration a third confinement regime exists, which is, in terms of heating power, located between the L- and the H-mode. This stationary confinement regime is referred to as I-mode and is characterized by improved energy, but L-mode like particle confinement (see Figure 2.3b,c).

As the H-mode the I-mode develops a pedestal in T_e and T_i, while the density keeps its L-mode gradient. The I-mode was discovered at AUG in the 1990s [48]. Since then I-mode physics studies have been performed on several devices and mainly pushed forward by the two tokamaks Alcator C-mod[7] and AUG [49, 50]. The present work does not focus on the physics of the I-mode, but a few properties and latest research results of the I-mode are mentioned here for completeness and to distinguish it from other L-H transition phenomena.

With the I-mode a weakly coherent mode (WCM) develops (see Figure 2.3b), which can be detected by different reflectometry systems [51]. The WCM is localized very close to the plasma edge $\rho_{\text{pol}} \approx 0.995$ and is considered to be responsible for the L-mode-like particle transport in I-mode [52]. In this work it is used as an indicator of the I-mode.

Often it is observed that the I-mode develops gradually from the L-mode, while the transition from I-mode to H-mode is sharper due to the rise in density. Measurements of the power threshold from the L- to I-mode transition (P_{LI}) and from the I-mode to the H-mode transition (P_{IH}) show that the I-mode existence window in P_{heat} increases with increasing B_ϕ [53].

In I-mode ELMs are absent, but latest studies show that pedestal relaxation events (PDEs) [54] can occur, which are intermittent edge-localized instabilities in a weakly developed I-mode, but become more regular and larger in a more developed I-mode, i.e. closer to H-mode conditions (see Figure 2.3c). Although these PDEs are not located at the ideal peeling-ballooning boundary, they act like ELMs and expel heat and particles from the confined plasma [54].

The I-mode should not be confused with the I-phase. The I-phase is a transient event, characterized as L-H dithers (see also Section 3.2), which occurs only during a short time window at the L- to H-mode transition.

---

[7] Alcator C-mod was a tokamak with a high magnetic field (up to 8 T), located in Cambridge, Massachusets, USA.

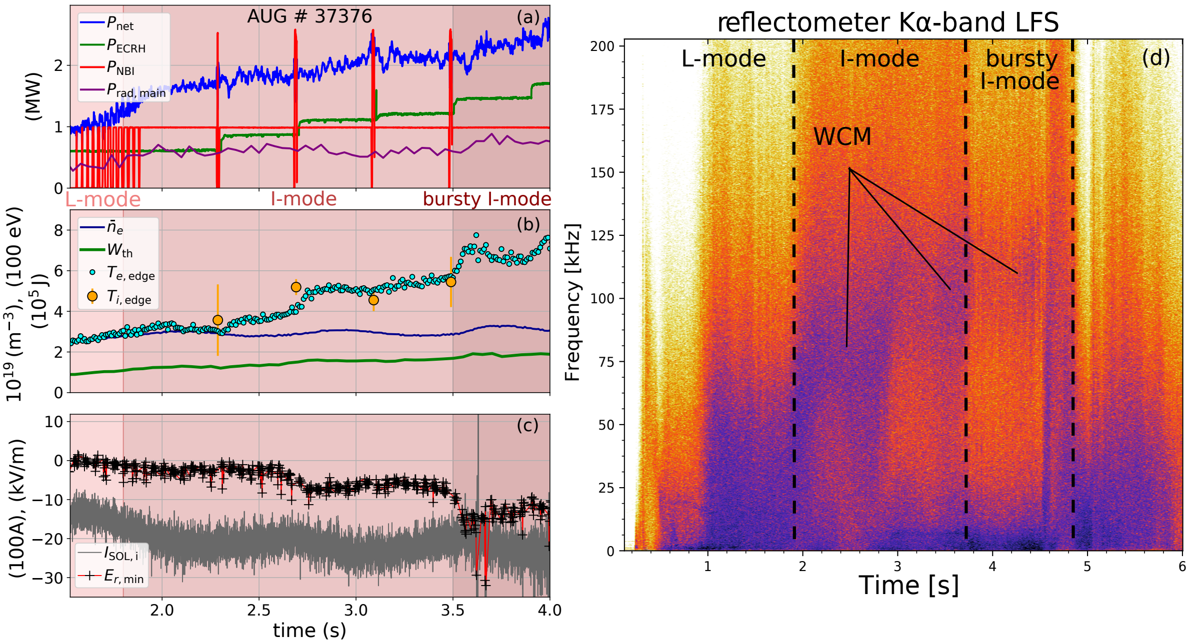

Figure 2.3: *Development of an I-mode in unfavourable drift configuration.* Time traces of (a) heating power, (b) edge ion and electron temperature, stored thermal plasma energy and edge density and (c) the shunt current of the inner divertor and the minimum of the radial electric field. (d) Evolution of the WCM visible in the density fluctuation measurements. When increasing the heating power the plasma transits smoothly from L- to I-mode. The edge electron and ion temperature increase, the minimum of E_r decreases, while the density stays constant. Close to the H-mode the I-mode develops PDEs which are visible in the shunt current and the radial electric field measurements. The frequency of the WCM also increases with the development of the I-mode.

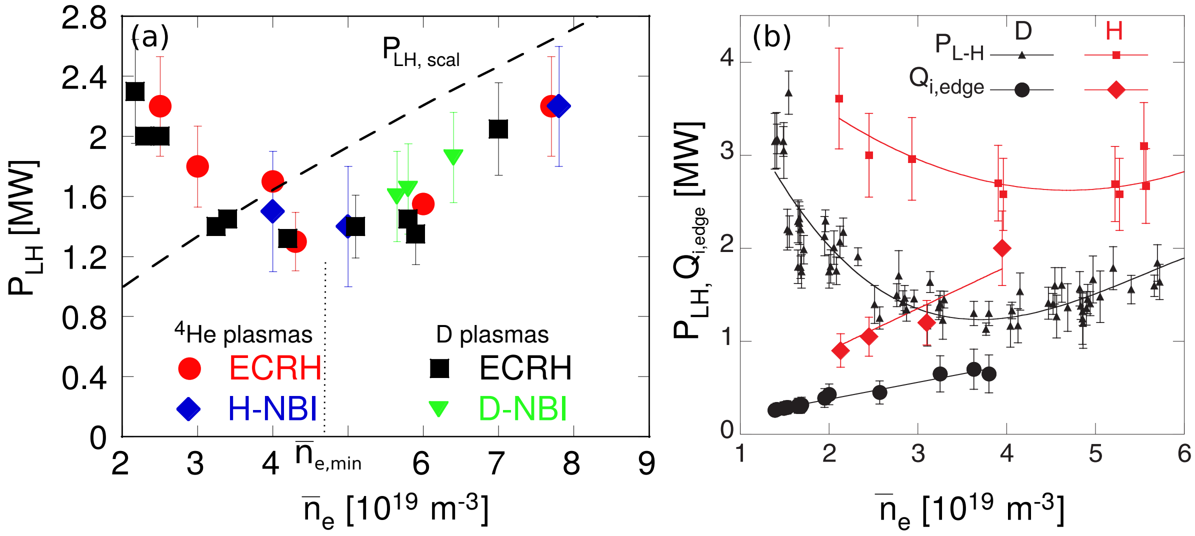

Figure 2.4: (a) H-mode power threshold of D and He plasmas versus line-averaged density with ECRH and NBI heating. (b) H-mode power threshold and edge ion heat flux at the L-H transition in D and H plasmas versus line averaged density. P_{LH} shows a parabolic behaviour on $\bar{n}_e$, whereas $Q_{i,\mathrm{edge}}$ increases linear with $\bar{n}_e$. All data are from the AUG tokamak. Figures adapted from [55, 56]

2.4.2 The H-mode Power Threshold

Figure 2.4 shows the H-mode power threshold at AUG for D and He plasmas plotted against the line-averaged electron density $\bar{n}_e$. P_{LH} exhibits a parabolic behaviour with $\bar{n}_e$, with its minimum value at $\bar{n}_{e,\mathrm{min}}$. The decreasing branch of P_{LH} with $\bar{n}_e$ smaller than $\bar{n}_{e,\mathrm{min}}$ is referred to as the low-density branch, whereas the branch with $\bar{n}_e$ larger than $\bar{n}_{e,\mathrm{min}}$ is called the high-density branch.

First, only D plasmas are considered, while the dependence of P_{LH} on the plasma species is discussed in Section 2.4.2.3. Several multi-machine scaling exist for the high-density branch of P_{LH} in D plasmas (see Figure 2.4a), where the latest and now commonly used one delivers [57]:

$$P_{\mathrm{LH,scal}} = 0.049\,\bar{n}_e^{0.72} B_\phi^{0.8} S^{0.94}. \tag{2.56}$$

Here, $\bar{n}_e$ is the line-averaged electron density, B_ϕ the toroidal magnetic field and S the surface of the plasma volume. These quantities are the main dependencies of P_{LH} and it increases almost linearly with all three quantities in the high-density branch. The scaling law is based on experimental P_{LH} data from several tokamaks which all had carbon (C) as first wall material, except one, Alcator C-Mod which has a first wall made from molybdenum.

2.4.2.1 Edge Ion Heat Flux

In order to understand the existence of the density minimum P_{LH} has to be separated in its contribution of ion and electron heat flux (see Equation 2.50). Thus, $P_{\mathrm{LH}} = Q_i^{\mathrm{LH}} + Q_e^{\mathrm{LH}}$, where $P_{\mathrm{rad,main}}$ is assumed to be negligible. As Figure 2.4b shows Q_i evaluated at $\rho_{\mathrm{pol}} = 0.98$, the edge ion heat flux $Q_{i,\mathrm{edge}}$, is linear in $\bar{n}_e$ at the L-H transition. This means a critical value in the edge ion heat flux has to be reached in order to enter H-mode. The non-linear dependence of P_{LH} on $\bar{n}_e$ can then be understood as follows. At low density the electron-ion coupling is low and, therefore, also the heat transfer from electrons to ions (see Equation 3.6). Thus, more external heating power is needed to increase the heat flux in the ions, while at high $\bar{n}_e$ the coupling between electrons and ions is sufficient to build up a critical ion heat flux with less total heating power. In fact it is found that P_{LH} is minimal for a fixed value $\tau_{\mathrm{E}}/\tau_{ei} \approx 9$ for different fusion devices [58]. Here, τ_{E} is the energy confinement time and $\tau_{ei} = 1/\nu_{ei}$ the mean collision time for e-i collisions.

A scaling-law for $Q_{i,\mathrm{edge}}$ at the L-H transition in D plasmas has been derived in [59] and it reads:

$$Q_{i,\mathrm{scal}} = 0.0029\, \bar{n}_e^{1.05} B_\phi^{0.68} S^{0.93}, \tag{2.57}$$

which yields similar exponents as $P_{\mathrm{LH,scal}}$.

The observation of a fixed $\tau_{\mathrm{E}}/\tau_{ei} \approx 9$ leads to a scaling law of the density minimum $\bar{n}_{e,\mathrm{min}}$:

$$\bar{n}_{e,\mathrm{min}} = 0.7\, I_{\mathrm{p}}^{0.34} B_\phi^{0.62} a^{-0.95} \left(\frac{R_0}{a}\right)^{0.4}, \tag{2.58}$$

where $I_{\mathrm{p}}^{0.34}$ is the plasma current, B_ϕ the toroidal magnetic field, a the minor and R_0 the major radius.

2.4.2.2 Dependence of P_{LH} on the Magnetic Configuration

At several tokamaks it has been observed that P_{LH} increases by about a factor of two if the ion ∇B-drift ($v_{\nabla B \times B,i}$) points away from the primary X-point for otherwise comparable plasma parameters [53,60,61]. According to Equation 2.7, the direction of $v_{\nabla B \times B}$ can be reversed if the direction of the magnetic field (i.e. the direction of B_ϕ) is reversed. Due to the associated increase of P_{LH} the magnetic configuration which has $v_{\nabla B \times B,i}$ pointing away from the X-point is referred to as the unfavourable drift configuration, while the magnetic configuration in which P_{LH} is lower and $v_{\nabla B \times B,i}$ points towards the X-point is labelled favourable drift configuration. In Figures 2.6 and 2.7 for each of the two magnetic configurations two examples are given.

From Equations 2.6 and 2.9 it can be seen that with the reversal of B_ϕ also $v_{E \times B}$ and v_{dia} change direction. This sign change has to first order no consequences on plasma transport in the confined plasma as long as the absolute values of the drifts do not change. In the SOL, however, a complex interaction of Pfirsch-Schlüter, $E \times B$ and diamagnetic flows leads to differences in the parallel SOL flows. In the favourable drift configuration the SOL flows are directed towards the inner target while in unfavourable drift configuration they are more balanced between inner and outer target. This is found experimentally and in SOL modelling [62]. Therefore, it is considered that changes in the divertor conditions lead to a change of the upstream E_r in the SOL. In this way, the outer E_r gradient could be modified without changing E_r in the confined plasma.

So far a direct comparison of E_r in the SOL in favourable and unfavourable drift configuration has neither been assessed experimentally nor in SOL simulations. Modelling of E_r in other modified magnetic configurations and divertor conditions (e.g. strike line on the vertical target versus strike line on the horizontal target or closed versus open divertor) have shown that the upstream E_r in the SOL can be affected [63]. Interestingly, in all simulations a higher SOL-E_r is found in conditions where P_{LH} is decreased, whereas E_r is lower in conditions in which P_{LH} is high. These observations could point to a leading role of the outer E_r gradient in the L-H transition physics. A higher SOL-E_r leads to an increased outer E_r gradient and a stronger shear in $v_{E\times B}$ ($\gamma_{E\times B}$). Thus, in the paradigm of a critical $\gamma_{E\times B}$ needed at the L-H transition less heating power is required to build-up the critical $\gamma_{E\times B}$ in order to suppress turbulence at the plasma edge.

In this work it was addressed experimentally whether E_r in the SOL and the outer E_r gradient are different in L-modes in favourable compared to unfavourable drift configuration and their effect on the L-H transition. Therefore, E_r in the SOL and the plasma edge as well as edge kinetic profiles were investigated and compared in L-modes of matched plasma parameters as well as at the confinement transitions from L- to H-mode, L- to I-mode and I- to H-mode (L-H, L-I and I-H transitions). The results of these experiments are presented in Chapter 7.

2.4.2.3 Isotope Effect

Another dependence of P_{LH} observed at different tokamaks is linked to the main ion species of the plasma. Experiments with hydrogen isotopes (H, D, T) showed that P_{LH} scales with the inverse of the isotope mass m_i [64]. Experiments at AUG have shown that not only P_{LH} but also the edge ion heat flux $Q_{i,\mathrm{edge}}$ at the L-H transition is increased by about a factor of 2 in H compared to D plasmas (see Figure 2.4b). Since $T_{i,\mathrm{edge}}$ and $\nabla T_{i,\mathrm{edge}}$ as well as E_r were found to be comparable in H and D plasmas at the L-H transition, it was concluded, with use of Equation 2.11, that the ion heat transport in hydrogen is increased compared to deuterium plasmas and that $\chi_{\mathrm{H}} \geq \chi_{\mathrm{D}}$ in L-mode [56]. The increased heat and also increased particle transport in H compared to D is known as the isotope effect. A theoretical explanation for increased heat and particle transport in L-mode at the plasma edge has been given recently and is connected to the dominant turbulence present in the plasma edge of L-mode [65–67].

SOL modelling results indicate that the upstream E_r (i.e. E_r at the OMP) in the SOL changes with the plasma main ion species [68]. It increases with m_i, leading to a steeper outer E_r gradient for deuterium than for hydrogen plasmas. This could, in the framework of a critical $\gamma_{E\times B}$ needed for turbulence suppression and the access to H-mode, explain the higher P_{LH} in H compared to D plasmas.

L-H transition experiments conducted at JET in mixed hydrogen-deuterium (HD) plasmas revealed a non-linear dependence of P_{LH} on the relative hydrogen content $f_{\mathrm{H}} = n_{\mathrm{H}}/(n_{\mathrm{H}} + n_{\mathrm{D}})$, which differs from the simple $1/m_i$-dependence of P_{LH} observed in pure hydrogen isotope plasmas [69].

The H-mode power threshold in He plasmas, $P_{\mathrm{LH}}(\mathrm{He})$, varies, depending on the fusion device, between 1 and $1.4\,P_{\mathrm{H}}(\mathrm{D})$. At AUG $P_{\mathrm{LH}}(\mathrm{He}) \approx P_{\mathrm{LH}}(\mathrm{D})$, whereas at JET and DIII-D [8] $P_{\mathrm{LH}}(\mathrm{He}) > P_{\mathrm{H}}(\mathrm{D})$ [70, 71]. The reasons for these differences are still unknown, but it could be connected to the fact that AUG operates normally with a closed divertor, while the divertor geometry of JET and especially the divertor geometry at DIII-D are open. Differences in P_{LH} with an open and closed divertor geometry have been observed at several tokamaks and could be connected to the different recycling behaviour of closed and open divertors [72].

Another difference between the AUG and JET tokamak is that at AUG no shift of $\bar{n}_{e,\mathrm{min}}$ is observed when changing the plasma species while at JET a shift of $\bar{n}_{e,\mathrm{min}}$ to

---

[8] DIII-D is a tokamak operated in San Diego, California, USA, which has a high flexibility in the plasma shaping.

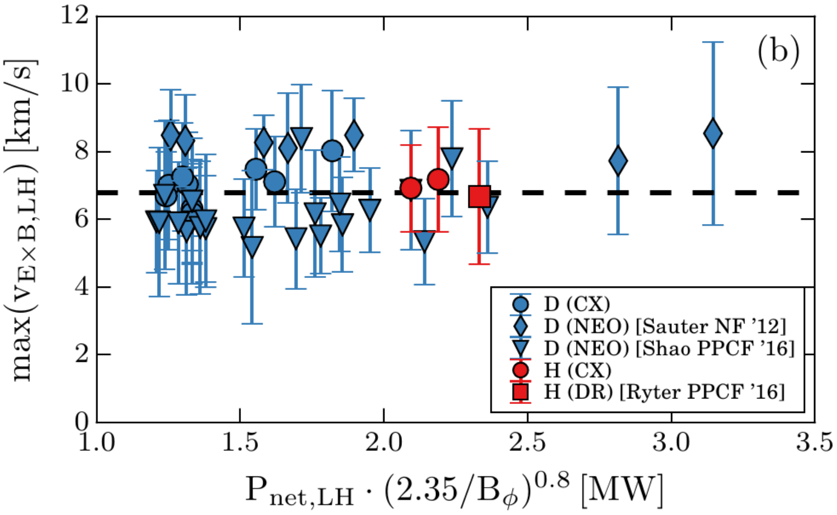

Figure 2.5: Proxy of $E{\times}B$-velocity shear ($\gamma_{E\times B}$), measured at the L-H transition, plotted against the H-mode power threshold normalized to the magnetic field. The constant $\gamma_{E\times B}$ found at the L-H transition can explain the almost linear dependence of P_{LH} on B_ϕ. Since $\gamma_{E\times B}$ is constant for a wide range of densities and for H and D isotopes it is considered to be responsible for the H-mode onset. Figure from [74].

higher values is observed in H compared to D plasmas [69]. Also the behaviour in mixed hydrogen-helium plasmas is different between AUG and JET. At AUG a reduction of $P_{\mathrm{H}}(H)$ has been observed if the He concentration $c_{\mathrm{He}} = n_{\mathrm{He}}/n_e \gtrsim 30\,\%$, whereas at JET a reduction of $P_{\mathrm{H}}(H)$ by $20\,\%$ is observed with $c_{\mathrm{He}} \approx 5\,\%$ [69, 73].

In order to better understand the differences of P_{LH} in the different ion species plasmas L-H transition in pure H, D, He as well as in mixed hydrogen-deuterium and in hydrogen-helium plasmas were performed at AUG. Measurements of kinetic edge profiles ($T_{i,e,\mathrm{edge}}, n_{e,\mathrm{edge}}$), rotation ($v_\phi, v_\theta$) and E_r in the plasma edge and the SOL were taken in L-modes of matched plasma parameters and at the L-H transition. The results of these experiments are presented in Chapter 8.

2.4.3 The Role of the Radial Electric Field in the L-H Transition

Observations of the importance of the $E \times B$-velocity shear ($\gamma_{E\times B}$) in the formation of the H-mode edge transport barrier (see Section 2.4.1.1) hint to a critical role of $\gamma_{E\times B}$ also for the access into H-mode. It is considered that the L-H transition occurs as soon as $\gamma_{E\times B}$ is larger than the growth rate of the turbulence, γ_{turb}. Only then $\gamma_{E\times B}$ can lead to the suppression of turbulence.

Experiments at the AUG tokamak have shown that $\max|v_{E\times B}| \propto \gamma_{E\times B}$ is constant at the L-H transition for a wide range of densities and magnetic field strength (see Figure 2.5) [74]. This critical value in $v_{E\times B}$ can, therefore, also explain the almost linear dependence of P_{LH} on B_ϕ (see Equation 2.56), since $v_{E\times B} = -E_r/B$. Follow-up L-H transition experiments also indicate that the inner E_r gradient is the important E_r gradient for the L-H transition, since it is found in turbulence measurements that the turbulence strength first decreases in the region of the inner E_r gradient, i.e. $\rho_{\mathrm{pol}} \approx 0.96 - 0.995$ [75].

Assuming that a critical $\gamma_{E\times B}$ is needed for the H-mode access the generation of this poloidal shear flow and the dominant contributions to it are not clear. Different causes are possible and it might be that purely the pressure gradient via the diamagnetic term is sufficient and responsible to cause the shear in the $E\times B$-flow, i.e. $v_{E\times B} = v_{\mathrm{dia}}$. Also other contributions to $v_{E\times B}$ are discussed like zonal flows which are shear flows generated by turbulence stresses, which can, due to their flow structure, lead to a reduction of the turbulence [30]. Such a predator-prey like behaviour is often considered to be responsible for the L-H transition as normally an intermediate phase of fast L-H and H-L back transitions (L-H dithers or I-phase) is observed between L- and H-mode (see Section 3.3). On the other hand, experimental data indicate that these L-H dithers can be produced by the interplay of turbulence with the gradient pressure without the need of zonal flows [76, 77]. In either case the main ion pressure gradient is a crucial element in the paradigm of a critical $\gamma_{E\times B}$, since it sets the background condition for the build-up of a sufficiently large $\gamma_{E\times B}$ to suppress turbulence and, thus, enter H-mode.

2.5 Coordinate System and Magnetic Configurations

As mentioned before, AUG employs a left-handed coordinate system for the torus coordinates (R, ϕ, θ). According to the tokamak coordinate conventions it is a COCOS 17 system [78]. In this section the sign conventions of AUG are introduced and the different magnetic configurations (favourable and unfavourable drift configuration) used in the present work are described.

2.5.1 Sign conventions

ϕ is positive if it is counter-clockwise viewed from above. θ is positive if it is clockwise viewed from the front, i.e. it points vertically downward at the OMP. In the standard configuration (see Figures 2.6a and 2.7a) the toroidal plasma current I_{p} and the poloidal magnetic field B_θ are both positive, while the toroidal magnetic field component B_ϕ is negative. Also the NBI points into the positive toroidal direction, thus, it is co-current. A positive toroidal rotation v_ϕ is co-current, while poloidal rotation velocities v_θ which are vertically upward at the LFS are negative and in the electron diamagnetic drift direction.

2.5.2 Favourable and Unfavourable Drift Configuration

The AUG standard configuration is a lower single-null (LSN) plasma, which means that the primary X-point is located in the lower divertor. Since $v_{\nabla B\times B,i}$ points towards the primary X-point the standard configuration is a favourable drift configuration. An unfavourable drift configuration can be achieved by either changing the plasma shape to an upper single-null plasma (USN), where the primary X-point is in the upper divertor, or, remaining a LSN plasma, the B-field, i.e. B_ϕ, is reversed (see Equation 2.7). An USN plasma with reversed B_ϕ is again a favourable drift configuration.

Changing also the direction of the current would lead to 8 different cases. However, not all of them are technically achievable at AUG and some of them are also redundant. Therefore, only the four different magnetic configurations and their respective names are shown in Figure 2.6 (poloidal cross section) and in Figure 2.7 (bird's eye view) which were used in this study. The directions of $v_{\nabla B\times B,i}$, v_{dia} and $v_{E\times B}$ are indicated with blue, black and magenta arrows in the figures.

In the standard configuration (LSN favourable, blue) the electron diamagnetic drift points upwards, while the ion diamagnetic drift directs downwards at the LFS. The directions reverse on the HFS. Since the NBI injects co-current, v_ϕ is co-current in the plasma core. Thus, in an NBI heated plasma, the radial electric field in the core plasma is positive. This is depicted by the magenta radial arrows in Figure 2.6 and the schematic radial profiles of E_r in Figure 2.7. At the plasma edge the radial electric field is negative, since at least in H-mode $E_r \approx \nabla_r p_i/(en_i)$, and positive in the SOL with $E_r \approx \nabla_r T_{e,\mathrm{OMP}}$. The direction of $v_{E\times B}$ changes accordingly and it is positive for the plasma core and the SOL (i.e. directed clockwise if viewed from the front) and negative (i.e. directed counter-clockwise if viewed from the front) in the plasma edge.

For the USN unfavourable drift configuration (orange) the signs of the plasma parameters and the drift directions are unchanged compared with the LSN favourable drift configuration. However, since the primary X-point of the plasma is located in the upper divertor, $v_{\nabla B\times B,i}$ points away from the primary X-point. In this drift configuration P_{LH} is increased.

For a clear comparison to the USN unfavourable drift configuration, experiments were also performed in the USN favourable drift configuration (purple). This guarantees that the divertor geometry (open vs. closed divertor) does not influence the L-H transition. For the USN favourable drift configuration B_ϕ is reversed, i.e. $B_\phi > 0$, and, thus, all drifts change their direction. Since I_{p} and B_θ are unchanged, the helicity of the field lines changes from left-handed to right-handed. The NBI injection as well as v_ϕ are still co-current, hence, E_r remains positive in the plasma core.

For the unfavourable drift configuration using the lower divertor (LSN unfavourable, red) a slightly different approach has to be followed. By construction the lower divertor only allows for field lines with left-handed helicity. Thus, besides a reversal of B_ϕ also I_{p} has to be reversed (this is also referred to as reversed I_{p}/B_ϕ) to keep the left-hand helicity. A sign change of I_{p} implies a sign change of B_θ. Due to the change of sign in B_ϕ, the drifts change also their direction compared to the LSN favourable drift configuration. Thus, $v_{\nabla B\times B,i}$ points away from the primary X-point and P_{LH} is found to be increased as well. However, due to the reversal of I_{p} the NBI injects counter-current in this configuration. This leads to a v_ϕ which is still positive, but counter-current and makes that E_r becomes negative in the plasma core, since $E_r \approx v_\phi B_\theta$ there. This also implies that the resulting $v_{E\times B}$ in the plasma core does not change sign compared to the LSN favourable drift configuration.

In all four drift configurations $v_{E\times B}$ points in the electron diamagnetic drift direction at the plasma edge, while it points in the ion diamagnetic drift direction in the SOL.

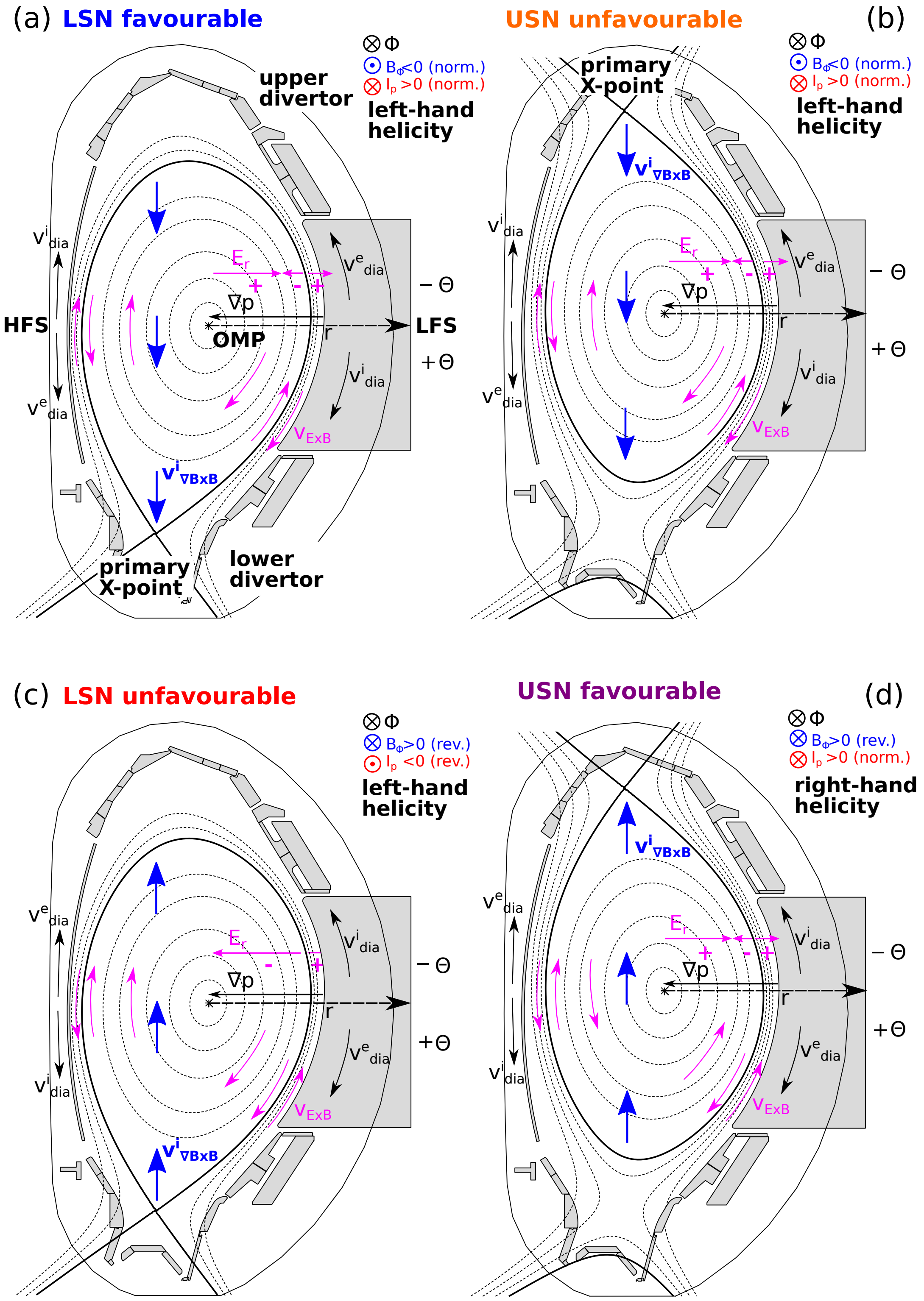

Figure 2.6: Poloidal cross sections of the four possible magnetic configurations to achieve favourable and unfavourable drift configurations at AUG. The sign conventions are the AUG sign conventions and the directions of the poloidal drifts are shown for each drift configuration.

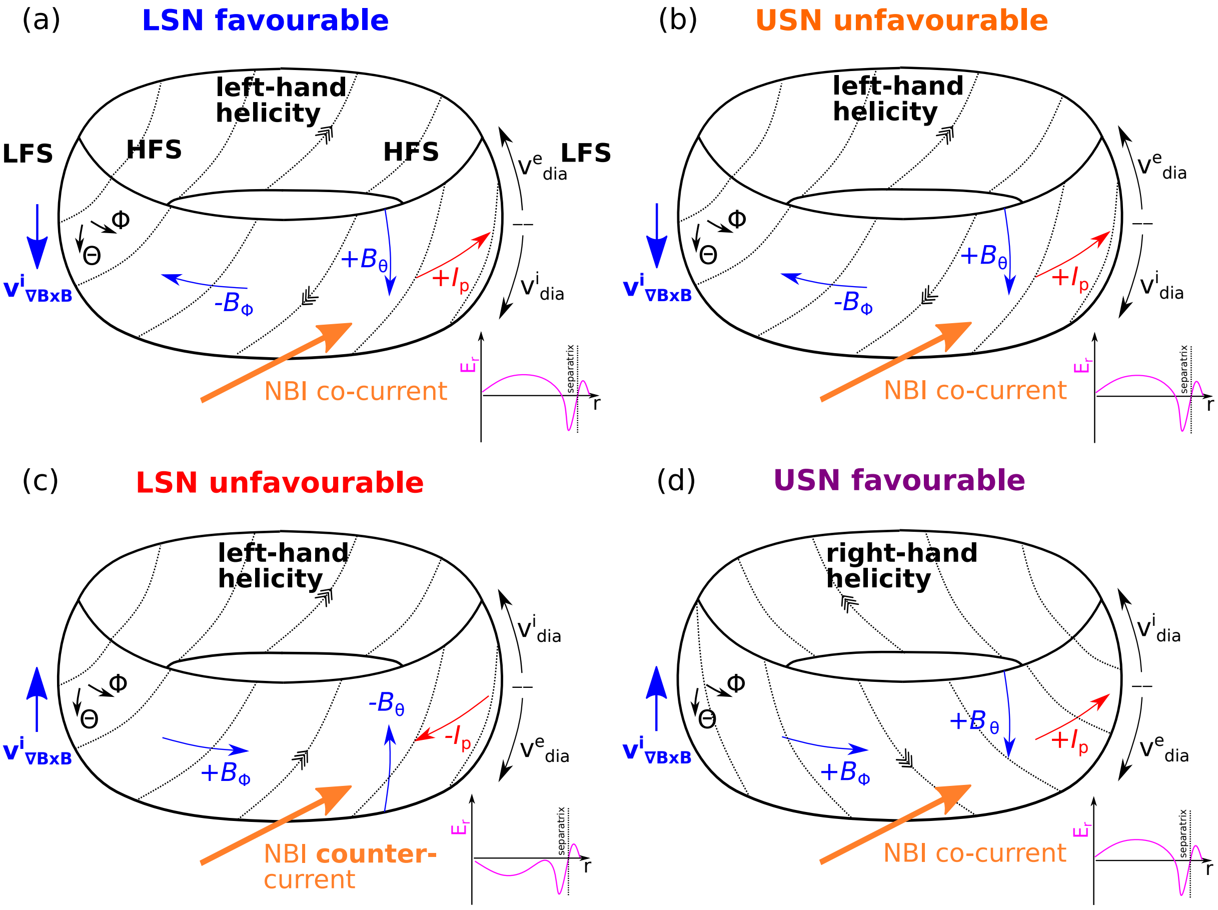

Figure 2.7: Bird's eye view of the four possible magnetic configurations to achieve favourable and unfavourable drift configurations at AUG. The signs for the plasma current directions and the magnetic fields are given as defined at AUG. Furthermore, a radial profile of E_r is given assuming a toroidal rotation which is dominated by the torque input of the NBI.

3 Methodology

For the conduction of the experiments at the AUG tokamak and the analysis of the experimental data different plasma diagnostics and analysis methods were employed, which are presented and discussed in the following.

3.1 Plasma Diagnostics

3.1.1 Integrated Data Analysis

Several diagnostics are available at AUG to measure the electron temperature T_e and the electron density n_e. Some of them cover the complete radial range, like Thomson scattering (TS) and electron cyclotron emission (ECE), while others like the lithium- and helium-beam emission spectroscopy (LIB and HEB), deliver edge measurements with a high radial precision. The TS and HEB diagnostics are both able to measure n_e and T_e simultaneously. Please note, the He-beam emission spectroscopy (HEB) is not the same as the He II spectroscopy (HES) diagnostics, which was developed in the course of this thesis. The He-beam emission spectroscopy detects the He I line from which T_e and n_e can be inferred [79].

Integrated data analysis (IDA) seeks to combine the measurements of these different diagnostics coherently using Bayesian probability theory [80]. In this way data inconsistencies and systematic errors can be detected. Thus, IDA delivers T_e and n_e profiles covering the complete radial range with high radial and temporal resolution. IDA also employs forward models for the correct interpretation of the raw data of the respective diagnostics.

In the standard IDA evaluation data from the ECE and the TS systems are used to determine T_e profiles. For the n_e profiles data from TS, the Li-beam and the deuterium cyanide laser interferometry (DCN) are used. The latter delivers averaged density profiles $\bar{n}_e$ with a precise absolute calibration [80].

In the present work, for the specific analysis of edge profiles, $T_{e,\mathrm{edge}}$ and $n_{e,\mathrm{edge}}$, IDA was often augmented by measurements from the He-beam, since it delivers T_e and n_e data across the separatrix with a high radial and temporal resolution [81]. It is indicated in the following when HEB data were employed in IDA.

3.1.2 Beam-based Charge Exchange Recombination Spectroscopy

Charge exchange recombination spectroscopy (CXRS) delivers radial profiles of the temperature T_A, the rotation $v_{\mathrm{rot},A}$ and density n_A of an impurity ion A [82]. The standard CXRS systems at AUG employ the neutral beam injection (NBI) as a neutral source (D or H) for the charge exchange reactions. Therefore, this measurement technique is referred to as beam-based CXRS in contrast to the gas puff-based CXRS system which was characterised in the course of this thesis (see Section 5.1).

There are several CXRS systems installed at AUG on both NBI injection systems. Taken all CXRS systems together they cover almost the full plasma radius from the LFS to the HFS. Three toroidal CXRS systems cover the core and edge plasma and one poloidal is installed at the plasma edge. The edge systems cover about $\rho_{\text{pol}} \approx 0.95 - 1$. The toroidal and poloidal alignment of the lines of sight (LoS) allows for measurements of the toroidal and poloidal component of the impurity rotation, $v_{\phi,A}$ and $v_{\theta,A}$.

A well established procedure is the analysis of the CX lines from low-Z impurities (B,N), which are fully ionized in the confined plasma. Boron is present in the fusion plasma due to the boronisation process (see Section 1.4), whereas small amounts of N can be intentionally seeded into the plasma for CXRS measurements.

The low-Z impurities are in thermal equilibrium with the main ions, therefore, it is a valid assumption that $T_i = T_A$. Thus, CXRS delivers radial profiles of the ion temperature T_i via Doppler broadening of the spectral lines and plasma rotation via the Doppler shift of the lines. The impurity density n_A can be inferred from the radiance L_A of the investigated CX line. For this the neutral distribution of the NBI systems has to be known [83]. From the CXRS measurements also E_r can be determined according to Equation 2.32.

Each of the two NBI injection systems consists of 4 beam lines, where each beam line delivers 2.5 MW of heating power. Although the beam lines can be operated independently, in standard operation this amount of heating power triggers almost instantaneously an L-H transition ($P_{\text{LH}} \approx 1\,\text{MW}$). In order to have T_i measurements in L-mode avoiding an L-H transition the NBI is turned on at certain time points for a short period of time (beam blips) in which the CXRS measurements are taken.

In order to increase the radial coverage of the edge measurements a radial sweep of the plasma edge through the LoS can be applied. This technique is also known as R_{aus} scan.

3.1.3 Doppler Reflectometry

A complementary system for E_r measurements which is used in this thesis is Doppler reflectometry (DR). For DR measurements a microwave beam is launched into the plasma. Depending on its frequency the beam gets reflected at a certain cut-off surface. In case of density fluctuations $\tilde{n}$ the cut-off surface is corrugated and works like a reflection grating for the incoming microwave beam. Normally the -1st order of the scattered beam is detected. In this way the emitting microwave antenna can also be used as the receiving antenna.

In case the density fluctuations move relatively to the receiving antenna, which is aligned perpendicular to the magnetic field, a Doppler shift (ω_{D}) is detected, with:

$$\omega_{\text{D}} \approx u_{\perp} k_{\perp}, \tag{3.1}$$

where $u_{\perp}$ is the perpendicular velocity of the density fluctuations and $k_{\perp}$ the perpendicular wave vector of the scattered beam.

The measured $u_\perp$ of the density fluctuations is a sum of $v_{E\times B}$ and the phase velocity v_{ph} of the turbulence producing the density fluctuations:

$$u_\perp = v_{E\times B} + v_{\mathrm{ph}}. \tag{3.2}$$

If v_{ph} is small the radial electric field can be approximated by:

$$E_r \approx u_\perp B = \frac{\omega_{\mathrm{D}} B}{k_\perp}. \tag{3.3}$$

Since the DR technique relies on the presence of density fluctuations, E_r measurements in H-mode are challenging for these systems due to the reduced turbulence level. However, in L-mode the DR systems deliver highly radially resolved DR profiles, where the time resolution can be in the µs range.

AUG has an edge and a core DR system. The edge system (DR1) is a V-band Doppler reflectometer with a frequency range of 50 – 75 GHz and the core system (DR2) is a W-band Doppler reflectometer with a frequency range of 75 – 110 GHz.

Since the cut-off surface depends on the magnetic field and the plasma density, the radial position of the DR measurements can vary. A beam tracing code has to be used to calculate the radial position of the back-scattered wave. At AUG the ray tracing code TORBEAM is used for this [84].

3.1.4 Langmuir Probes

Langmuir probe (LP) measurements were taken at the outer divertor target in order to be able to relate the divertor target quantities ($V_{\mathrm{fl}}, T_{e,\mathrm{t}}$) to the upstream plasma quantities (E_r, $T_{e,\mathrm{OMP}}$). Two arrays of LPs are installed in the targets of the outer divertor at AUG, with a distance of about 2 cm [85].

Langmuir probes are conductors which are introduced into the plasma and are isolated from the surrounding wall. An external voltage is applied to the LPs and the produced current flux is detected. In this way the characteristic curve of the LP (current vs. voltage) is measured, from which $V_{\mathrm{fl}}, T_{e,\mathrm{t}}$ and $n_{e,\mathrm{t}}$ can be deduced.

In order to increase the radial resolution of the LP measurements strike point (SP) sweeps can be applied similar to the plasma sweeps. In a SP sweep the plasma is moved slowly along the divertor targets.

3.1.5 Equilibrium Reconstruction

The CLISTE code is an iterative solver that uses information from different poloidal magnetic measurement coils to solve Equation 2.52 [86, 87]. Other magnetic data can be taken into account in order to constrain the results on the equilibrium further. This leads to an equilibrium which is referred to as the EQH equilibrium.

In another approach the Grad-Shafranov equation is coupled to the current-diffusion equation. Other constraints on the equilibrium e.g. the measurements of the thermal pressure profile are taken into account in the framework of Bayesian probability theory [88]. This magnetic equilibrium is referred to as the IDE equilibrium.

In the course of this thesis it was found that in plasma conditions in which B_ϕ is reversed the EQH equilibrium yields higher systematic uncertainties on separatrix position and confinement quantities like W_{th}. Therefore, if plasmas with different drift configurations were compared the IDE equilibrium was employed.

3.2 Discharge Design

Figure 3.1 shows the reference plasma discharge # 35842. Several versions of this discharge with modifications of different plasma parameters were performed and analysed in this study. The reference discharge is a lower-single-null (LSN), low-δ[1] D plasma with a toroidal magnetic field $B_\phi = -2.5\,\mathrm{T}$ at the magnetic axis, a plasma current, $I_{\mathrm{p}} = +800\,\mathrm{kA}$ and $q_{95} = -5$ (safety factor at 95 % of the magnetic flux). This means that the $v_{\nabla B \times B,i}$ points towards the X-point, thus, it is a favourable drift configuration (see also Section 2.5.2).

Small power steps of 200 to 300 kW are used to trigger the L-H transition. An example ECRH power ramp is shown in Figure 3.1a. ECRH X2 mode heating of 140 GHz is used which deposits the heating power in the plasma center, at the magnetic axis. The power steps are small enough to pinpoint P_{LH} and chosen to be at least 150 ms long to reach steady-state conditions before the next heating step ($\tau_{\mathrm{E}}(\mathrm{D}) = 100 - 140\,\mathrm{ms}$ in the investigated L-mode conditions). At the end of each heating step a 12 ms long beam blip of 2.5 MW is applied for CXRS measurements. The beam blip is a small perturbation to the plasma and increases P_{net} by about 200 kW for approximately 50 ms. This amount of heating is within the uncertainties of the P_{LH} determination, but it is regularly observed that the beam blip triggers the L-H transition. However, the H-mode can then only be sustained if after the perturbation by the beam blip sufficient additional heating power is applied. Otherwise the plasma transits back into L-mode.

Figure 3.1b shows the time traces of the core and edge line-averaged densities of the DCN interferometer ($\bar{n}_{e,\mathrm{core}}$ and $\bar{n}_{e,\mathrm{edge}}$) (see Section 3.1.1). The density for the reference discharge was chosen to be at the density minimum $\bar{n}_{e,\mathrm{min}} \approx 4.5 \times 10^{19}\mathrm{m}^{-3}$ [56]. In most of the discharges feed forward gas fuelling was used. Gas fuelling rates of about 3×10^{21} el/s for D and 5.5×10^{21} el/s for H are needed to get this desired density. If the intrinsic B concentration was too low, small amounts of N were injected into the plasma for CXRS measurements. The low-Z impurity content was monitored with the CXRS diagnostics and found to be low, normally below 1 %. The time trace of the He gas flow rate, needed for the He II spectroscopy diagnostics (see Section 5.2), is also shown in 3.1b together with the evolution of W_{th}.

Starting from the reference discharge several modifications were applied to it, and the impact on the L-H transition and the edge radial electric field E_r were studied. For example the heating ratio of direct electron and ion heating was changed by employing a NBI instead of an ECRH power ramp. Such an NBI power ramp is accomplished by a changing duty cycle of the power modulation. The same discharge was also performed with different main ion species (D, H, He) and with mixtures of those species. Lower and higher plasma densities were investigated and the magnetic field configuration was changed to study E_r in the unfavourable drift configuration (see Section 2.5.2).

---

[1] δ is the triangularity of a plasma and, thus, a measure for the plasma shape. It is defined as the radial distance of the X-point from R_0 normalized by the minor radius a.

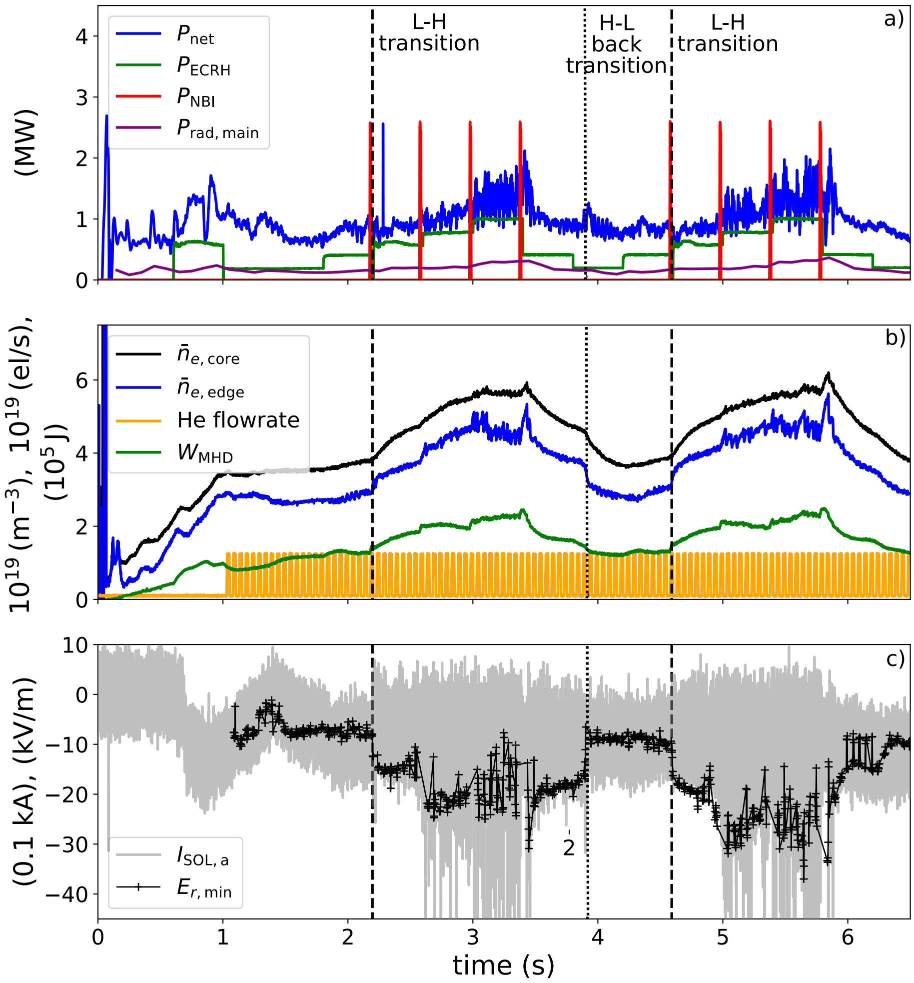

Figure 3.1: *Reference L-H transition discharge.* Time traces of (a) auxiliary heating power and main chamber radiation, (b) of the line-averaged plasma density at core and edge and of the stored thermal energy. Also the signal of the He gas puff for He II spectroscopy is shown. (c) Evolution of the minimum of E_r and the signal of the outer shunt current measurement, which is a precise indicator of the L-H transition time. The L-H transitions and the H-L back transition are indicated.

3.3 Determination of the L-H Transition Time and Power

The L-H transition times are indicated by the vertical dashed lines in Figure 3.1. As explained in Section 2.4.1.1 the H-mode is characterized by improved particle and energy confinement compared to the L-mode. Thus, the time point of the L-H transition t_{LH} can be determined from a strong increase of $\bar{n}$ and W_{th}. At this time point the plasma enters first an oscillatory regime of L-H dithers before it develops into an H-mode with type-I ELMs [89, 90]. To further pinpoint t_{LH}, additional measurements are investigated, which show a modulation of the signal due to the L-H dithers and the ELMs. These are the shunt current measurements in the inner and outer target tiles, $I_{\mathrm{SOL,i}}$ and $I_{\mathrm{SOL,a}}$ and poloidal magnetic field fluctuation $\dot{B}_\theta$ measurements of two Mirnov coils located close to the primary and secondary X-point. The time signal of $I_{\mathrm{SOL,a}}$ is shown in Figure 3.1c. This definition of t_{LH} is consistent with the one used in previous L-H transition studies at AUG [74].

Also shown in Figure 3.1c is the evolution of the minimum in the edge radial electric field ($E_{r,\mathrm{min}}$) as it is measured with He II spectroscopy (see Section 5.2). It is found to be another good indicator of the L-H transition, since the $E_{r,\mathrm{min}}$ starts to decrease at the L-H transition, while in L-mode it is rather constant. As can be seen in the figure and was found before [91], type-I ELMs affect $E_{r,\mathrm{min}}$.

The time trace of P_net (see Equation 2.50) is depicted in Figure 3.1a. P_LH is defined as P_net at t_LH.

For a correct determination of P_LH also the main chamber radiation $P_\mathrm{rad,main}$ should be subtracted from P_net. A typical source for high $P_\mathrm{rad,main}$ is tungsten (W) in the plasma center. The evolution of $P_\mathrm{rad,main}$ at the L-H transition is shown in Figure 3.1a. It is reconstructed by means of 2D tomography from the bolometer signals [92]. In most of the presented discharges $P_\mathrm{rad,main}$ is low, between 200 and 500 kW and varies little at the L-H transition.

Indicated in Figure 3.1 is also the transition from H-mode into L-mode (H-L back transition). For the H-L back transition the same signals can be used to determine t_HL and P_HL is then defined as P_net at t_HL. Edge profiles of L-H and H-L back transitions are compared in Section 8.2.2.1.

3.4 Analysis Methods

3.4.1 Power Balance Analysis

Power balance analysis is performed in order to determine the surface-integrated ion and electron heat fluxes Q_i and Q_e, respectively. For this the transport code ASTRA was employed [93], using the following equations:

$$Q_i = Q_{i,\mathrm{direct}} + Q_{ei} \tag{3.4}$$

and

$$Q_e = Q_{e,\mathrm{direct}} - Q_{ei} - P_\mathrm{rad,main}. \tag{3.5}$$

Hereby are $Q_{i,\mathrm{direct}}$ and $Q_{e,\mathrm{direct}}$ the contributions to the heat flux due to direct heating of the ions and electrons, respectively. As described in Section 1.4 this can be accomplished by means of different auxiliary heating methods. To determine the exact heat deposition profile of the ECRH the microwave beam tracing code TORBEAM [84] was used and for the NBI deposition the real-time code RABBIT [94] was coupled to ASTRA. $P_\mathrm{rad,main}$ was neglected in the calculations since it is found to be small, but it was taken into account in the uncertainties of Q_e and Q_i.

Q_{ei} is the surface-integrated heat flux due to collisional heat exchange between electrons and ions. In purely ECRH plasmas this is the only contribution to Q_i. Q_{ei} is the volume integral of the equipartition power density p_{ei} which is given by:

$$p_{ei} = 0.00246 \ln \mathit{\Lambda}\, n_e \frac{T_e - T_i}{T_e^{3/2}} \sum_i n_i \frac{Z_i^2}{A_i}, \tag{3.6}$$

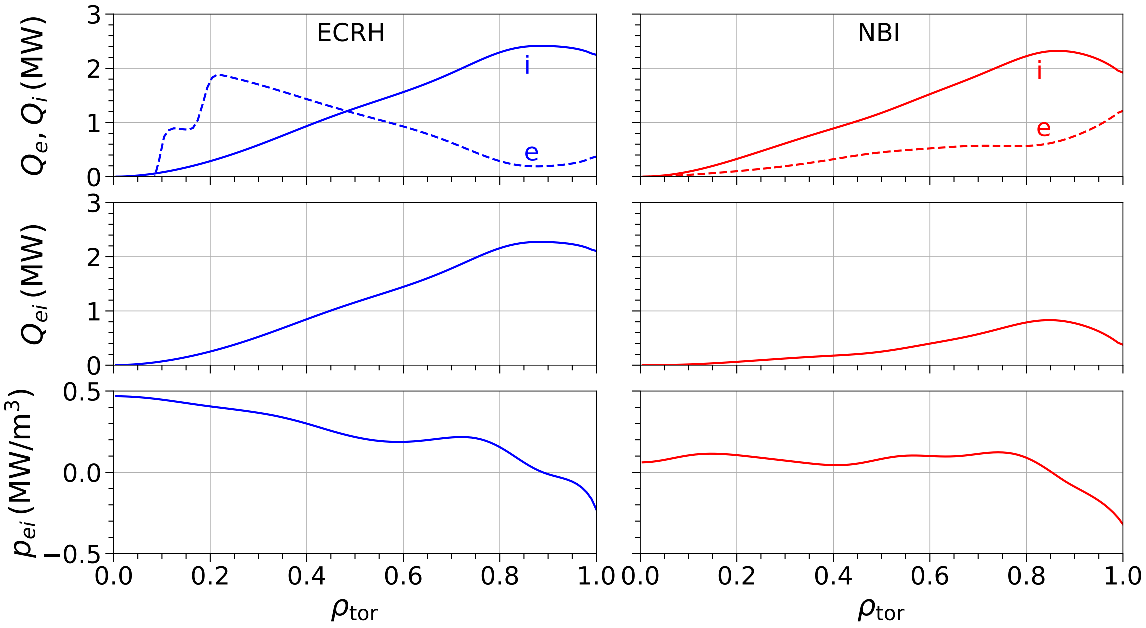

Figure 3.2: Radial profiles of the total electron (solid) and ion (dashed) heat fluxes Q_e, Q_i, of the heat flux due to equipartition Q_{ei} and of the equipartition power p_{ei} for a ECRH (left) and a NBI (right) heated discharge L-mode discharge at the L-H transition.

where n_e, T_e, n_i and T_i are the respective electron and ion density and temperature radial profiles and Z_i and A_i charge and mass of ion i. The Coulomb logarithm, $\ln \Lambda$, is approximated by:

$$\ln \Lambda = 15.9 - 0.5\, \ln n_e + \ln T_e. \tag{3.7}$$

p_{ei} strongly depends on the input electron and ion kinetic profiles. All profiles are evaluated during steady-state plasma phases. The T_e and n_e profiles are taken from IDA (see Section 3.1.1) and the T_i profiles from the beam-based CXRS measurements (see Section 3.1.2), which were acquired during beam blips in ECRH plasmas. The n_i profiles are deduced from the measured n_e and impurity density profiles.

Two examples of radial Q_i, Q_e and Q_{ei} profiles for an ECRH (left) and an NBI heated discharge (right) are presented in Figure 3.2.

The total ion heat flux at the plasma edge, $Q_{i,\mathrm{edge}}$, is evaluated at the radial position of $\rho_{\mathrm{tor}} = 0.95$, which corresponds for most of the evaluated discharges to a value of $\rho_{\mathrm{pol}} \approx 0.98$.

3.4.2 Kinetic Profile Alignment

Profiles investigated and presented in this work are all mapped to the outer mid-plane (OMP). Since the different diagnostics are located at different poloidal and toroidal locations and also the equilibrium mapping is not perfect, sometimes profiles have to be shifted radially in order to be brought into agreement with other diagnostics. In the IDA framework such relative shifts between the diagnostics are taken into consideration, however, still uncertainties in the separatrix position can exist. For an accurate analysis of edge profiles it is crucial to determine the separatrix position with sufficient precision. A simple 1D SOL model based on heat conduction can be used to determine the upstream electron temperature at the separatrix $T_{e,\mathrm{sep}}$ from the maximum of the parallel heat flux measured at the divertor. This model is known as the two-point model [37] and reads:

$$T_{e,\mathrm{sep}} = \left(\frac{7}{4} \frac{P_{\mathrm{sep}}}{\kappa_0^e} \frac{L_{\mathrm{c}}}{A_{\mathrm{SOL}}} \right)^{\frac{2}{7}} , \tag{3.8}$$

where L_{c} is the connection length from the OMP to the divertor target, A_{SOL} is the cross-sectional area of the SOL perpendicular to the magnetic field and $\kappa_0^e \approx 2000(\mathrm{eV})^{7/2}\mathrm{Wm}^{-1}$ the Spitzer-Härm conductivity constant for electrons. In type-I ELMy H-mode discharges $T_{e,\mathrm{sep}} = 80 - 120\,\mathrm{eV}$, whereas in L-mode $T_{e,\mathrm{sep}} = 50 - 80\,\mathrm{eV}$.

In this work the approach was the following. The separatrix temperature was calculated using Equation 3.8. The T_e profiles were shifted such that $T_{e,\mathrm{sep}}$ complies with the two-point model. The n_e profiles were shifted by the same amount as the TS- or HEB-T_e profiles had to be shifted and the n_e profiles from other diagnostics were adjusted accordingly. The T_i profiles were not shifted, but for uncertainty estimations of the $(\nabla_r p_i)/(en_i)$ term a relative shift of $\pm 5\,\mathrm{mm}$ was assumed. For the radial mapping of the DR-E_r profiles the validated n_e profiles were used.

4 Experimental Set-up

The diagnostics which is introduced in this chapter is an active spectroscopy system. Active spectroscopy is referred to the measurement of light emitted by the plasma due to interaction with an intentionally introduced light or particle source. This allows for locally resolved measurements of plasma quantities under the condition that the introduced source does not strongly perturb the plasma and as such, change the measured quantities.

4.1 Components

The experimental set-up developed and used in the course of this thesis consists of a gas inlet system with a piezoelectrically driven gas valve for injection of room-temperature neutrals (here D_2 and He) into the plasma and a spectroscopic system, collecting the emitted light from the interaction of the plasma with the injected neutrals to deduce important plasma properties. The piezo gas valve is mounted inside the plasma chamber of AUG on the LFS at the height of the mid-plane. The emitted light is collected by two optical heads installed inside the plasma chamber, which have toroidally and poloidally aligned viewing chords. Figure 4.1 shows the set-up of the in-vessel components, with the piezo gas valve coloured in red and the toroidal and poloidal optical head in yellow and blue, respectively. The light is guided from the vessel to the spectrometer via optical fibres, where it is spectrally resolved and imaged on a CCD camera. In order to deduce the plasma quantities of interest correctly from the collected data, all components of the set-up were carefully calibrated and characterized, which is presented in the following sections.

4.2 Gas Inlet System

The custom-made gas inlet system consists of the piezo-driven gas valve inside and the gas supply and valve control system outside the plasma chamber. The piezo gas valve was already installed and has been used before for T_e- and n_e-measurements via helium beam spectroscopy [81]. For this reason it was to a large extent already characterized and calibrated [95]. The most relevant characteristics of the gas valve together with additionally performed calibrations are presented in Section 4.2.1. The gas supply system was re-designed to comply with the German safety rules for operation with explosive gases [96]. The details about the new design are given in Section 4.2.2.

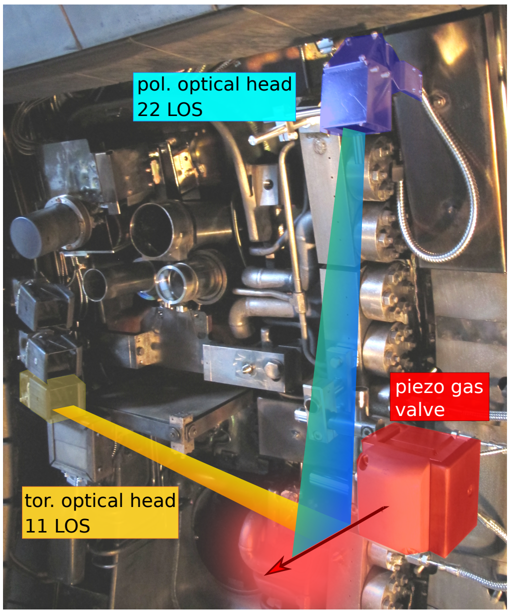

Figure 4.1: In-vessel view of the experimental set-up with the piezoelectrically driven gas valve (coloured in red), which injects room-temperature neutrals into the plasma. The two optical heads with toroidally (yellow) and poloidally (blue) aligned viewing chords collect the light emitted by the plasma ions due to their interaction with the injected gas.

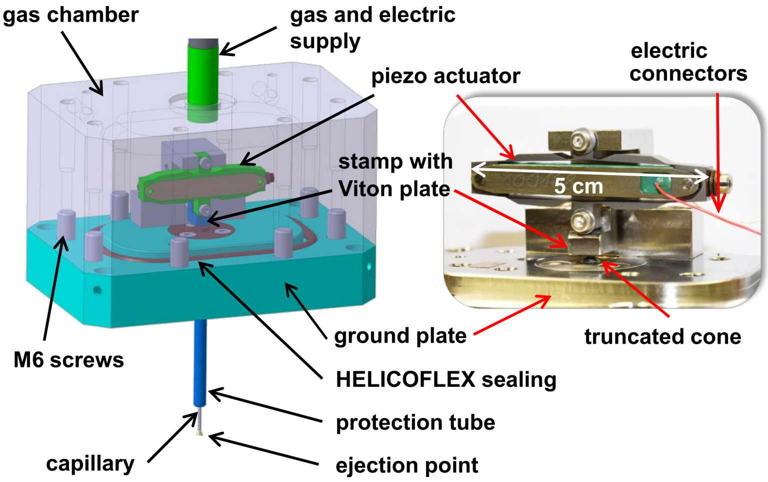

Figure 4.2: *Left:* CAD drawing of the in-house built piezoelectrically driven gas valve with indications of its most important components. *Right:* Picture of the piezo actuator mounted on the ground plate. Figure adapted from [95].

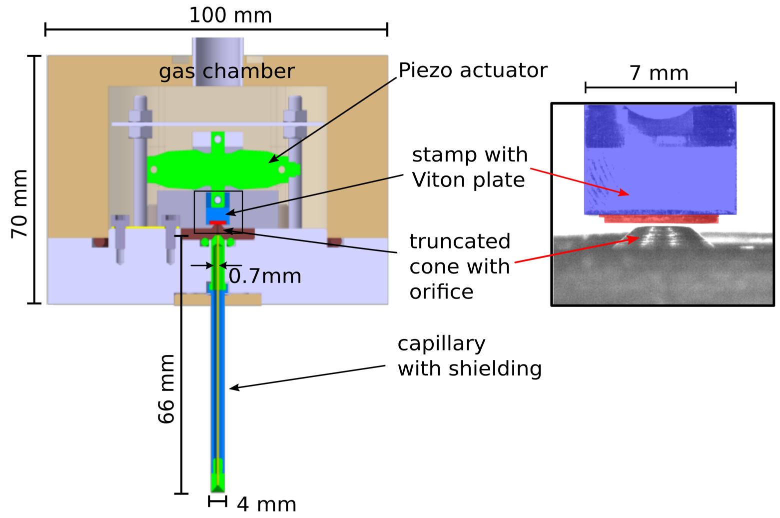

Figure 4.3: *Left:* Cross section of the piezoelectrically driven gas valve. *Right:* Zoom-in-picture of stamp with the Viton sealing towards the capillary orifice. Figure adapted from [95].

4.2.1 Design of the Gas Valve

The structure of the piezoelectrically driven gas valve is shown on the left of Figure 4.2. The walls of the gas chamber and the ground plate with a gas capillary of 66 mm length and 700 µm diameter are made from stainless steel with a total mass of about 3 kg [95]. The surrounding box is sealed towards the ground plate with a HELICOFLEX metal sealing [97], which allows filling pressures of the gas chamber of up to 100 bar [95]. The dimensions of the gas valve are $10 \times 7 \times 7\,\mathrm{cm}^3$ and it encloses a gas volume of about $100\,\mathrm{cm}^3$. In this volume the piezo actuator, a PX 500 linear positioning stage (see right side of Figure 4.2) with the dimensions $52 \times 20 \times 8\,\mathrm{mm}^3$ [98], is mounted to the ground plate. A stamp with a Viton elastomer plate of 5 mm diameter and 1.5 mm thickness is fixed to the piezo actuator [99]. Different elastomers have been tested in the laboratory as sealing materials before installing the gas valve in the plasma chamber. Viton was the most robust material to withstand the temperature of the baking process (see Section 1.4). The Viton plate seals the gas chamber towards the opening of the gas capillary, a truncated cone with an orifice of 400 µm.

Without load the stroke of the piezo actuator is 500 µm in a voltage range of −20 V to +130 V. A pressure force of the piezo actuator on the orifice of about 3 N is needed to guarantee proper sealing of the valve when no external voltage is applied to the piezo actuator (default closed), but also reliable opening of the gas valve when the maximum voltage of 130 V is applied to the piezo actuator. A 30V300 OEM piezo controller [100] together with Siemens SIMATIC is the control unit of the piezo actuator. It delivers a rectangular output signal with a modulation frequency of up to 100 Hz.

The gas valve is mounted in the vacuum vessel of AUG next to the neutral beam injector and connected via vacuum feed-throughs with the gas and electric supply. The direction of the capillary and thus, the gas injection, is sought to be as radial as possible (see Section 4.3.2.3). It is located at the OMP, i.e. its vertical position is about 6 cm above the zero position, which is for the later presented discharges (see Section 3.2) close to the height of the magnetic axis (see also Figure 4.8b). The thin gas capillary is enclosed with a protection tube and the gas valve shielded against plasma particle interaction with a tile fully made from tungsten. The gas valve is also equipped with a Pt100 thermo-couple inside the gas chamber and an active water cooling system outside (see Figure 4.1) such that during plasma operation the temperature of the gas valve stays below 30 °C, to guarantee a reliable functioning of the piezo actuator, which is known to decrease performance when operated above 50 °C [95].

4.2.2 Design of the Gas Supply and Pump System

In Figure 4.4 a scheme of the gas supply circuit is shown. The system is built from stainless steel pipes and vacuum-tight connectors [101], to guarantee safe operation. It has been leak-tested against low and excess pressure and certified by DEKRA [102]. The system consists of three parts which are galvanically insulated.

The first part is the actual gas supply unit, placed outside the torus hall in a skeleton container. The gas bottles R1 and R2 (see Figure 4.4) are equipped with a pressure-relief valve and pressure regulators (PR1 and PR2), so that the system can maximally be filled with 6 bar. The working gas, normally helium (He) gas with 99.999 % or deuterium (D_2) gas with 99.8 % purity, can be chosen remotely via the pneumatic valves V1 and V2, respectively. Normally He gas with 99.999 % or D_2 gas with 99.8 % purity are used, but also H_2 and N_2 gas can be connected. The pneumatic valves are by default closed and are controlled in such a way that only one type of gas can be in the system at a given time.

The gas supply unit is connected via the pneumatic valve V3 to the gas supply board, located inside the torus hall, next to the plasma chamber. The gas reservoir R3 of 500 ml is needed to guarantee a stable pressure in the system during operation and, thus, a constant gas flow rate (see Section 4.2.3) through the piezo gas valve. R3 is filled with the desired pressure using an electric throttle valve (TV). This valve can be bypassed with the pneumatic valve V4 (default closed) when pumping the gas supply system. The gas pressure in the system is surveyed with two piezoresistive pressure gauges by Bürkert, S1 in the range of 1 to 500 mbar and S2 in the range of 0.5 to 20 bar [103]. V5 separates S1 from the system for pressures higher than 500 mbar. V6 is the safety valve towards the flange of the torus, where the gas is led into the valve (R4) via a vacuum feed-through. V7 is another pneumatic valve which connects the gas supply system of the piezo valve with the pumping unit.

The pumping unit is shared by several gas inlet systems, but only one system can be pumped at a given time. The pumping unit is equipped with another piezoresistive pressure gauge and an ATEX approved DUO 11 rotary vane pump by Pfeiffer Vacuum [104], with a throughput of $10.5\,\mathrm{m^3\,h^{-1}}$. The pumping system is also used to regularly test the total gas supply system against leakage. To be leak-proof the system, which has a volume of about 880 ml, has to sustain a pressure below 5×10^{-2} mbar for 60 s.

4.2.3 Calibration and Characterization of the Gas Valve

Since the piezoelectrically driven gas valve has been in use for He beam spectroscopy before [81], it has already been largely calibrated and characterized. The flow rate calibration of the gas valve was extended to various gas species and pressures up to 2 bar.

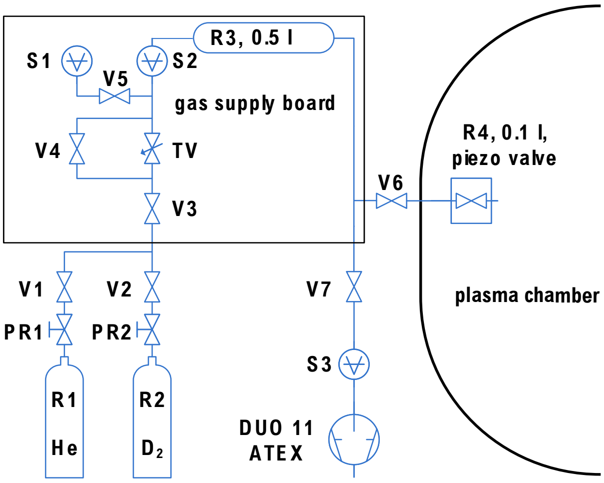

Figure 4.4: Scheme of the gas supply circuit, which consists of three parts: The gas supply outside of the torus hall, the gas supply board located in the torus hall next to the plasma chamber and the pumping system (adapted from [79]).

Thus, the most relevant properties of the gas valve and the flow rate calibration procedure are presented in the following.

4.2.3.1 Flow Rate

The mean particle flow rate per gas pulse is determined employing the ideal gas equation

$$pV = Nk_{\mathrm{B}}T, \tag{4.1}$$

with p the pressure in the gas chamber, V the volume of the gas chamber, N the number of gas particles, $k_{\mathrm{B}} = 1.38 \times 10^{-23}$ J/K the Boltzmann constant and T the temperature of the gas. The flow rate of the gas valve is determined by the flow regime, which, in turn, depends on the ratio of the mean free path length between two gas particle collisions, λ_{mfp}, and the characteristic length D_{sys} of the system. For the gas valve the determining parameters are, thus, the gas pressure in the system, the gas species and the diameter of the capillary [95]. For the investigated gas pressures and gas species λ_{mfp} ranges from 10^{-7} m to 10^{-5} m at 300 K, thus $\lambda_{\mathrm{mfp}} << D_{\mathrm{sys}}$, and the viscous gas flow can be described using the fluid equations. For low gas pressures (up to about 150 mbar, see Figure 4.5) the gas flow is laminar and described by the Hagen-Poiseuille equation, which has a quadratic dependence on the gas pressure [95, 105]. For higher gas pressures, the gas flow becomes friction limited, i.e. the capillary diameter of 700 µm limits the gas flow and the flow rate becomes linearly dependent on the gas pressure [95, 106].

The mean particle flow rate for the molecular gases H_2, D_2, N_2 and the atomic gas He was measured in a laboratory set-up. For this purpose the gas valve was, together with the gas supply board, installed in a test chamber with a volume of 491 ± 5 l and a background pressure of about 10^{-7} mbar. The test chamber is equipped with a baratron pressure gauge and the temperature inside the chamber was kept at 26 °C. The flow rate was determined for different gas pressures in the piezo valve, ranging from 10 mbar to 2 bar. The number of injected particles $\mathit{\Delta} N$ into the test chamber was counted by measuring the pressure increase $\mathit{\Delta} p$ in the test chamber after gas injection and using Equation 4.1. Per measurement point one gas pulse was triggered, where the opening time of the gas

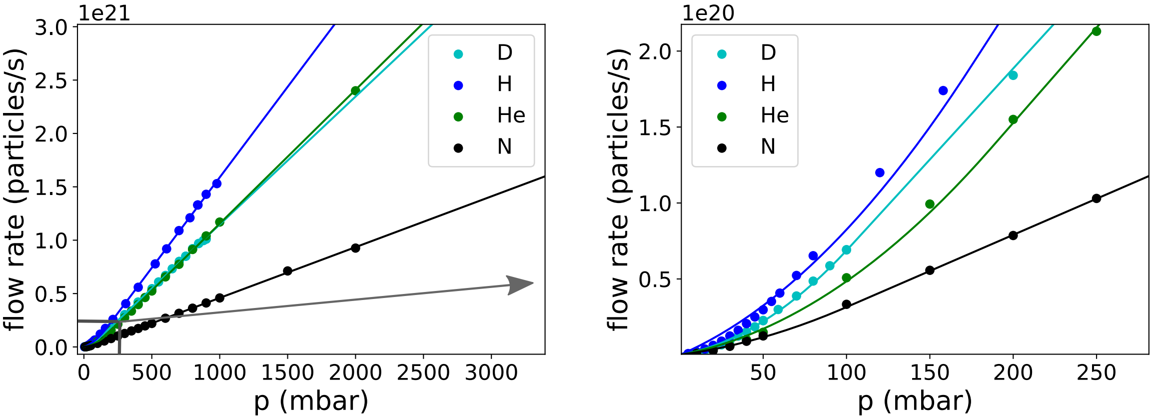

(a) Quadratic and linear flow regime

(b) Zoom into the quadratic flow regime

Figure 4.5: Experimentally determined flow rate of the piezoelectrically driven gas valve for four different gas species. The least-square fit to the data points consists of a continuously differentiable function with a quadratic pressure dependence at low gas pressures (b) and a linear dependence at high gas pressures (a).

valve was adjusted to have about the same number of injected particles, in order to be in the same sensitivity range of the pressure gauge. The experimentally determined flow rate for the four different gases is shown in Figure 4.5. It was fitted with a continuously differentiable function of quadratic dependence for $p < p_0$ and with a linear function for $p > p_0$. p_0, the pressure where the flow regime changes, was given as a free parameter. A cross check of the flow rate measured in the laboratory set-up was done after installing the piezo gas valve in the torus. Then, following an analogous procedure as in the laboratory, the flow rate was determined in the plasma chamber, which has a volume of $40.0 \pm 0.1\,\mathrm{m}^3$. The measured flow rates agreed within the uncertainties for all four gas species.

4.2.3.2 Gas Cloud Shape

Another important characteristic of the injected gas cloud is its geometry. The gas cloud shape was measured in the above described laboratory set-up. The gas neutrals were made visible by injecting them with the gas valve into a current controlled helium glow discharge with a background pressure of 4×10^{-4} mbar [95]. The light emitted by the excitation of the injected gas neutrals with the background helium was captured with a fast camera, a Phantom v711 produced by Vision Research, which has a frame rate of up to 10 kHz [107]. It was found that the gas expands in a cone with a 2D symmetric Gaussian density distribution perpendicular to the injection direction and it exhibits a quadratic decay in the direction of the injection. The opening angle was determined from the FWHM of the fitted 2D Gaussian distributions to the experimental data. The values for helium and deuterium and the respective gas pressure are given in table 4.1.

The opening angle of the gas cloud depends slightly on the injected gas species. At all investigated pressures the opening angle was constant, however, measurements at low gas pressure (below 200 mbar) could not be assessed since the measured signal became to weak. Therefore, it can not be excluded that with lower pressures in the gas system the beam shape changes (i.e. an increase of the opening angle).

gas type	pressure (mbar)	opening angle (degree)
He	5000	40 ± 3
D	600	50.8 ± 1

Table 4.1: Full opening angle of the gas cloud of the piezoelectrically driven gas valve. The cloud shape was measured for helium and deuterium gas in a laboratory set-up using a helium glow discharge.

Connected to the beam shape is the expansion velocity of the gas particles leaving the capillary. The velocity distribution is assumed to be thermal, which delivers for helium atoms at 300 K a mean velocity of 1.24 km/s. However, the forward model described in Section 5.2.5 indicates that the particles also might leave the gas valve with a speed which is up to two times the thermal velocity.

4.2.3.3 Performance

For calibration and for experimental operation the gas valve is always fully opened, i.e. the maximum voltage range from -20 to 130 V is applied. The switching time is then about 3.1 ms which is comparable to the acquisition time of the spectroscopic system of 2.45 ms (see Section 4.3). The switching time of the gas valve could be reduced by not applying the full voltage range to the piezo actuator. However, then the stroke of the piezo actuator is decreased, which might limit the resulting gas flow. Also operation of the piezo element above 40 °C) reduces the stroke [95].

In Figure 4.6 the signal of the piezo valve control voltage (black) is shown, which was averaged over 30 periods from the gas puff cycle and each period was shifted relative to the decreasing flank (conditional averaging). Also shown is the detected radiance signal of the He II spectral line at 468.571 nm (red). The measurement was taken in a 3 s long time window of a stable L-mode phase with constant heating and constant density (discharge # 36965). The conditional averaging reveals that the control voltage exhibits a periodic jitter of about 3 ms in the pulse length. Besides this the control voltage exhibits an absolute jitter of 9 ms (not shown in the figure). The black solid line imitates the acquisition of the control voltage signal by the spectroscopic system, which is a smoothing over 2.45 ms.

The intensity signal (red) as measured from the injected He follows the time trace of the piezo gas valve with a time delay of about 3 ms. This delay has been already observed in laboratory tests when monitoring the piezo movement with the fast camera [95]. It can be attributed to a delayed response of the piezo actuator due to its capacity and mechanical inertia. The detected He II signal also shows that after closing the piezo actuator it takes about 5 ms until the intensity level decreases to the background level. This exponential decay is due to a delayed flow out of the capillary. Furthermore, it is also observed that the piezo actuator exhibits a damped oscillation when closing (not shown in the figure) [95]. This can lead to a short re-opening of the gas valve before closing completely. For this reason the piezo gas valve is normally operated in the way that it is periodically closed for at least 20 ms. In this way sufficient time frames of background signal can be collected. Up to three frames of passive signal before and after the opening of the gas valve are averaged and subtracted from the detected signal where the time frames acquired during the switching times are ignored (see also Section 5.1).

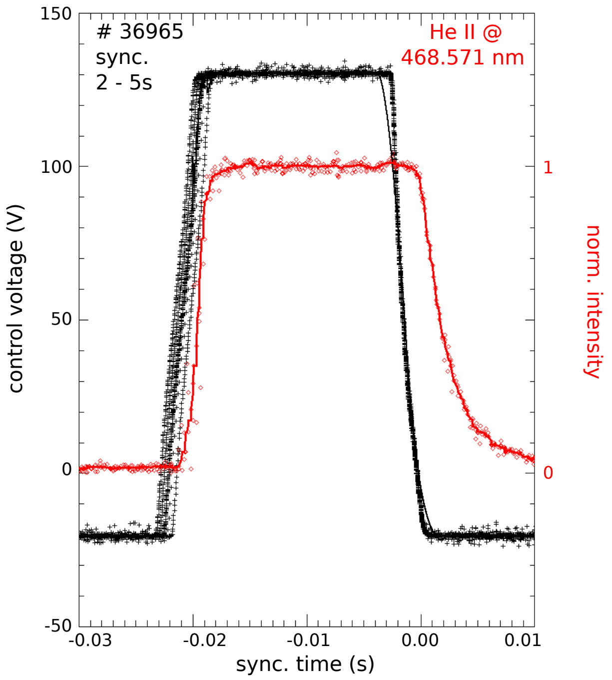

Figure 4.6: Time trace of the piezo gas valve control voltage (black crosses), synchronized to the decreasing flank. The black line is a smooth of 2.45 ms over this signal, which imitates the acquisition of this signal by the spectroscopic system. The red data points show the synchronized signal of the normalized intensity of the He IIline at 468.71 nm. The red line is the average of this signal.

4.3 Spectroscopic System

The spectroscopic system consists of two in-vessel optical heads which are connected via optical fibres to a Czerny-Turner-like spectrometer. The specifications and the operating principle of the optics and the spectrometer are given in Section 4.3.1.1 and 4.3.1.2, respectively. The different applied routines to calibrate the experimental set-up are described in Section 4.3.2.

4.3.1 Components

4.3.1.1 In-vessel Optics

One optical head (coloured in yellow in Figure 4.1) is aligned toroidally, which means it is mounted in such a way that it views the ejection axis of the piezo gas valve from the horizontal direction. The poloidal head (coloured in blue in Figure 4.1) views the ejection axis from the vertical direction. The alignment of the in-vessel optical heads to be as tangential as possible to the flux surfaces is crucial to measure the quantities of interest, e.g. the toroidal and poloidal particle velocities, at the correct measurement position (see Section 4.3.2.1).

The toroidal head has 11 and the poloidal head 22 LoS which are focussed on the ejection axis of the piezo gas valve. The optical fibres with a diameter of 400 µm are stacked in two rows in the optical head, thus, they are separated by about 0.4 mm. The radial resolution of the toroidal LoS increases from 3 mm further outside to 6 mm further inside

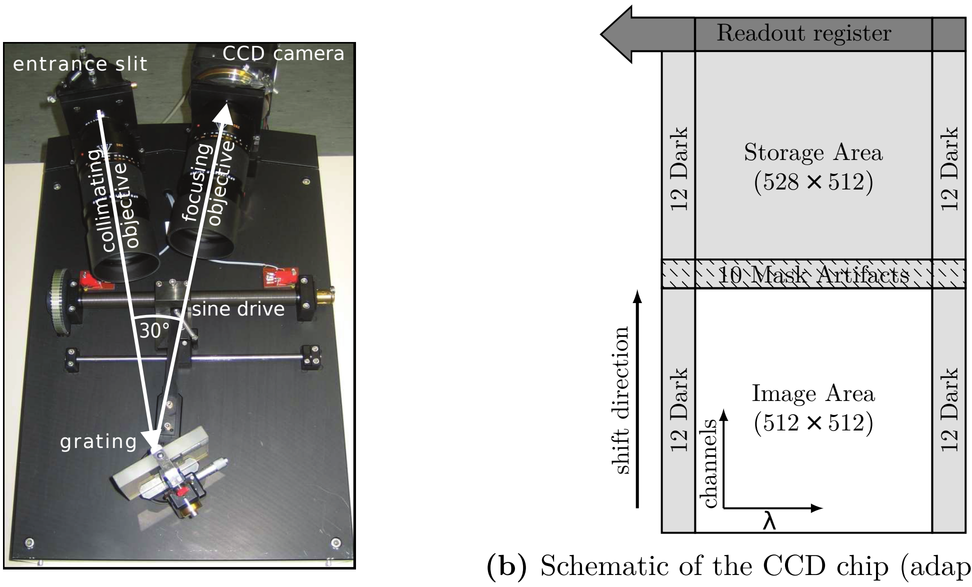

(a) The Spectrometer (adapted from [43].

(b) Schematic of the CCD chip (adapted from [108]).

Figure 4.7: The Czerny-Turner-like spectrometer (here f/4 and not f/2.8) consists of two objective lenses, a 50 µm broad entrance slit, a movable grating with 2400 lines/mm and a CCD camera with a 512 × 512 pixels CCD-chip operated in the transfer area mode.

the plasma and leads to a radial coverage of $R = 2.138$ to 2.154 m at the measurement position. The radial resolution of the poloidal LoS increases from further outside to inside from about 3 mm, this is the limit given by the diameter of the LoS beam, to 9 mm. The radial range covers 2.115 to 2.172 m at the measurement position. Lenses in the optical heads bundle the light onto the optical fibres. The f/2.7 plano-convex lens in the toroidal head has a focal length f of 85 mm and is made from silica. In the poloidal head the light is guided with a mirror through a borosilicate-crown glass (N-BK7) f/2.5 plano-convex lens, with $f = 50$ mm. The fibres and other optics are only transparent for light in the visible range. The glass fibres are protected against plasma radiation with a metal shielding. Otherwise they can be damaged, what leads to a strong reduction of the light transmission. The optical heads are equipped with a mechanical ferromagnetic shutter. This shutter opens only during plasma operation and, thus, prevents the coating of the optical components which occurs for example during the process of boronisation (see Section 1.4).

4.3.1.2 Spectrometer

The high throughput f/2.8 Czerny-Turner-like spectrometer (see Figure 4.7a) is located outside the torus hall in a dark room and covered with a black box to shield the apparatus against stray light. The spectrometer utilizes two objective lenses of the type Leica APO-ELMARIT-R [109] instead of curved mirrors in order to decrease optical aberrations like astigmatism and coma [110]. 25 optical fibres are stacked vertically and connected to the entrance slit of the spectrometer, which has a width of 50 µm. The light is collimated with a f/2.8 objective lens with $f = 280$ mm. The collimated light is spectrally resolved with a movable reflection grating with a grating constant of $g = 2400$ lines/mm. The grating can be turned remotely with a sine drive to choose the wavelength of interest.

The focusing objective with an f/2.8 lens and $f = 280\,\text{mm}$ is mounted at an angle of 30° to the collimating lens. Thus, the $m = -1^{\text{st}}$ order of the interference pattern is monitored on the CCD camera, where the x-direction of the chip contains the wavelength and the y-direction the radial information of the measurement. The CCD camera is a Princeton Instruments ProEM 512B+_eXcelon, a back-illuminated, frame-transfer CCD camera with on-chip multiplication gain [111]. Its CCD chip, shown in Figure 4.7b, consists of an active sensor area of 512 × 512 16 µm pixels, the frame-transfer mask area of 512 × 528 pixels and additional 12 dark pixels on each side. The CCD camera is thermoelectrically cooled using a Peltier cooler to reach a detector temperature of $-70\,°\text{C}$ [112]. This reduces the dark current of the CCD camera and increases the on-chip multiplication gain [113].

The time resolution t_{exp} of the spectroscopic system is mainly set by the read-out time of the CCD chip. The read-out frequency of the multiplication gain register is 10 MHz. In order to reduce the read-out time and the read-out noise, pixel ranges which are illuminated by the same optical fibre, so-called regions of interest (ROIs), consisting of about 20 pixels, are binned together into channels. Thus, the number of rows to be read out reduces from 512 to 25. Together with the shifting time of the pixel rows to the read-out register, which is set to $t_{\text{s}} = 0.6\,\mu\text{s/row}$, this results in a time resolution of $t_{\text{exp}} = 2.45\,\text{ms}$. A further reduction of t_{exp} to the µs-range as described in [114] has not been applied yet, since it implies a reduction of the radial resolution and/or radial coverage of the measurement, but is considered for future work (see also Section 9.2) to study phenomena which are faster than the time scale of the measurement.

4.3.2 Calibration of the Spectroscopic System

The calibration of the spectroscopic system is important and critical in order to extract the correct quantities from the data as density, velocity and temperature of the investigated impurity ions. For this reason, before and after an experimental campaign a calibration of the complete experimental apparatus is performed, including the calibration of alignment of the optics (see Section 4.3.2.1), the radiance of the detected light (see Section 4.3.2.2), the wavelength axis of the CCD chip (see Section 4.3.2.3) and the instrument function of the spectrometer (see Section 4.3.2.4).

4.3.2.1 Geometry Calibration

The alignment of the in-vessel optical components and of the piezo gas valve is done in an iterative process. The optical fibres are back-illuminated, producing a light cone in the vessel which represents the LoS. The coordinates of the lens position and of 3 to 4 positions along each LoS are measured with the 3D measurement technology provided by FARO [115]. Also the coordinates of the injection point of the gas valve and its normal vector are determined with this technology. These values are then converted into the coordinate system of the torus and the data points along each LoS are fit with linear fits which are imposed to go through the lens position. Thus, the radial, toroidal and poloidal alignment of the diagnostic components can be checked and, if needed, their positioning is adjusted and re-calibrated. This leads to a measurement accuracy of the geometry of the in-vessel components of below 1 mm.

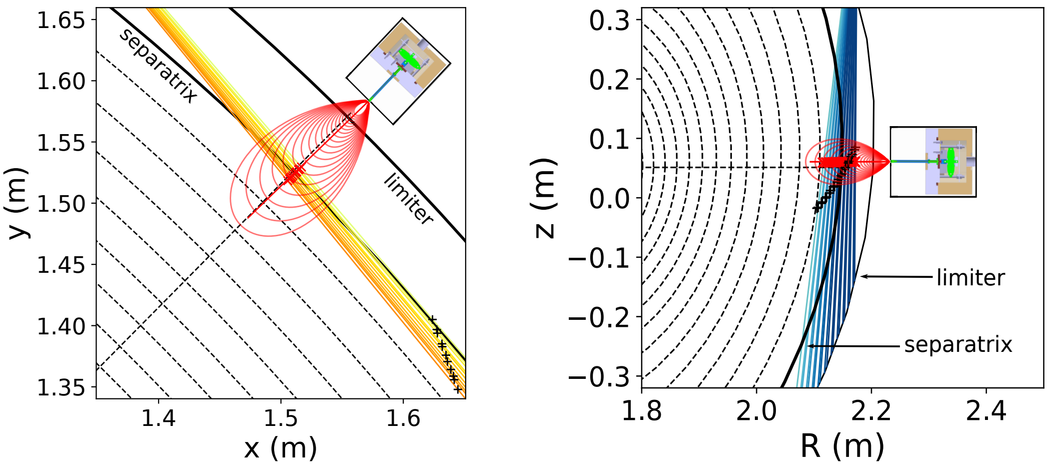

(a) Toroidal View **(b)** Poloidal View

Figure 4.8: Alignment of the optical components in the plasma vessel: The red lines indicate regions of constant density of the piezo gas valve and the injection axis. The yellow lines show the 11 toroidal LoS and the blue lines the 22 poloidal LoS. The red crosses give the intersection points with the gas cloud (measurement position) and the black crosses indicate the location where the LoS are tangential to the flux surfaces.

Figure 4.8 shows the final alignment of the optical components for the experimental campaign of 2018/2019 when most of the later presented experiments were performed. In Figure 4.8a a top-down view presents the geometry of the 11 toroidal LoS (yellow/orange) with respect to the injection axis of the piezo gas valve (red) and Figure 4.8b the 22 poloidal LoS (blue/green) and the gas valve geometry (red). As can be seen from Figure 4.8a, the injection axis is aligned to be as radial as possible. The red crosses indicate the measurement position, which is the weighted average of each LoS with the density distribution of the gas cloud as measured in the laboratory experiments (see Section 4.2.3). Please note that interaction of the injected gas with the plasma particles leads to a change of the gas cloud shape which then influences the measurement position. This is described for the case of HeII spectroscopy in more detail in Section 5.2.5. The black crosses in Figure 4.8 indicate the position where the LoS is tangential to the magnetic flux surface. This position depends on the chosen plasma shape and the presented case is the reference discharge # 35842 (see Section 3.2), a low-shaped LSN plasma in favourable drift configuration with $B_\phi = -2.5\,\mathrm{T}$ at the magnetic axis, a plasma current of 0.8 MA and $q_{95} = -5$.

Due to geometric restrictions the optical components must be positioned behind the limiter in order to reduce plasma interaction. Therefore, the toroidal optical head can only be aligned in a way that its LoS are tangential, i.e. toroidal, to the field lines at a position several cm behind the actual measurement position (see Figure 4.8a). Thus, for the determination of the toroidal velocity, the projection of the LoS at the measurement position has to be taken into account (see Section 5.1). For the poloidal LoS (see Figure 4.8a), the measurement points are almost at the same position where the LoS are tangential to the flux surfaces. Therefore, the error arising on the poloidal velocity due to the imperfect poloidal alignment is below 1 % for all LoS.

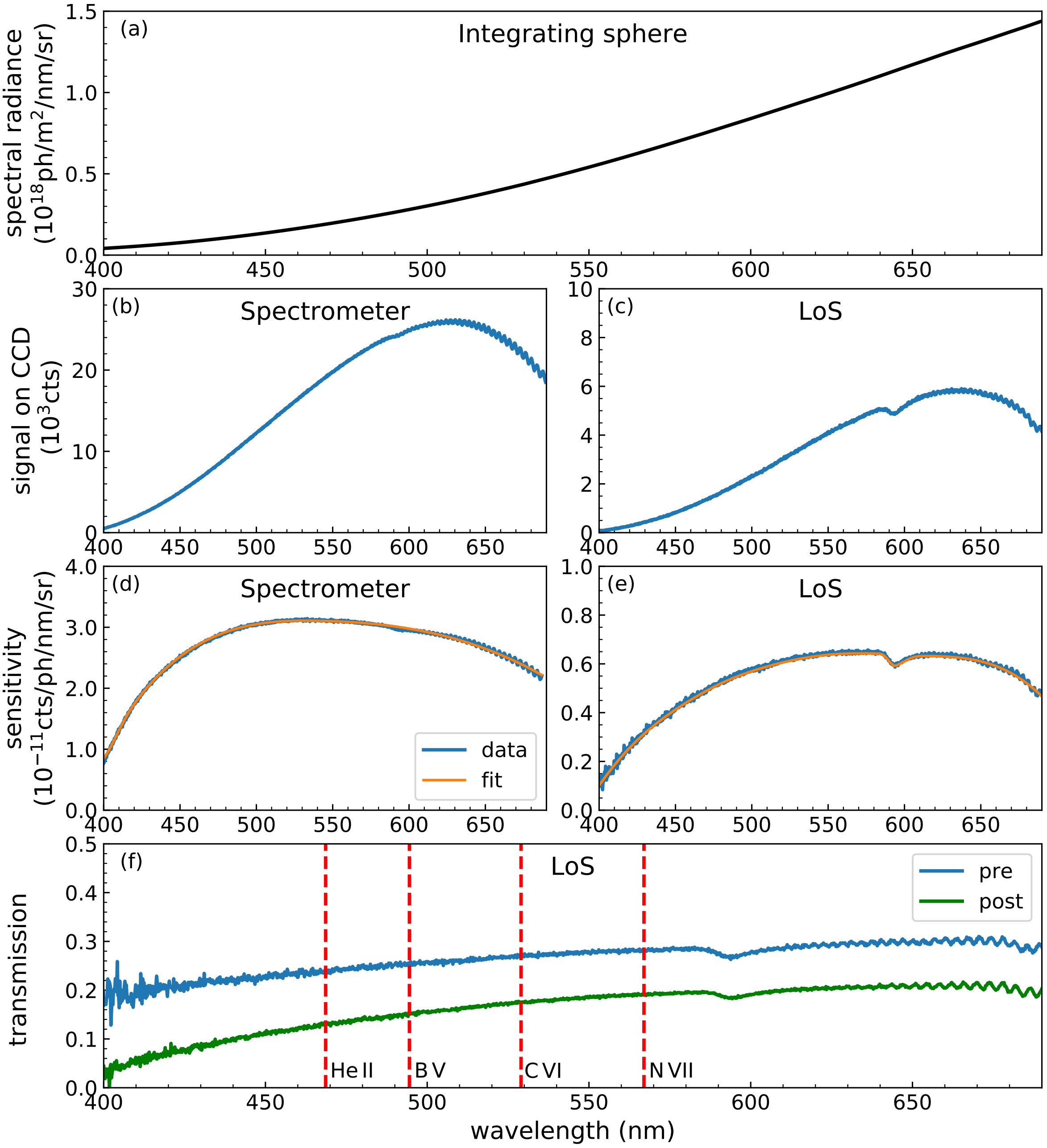

Figure 4.9: Radiance calibration: The known spectral radiance of the integrating sphere (a) is measured with the spectrometer only (b) and the complete optical set-up (c) over the visible wavelength range to determine the sensitivity of each spectrometer channel (d) and LoS (e). (f) Example of the decrease of the transmission for one LoS during an experimental campaign. The red dashed lines indicate the wavelength of investigated impurity spectral lines.

4.3.2.2 Radiance Calibration

The sensitivity S of the diagnostic set-up has to be quantified to be able to later relate the detected counts on the CCD chip to the radiance of the spectral line in order to deduce absolute values for the impurity density (see Section 5.1). For this purpose a stable light source, an integrating sphere Model Unisource 1200 produced by Labsphere [116], with known spectral radiance L_λ is used. The sensitivity is determined for two subsystems of the diagnostic, namely for the in-vessel components including the optical fibres and, separately, for the spectrometer with its connectors to the optical fibres. This gives additional flexibility during the course of an experimental campaign, as it allows to chose different LoS settings for different experiments and connect them to different spectrometers without the need of a new sensitivity calibration for each set-up change.

The integrating sphere is put in front of the optics (either the optical heads or the optical fibres connected to the spectrometer channels) such that all detection cones of the optics are covered by the light source. The light emitted by the sphere is measured over the visible wavelength range from 400 nm to 700 nm. For this the spectrometer grating is continuously turned during acquisition. This movement is performed slowly, such that within one time frame of acquisition t_{exp} the wavelength change $\Delta\lambda$ is so small that L_λ can be assumed constant. Thus, the count rate $n_{\mathrm{counts}}/t_{\mathrm{exp}}$ on each pixel (x_{pix}) gives information about the corresponding transmission efficiency at the wavelength λ and the sensitivity S of each channel, pixel and wavelength can be determined:

$$S = S(\lambda, x_{\mathrm{pix}}, \mathrm{channel}) = \frac{n_{\mathrm{counts}}(\lambda, x_{\mathrm{pix}}, \mathrm{channel})}{L_\lambda \Delta\lambda t_{\mathrm{exp}}}. \tag{4.2}$$

The sensitivity of a spectrometer is mainly given by its acceptance angle, its etendue and losses due to vignetting, while transmission losses in the optical components originate from light scattering, light absorption and fibre optics splicing [117–119].

In Figure 4.9a the spectral radiance of the integrating sphere is shown plotted against the wavelength. Figures 4.9b and 4.9c show the measured count rates at the central pixel for one spectrometer channel and one LoS, respectively. In Figures 4.9d and 4.9e the corresponding sensitivities are depicted. The sensitivity curve exhibits a dip at about 600 nm which can be attributed to light absorption by water molecules in the optical fibres. The oscillatory behaviour at higher wavelength is due to optical etaloning, an interference effect occurring when a back-illuminated CCD chip is illuminated with coherent light between 600 and 1100 nm [120]. The sensitivities are fitted with bivariate splines (orange lines in Figures 4.9d and 4.9e) for each spectrometer channel, pixel and wavelength.

Although the optical heads are shielded with magnetic shutters, a deterioration of their optical components in the course of an experimental campaign is observed. The main mechanisms leading to a reduction of their transmission are neutron damages and coating of the optical components. This reduction is wavelength-dependent and normally stronger for the poloidal optical head, since it consists of two optical components, a mirror and a lens, which can be damaged. For this reason, after an experimental campaign another sensitivity calibration (post) is performed to cross-check with the previous one (pre). As can be seen in Figure 4.9f the transmission reduction can be as much as 50 % in the blue wavelength range while it is on average 20 % in the red wavelength range. It is found that the deterioration of the components happens step-wise over time. Hence, the post-calibration helps to quantify the uncertainties on the reconstruction of the impurity density. Between two experimental campaigns the surfaces of the optical components are cleaned or they are replaced by new ones.

4.3.2.3 Wavelength Calibration

The determination of the wavelength axis of the CCD chip is needed to relate the detected signal at a certain pixel position to the wavelength of the emitted light. This calibration is very important due to its impact on the deduction of the radial electric field from the impurity velocities (see Section 5.1), which in turn are deduced from the Doppler shift of the wavelength of the investigated spectral line.

The linear dispersion of the spectrometer is determined following the approach in [110]. The wavelength axis of a spectrometer with reflection grating is given by the following grating equation:

$$mg\lambda = \cos\gamma(\sin(\theta_1 + \phi_1) + \sin(\theta_2 + \phi_2)), \tag{4.3}$$

where m is the diffraction order, g the grating constant, λ the wavelength, γ the vertical angle of an off-axis ray to the optical axis, θ_1 and θ_2 the entrance and diffraction angle, respectively, and ϕ_1 and ϕ_2 the horizontal angle to the optical axis at the entrance slit and the imaging plane, respectively (see also Figure 4.10a). The angles ϕ_1, ϕ_2 and γ are given by optical geometry: $\tan\phi_1 = x_1/f_1$ and $\tan\phi_2 = x_2/f_2$ and $\tan\gamma = y_2/f_2 = y_1/f_1$ (see Figure 4.10a) The central wavelength λ_0 is defined as the wavelength at the optical axis, where $\phi_1 = \phi_2 = \gamma = 0$:

$$\lambda_0 = \frac{\sin\theta_1 + \sin\theta_2}{mg}. \tag{4.4}$$

The reciprocal linear dispersion of the CCD chip can be deduced by differentiating Equation 4.3 with respect to x_2 and using Equation 4.4 to:

$$\frac{\partial\lambda}{\partial x_2} = \frac{\lambda_0}{f_2}\frac{\cos\gamma\cos(\theta_2 + \phi_2)\cos^2\phi_2}{\sin\theta_1 + \sin\theta_2} \tag{4.5}$$

As can be seen from Equation 4.5 the dispersion and, thus, the imaged wavelength range depend on λ_0. For He II$\lambda_0 = 468.571\,\mathrm{nm}$ and the average dispersion is about 0.023 nm/pixel, which leads to an imaged wavelength range of about 463 nm to 474 nm.

The dependence of λ on γ leads to a curved image on the CCD chip (see Figure 4.10b). Since the physical dimension of the CCD chip of 8.2 mm × 8.2 mm is much smaller than the focal length of the focusing objective ($f_2 = 280\,\mathrm{mm}$) $\gamma << 1$. Thus, an expansion of Equation 4.3 in γ to second order leads to the following expression:

$$\Delta x_2 = \frac{\lambda}{\lambda_0}\frac{\sin\theta_1 + \sin\theta_2}{2f_2\cos(\theta_2 + \phi_2)}y_2^2. \tag{4.6}$$

The produced image on the CCD-chip has a parabolic shape (see Figure 4.10b and Figure 4.12a), where the strength of the curvature depends on λ_0.

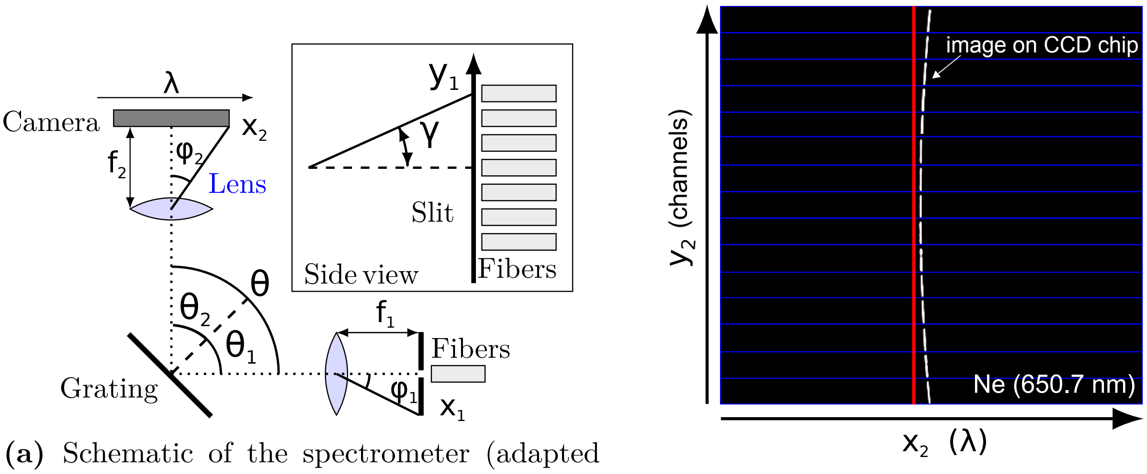

(a) Schematic of the spectrometer (adapted from [108])

(b) Parabola on CCD chip (adapted from [43])

Figure 4.10: The diffraction of vertically stacked optical fibres in the spectrometer leads to a parabolic projection on the CCD chip.

To determine the wavelength axis λ, the free parameters λ_0 and f_2 have to be determined for each channel. This is done by a forward model fitting highly-resolved calibration spectra from a calibration (Ne I or Xe I) lamp, acquired at the positions of the He II(468.571 nm), B V (494.467 nm), C VI (529.059 nm) and N VII (566.937 nm) lines [108]. The calibration lamps emit line radiation which is well characterized and in the wavelength range of interest. The exact wavelength positions are taken from the NIST atomic spectra database [121].

The spectra with sub-pixel resolution (see Figure 4.11) are achieved by slightly moving the grating for each acquired frame in order to minimally change the wavelength at a certain pixel position. The acquired spectra are brought into agreement by shifting them rigidly according to this movement. The resulting high resolution spectra are fitted with Gaussian lines (orange lines in Figure 4.11). Besides the parameters λ_0 and f_2, the instrument function of each channel (see Section 4.3.2.4) and the parabola are fitted (see Figure 4.12a-c). Also a deviation of the central wavelength from the parabolic shape in x-direction Δx due to a displacement of the optical fibres in front of the entrance slit as well as a vertical offset of the parabola in y-direction Δh, caused by an eventual misalignment of the optical axis, are determined (see Figure 4.12a). With this procedure an accuracy of the determination of the wavelength axis of less than 2 pm can be achieved, which translates into an uncertainty of the velocity profile of less than 1 km/s.

This completes the characterisation of the system. Still, the second wavelength calibration is updated for each single measurement to take into account systematic errors originating from changes in the ambient conditions of the spectroscopic system and mainly from mechanical uncertainties of the sine drive motor moving the spectrometer mirror. The latter results in a deviation of the actual central wavelength from the calibrated central wavelength. To determine this deviation, the two outermost of the 25 spectrometer channels used for the measurement are always connected to a calibration lamp. Their acquired spectra are fitted and the difference in the central wavelength is determined. If this difference is the same for both calibration channels this implies that the dispersion and the determined parabola shape have not changed. Then the wavelength axis of the 23 other channels is shifted rigidly by this difference. In this way the systematic error on the rotation determination can be reduced to below 1 km/s.

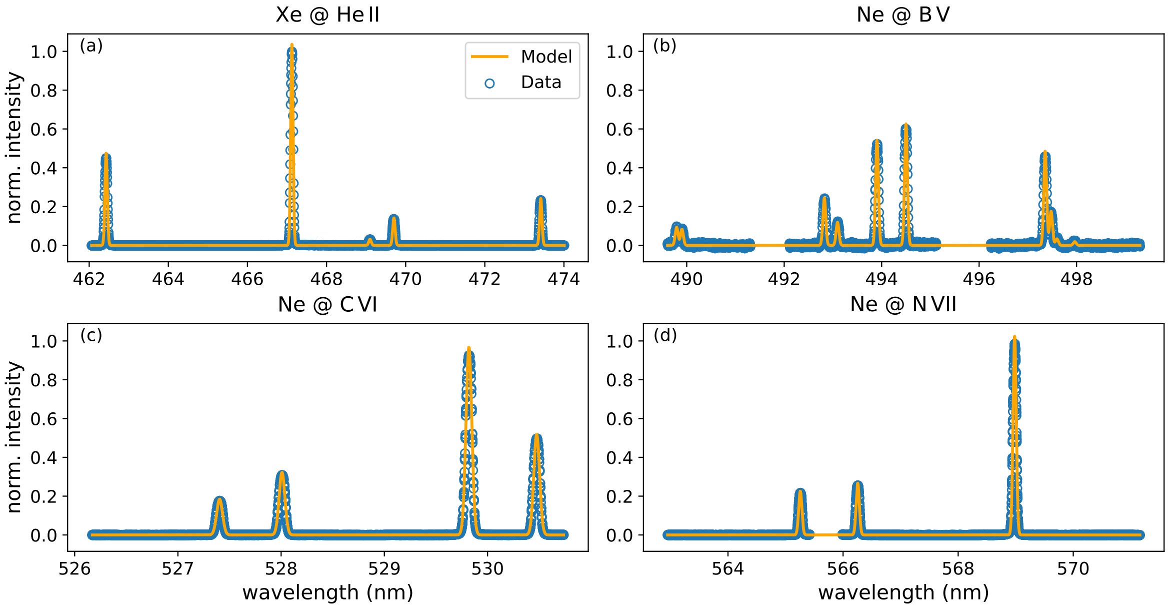

Figure 4.11: Wavelength calibration: A forward model is used to determine the wavelength axis of the CCD chip. For this the central wavelength and focal length of each channel are determined from Gaussian line fits to sub-pixel resolved calibration spectra from a Ne I and Xe I lamp acquired at different wavelength positions (a-d).

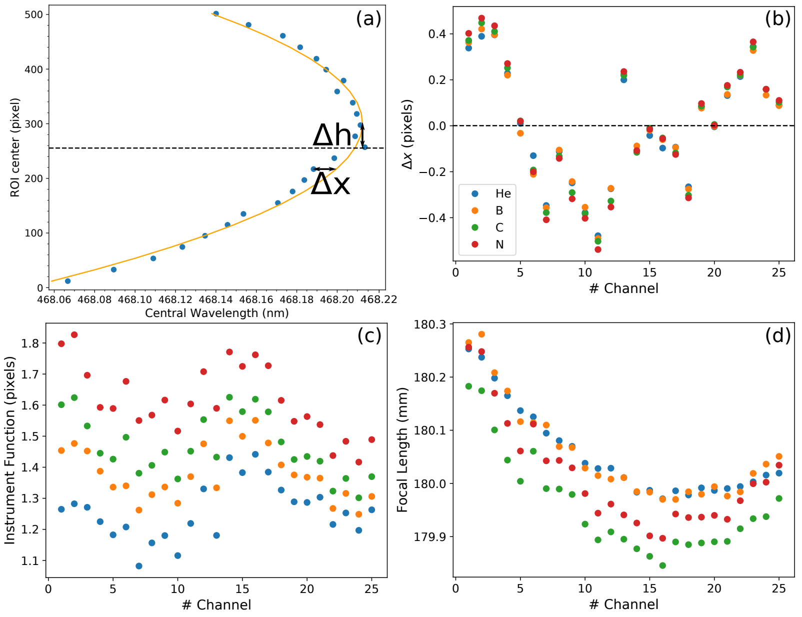

Figure 4.12: (a) Fit of the parabola to the calibration data, indicating Δx and Δh at the He IIwavelength. Δx (b), the instrument function (c) and the focal length (d) are determined at several wavelengths for each channel using a forward model.

4.3.2.4 Instrument Function

The temperature of the measured plasma impurity is deduced from the Doppler broadening of the spectral line (see Section 5.1). However, the measured line width is a convolution of the Doppler broadening and the broadening of the line shape of the spectrometer, the so-called instrument function. If the instrument function can be approximated with a sum of Gaussian lines the deconvolution can be done analytically during the fitting process of the spectral line. Since the slid width of the spectrometer is small (50 µm), the instrument function can be approximated with a single Gaussian. The measured line width is then the root mean square of the instrument function and the Doppler broadening.

Since the spectral lines of the calibration lamp exhibit negligible Doppler broadening, the instrument function of each channel can be deduced from the fit of the high-resolution calibration spectra (see Section 4.3.2.3). The resulting widths in pixels are shown for four different wavelengths in Figure 4.12, which translates for the He II line to an apparent temperature of about 15 eV. Still, He temperatures below 15 eV can be determined down to temperatures of about 2 – 5 eV.

4.3.2.5 Further Calibrations

SNR Determination In another calibration the SNR of the spectroscopic system is determined. The signal noise consists of three contributions [113]. The photon noise σ_S, the dark noise σ_D and the read-out noise of the detector σ_R.

The incoming photons follow a Poisson distribution, which converges for large numbers to a Gaussian distribution, thus, σ_S is the standard deviation of the total number of photons arriving at each pixel S. Since the CCD chip features on-chip multiplication, both the signal and the noise are multiplied by the gain factor G, which is the conversion factor of photons to counts. σ_D is, like the photon noise, the standard deviation of the dark-related signal D. It is small for the here presented cooled CCD camera operated at ms exposure time and can therefore be neglected. σ_R occurs during digitization and, thus, after the on-chip multiplication.

The SNR is determined the following way. The spectrometer is connected to a stable light source. In several acquisitions S is varied and σ_S calculated, which gives G. For the presented camera $G = 7.95\,\mathrm{e}^-/\mathrm{cts}$. σ_R is the measured noise of the background signal and for the presented camera it is $8.72\,\mathrm{e}^-\mathrm{rms}$.

EM Gain Calibration The CCD camera is operated using the em gain readout register, where the incoming photon signal can be amplified. During all other calibration procedures the em gain is set to 1, i.e. no amplification is applied. However, during experiments an em gain > 1 is applied if the SNR is too low. Since it was found that the actual amplification is lower than the set em gain and it is signal-dependent [122], the em gain is also calibrated. For this purpose the CCD camera is connected to a stable light source and the em gain is scanned from 1 to 30, while adjusting the exposure time such that the detected counts range from about 600 cts to 35 000 cts. In Figure 4.13 the measured amplification is plotted against the set em Gain for several count levels.

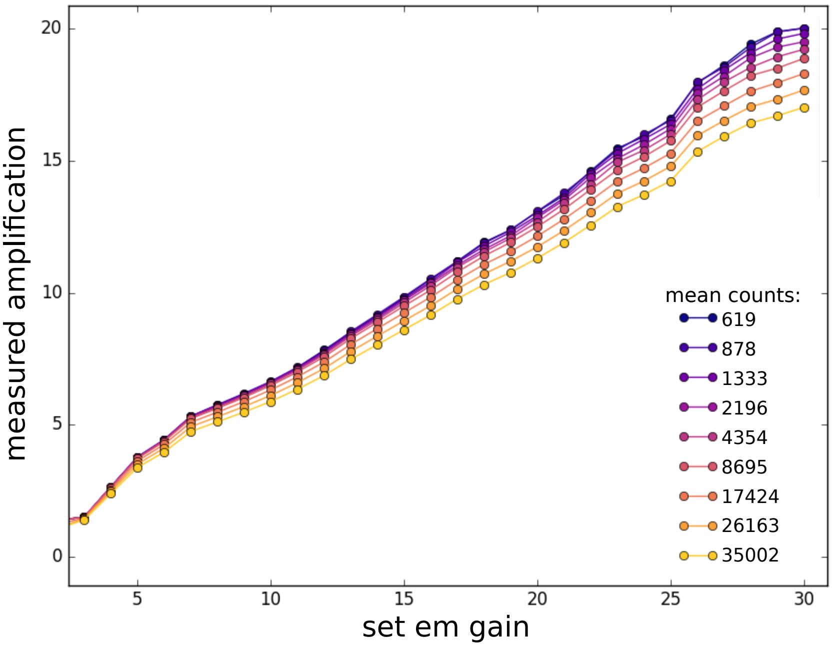

Figure 4.13: *Em gain calibration* The amplification of the signal of a stable light source is measured at different count levels, scanning the em gain of the CCD camera.

4.4 Operation

Figure 4.14 shows the GUI of the piezo gas valve control unit. At the beginning of an experiment day the gas inlet system is pumped and, in case it was filled with a different gas species before, purged with the desired gas. The pressure in the system is chosen in a way that the particle flow rate is not too high to disturb the plasma, but still leads to a high measurement signal on the CCD camera, without leading to saturation of the CCD chip.

If needed, the absolute amount of injected particles can be further adjusted by changing the modulation frequency or the starting time of the gas injection (see Figure 4.14). Usually the gas valve is opened for 30 ms with a frequency of 100 Hz or 200 Hz, so that it is synchronized to the modulation of the He beam spectroscopy gas puff, which is normally operated with a frequency of 100 Hz. Furthermore, such a modulation also allows simultaneous measurements of the beam-based edge CXRS system, which can be disturbed by the gas injection since its LoS cross the gas cloud.

Typically 5 to 6 toroidal and up to 20 poloidal LoS are connected to the spectrometer. The spectrometer settings can be accessed and controlled via LabVIEW, where the central wavelength of the spectrometer can be set and the em gain can be adjusted in such a way that the signal will not saturate.

Before each plasma discharge a central clock triggers the acquisition of the diagnostics to relate the time bases of all measurements. The spectrometer acquires 2500 frames with 2.45 ms during the plasma discharge. Further 1000 background frames are acquired after the discharge and other 1000 frames for the wavelength calibration (see Section 4.3.2.3).

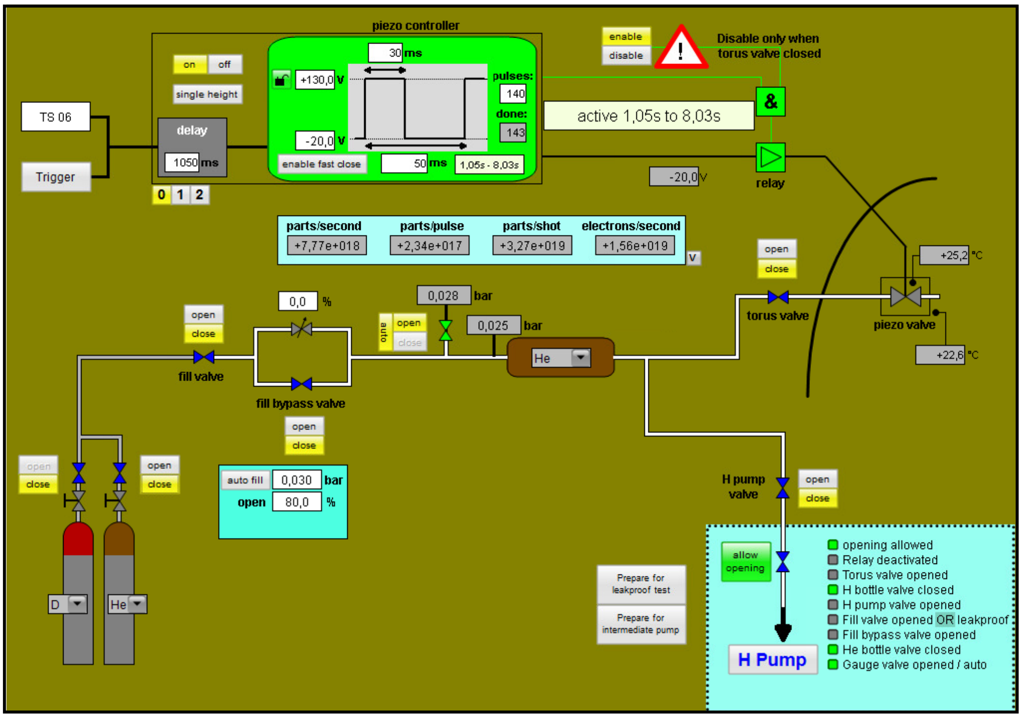

parts/second	parts/pulse	parts/shot	electrons/second
+7,77e+018	+2,34e+017	+3,27e+019	+1,56e+019

- 🟩 opening allowed
- ■ Relay deactivated
- ■ Torus valve opened
- 🟩 H bottle valve closed
- ■ H pump valve opened
- ■ Fill valve opened OR leakproof
- ■ Fill bypass valve opened
- 🟩 He bottle valve closed
- 🟩 Gauge valve opened / auto

Figure 4.14: The GUI of the piezo gas valve control unit.

5 Spectroscopic Methods

In the course of this thesis two different spectroscopy methods were studied, employing the experimental set-up presented in Chapter 4. The goal was in both cases to determine the radial electric field (E_r) across the separatrix at the the outer mid-plane. In the following the two spectroscopy methods are presented, the underlying atomic processes are introduced, the deduction of the plasma quantities from the detected line spectra is presented and their limitations in the determination of E_r are shown.

5.1 Charge Exchange Recombination Spectroscopy

5.1.1 Atomic Processes

Charge exchange recombination spectroscopy (CXRS) is a method where line emission originating from the atomic charge exchange (CX) process is spectrally resolved [82]. The CX process is present in different forms everywhere in the plasma, where an electron from a neutral donor $D^0(n_d)$ with principle quantum number n_d is transferred into the excited state n_2 of a recombined ion $A^{(Z-1)+}$ with charge state $Z-1$ [37, 82]. The de-excitation of the ion $A^{(Z-1)+}(n_2)$ to the lower binding state n_1 leads to the emission of a photon with energy $h\nu$.

The CX process can be written in the following form:

$$A^{Z+} + D^0(n_d) \quad \rightarrow \quad A^{(Z-1)+}(n_2) + D^+ \quad \rightarrow \quad A^{(Z-1)+}(n_1) + h\nu + D^+. \tag{5.1}$$

Since in this charge transfer process energy and momentum is conserved [82], the emitted line radiation from $A^{(Z-1)+}$ contains information about the ion population A^{Z+} in its original charge state Z. From the Doppler broadening of the emitted spectral line $h\nu$ the ion temperature $T_{A^{Z+}}$ and from its Doppler shift the flow velocity $v_{A^{Z+}}$ can be determined. The impurity density $n_{A^{Z+}}$ can be determined from the radiance $L_{A^{Z+}}$ of the line emission.

The here presented active CXRS method focusses on CX reactions between externally introduced neutral hydrogenic atoms (mostly D, but also H) and low-Z plasma impurities. Low-Z impurities are preferred for CXRS in the visible spectral range as in typical fusion plasma conditions they are fully ionized over the complete radial range of the confined plasma, and, therefore, only exhibit few distinct active CX lines in the spectrum. The most relevant spectral lines in the visible wavelength range for this thesis are $\mathrm{He}^{+}(n = 4 \rightarrow 3)$ at 468.571 nm, $\mathrm{B}^{4+}(n = 7 \rightarrow 6)$ at 494.467 nm, $\mathrm{C}^{5+}(n = 8 \rightarrow 7)$ at 529.059 nm and $\mathrm{N}^{6+}(n = 9 \rightarrow 8)$ at 566.937 nm.

Since CX is a resonant atomic process, the cross-sections are highest for charge transfers with minimal change in the electron's binding energy [82]. Therefore, the resonant principle quantum number n_{res} of the impurity ion A depends on n_d. Furthermore, the

CX cross section σ_{CX} increases with n_d as n_d^4 [123, 124]. Although for thermal neutrals the neutral density $n_{D^0}(n_d = 2) \approx 1\,\%\, n_{D^0}(n_d = 1)$, CX reactions between the plasma impurities and the neutral donors in the excited state $D^0(n = 2)$, which lead to light emission in the visible range, are dominant [124, 125]. Thus, for the here presented gas puff-based CXRS system, the $n_{D^0}(n_d = 2)$ distribution of the gas cloud is needed to reconstruct the impurity density profile $n_{A^{Z+}}$ from $L_{A^{Z+}}$ of the investigated CX line (see for this Equation 5.8).

The piezo valve injects room-temperature D_2 molecules into the plasma. When they enter the confined plasma region they dissociate isotropically in two Franck-Condon neutrals with each having a kinetic energy of about 3 eV [124]. As neutral atoms D^0 they interact with the plasma ions i^+ and electrons e^- via:

$$D^0 + i^+ \rightarrow D^+ + i^0 \qquad \text{charge exchange,} \tag{5.2}$$

$$D^0 + e^- \rightarrow D^+ + 2e^- \qquad \text{electron impact excitation.} \tag{5.3}$$

The CX reaction, which is the dominant of both processes, leads to the generation of neutrals with high energy [126]. These energetic neutrals can penetrate further into the plasma and undergo other CX reactions or get ionized by electron impact excitation. The presented interaction processes of the injected D_2 molecules with the bulk plasma get currently implemented in the 3D code FIDASIM [127, 128] to model the $n_{D^0}(n_d = 2)$ distribution of the piezo gas valve [129]. An experimental approach to determine this distribution is to measure the Balmer line emission of the injected neutrals.

5.1.2 Deduction of Plasma Quantities

5.1.2.1 Active Signal

From the active CX signal (see Figure 5.1) several information about the plasma impurities can be deduced [82]. The investigated plasma impurities are thermalized, i.e. they exhibit a Maxwellian velocity distribution. Thus, the resulting spectral line can be fit with a Gaussian line shape:

$$I(\lambda) = I_0 \sqrt{\frac{m_{A^{Z+}} c^2}{2\pi k_{\mathrm{B}} T_{A^{Z+}} \lambda_0^2}} \exp\left(-\frac{1}{2}\frac{(\lambda - \lambda_0)^2}{\sigma^2}\right). \tag{5.4}$$

Hereby is $I(\lambda)$ the line shape function of the investigated spectral line normalized to a radiance of I_0. $m_{A^{Z+}}$ is the mass and $T_{A^{Z+}}$ the temperature of the impurity ion A^{Z+}, c the speed of light, k_{B} the Boltzmann constant and σ, λ and λ_0 are the standard deviation, the observed and the theoretical central wavelength of the spectral line, respectively.

Since it can be assumed that Doppler broadening is the dominant line-broadening mechanism, $T_{A^{Z+}}$ can be deduced from the width of the Gaussian line:

$$T_{A^{Z+}} = \frac{m_{A^{Z+}} c^2}{\lambda_0^2 e^2} \sigma^2, \tag{5.5}$$

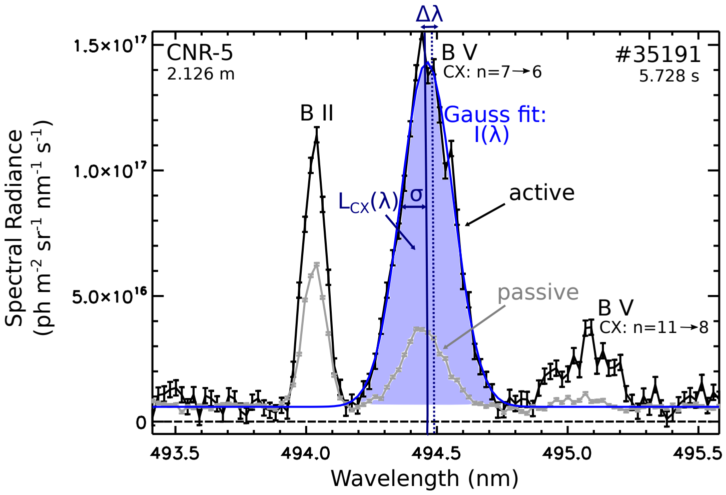

Figure 5.1: Example of a line spectrum from the gas puff-based CX system: CX reactions between the injected D neutrals and B^{5+} impurity ions from the plasma lead to line emission of excited B^{4+}. The black data show the line spectrum as acquired when the gas puff is on (active signal), the grey data show the subtracted background signal, determined when the gas puff is off (passive signal). A Gauss fit to the active CX line of the $n = 7 \to 6$ transition at 494.467 nm delivers valuable information about the plasma. From the Doppler width the temperature of B^{5+} can be deduced, from the Doppler shift its rotation velocity and from the line intensity the local B^{5+} density.

with e being the electric charge. For typical edge conditions where the main ion temperature $T_i \approx 150\,\mathrm{eV}$ and the main ion density $n_i \approx 2.0 \times 10^{19}\,\mathrm{m}^{-3}$ the time needed that the low-Z impurity species A^{Z+} and the main ions i reach thermal equilibrium τ_{therm} is in the range of a few tenths µs [108]. This thermal equilibration time is two orders of magnitude smaller than the time resolution of the spectroscopic system. Therefore, it is true that:

$$T_{A^{Z+}} \approx T_i. \tag{5.6}$$

The Doppler shift of the spectral line $\Delta\lambda = \lambda - \lambda_0$ is directly connected to the rotation velocity vector $\boldsymbol{v}_{\mathrm{rot},A^{Z+}}$ of A^{Z+} via:

$$\frac{\Delta\lambda}{\lambda_0} = \frac{\boldsymbol{v}_{\mathrm{rot},A^{Z+}} \cdot \boldsymbol{e}_{\mathrm{LoS}}}{c}, \tag{5.7}$$

where $\boldsymbol{e}_{\mathrm{LoS}}$ is the unit vector of the line of sight (LoS). The use of poloidally and toroidally aligned LoS (see Section 4.3.2.1 for the alignment procedure) gives the possibility of measuring separately the toroidal and poloidal contributions of $\boldsymbol{v}_{\mathrm{rot},A^{Z+}}$, which enter via Equation 2.32 in the determination of E_r.

The sign convention in AUG and the geometry of the experimental set-up is such that for the toroidal LoS a blue shift of the central wavelength leads to positive toroidal rotation, while for the poloidal LoS a blue shift of the spectral line leads, in normal configuration, to negative poloidal rotation, i.e. a movement vertically upwards at the LFS and, thus, in the electron diamagnetic drift direction (see also Section 2.5.2).

The integrated spectral radiance $L_{A^{Z+}}$ of the active CX line λ is linked to the local impurity density $n_{A^{Z+}}$. For CX reactions between a gas cloud and the plasma impurities this gives[1]:

$$L_{A^{Z+}}(\lambda) = \frac{h\nu}{4\pi} \int_{\mathrm{LoS}} \sum_{n_d=1}^{n_{d,\mathrm{exc}}} n_{A^{Z+}}\, n_{D^0}(n_d) \langle \sigma_{\mathrm{CX}}^{\lambda}(v) v \rangle_{\mathrm{eff}} dl. \tag{5.8}$$

The integral is hereby taken along one LoS. $\langle \sigma_{\mathrm{CX}}^{\lambda}(v) v \rangle_{\mathrm{eff}}$ denotes the Maxwellian average of the total effective CX rate coefficient, where $\sigma_{\mathrm{CX}}^{\lambda}(v)$ is the total effective CX cross section of the transition $A^{(Z-1)+}(n = n_2 \rightarrow n_1)$ at the wavelength λ [2] and $v = |\boldsymbol{v}_{D^0}(n_d) - \boldsymbol{v}_{A^{Z+}}|$ is the relative velocity of the two reaction partners. $\langle \sigma_{\mathrm{CX}}^{\lambda}(v) v \rangle_{\mathrm{eff}}$ is documented in the Atomic Data and Analysis Structure (ADAS) database [130].

If the intersection length l of the LoS and the neutral source is small and the LoS are tangent to the flux surfaces, $n_{A^{Z+}}$, $n_{D^0}(n_d)$ and $\langle \sigma_{\mathrm{CX}}^{\lambda}(v) v \rangle_{\mathrm{eff}}$ can be assumed constant. Furthermore, the summation over n_d reduces to the $n_d = 2$ level for the gas puff-based CXRS system.

The advantage of the new gas-puff based system (see Chapter 4 compared to the conventional beam-based CXRS system (see Section 3.1.2) is that the interaction volume between the injected gas cloud and the LoS is smaller leading to more localized emission of the active CX signal. Furthermore, the fast modulation of the piezo gas valve enables a fast and reliable determination of the background signal and, thus, simplifies the separation of the active CX signal from the passive signal.

5.1.2.2 Passive Signal

As can be seen in Figure 5.1, passive signal from other impurities, different charge states of the same plasma impurity and other processes exciting the same signal line account to the background signal. Of particular interest is the latter, which has to be separated from the active CX line. Passive signal at the same wavelength as the CX line of A^{Z+} originates from light collected along the LoS, which originates from electron impact excitation of $A^{(Z-1)+}$ and CX reactions of A^{Z+} with background neutrals not injected by the piezo gas valve [124, 131].

If the neutral particles injected by the gas valve do not change the local plasma conditions then it can be assumed that the passive signal is not affected by the gas injection. Thus, the passive contribution to the spectrum can be determined from the signal when the gas puffing is off and can be subtracted from the active signal. Care is taken in the determination of the passive signal and normally three to five frames before and after a gas pulse are averaged, where phases in which the plasma conditions are not stable, the magnetic equilibrium changes or frames disturbed by an ELM are rejected from the background subtraction.

---

[1] For CX reactions with a neutral beam injection Equation 5.8 reads different, because the three beam energies have to be taken into account, see e.g. [83].

[2] The denotion 'eff' means that in $\langle \sigma_{\mathrm{CX}}^{\lambda}(v) v \rangle_{\mathrm{eff}}$ the cross sections for direct CX into the excited n_2 level as well as CX into higher $n > n_2$ levels with subsequent cascades into the n_2 level are included. Furthermore, all allowed transitions into different orbital angular momentum levels l are summed up, while atomic fine structure splitting is not resolved [82].

5.1.2.3 Corrections to the Measured Signal

Corrections corrupting the measured signal have to be quantified and, where required, taken into account in order to deduce the plasma quantities correctly from the measured spectra. In the following corrections are presented, which are due to Zeeman and fine structure splitting of line spectra, imperfections in the geometrical alignment, cross section effects and cross-talk on the CCD chip.

Zeeman and Fine-Structure (FS) Corrections Due to the high temperature in fusion plasmas the Doppler broadening dominates the broadening of the investigated spectral line and fine structure and Zeeman components are normally not resolved [132]. These single components are Gaussian-shaped lines of varying intensity with the line width of the true ion temperature T_i at wavelengths around λ_0. Thus, the measured line as a superposition of these Gaussian-shaped lines is only nearly Gaussian with an apparent line width which overestimates the ion temperature. This superposition also leads to a deviation from the actual center of mass wavelength and, thus, to an additional component in the experimentally determined Doppler shift. These deviations are corrected automatically during the fitting procedure by means of correction curves which are a function of the apparent ion temperature and the apparent center of mass wavelength [133, 134]. For these correction curves full l-mixing of the Zeeman components is assumed and their relative intensities are calculated from the angle between the local magnetic field strength $\boldsymbol{B}$ and $\boldsymbol{e}_{\mathrm{LoS}}$.

Geometry Corrections Further corrections of the measured toroidal and poloidal rotation velocities $v_{\phi,A}$ and $v_{\theta,A}$ come from deviations of the LoS from the toroidal and poloidal direction. Although these deviations are sought to be minimized in the alignment process (see Section 4.3.2.1), they are present and, for the poloidal direction, are time-dependent and vary from discharge to discharge, since the plasma shape changes. To account for these imperfections, the projection of $\boldsymbol{e}_{\mathrm{LoS}}$ on the toroidal and poloidal plane is calculated for each measurement position and time point and the geometric correction is applied to $v_{\phi,A}$ and $v_{\theta,A}$ during the fitting process. For the plasma shapes used in this work (see Section 3.2), this correction is below 1 % of the measured velocities. An additional error in $v_{\phi,A}$ and $v_{\theta,A}$ due to the LoS geometry is the reciprocal projection of $v_{\phi,A}$ on $\boldsymbol{e}_{\mathrm{LoS},\theta}$ and $v_{\theta,A}$ on $\boldsymbol{e}_{\mathrm{LoS},\phi}$. A sensitivity study showed that only for $|\boldsymbol{v}_{\mathrm{rot},A}| > 100\,\mathrm{km/s}$ this error would account for more than 1 km/s, which is a much higher value for the toroidal and poloidal rotations than observed at the plasma edge. Thus, the latter correction is not taken into account, as it would require a recursive fitting procedure of the poloidal and toroidal velocities.

Cross Section Effects The CX rate coefficient entering Equation 5.8 is energy-dependent, since it depends on the relative velocity v between the donor neutrals and the electron receiving ions. This implies that faster impurity ions are more likely to emit a CX photon, what leads to a slight modification of the line width, the line intensity and the line shift. The strength and the sign of this modification depends on several parameters: the direction of observation, the LoS geometry with respect to the neutral flow direction, the neutral energy and their possible drift velocity as well as on parallel and perpendicular flows of the impurity ions [34, 135]. In a similar way the gyration of an ion A around

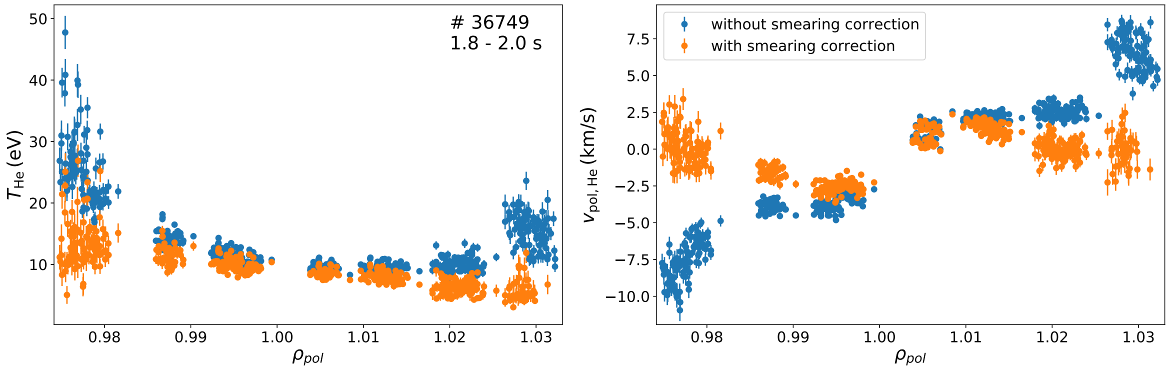

Figure 5.2: Smearing Correction: Radial profiles of the He$^+$ temperature (left) and poloidal rotation (right) are shown with and without smearing correction. For the blue data cross-talk between the channels of the CCD chip was not removed, while the orange data points are corrected for the cross-talk signal. Cross-talk leads especially for channels further outside on the CCD chip to strong deviations of the apparent temperature and rotation profiles from the actual ones.

the field line (see Section 2.1.1.1) connected with its finite lifetime in the excited state n_2 can lead to an additional apparent line shift in the poloidal plane [136, 137]. These energy-dependent cross section effects taken together partially compensate and, thus, lead to only small corrections of L_A, T_i and $\boldsymbol{v}_{\mathrm{rot},A}$ at the plasma edge [43, 124] and are, therefore, neglected.

Cross-talk on the CCD Chip Signal from cross-talk between different channels (ROIs) of the CCD chip occurs on each channel k and has to be removed. It has two contributions: Light from other fibres can reach channel k due to imperfections of the optical imaging. This first contribution to the cross-talk signal is proportional to the exposure time t_{exp}. During calibration of the CCD chip it was found that this contribution to the cross-talk is small. The second contribution is due to illumination of the channel k during the shifting time t_s. This is also called the smearing signal. It is nearly the same for all 25 channels if the incoming photon rate is not strongly changing during the shifting procedure. This can be assumed in stable plasma conditions, excluding frames acquired during e.g. an ELM activity.

The smearing signal is determined for each acquisition time point during the plasma discharge from the signal which is produced on the two channels used for wavelength calibration, which are not connected to LoS in the plasma chamber, but to the wavelength calibration lamp (see Section 4.10). This signal is scaled for each channel to its ROI size and subtracted from the total detected signal on each channel.

Figure 5.2 shows a comparison of the temperature T_{He} and rotation $v_{\mathrm{rot,He}}$ profile measured with He II spectroscopy (see Section 5.2), deduced with and without smearing correction. Although these quantities are determined with another spectroscopy method, the shown differences apply equally to the CXRS method. The deviation of the uncorrected temperature and rotation values from the corrected ones becomes larger, the further outside the channels are located on the CCD chip. While the smearing signal occurs at the same pixel position the wavelength range imaged on one channel changes due to the parabolic projection of the vertically stacked fibres onto the CCD chip in the spectrometer (see Section 4.6). The most central channels on the CCD-chip contribute most to the smearing signal which leads for channels positioned further outside on the CCD chip to a stronger broadening of the investigated spectral line and a stronger shift of the line center.

5.1.3 Derivation of the Radial Electric Field

As described in Section 2.2.3, E_r is set by the main ions, but the impurity vertical and parallel flows adjust to this E_r in a way that the radial force balance (Equation 2.32) is fulfilled. Thus, E_r can be also deduced from the diamagnetic contribution and the perpendicular and parallel flows of an impurity species A. Since $p_A = n_A k_\mathrm{B} T_A$, all quantities are measured by CXRS, except the magnetic field components B_ϕ and B_θ, which can be taken from the magnetic equilibrium reconstruction (see Section 3.1.5).

However, the three terms determining E_r weight differently for the impurities than for the main ions. As discussed in Section 2.4.1.1, E_r in H-mode at the plasma edge is mainly determined by $(\nabla_r p_i)/(en_i)$.

For the investigated impurity species A with $Z_A = 5 - 7$ the diamagnetic term becomes small. Also $v_{\phi,A} B_\theta$ is often negligible due to the smallness of B_θ. Thus,

$$E_r \approx -v_{\theta,A} B_\phi \tag{5.9}$$

for the investigated impurity ions A^{Z+}. Since E_r is typically negative at the plasma edge in the confined region, this relation also implies that the impurities rotate in the electron diamagnetic drift direction (see Figure 2.6).

Since $B_\theta << B_\phi$ and, thus, $B \approx B_\phi$ another approximation can be made on the determination of $v_{E \times B}$:

$$v_{E\times B} \approx v_{\theta,A}, \tag{5.10}$$

where the sign of $v_{\theta,A}$ always equals the sign of $v_{E\times B}$.

Please note that deviations from this approximation are discussed in the thesis where necessary.

5.1.4 Comparison with Beam-based CXRS

Figure 5.3 shows typical radiance, temperature and rotation profiles, acquired with the new gas puff-based CXRS system (blue), from here on called CNZ. The resulting profiles are compared with the profiles reconstructed from the beam-based CXRS toroidal system (CMZ, orange data) and the poloidal system (CPZ, green data). For the gas puff-based system it was found that a good SNR can be achieved for a gas pressure of about 500 mbar in the gas supply system, which corresponds to a particle flow rate of D_2 molecules of about 5×10^{20} particles/s. This flow rate is still low enough to neither impact on the ambient plasma conditions nor acting as an additional source of particle fueling.

By construction the beam-based CXRS system and the gas puff-based system are in close vicinity in the plasma chamber. Thus, the LoS of the CMZ system pass through the gas cloud of the CNZ system. This leads to a distortion of the passive signal of the CMZ signal, while the signal of the CNZ gets distorted during a switching on or off of

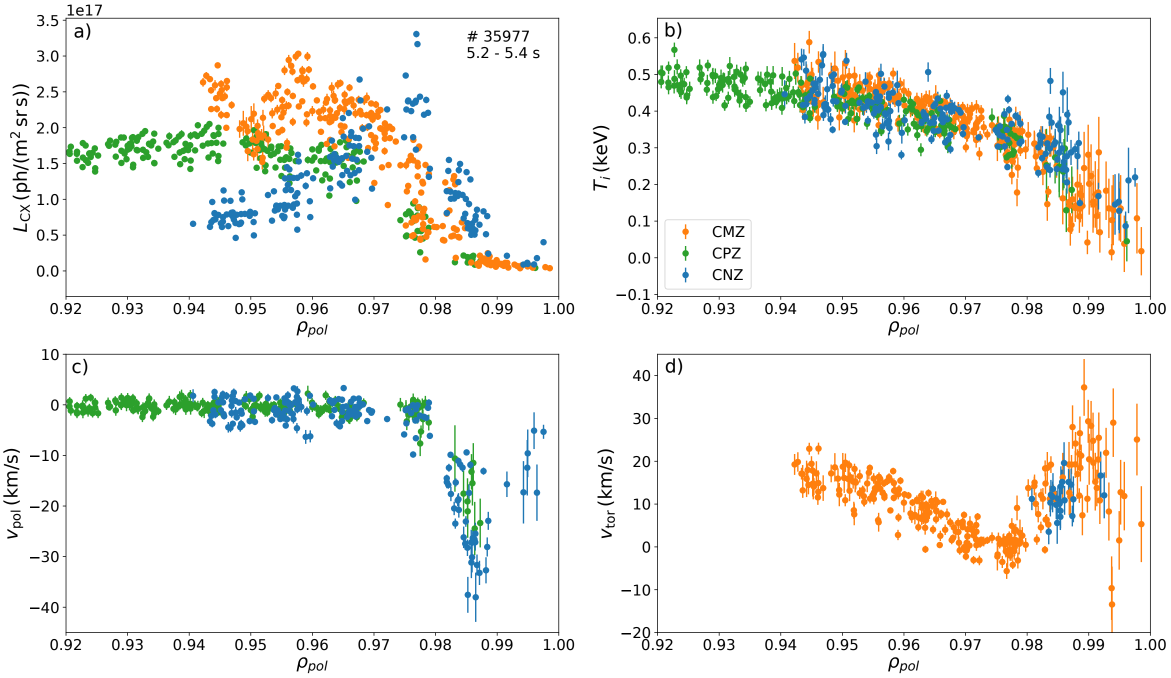

Figure 5.3: Good agreement of measured radiance, temperature and rotation velocitiy profiles in H-mode is found between the new gas puff-based CXRS system (blue data) and the conventional beam-based CXRS toroidal (orange) and poloidal (green) systems.

the NBI source, which is used as neutral reservoir for the beam-based CXRS system (see Section 3.1.2). This reciprocal influence does not allow for the simultaneous use of the two diagnostics, but data acquisition has to be alternated, which can be achieved by adjustment of the timing of the gas puff modulation (see Section 4.4) to the operation of the NBI operation. The data shown in Figure 5.3 are taken from a discharge were both systems measured the CX signal of N^{7+}. The data are ELM-synchronized and from a time window where first the beam-based CXRS and then the gas puff-based CXRS was turned on, while the plasma parameters and the input power were kept constant.

The comparison shows that both the ion temperature profiles and the poloidal and toroidal rotation profiles agree among the different diagnostics. Since the radial range of the toroidal LoS of the CNZ system is limited (see Figure 5.3d), for the T_i profile reconstruction (Figure 5.3b) only the poloidal LoS were used. No radial shift was applied to any experimental data, but the data have been filtered by criteria on the goodness of the fit to the spectra. Furthermore, for the CNZ system, molecular lines (see the following section) were removed from the line spectra before the fitting procedure.

The comparison of the radiance profiles of the different systems (Figure 5.3a) shows that in stable H-mode conditions the signal of the CNZ system is higher for $\rho_{\mathrm{pol}} > 0.98$ compared to the CMZ and CPZ systems. This is in line with the measurement of the poloidal velocity profile (Figure 5.3c), which can be reconstructed up to the separatrix for the CNZ system, while for the CPZ system data are only available up to $\rho_{\mathrm{pol}} \approx 0.99$. For values of $\rho_{\mathrm{pol}} < 0.98$ the radiance of the CNZ system decreases quickly and becomes smaller than of the beam-based CXRS systems for $\rho_{\mathrm{pol}} \approx 0.96$. In this radial range the abundance of thermal D^0 neutrals decreases strongly, as they get ionized or leave the measurement region via CX reactions with plasma main ions. This limits the gas puff-based CXRS system to measurements in the plasma edge region. As stated before, efforts are currently undertaken to be able to reconstruct the n_A profiles from the radiance profiles for the CNZ system by modelling the neutral distribution. For this reason a comparison of reconstructed n_A profiles from both CXRS systems is not shown here.

5.1.5 Limitations

Several limitations of the gas puff-based CXRS system lead to the conclusion that this method can not be used for studying processes outside the separatrix in the near SOL, i.e. $\rho_{\mathrm{pol}} > 1$. These different limitations are discussed in the following.

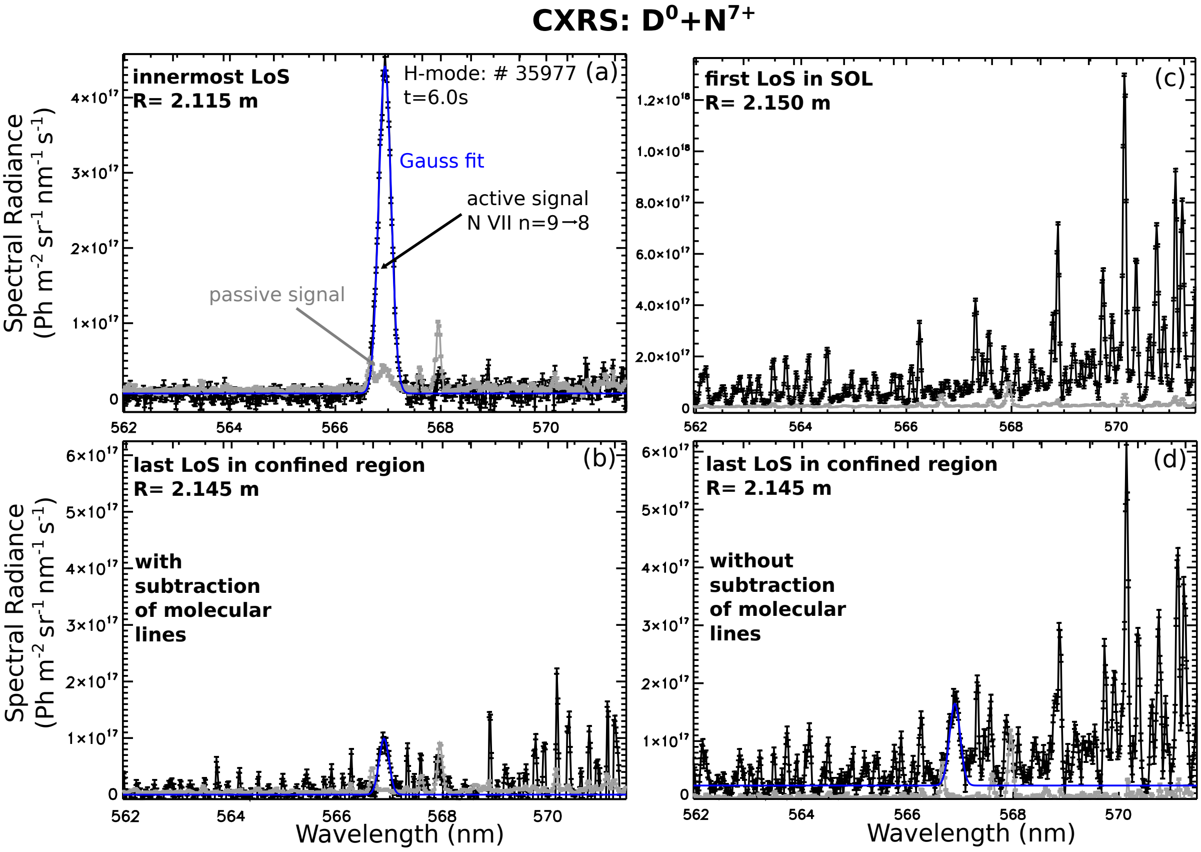

Figure 5.4: Example spectra of the N VII line acquired with the gas puff-based CXRS system. The upper left plot shows a clean spectrum as for a LoS detecting the confined plasma region. The upper right plot shows the spectrum of a LoS probing the near SOL. No N VII CX line is detected any more, but strong molecular lines from the gas puff are found in the spectrum. The lower panels show an identical spectrum with subtraction of molecular lines from it (left) and without (right).

Molecular Lines Figure 5.4 displays line spectra of the N VII CX line at different radial measurement positions. Figure 5.4a shows the typical CX spectrum, with the active CX line and the Gauss fit to the active line, as well as the contributions of the passive fit, which is small. At larger R positions, i.e. closer to the separatrix, the active signal decreases and molecular lines start to appear, which also overlay the active CX line (Figure 5.4d). If these molecular lines are not subtracted they distort the active CX signal and lead to artefacts in the reconstructed impurity radiance, temperature and rotation profiles, especially in the SOL region. This can be also seen in Figure 5.5, where the blue data points originate from fitted experimental data with molecular lines, while for the orange data the signal due to molecular lines was subtracted from the spectra of all LoS. In Figure 5.4b the same spectrum as in Figure 5.4d is shown after removal of molecular lines. The subtraction of the molecular signal can not be accomplished by the usual background subtraction since the molecular lines occur due to the gas puffing of D_2 molecules and, thus, they are inherent to the active signal of the CX measurements. For this reason another approach has to be taken. The outermost LoS is assumed to only exist of molecular lines, which is, as will be shown later, a valid assumption. The wavelengths of the in this way identified molecular lines have been cross-checked with a database of known D_2 lines [138]. The line spectrum of the outermost LoS is then scaled and shifted to match the intensity and wavelength axis of the molecular line spectrum of the other LoS and is subtracted from their spectra. In this way the molecular lines can be largely removed from the line spectra.

No Existence of Fully Ionized Plasma Impurities in the SOL After removal of the molecular lines from the CX spectrum it becomes clear that, as soon as the measurement monitors the region outside the separatrix, the abundance of fully ionized impurities vanishes. This is evident from the spectra of the N VII CX line, where the line spectrum of the first LoS monitoring a radial location outside the separatrix is shown in the top right plot in Figure 5.4. The region of the active line is marked in blue, but no active CX signal is detected.

Also reconstructions of the radial edge profiles of B V (see Figure 5.5) suggest a low abundance of fully ionized impurities in the SOL. The orange points show the fitted data after molecular lines were removed from the spectra. In the SOL, marked in grey in the figure, the SNR becomes so small that the profiles can not be reliably reconstructed.

Please note, the error bars only represent statistical uncertainties. However, also systematic deviations seem to be present.

Low Signal in L-mode Although it was observed that under special conditions, e.g. an H-mode with high N seeding, the gas puff-based CXRS method can deliver radial temperature profiles beyond the separatrix, this measurement method can not be used for SOL studies in all confinement regimes. As described in Section 2.4.1.1, the L-mode features low particle and energy confinement, also the impurity ions are poorly confined. This lower impurity content reduces also the signal strength of the CXRS method. As can be seen in Figure 5.6 the radiance of the N VII CX line in L-mode (blue) is about a factor of four lower than for the H-mode plasma (blue) over the investigated radial range. The profiles were taken from two stable L-mode and H-mode phases with constant heating. Except the external input power other parameters like gas fuelling or the plasma shape were the same. For the H-mode data only inter-ELM phases were used. No radial alignment was performed.

Low Signal for CX with He Neutrals In order to avoid the occurrence of molecular lines in the CX spectra, active CXRS between impurity ions and neutral He as donor gas was tested. For this method He flow rates in the order of 5×10^{20} particles/s, similar to the ones for CXRS on hydrogenic neutrals, were needed. These relatively high He flow rates make this method not usable as a standard measurement method, since it can lead to high influxes of He into the plasma.

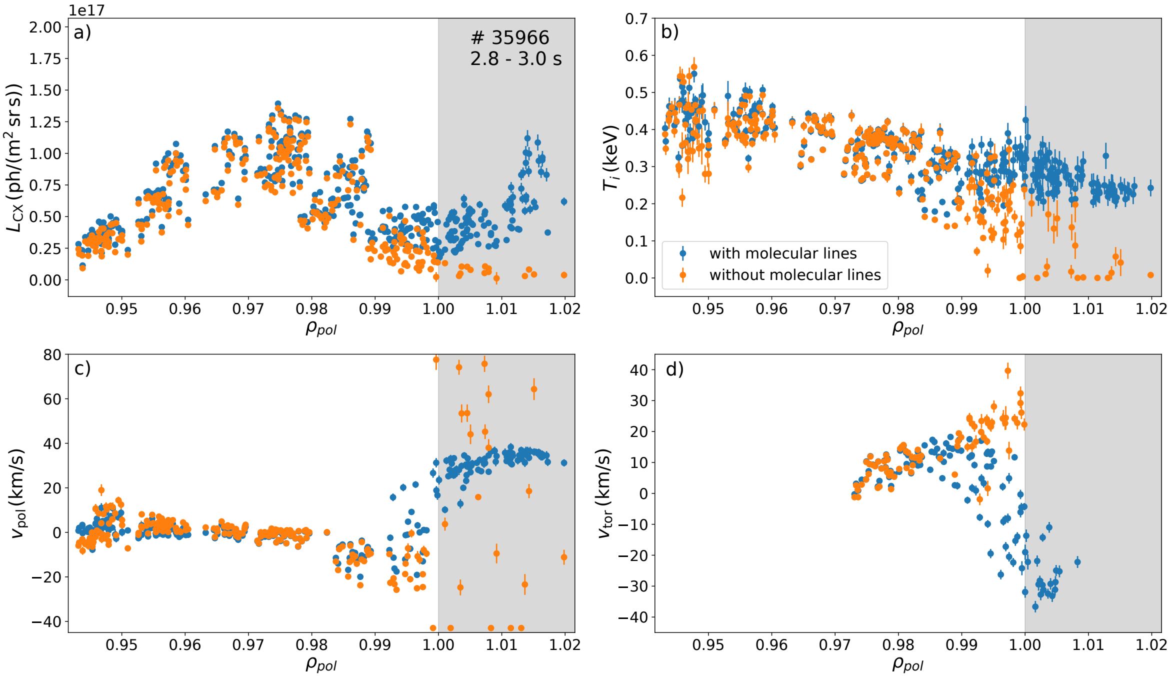

Figure 5.5: Influence of molecular lines on reconstructed profiles from CXRS. For the blue data signal originating from molecular D_2 lines was not subtracted from the B V line spectrum before the fitting of the active CX line, while for the orange data it was subtracted. The molecular lines overlay the active CX line and, thus, lead to a distortion of the reconstructed radial profiles, particularly in the SOL. If the signal of molecular lines is taken into account, the actual active CX signal becomes low in the SOL, such that a reconstruction of profiles is actually not possible.

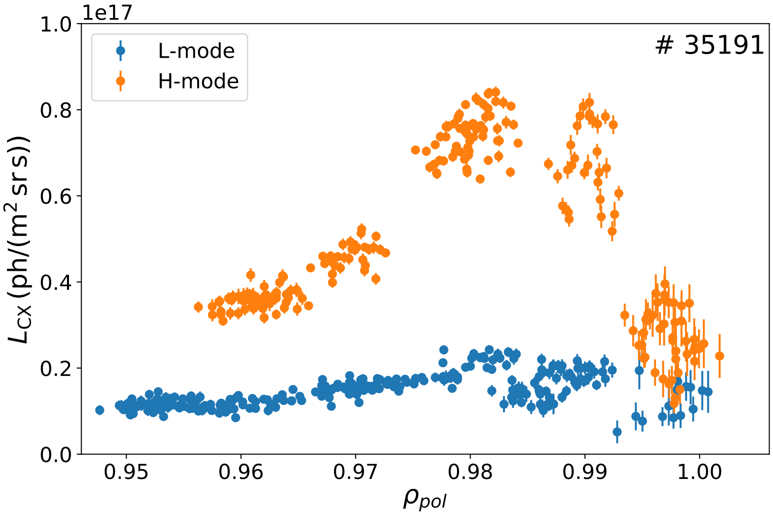

Figure 5.6: Comparison of the radiance profile measured with the gas puff-based CXRS method in a stable L- and H-mode phase of the same plasma discharge. The radiance in L-mode (blue data) is about a factor of 4 lower than in H-mode (orange data), although all plasma parameters, except the heating power, were the same. For the H-mode data only inter-ELM phases were used.

The cross sections for CX reactions with He neutrals are comparable with the cross sections for CX on hydrogenic neutrals [130], but the He gas puff reaches less far into the plasma [124, 139]. Also with this method CX signal outside the separatrix could only be reached in highly seeded H-modes.

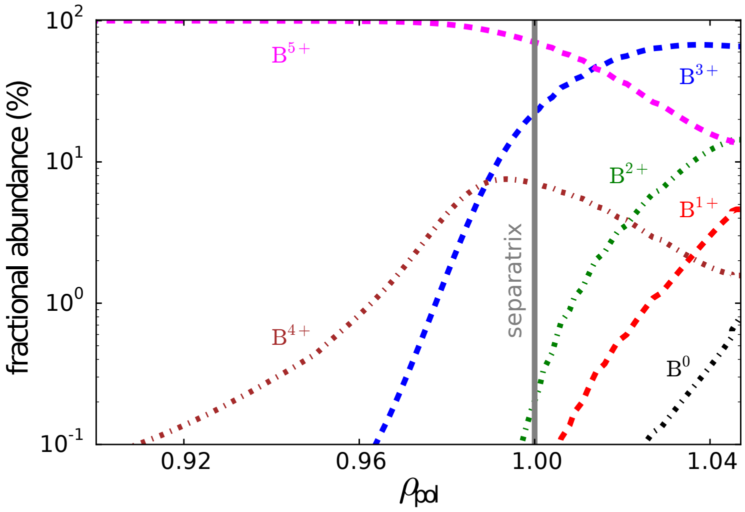

Figure 5.7: Charge stage distribution of boron in an H-mode as modeled by STRAHL [140]. The code predicts a high relative abundance of He-like boron at the separatrix, which could be used for CXRS at the separatrix. The resulting CX signal, using the gas puffed-based CXRS system, was found to be too low to use this method for CXRS at the separatrix.

No Signal for CX with Partially Ionized Impurities Figure 5.7 shows the charge state distribution of boron in the plasma edge and near SOL region as calculated by the 1-D impurity transport code STRAHL [140] for an H-mode plasma. According to the model He-like ions like B^{3+} and N^{5+} have a high fractional abundance in the near SOL region, outside the separatrix. For this reason CX reactions of He-like ions with hydrogenic neutrals (B III ($n = 7 \rightarrow 5$) at 447.112 nm and N V ($n = 7 \rightarrow 6$) at 494.456 nm) were investigated as well. However, these CX reactions did not deliver a detectable signal, which suggests that the absolute abundance of the low-Z He-like ions in the investigated radial range around the separatrix is too low. The reason for this is that for CX with thermal neutrals the excited states (n=2) are important (see above), but the excitation of neutrals in the SOL is much less.

5.2 He II Spectroscopy

The second spectroscopic method developed to measure the radial electric field is based on investigating the line emission of singly ionized He and is abbreviated in the following as HES. Neutral He is introduced into the plasma via the piezo gas valve, gets ionized and the emitted light from the He II($n = 4 \rightarrow 3$) at 468.571 nm is detected. With this method a good SNR can already be achieved for low gas pressures of about 30 mbar in the gas supply system, which corresponds to a particle flow rate of about 1×10^{19} particles/s.

This particle flow rate is more than two orders of magnitude lower than the typical flow rates used for plasma fuelling and, thus, it is non-perturbative to the plasma. As will be shown later, the HES diagnostics delivers good signal between $\rho_{\mathrm{pol}} \approx 0.97$ and 1.02, which makes this diagnostics suitable for E_r studies across the separatrix.

5.2.1 Atomic Processes

In the following the most relevant atomic processes are presented which lead to the production of $\left(\mathrm{He}^+\right)^*$, where the * denotes an excited state of the He^+ ion, i.e. the main quantum number n is larger than 1. Collisions with electrons (e^-) or plasma ions i^+ lead to excitation of the He^+ ions, while spontaneous emission as well as electron and ion impact de-excitation are responsible for a decrease of the $\left(\mathrm{He}^+\right)^*$ population:

Excitation Processes:

$$e^- + \mathrm{He}^+ \rightarrow e^- + \left(\mathrm{He}^+\right)^* \qquad \underline{\text{electron impact excitation}} \tag{5.11}$$

$$i^+ + \mathrm{He}^+ \rightarrow i^+ + \left(\mathrm{He}^+\right)^* \qquad \text{ion impact excitation.} \tag{5.12}$$

De-excitation Processes:

$$e^- + \left(\mathrm{He}^+\right)^* \rightarrow e^- + \mathrm{He}^+ \qquad \underline{\text{electron impact de-excitation}} \tag{5.13}$$

$$i^+ + \left(\mathrm{He}^+\right)^* \rightarrow i^+ + \mathrm{He}^+ \qquad \text{ion impact de-excitation} \tag{5.14}$$

$$\left(\mathrm{He}^+\right)^* \rightarrow \mathrm{He}^+ + h\nu \qquad \underline{\text{spontaneous emission}}. \tag{5.15}$$

The sources for the He^+ production are electron and ion impact ionization of neutral He and charge exchange of He^{2+} with neutral i^0 [3]:

Sources of He^+:

$$e^- + \mathrm{He}^0 \rightarrow e^- + \mathrm{He}^+ \qquad \underline{\text{electron impact ionization}} \tag{5.16}$$

$$i^+ + \mathrm{He}^0 \rightarrow i^+ + \mathrm{He}^+ \qquad \text{ion impact ionization} \tag{5.17}$$

$$i^0 + \mathrm{He}^{2+} \rightarrow i^+ + \mathrm{He}^+ \qquad \text{charge exchange} \tag{5.18}$$

$$e^- + \mathrm{He}^{2+} \rightarrow \mathrm{He}^+ \qquad \text{radiative recombination.} \tag{5.19}$$

---

[3] In optically thick plasmas, at high electron densities and low electron temperatures also different recombination processes are important for the He^+ production [79, 141].

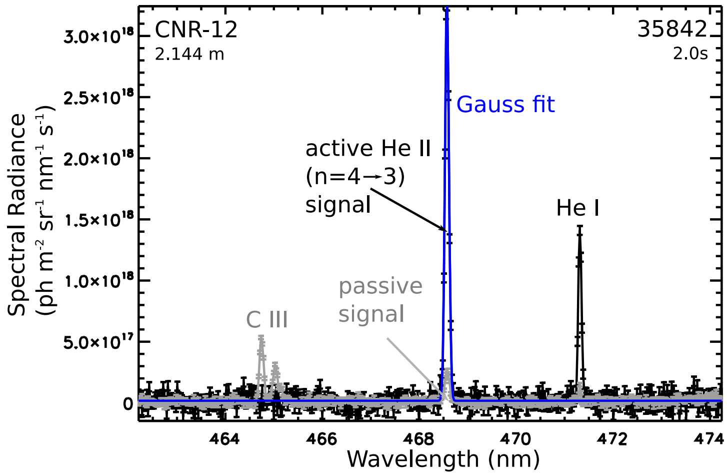

Figure 5.8: Line spectrum of the He II($n = 4 \rightarrow 3$) line at 468.571 nm. With HES this line is produced by electron impact excitation of He neutrals injected through the piezo gas valve into the plasma. The active line is fit with a Gaussian line to deduce the He$^+$ temperature, the Doppler shift of the He II line and its radiance. This spectroscopy method exhibits a good SNR and the passive contribution is small.

The sinks which lead to a decrease of the He$^+$ population are secondary ionization, producing He^{2+} ions, and charge exchange of He$^+$ with i^0, producing He^0.

Sinks of He$^+$:

$$e^- + \mathrm{He}^+ \rightarrow e^- + \mathrm{He}^{2+} \qquad \underline{\text{secondary electron impact ionization}} \tag{5.20}$$

$$i^+ + \mathrm{He}^+ \rightarrow i^+ + \mathrm{He}^{2+} \qquad \text{secondary ion impact ionization} \tag{5.21}$$

$$i^0 + \mathrm{He}^+ \rightarrow i^+ + \mathrm{He}^0 \qquad \text{charge exchange} \tag{5.22}$$

$$e^- + \mathrm{He}^+ \rightarrow \mathrm{He}^0 \qquad \text{radiative recombination.} \tag{5.23}$$

Employing the respective rate coefficients $q^{j,k}_{\mathrm{proc}} = \langle \sigma^{j,k}_{\mathrm{proc}} v \rangle$ for each of the shown processes and energy levels $j \neq k$ [4] leads to time-dependent differential equations which determine the He$^+$ density populating the energy level with principal quantum number $n = k$. In typical plasma conditions the most important processes are electron impact excitation and de-excitation, electron impact ionization and spontaneous emission [142].

5.2.2 Deduction of Measured Quantities

5.2.2.1 Active Signal

Figure 5.8 shows the spectrum of the He II($n = 4 \rightarrow 3$) line at 468.571 nm. Like for the CXRS method the active contribution of the spectral line is fit with a Gaussian-shaped line and from the line width of the fit the temperature of He$^+$, T_{He}, can be deduced (see Equation 5.5) as from the Doppler shift the rotation velocity of He$^+$, $v_{\mathrm{rot,He}}$, (see Equation 5.7) can be inferred.

---

[4] $\langle \sigma^{j,k}_{\mathrm{proc}} v \rangle$ denotes the Maxwellian average over the product of the cross-section $\sigma^{j,k}_{\mathrm{proc}}$ of the respective process with the relative velocity v of the two reaction partners (see also Section 5.1.2.1).

Similar as described in Section 5.1.2.1, the local He$^+$ density, n_{He^+} can be determined from the radiance L_{He} of the He II($n = j \rightarrow k$) line. For HES this looks like:

$$L_{\mathrm{He}} = \frac{1}{4\pi} \int_{\mathrm{loS}} n^j_{\mathrm{He}^+} A_{j,k} \mathrm{d}l = \frac{1}{4\pi} \int_{\mathrm{LoS}} n_e n_{\mathrm{He}^+} \mathrm{PEC}_{j,k}(n_e, T_e)\, \mathrm{d}l, \tag{5.24}$$

where $n^j_{\mathrm{He}^+}$ denotes the density of He$^+$ ions in the energy level $n = j$, $A_{j,k}$ the Einstein coefficient of the specific transition, induced by spontaneous emission, n_e and T_e the local electron density and temperature, respectively, and $\mathrm{PEC}_{j,k}(n_e, T_e)$ the photo emission coefficient. The last is a measure for the number of photons emitted by the specific transition $n = j \rightarrow k$. The calculation of the emission profile of He II($n = 4 \rightarrow 3$) shows that photo emission due to electron impact excitation (see Equation 5.12) is at least a factor of four higher compared to the other two possible processes, namely charge exchange or recombination [141]. With this simplification and knowing the LoS and gas-puff geometry, n_{He^+} can be determined from the following equation:

$$L_{\mathrm{He}}(\lambda = 468.571\,\mathrm{nm}) = \frac{1}{4\pi} \int_{\mathrm{LoS}} n_e n_{\mathrm{He}^+} \mathrm{PEC}^{\mathrm{exct}}_{4,3}(n_e, T_e)\, \mathrm{d}l. \tag{5.25}$$

For the n_{He^+} reconstruction, experimental T_e and n_e profiles from the IDA diagnostics are used (see Section 3.1.1) and evaluated at the measurement position. The corresponding $\mathrm{PEC}^{\mathrm{exct}}(n_e, T_e)$ is taken from the ADAS database [130]. The L_{He} profiles are fit with Legendre-polynomials as it is suggested in [143]. Figure 5.9 shows an example of an n_e profile, the corresponding $\mathrm{PEC}^{\mathrm{exct}}$, the measured and fit L_{He} profile and the reconstructed n_{He} profile for an L-mode plasma taken at 2 s for the reference discharge presented in Section 3.2. While n_e, $\mathrm{PEC}^{\mathrm{exct}}$ and L_{He} increase towards lower ρ_{pol}, the reconstructed n_{He} increases towards the separatrix and reaches its maximum in the near SOL. The decrease of n_{He} in the far SOL is not shown here, but it is found when solving the set of differential equations presented in the section before that He$^+$ exists only in a small region around the separatrix [141, 144] .

One exception is the investigation of the He II line by means of HES in plasmas with He as the main ion species. Then the charge exchange process between He^{2+} and the injected He neutrals becomes important due to the resonant nature of the charge transfer (see also Section 5.1.1). Under these circumstances the active He II line at 468.571 nm consists of two contributions and can not be fit with one single Gaussian line any more, but two Gaussian lines have to be used (see Figure 5.10). The stronger signal still arises from electron impact excitation processes and the resulting Gaussian line has a line width of only a few eV, while the charge exchange process results in a Gaussian line with a line width of about 100 eV, which is in line with T_i measurements by CXRS of other plasma impurities at the plasma edge [43, 108].

5.2.2.2 Passive Signal

The passive signal originates from background He particles not injected by the piezo gas valve, which undergo the above described atomic processes and their light is collected along the LoS. As described in Section 5.1, the background frames are taken during the off-phases of the gas valve modulation, averaged and subtracted from the measured signal to only get the active contribution to the He II signal for the fitting procedure. As can

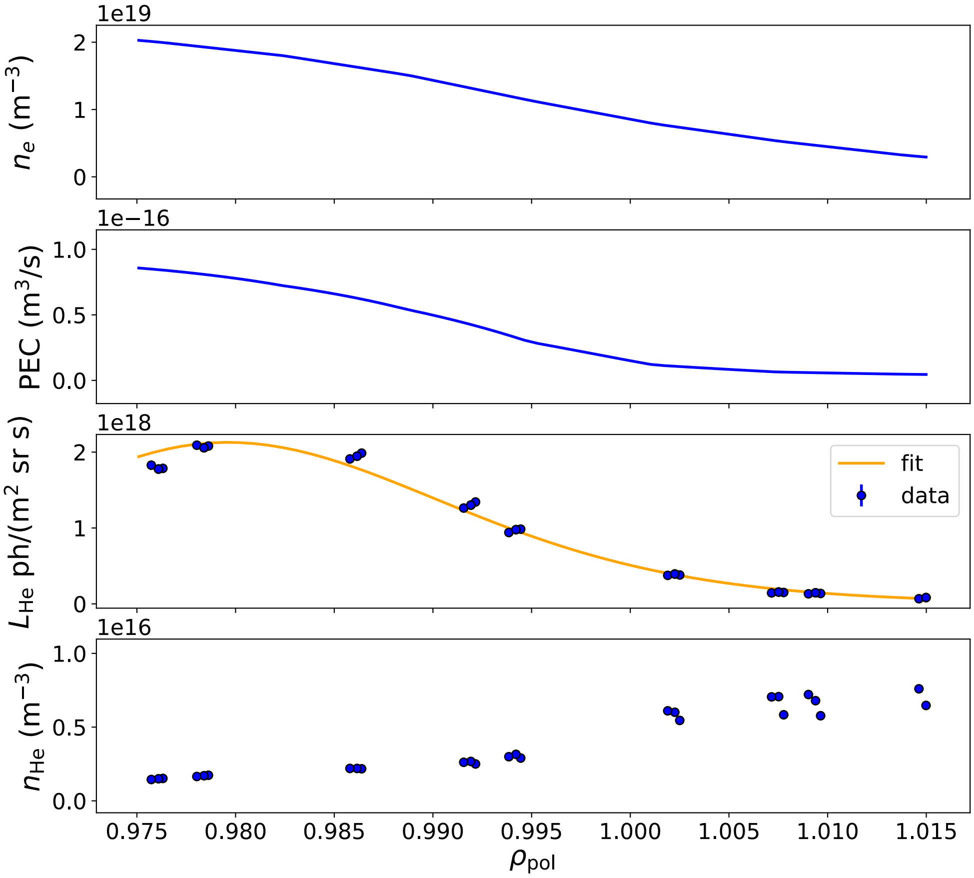

Figure 5.9: The radial profiles of n_e, PEC$^{\text{exct}}$ and L_{He} and the reconstructed n_{He} profile are shown for a L-mode phase of the reference discharge presented in ... . With help of the electron profiles n_e and T_e and the PEC for electron impact excitation the He$^+$ density can be reconstructed from the measured L_{He} of the He II line. The reconstruction shows that He$^+$ exists only in a small region around the separatrix.

be seen in Figure 5.8, the passive contribution (grey) is small compared to the active signal (black).

5.2.2.3 Corrections to the Active Signal

The corrections which are applied to the CXRS measurements and were presented in 5.1.2.3) also have to be applied to HES measurements and are of the same order of magnitude or smaller, because cross-section corrections are larger for a higher temperature and rotation. The only correction which is not applied is the correction of the Zeeman/FS splitting to the rotation measurement, because a detailed calculation showed that its impact on the rotation is small.

In Figure 5.11 the deviation of the central wavelength due to Zeeman/FS splitting from the actual center-of-mass (CoM) wavelength at 468.571 nm is shown as a function of the real temperature of the He$^+$ ions, which is in the range of 5 to 20 eV (see also Figure 5.12). The calculation was performed for a magnetic field strength of 2 T, the local field strength at the measurement position of the experimental set-up under standard plasma operation conditions. The angle between LoS and magnetic field vector was set to 90°, which gives an upper limit to the shift of the central wavelength. In conclusion the correction to all

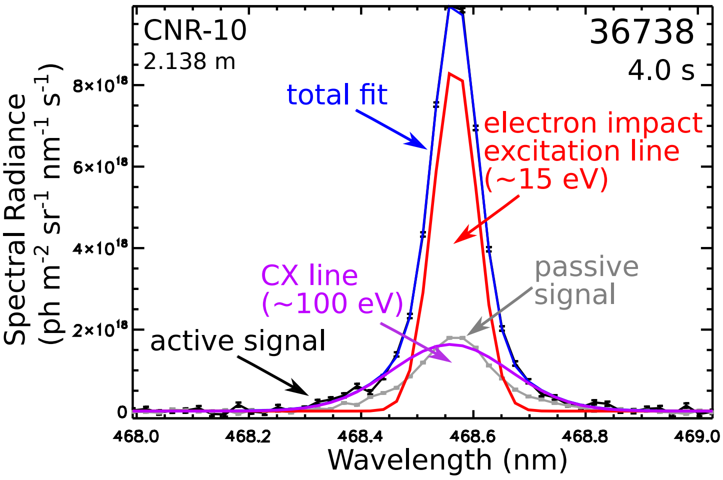

Figure 5.10: Typical spectrum of the He II($n = 4 \rightarrow 3$) line in a He plasma. Besides the active line due to electron impact excitation of the injected He particles, CX between He^{2+} plasma ions and injected He^0 neutrals becomes important. The active line therefore has to be fit with two Gaussian lines.

measurement positions is smaller than 0.5 km/s, which is below the uncertainties of the velocity measurement.

5.2.2.4 Example Profiles and Limitations of the Measurement

It should be noted that the reconstructed quantities T_{He}, $v_{\mathrm{rot,He}}$, and L_{He} are not inherent to the plasma and, thus, in contrast to the CXRS method, do not represent any local measurement of T_i or the density and rotation of plasma He impurities. These measured local quantities give a picture of the development of the injected He neutral cloud due to its interaction with the plasma. Measured radial profiles of T_{He}, $v_{\mathrm{rot,He}}$, and L_{He} are shown in Figure 5.12. From them it can be seen that the observed gas cloud develops in an anisotropic way, leading to differences in the observed toroidal and poloidal temperature distribution and in the radiance in toroidal and poloidal direction.

The radial profiles given in Figure 5.12 are taken from a 200 ms long time window of a stable L-mode phase of the reference discharge (see Figure 3.1), right before the L-H transition takes place. The T_{He} profile is flat, showing temperatures of around 10 to 15 eV for the poloidal direction and around 5 eV for the toroidal direction. As will be discussed in more detail in Section 5.2.5 the measured temperature is not the local temperature of the bulk plasma, since the He^+ ions undergo the second ionization faster than they are thermalized [143].

In such plasma conditions the measured toroidal rotation normally exhibits negative values of around -5 to -8 km/s, which become positive in the confined plasma region. The structure of the profile can vary strongly, exhibiting negative and positive gradients, but so far, no systematic dependence on plasma parameters has been found. However, as a comparison with the synthetic HES diagnostics (Section 5.2.5) supports the interpretation that the measured rotation profile is not the true toroidal rotation profile. The measured toroidal profiles are no local measurements, but a convolution of the LoS view and the He gas cloud, which spreads quickly in the toroidal direction. The observation set-up of the gas cloud is slightly tilted such that one side of the gas cloud is better observed

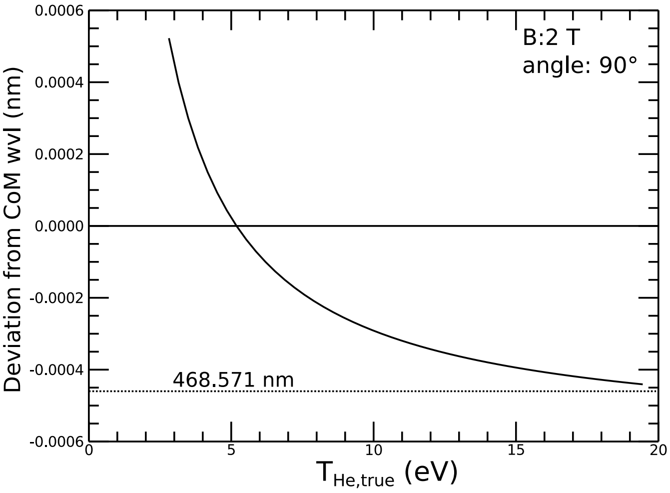

Figure 5.11: The figure shows the deviation of the determined central wavelength of the He II line from the CoM wavelength due to Zeeman splitting as a function of the true measured He^+ temperature. Even at low temperature the correction is small, such that the deviation of the measured rotation to the real rotation of the He^+ particles is below 0.5 km/s, i.e. $\Delta\lambda = 0.0008$.

than the other (see Figure 6.1). Locally at the gas puff the synthetic diagnostics sees only a negligible toroidal rotation. Thus, in the determination of E_r, using the radial force balance, the contribution from the toroidal rotation measurement is not taken into account.

The measurement of the poloidal rotation is more localized and does not suffer so strongly from the line integration effect. This has two reasons: first, the poloidal LoS can be better aligned with respect to the injection axis of the He gas cloud and the magnetic field lines (see also Figure 4.1) and second the divergence of the He gas cloud in the poloidal direction is not as pronounced as in the toroidal direction. In the direction perpendicular to the magnetic field, the particles only gyrate around the field lines (see Section 2.1.1.1) and a directed movement is mainly caused by the $E \times B$ drift which is in the order of a few km/s. The $E \times B$ drift causes that the measurement also contains non-local emission. Thus, detailed modelling using a synthetic diagnostics is performed (see Section 5.2.5).

Despite the aforementioned limitations, the main advantage of HES is the good SNR around the separatrix region. A comparison between the radiance of the He II line from HES (see Figure 5.12) and the radiance achieved from the gas puff-based CXRS method on fully ionized low-Z impurities (see Figure 5.6) shows that for much less gas input L_{He} is by one order of magnitude higher than L_{CX}. In HES radiance reaches its maximum at about $\rho_{\mathrm{pol}} = 0.98$ and decreases strongly, by almost two orders of magnitude, towards the near SOL. The strength of this decrease varies slightly with the plasma conditions, as the PEC depends on the local n_e- and T_e- values, but in all investigated L-mode discharges the signal became too low for measurement positions $\rho_{\mathrm{pol}} > 1.02$. This observation is not only represented in the drop of the radiance signal but also in the fit quality of the spectral line, and, with this, in the larger scatter of the temperature and rotation measurements. As explained before, the signal at $\rho_{\mathrm{pol}} < 0.98$ arises from He^+ ions originating from

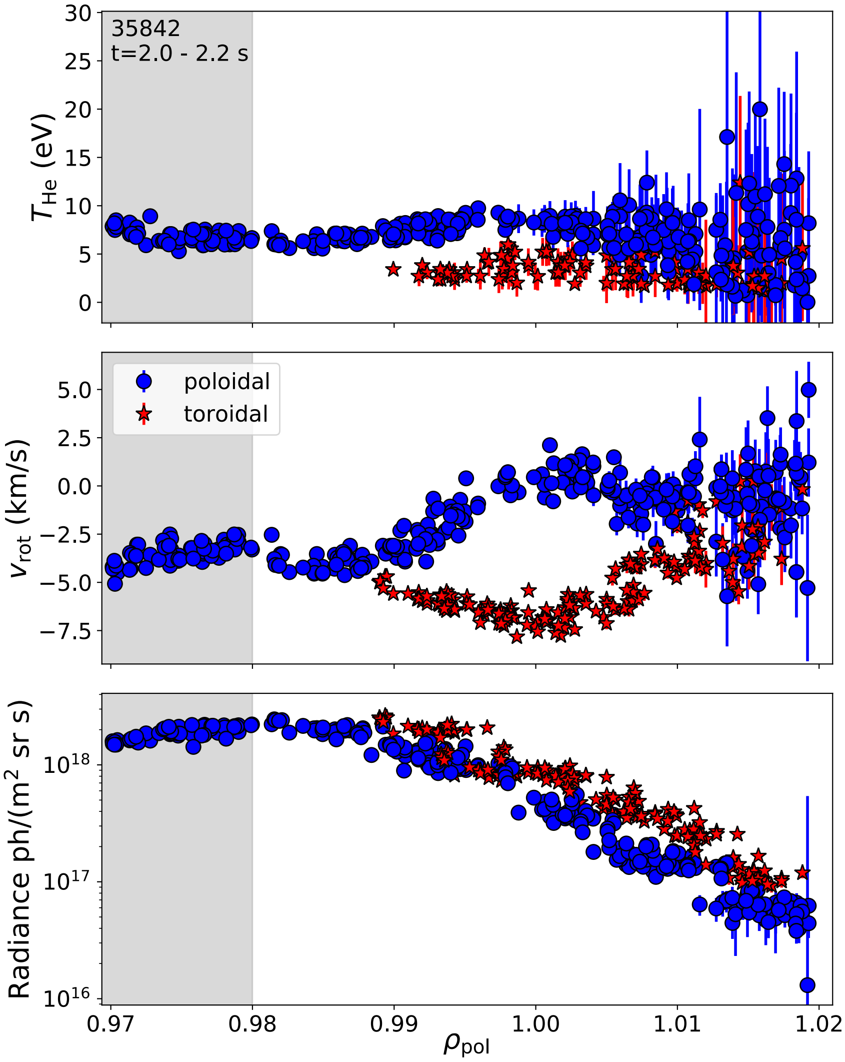

Figure 5.12: Example profiles of He^+ temperature, toroidal and poloidal He^+ rotation and its radiance. The measured He^+ quantities do not explicitly represent local plasma parameters. Furthermore, the radial range of the HES diagnostic is limited to a small region around the separatrix. However, the signal quality in this radial range is high and makes it possible to reconstruct the E_r profile at the separatrix from the He^+ profiles.

locations $\rho_{\mathrm{pol}} \geq 0.98$, and, thus, the measured radiance does not drop as fast as it would be expected from the radial existence of He^+ ions.

5.2.3 Derivation of the Radial Electric Field

As soon as the He neutrals get ionized they are subject to the present radial electric field. Almost instantaneously the He^+ ions adjust their toroidal and poloidal flows in such a way to comply with the radial force balance (see Equation 2.32) [5]. The importance of the three leading terms in the radial force balance are investigated for HES in the following.

---

[5] The time needed to adjust to the plasma E_r is assumed to be the time which is needed to run through one gyro-orbit, which is a fraction of a µs, while the excitation time of the He^+ ions is in the order of several µs.

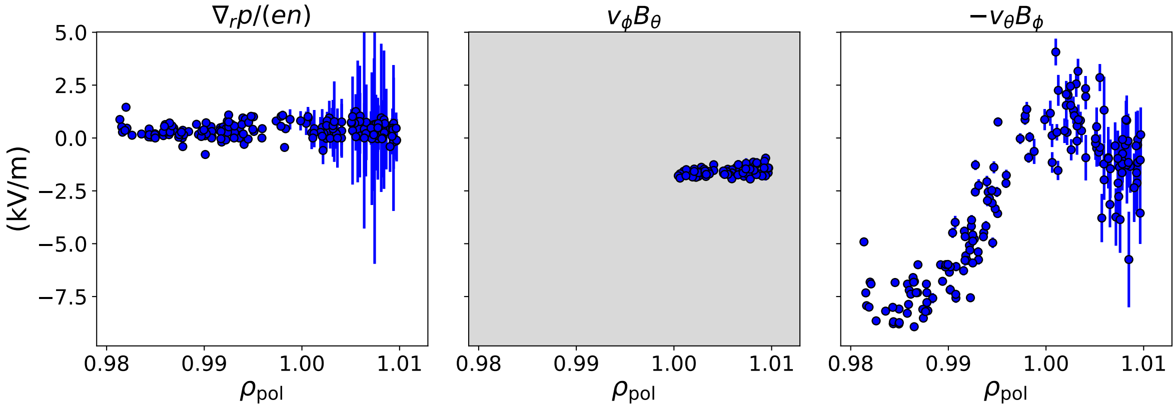

Figure 5.13: The three contributions to determine E_r from the experimental data of the HES diagnostics: The most important contribution comes from the $v_{\theta,\mathrm{He}}B_\phi$ term, while the diamagnetic term is small. The $v_{\phi,\mathrm{He}}B_\theta$ term is neglected in the reconstruction as it can not be fully and correctly determined with the current experimental set-up. Additionally, from the synthetic HES diagnostics it is known to be small.

As seen from Figure 5.12 the T_{He} profile is flat and relatively small. Thus, the diamagnetic contribution $\nabla_r(T_{\mathrm{He}}n_{\mathrm{He}})/(e\ n_{\mathrm{He}})$ of the He$^+$ ions is small. Also the term arising from the toroidal rotation $v_{\phi,\mathrm{He}}B_\theta$ is negligible due to the smallness of B_θ and the smallness of $v_{\phi,\mathrm{He}}$. Thus,

$$E_r \approx -v_{\theta,\mathrm{He}}B_\phi. \tag{5.26}$$

and $v_{\mathrm{E\times B}}$ can be approximated by $v_{\mathrm{pol,He}}$ with

$$v_{\mathrm{E\times B}} \approx v_{\theta,\mathrm{He}}. \tag{5.27}$$

Figure 5.13 shows the three different leading terms to E_r as they are reconstructed from the measured He$^+$ profiles shown in Figure 5.12. It can be seen that $v_{\theta,\mathrm{He}}B_\phi$ is the dominant term and the diamagnetic term is rather flat and gives just a small correction to $\dot{E_r}$The $v_{\phi,\mathrm{He}}B_\theta$ term is shaded in grey because it is not taken into account in the reconstruction of E_r for the reasons discussed before.

The good SNR of the HES method makes it possible for the first time at AUG that the evolution of E_r at the plasma edge can be monitored with a time resolution of 2.45 ms in all confinement regimes without the need of averaging over longer time windows. Furthermore, the simple relation between E_r and $v_{\mathrm{pol,He}}$ also allows for an approximate E_r profile in between two plasma discharges, which was not possible before with the other E_r diagnostics.

5.2.4 Characterisation

Figure 5.14 shows E_r profiles (bottom panel) from two identical discharges, namely the AUG discharges number 36964 (red) and 36965 (blue). These discharges were stable L-modes, heated with constant ECRH of 600 kW (see top panel). The blips of the NBI were used for CXRS measurements rather than heating the plasma, but, as stated before, the timing of the He injection for HES (middle panel) diagnostics was synchronized to the beam blip times. The plasma was run as a low-δ LSN plasma in fav. drift direction

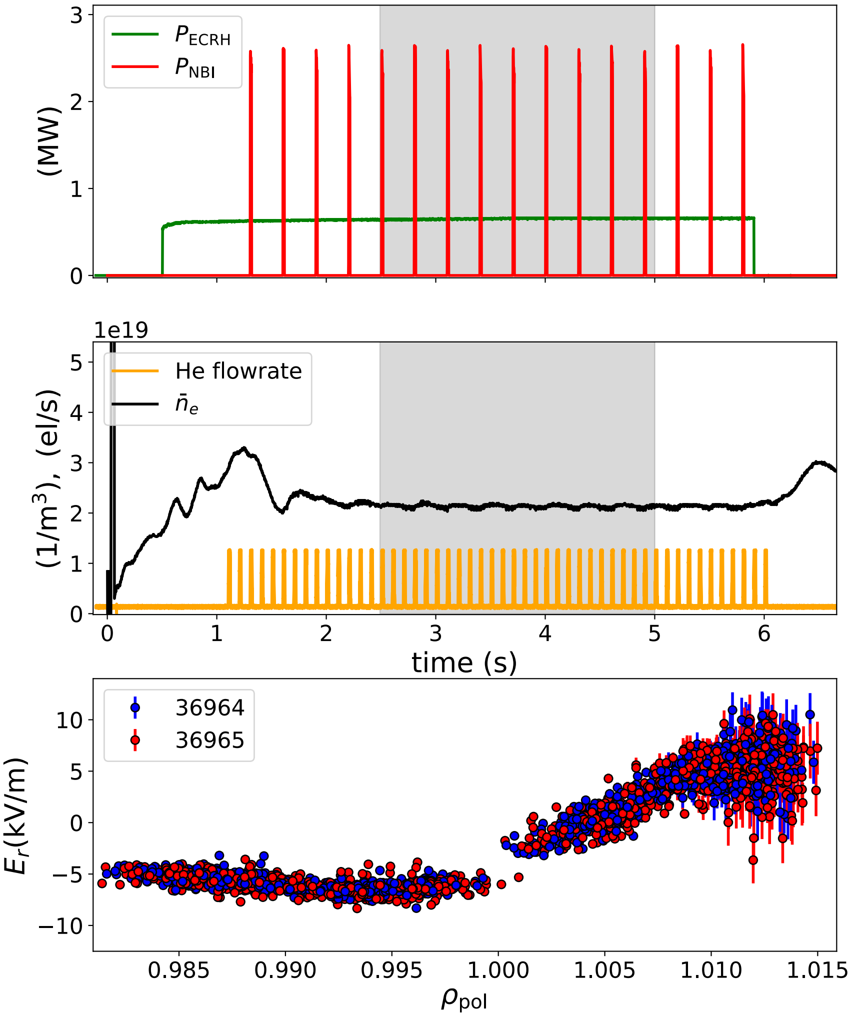

Figure 5.14: Time traces of two identical L-mode discharges with constant ECRH of 600 kW and density feedback control on $\bar{n}_e = 2.2 \times 10^{19}\,\mathrm{m}^{-3}$. The He flow rate for HES was synchronized to the NBI blips, which were used for CXRS measurements. The analysis of the HES profiles in the time window 2.5 to 5 s delivers a constant E_r profile and the data show only little scatter.

with $I_{\mathrm{p}} = 800\,\mathrm{kA}$, $B_{\mathrm{T}} = -2.5\,\mathrm{T}$ and $q_{95} = -5$. The central density (middle panel) was feed-back controlled and kept constant on $\bar{n}_e = 2.2 \times 10^{19}\,\mathrm{m}^{-3}$. The data for the E_r profile evaluation were taken from the time window 2.5 to 5.0 s (grey shaded area) and E_r was calculated as described in the section before for each data acquisition frame. As can be seen the reconstructed E_r profiles are constant in time, the data show only little scatter and the resulting profiles from the two discharges agree amongst each other. A constant E_r profile for constant plasma parameters can be expected, because the quantities determining E_r in the plasma edge $((\nabla_r p_i)/(en_i))$ and in the SOL $(-\nabla_r T_{e,\mathrm{OMP}}/e)$ (see Section 2.2.3) are constant in these two discharges (not shown).

In Figure 5.15 it is shown how the minimum of E_r in the confined plasma, $E_{r,\mathrm{min}}$, scales with the pedestal top and separatrix values of T_i, n_e and T_e. If E_r in the plasma edge region is given by $\nabla_r p_i/(en_i)$, then

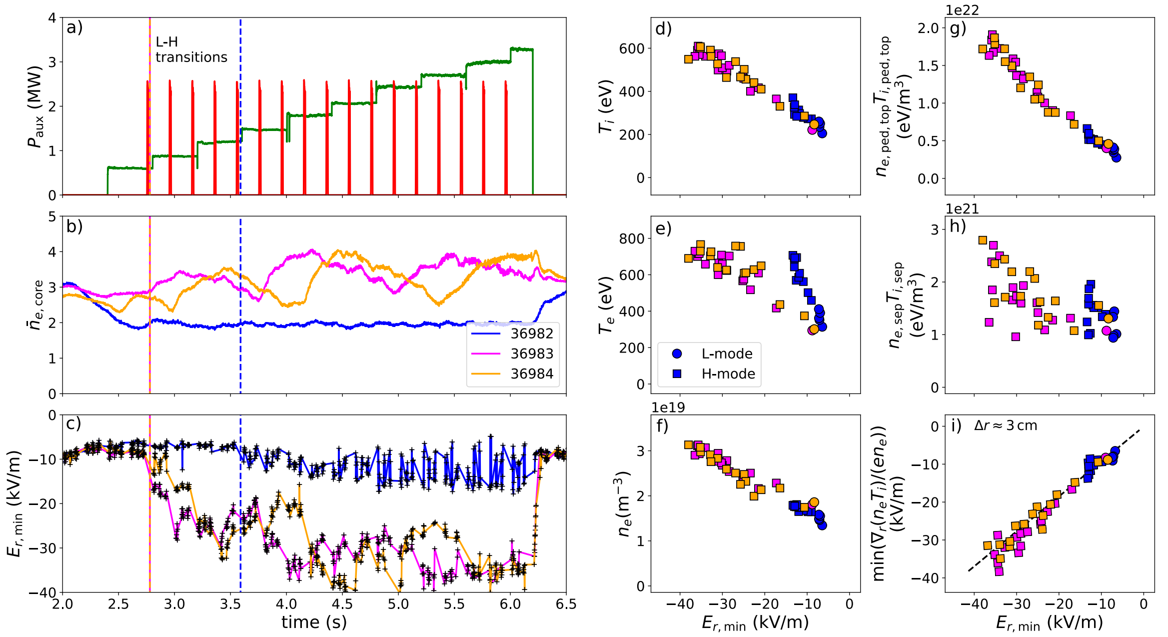

Figure 5.15: a) Time trace of an ECRH ramp with NBI blips used in three low-density feedback controlled D plasma discharges (b) to trigger an L- H transition (t_{LH} indicated by vertical lines). (c) Evolution of $E_{r,\min}$, determined with HES. $E_{r,\min}$ decreases with increasing heating power and exhibits a sudden decrease when the confinement regime is changed from L- to H-mode. (d)-(h) shows the relation of $E_{r,\min}$ with pedestal top and separatrix values of T_i, n_e and T_e. While $E_{r,\min}$ scales with the pedestal top values of T_i and n_e, it does not scale with T_e and their separatrix values. i) Identity relation of $E_{r,\min}$ and $\min(\nabla_r p_i/(en_i))$. This is an indication that E_r is indeed determined by the diamagnetic term in the plasma edge.

Assuming that E_r in the plasma edge is given by $(\nabla_r p_i)/(en_i)$ and the E_r-well has a constant width (both assumptions are correct for H-mode) [44], $E_{r,\min}$ can be approximated by the pedestal top (i.e. $\rho_{\text{pol}} \approx 0.95$) and separatrix values (i.e. $\rho_{\text{pol}} = 1$) of T_i, n_e and T_e as follows:

$$E_{r,\min} = \min\left(\frac{\nabla_r n_i T_i}{e n_i}\right) \approx \frac{T_{i,\text{sep}} n_{e,\text{sep}}}{e\Delta r n_{e,\text{sep}}} - \frac{T_{i,\text{ped,top}} n_{e,\text{ped,top}}}{e\Delta r n_{e,\text{sep}}} \propto -\frac{T_{i,\text{ped,top}} n_{e,\text{ped,top}}}{e\Delta r n_{e,\text{sep}}}. \tag{5.28}$$

Hence $E_{r,\min}$ is expected to scale with $n_{e,\text{ped,top}}$ and $T_{i,\text{ped,top}}$, but not with $T_{e,\text{ped,top}}$, if $T_{i,\text{sep}}, n_{e,\text{sep}}$ and Δr are constant. Figure 5.15 shows this analysis for three discharges of different density in which an ECRH ramp was applied similar as in the reference discharge. These discharges were density feedback controlled on a certain value of $\bar{n}_e$ (see Figure 5.15b). Figure 5.15c shows the evolution of $E_{r,\min}$ over time. As expected in H-mode $E_{r,\min}$ decreases with increasing heating power and it also exhibits a strong change at the L-H transition (marked with dashed lines in the plot). In Figures 5.15d-h the relations between $E_{r,\min}$ and $T_{i,\text{ped,top}}$, $n_{e,\text{ped,top}}$, $T_{e,\text{ped,top}}$, as well as the products $T_{i,\text{ped,top}}n_{e,\text{ped,top}}$ and $T_{i,\text{sep}}n_{e,\text{sep}}$ are shown. It is found that $E_{r,\min}$ scales linearly with $T_{i,\text{ped,top}}$, $n_{e,\text{ped,top}}$, and $T_{i,\text{sep}}n_{e,\text{sep}}$, independent of $\bar{n}_e$. This is not the case for $T_{e,\text{ped,top}}$ and $T_{i,\text{sep}}n_{e,\text{sep}}$. The latter is rather constant, as is assumed in Equation 5.28. Figure 5.15i shows that $E_{r,\min} \approx \min\left(\nabla_r(n_iT_i)/(en_i)\right)$. However, the assumptions and thus, this

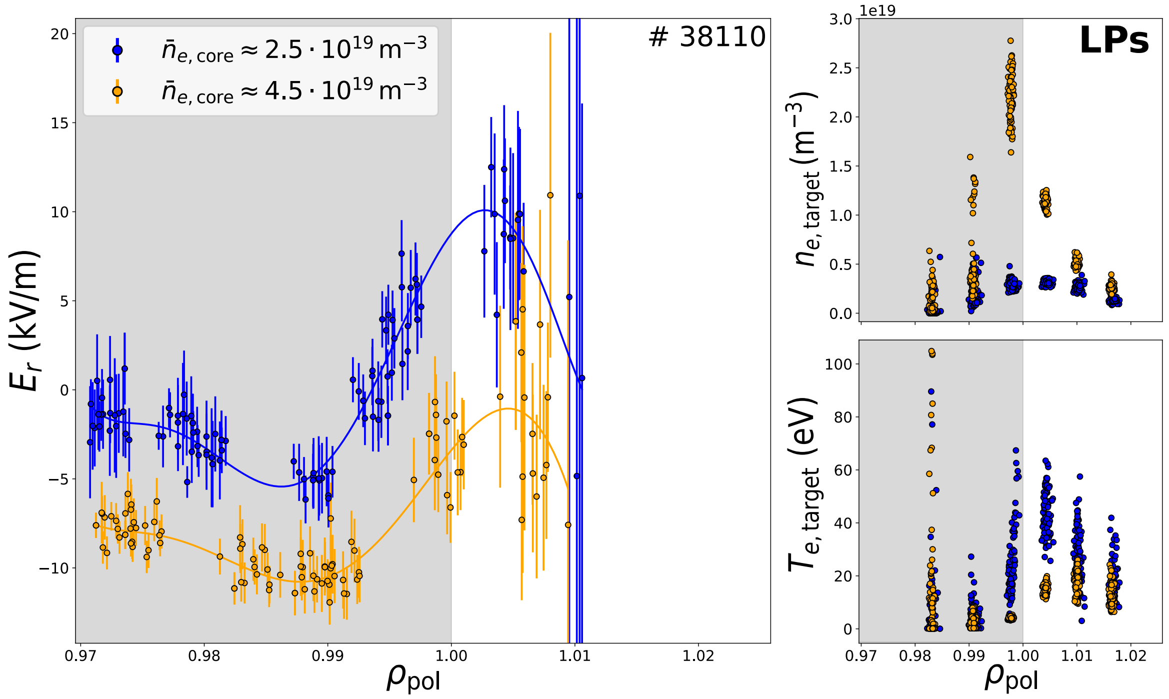

Figure 5.16: *Left:* E_r profiles acquired with HES in two stable L-mode phases of the same discharge with different $\bar{n}_{e,\mathrm{core}}$. Other plasma parameters and P_{sep} were the same in both phases. In the low density phase E_r^{SOL} is higher than in the high density phase, which is in line with target n_e and T_e profiles acquired with Langmuir probes at the outer divertor (*right*).

relation are true fro H-mode only. In L-mode deviations from this relation are found as will be shown in Chapter 7.

As shown in Section 2.2.5 the SOL-E_r scales with $-\nabla_r T_{e,\mathrm{target}}$. This normally means that a higher peak divertor target temperature leads to a higher upstream E_r and vice versa. Thus, a variation of the upstream E_r^{SOL} can be achieved by changing $\nabla_r T_{e,\mathrm{target}}$, where the latter mainly depends on the recycling capabilities in the divertor region [38]. If the same power is crossing the separatrix $P_{\mathrm{sep}} = P_{\mathrm{net}} - P_{\mathrm{rad,main}}$ a higher plasma density should lead, due to increased $n_{e,\mathrm{target}}$, to lower $T_{e,\mathrm{target}}$ and, thus, to a lower E_r. This is demonstrated in Figure 5.16, where upstream E_r profiles measured with HES and $n_{e,\mathrm{target}}$ and $T_{e,\mathrm{target}}$ obtained from Langmuir probe measurements are shown for two L-mode phases of discharge # 38110. The data are taken from 100 ms long time windows with constant heating $P_{\mathrm{sep}} \approx 600\,\mathrm{kW}$, but for the blue data $\bar{n}_{e,\mathrm{core}} \approx 2.5 \times 10^{19}\,\mathrm{m}^{-3}$ while for the yellow data $\bar{n}_{e,\mathrm{core}} \approx 4.5 \times 10^{19}\,\mathrm{m}^{-3}$. As expected in the low density case $n_{e,\mathrm{target}}$ is lower while the SOL-E_r and $\nabla_r T_{e,\mathrm{target}}$ are higher compared to the high density case. $E_{r,\mathrm{min}}$ is also different, so that the complete E_r profile is shifted. The reasons for this will be discussed in Chapter 7.

5.2.5 Synthetic Diagnostics

A synthetic diagnostics was developed in the context of this thesis to better understand the resulting line spectra, emissivity, rotation and temperature profiles acquired with the HES method. The synthetic diagnostics consists mainly of three parts: The modelling of the He gas cloud to determine the He^+ distribution, the modelling of the velocity distribution of the He^+ particles and the integration of the He^+ emission cloud along the LoS to simulate the measurement. Thus, the synthetic diagnostics also gives information on the interpretation of the measured quantities and on limitations in the determination of the E_r profiles.

5.2.5.1 Model

Necessary input parameters for the model are n_e and T_e profiles. Due to lack of experimental data in the SOL, the plasma main ion temperature profile is assumed to be equal to T_e or can be scaled by a factor f, such that $T_i = fT_e$. Also an E_r profile has to be given to the model to determine the poloidal velocity components of the He^+ particles. For this a synthetic E_r profile can be generated within the model from chosen values of $E_{r,\mathrm{min}}$, $E_{r,\mathrm{max}}$ and their radial localization. Further discharge parameters are the plasma main ion species, the magnetic equilibrium and the injected He particle flow rate, while the opening angle and the injection energy of the He gas cloud as well as the injection position of the gas valve and the LoS geometry are taken from the calibration data, but can also be artificially varied.

Starting from the metastable states-resolved He^0 distribution, calculated on a rectangular grid, the He^+ source rate is determined for each grid cell, using a set of differential equations taking into account the different atomic processes described in Section 5.2.1 with the corresponding reaction rates provided by ADAS [130]. This routine is taken from a forward model which has been developed for the thermal He beam diagnostics (see Section 3.1.1) [145]. In order to determine the abundance of He^+ at a certain location within the observation volume of the synthetic diagnostics, the resulting He^+ production rate has to be convoluted with the density distribution of the He^+ particles that results from a point source.

This density distribution is determined using a Monte-Carlo approach. First, an equally spaced grid spanning 2.5 m in the toroidal and 0.5 m in the poloidal direction on each side from the injection axis of the gas valve, with a radial extension given by the existence of He^+ cloud is produced. Each He^+ particle on the grid is attributed a velocity component parallel and perpendicular to the local magnetic field vector $\boldsymbol{B}$. The Monte-Carlo calculation starts by randomly attributing a parallel velocity to a born He^+ particle using as a probability distribution a Boltzmann distribution. However, the mean velocity of this distribution changes, since the temperature of the He^+ particles eventually adjusts to the local plasma temperature by collisions between the He^+ particles and the plasma ions. At each time step the thermalisation of the He^+ particles is continued while the particle keeps moving into the same direction until the end of a characteristic time, the slowing-down time. After that, a new velocity vector is randomly appointed using a Boltzmann probability distribution with the actual temperature of He^+. The mean velocity of this distribution changes since the temperature of the He^+ particles eventually adjusts to the local plasma temperature by collisions between the He^+ particles and the plasma ions. The calculation is repeated until the He^+ particle is either ionized or its distance to the model grid is larger then the grid size.

In the perpendicular direction only a movement due to the $E \times B$ velocity drift is assumed. Thus, the perpendicular velocity is calculated from the input E_r profile and the local magnetic field strength.

In each grid cell the information of particle density and velocity vectors in parallel and perpendicular direction is stored for several thousands of He^+ particles. In this way a parallel and perpendicular velocity distribution is available in each grid cell.

The resulting modelled He^+ gas cloud is multiplied by the respective local PEC and n_e and then projected on the toroidal and poloidal LoS. In this way the line spectra, the emissivity, velocity and temperature profiles measured by the HES diagnostics can be imitated. For the projection on the LoS the real geometry, which helps to understand the impact of geometrical and radial resolution effects or an idealized, ideal poloidal or toroidal geometry. Here, results are presented with an idealized geometry, whereas the real geometry was used for interpretive modelling of the HES-E_r profiles in Chapter 6.

5.2.5.2 Results

In the following the results are shown for an NBI heated L-mode plasma with H as main ion species[6] (AUG # 36749). The stable phase in the time window 1.9 – 1.98 s is right before the L-H transition. The T_e and n_e profiles are taken from the experiment and $T_i = T_e$ is assumed. The initial temperature of the injected He particles is 300 K. The synthetic E_r profile is parametrized in a way to fit the experimentally determined HES-E_r profile (see Figure 5.19, red line).

Temperature An estimate of the time scales for ionization of He^+ to fully ionized He, τ_{ion}, and for thermalisation of He^+ to the local plasma temperature by Coulomb collisions, τ_{therm}, shows that in the radial range across the separatrix the ratio $\tau_{\text{therm}}/\tau_{\text{ion}}$ changes strongly (see Figure 5.17). As can be seen from this figure, for $\rho_{\text{pol}} > 1.05$ $\tau_{\text{therm}}/\tau_{\text{ion}} << 1$ and the ratio increases towards the confined region, where at $\rho_{\text{pol}} = 0.9$ $\tau_{\text{therm}}/\tau_{\text{ion}} \approx 50$. In conclusion this means that in the confined region the He^+ particles get ionized before they reach thermal equilibrium with the plasma. In the SOL the thermalisation happens before the ionization. However, both characteristic times are long enough that the particles leave the field of view of the LoS before. Thus, the measured He^+ temperature does not equal the plasma ion temperature neither in the confined plasma nor in the SOL.

The synthetic diagnostics also reveals that due to the LoS geometry and the spreading of the gas cloud a different temperature profile is observed for the poloidal and toroidal LoS. In the poloidal direction the perpendicular velocity distribution of the center of the gas puff is detected, whereas in the toroidal direction the fastest parallel moving He^+ particles of the parallel velocity distribution have escaped from the observation volume before they emit a photon. Thus, the measured toroidal temperature, mostly originating from the parallel velocity distribution, is lower. For this reason the detected He II line signal is not fully Gaussian in the toroidal direction, what is also observed in the experiment.

Radiance The poloidal radiance profile of the synthetic diagnostic is shown in Figure 5.18. A comparison of the modelled profile with the corresponding experimental data shows good qualitative agreement (see Figure 5.18a). Quantitatively, the experimental data give a lower radiance. There are several possible reasons for this differences coming

---

[6] The use of H or D as main ion species has negligible impact on the resulting E_r profiles calculated by the HES diagnostics.

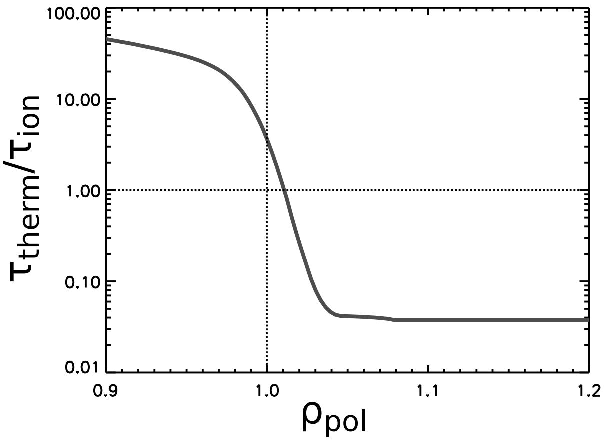

Figure 5.17: The ratio of thermalisation of He^+ to ionization of He^+ changes strongly in the radial range around the separatrix. Thus, the measured He^+ temperature does not necessarily represent the local temperature of the plasma.

from uncertainties in the atomic data, but also uncertainties in the shape of the gas cloud. The latter was namely determined for higher gas pressures in the system (see Section 4.2.3.2). Changing T_i by a factor of 2 as well as the initial energy of the neutral He particles has been found to have little influence on the resulting modelled radiance profile.

A big difference is that in the experimental analysis passive signal is collected along the LoS, which is subtracted to determine the active contribution. This is not needed for the synthetic diagnostics, since it does not model the passive contribution of the HES signal. This difference in the analysis method can lead to slight differences in the reconstructed radiance profiles. A reduction of the radiance can also originate from the degradation of the optical components over time, leading to a reduced sensitivity, which is not taken into account in the model.

Further information can be extracted if ρ_{pol} is weighted with the local emissivity. This is illustrated in Figure 5.18b. The weighted profile (dashed line) indicates from which radial location the collected light originates. It can be seen that from the SOL up to $\rho_{\mathrm{pol}} \approx 0.98$ the weighted and the original (unweighted) modelled radiance profile (solid line) agree. This means that the measured values of the different quantities originate from a localized region around the intersection of the LoS with the He^+ gas cloud. Further inside the plasma, at $\rho_{\mathrm{pol}} < 0.98$, this changes and the detected radiance originates mostly from radial positions with $\rho_{\mathrm{pol}} \approx 0.98$. The two arrows in Figure 5.18b visualize this effect. The reason for this effect is the poloidal drift of the He^+ particles. He^+ particles originating from further outside the plasma move into inner LoS and cross them at locations which are not localized around the intersection of the LoS with the He^+ gas cloud, but their light is collected along the LoS. This corruption of the inner LoS signal can not be overcome by subtraction of the passive signal as it is inherent to the He gas puffing. Hence, measured data from locations at about $\rho_{\mathrm{pol}} < 0.98$ have to be rejected.

Toroidal Rotation The model assumes that in the toroidal direction the He^+ particles exhibit no net velocity. However, the experimental data show an apparent toroidal velocity in the range of $|v_{\mathrm{tor}}| \approx 5\,\mathrm{km/s}$ (see Figure 5.12). This velocity is not real but arises due to two effects. First, as mentioned before, the He^+ particles with the largest velocity are

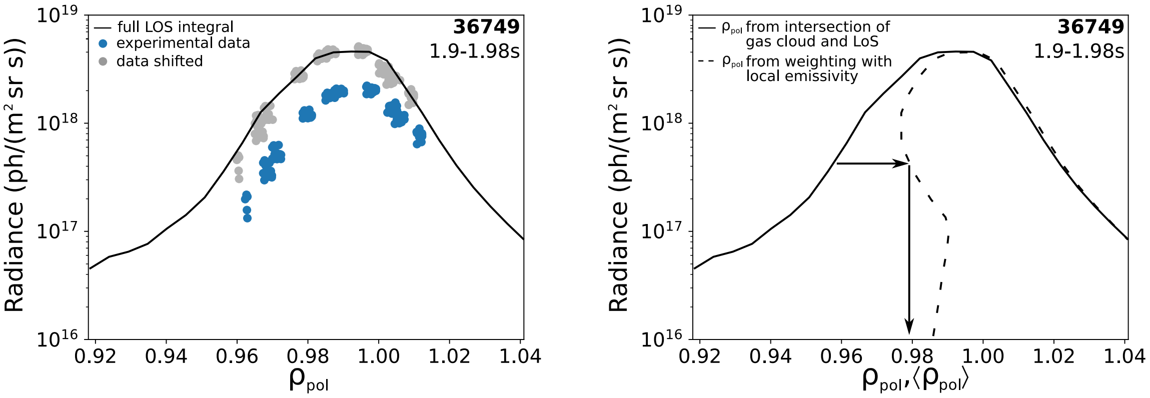

(a) Poloidal Radiance

(b) Radial Information of HES

Figure 5.18: (a) The radiance profile from the synthetic diagnostics (black solid line) is in good qualitative agreement with experimental data. This implies that the most important processes for modelling of the HES diagnostics are taken into account. The difference in the absolute values can be mainly explained by slight differences in the analysis method of the synthetic diagnostics compared to the experimental evaluation and uncertainties in the atomic data as well as the gas puff geometry. (b) The radiance profile using ρ_{pol} determined for each LoS and a mean ρ_{pol}, obtained by weighting ρ_{pol} with the local emissivity gives information on the local origin of the emitted light and shows that LoS probing $\rho_{\text{pol}} < 0.98$ mainly collect information from radial locations $\rho_{\text{pol}} \approx 0.98$. This means that the HES diagnostics does not deliver real information about the He^{+} particles for $\rho_{\text{pol}} < 0.98$.

found furthest away from the gas puff. These particles are streaming along field lines away from the injection position while not being thermalized sufficiently to exhibit a Maxwellian distribution. Second, the LoS are not perfectly toroidal and tangential to the magnetic field lines at the measurement position. Depending on the actual alignment of the toroidal LoS more light from He^{+} particles moving towards/away from the observation direction can be collected, leading to an apparent positive/negative rotation.

Poloidal Velocity and Radial Electric Field Figure 5.19 shows the E_r profile of the synthetic HES diagnostics (black solid line) calculated from the input-E_r profile (red solid line) which was produced from the actual measured HES E_r profile (blue data points). A comparison of the reconstructed E_r profile with the input E_r profile reveals that E_r can be well reconstructed by the HES diagnostics from the SOL over $E_{r,\text{min}}$ up to $\rho_{\text{pol}} \approx 0.97$. For $\rho_{\text{pol}} < 0.97$ the two E_r profiles start to deviate, where the reconstructed profile stays approximately at the value of $E_{r,\text{min}}$ and even shows another change of slope at about $\rho_{\text{pol}} = 0.96$. This effect was already discussed for the radiance profiles, where it was shown that the inner LoS detect light from He^{+} particles which originate from locations further outside. Since the synthetic diagnostics shows that the inner E_r gradient can not be resolved with the HES diagnostics, data points at $\rho_{\text{pol}} \lesssim 0.97$ are discarded for the actual HES diagnostics.

To further quantify the deviations between the synthetically measured E_r profiles and the input-E_r profiles a set of a scan of input-E_r profiles with different slopes of the inner and outer E_r gradient and different values for $E_{r,\text{min}}$ and $E_{r,\text{max}}$ was performed. This showed that in most cases the input-E_r profiles can be very well reconstructed in the SOL, with a slight overestimation of $E_{r,\text{max}}$ in the SOL by about 0.5 kV/m. The value of

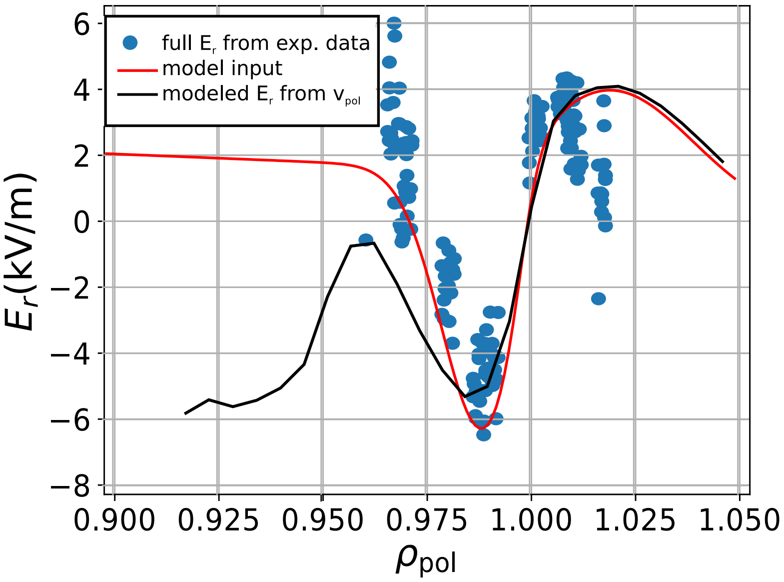

Figure 5.19: The black solid line depicts the E_r profile reconstructed from the poloidal velocity obtained from the synthetic diagnostics. The red line is a synthetic E_r profile created as input to the model of the HES diagnostics and represents the real existing E_r profile in the plasma edge. This profile was created in a way to fit the experimentally determined E_r profile measured with HES. A comparison of the different profiles shows that a correct reconstruction of E_r from HES can only be achieved from the near SOL up to $\rho_{\text{pol}} \approx 0.97$.

$E_{r,\text{min}}$ in the confined region is generally underestimated, in most cases by 0.5 kV/m, but it can be as high as 2.5 kV/m.

In conclusion this means that the E_r profile across the separatrix can be well reconstructed by the HES diagnostics, but a quantitative estimation of the outer E_r gradient is prone to large uncertainties, where a lower limit of it can be given. The findings from the synthetic diagnostics are useful for the interpretation of the experimental results. In Chapter 6 the synthetic diagnostics was used to quantify deviations observed between HES- and DR-E_r in different drift configurations. In the future the synthetic diagnostics can be used in a recursive way to determine the actual underlying E_r profile from the experimentally determined E_r profile.

5.2.6 Comparison with other E_r Diagnostics

5.2.6.1 Comparison with Beam-based CXRS

Figure 5.20 shows E_r measurements acquired with the beam-based CXRS system and the HES diagnostics in an H-mode plasma with constant heating power of about 4 MW. The profiles from the two diagnostics agree well with each other and combined they yield a complete radial profile of E_r from $\rho_{\text{pol}} = 0.92 - 1.025$. The data were acquired in the same time window and, to achieve better radial resolution of the profiles, an R_{aus} scan of the plasma was performed (see Section 3.1.2). The ELM frequency (see Section 2.4.1.1) was low in this discharge, about 100 Hz, leading to long inter-ELM phases. For the comparison of the CXRS measurements to the HES data only inter-ELM phases were used. No radial shift to the data was applied.

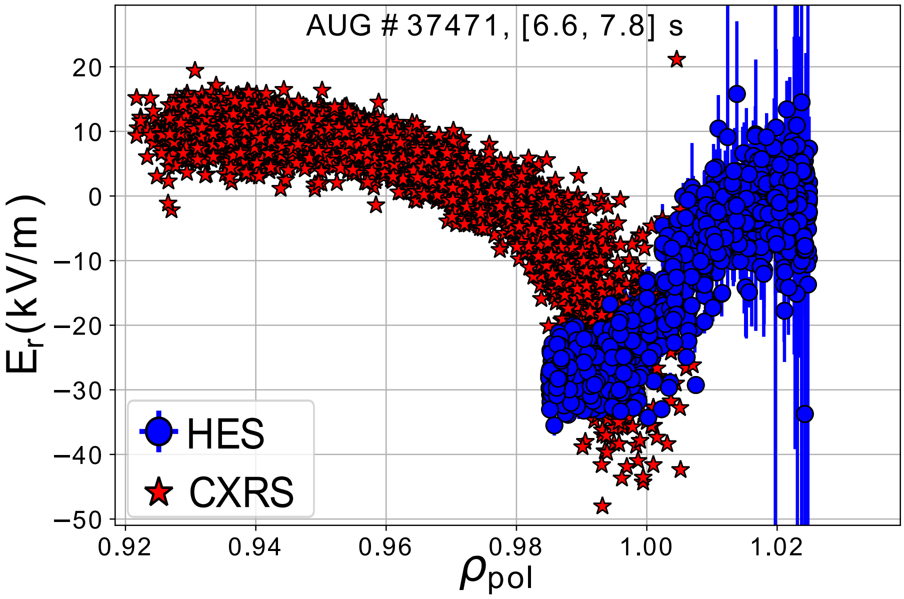

Figure 5.20: Comparison of E_r profiles from HES and beam-based CXRS in a stable H-mode phase with low ELM frequency. The data agree well and exhibit a $E_{r,\mathrm{min}}$ value of $-30\,\mathrm{kV/m}$ which is a typical value for an AUG H-mode with 4 MW heating power. A shift of $\rho_{\mathrm{pol}} = 0.005$ was applied to the HES diagnostics, while the profiles of the CXRS diagnostics were not shifted. In this way a complete E_r profile from the pedestal top to the near SOL can be reconstructed, since the CXRS signal can only resolve the inner E_r gradient up to $E_{r,\mathrm{min}}$, while HES resolves the outer E_r gradient.

Both diagnostics deliver an $E_{r,\mathrm{min}}$ value of $-30\,\mathrm{kV/m}$ which is a typical value for AUG H-mode plasmas. The CXRS data alone would suggest an even deeper $E_{r,\mathrm{min}}$, but the scatter of the data also becomes larger towards the separatrix due to the decreasing signal. On the other hand it was seen from the synthetic diagnostics that $E_{r,\mathrm{min}}$ is slightly overestimated by HES. Also the measured E_r gradient is weaker than the maximal observable gradient as suggested by the synthetic diagnostics. However, this example shows that with the HES system gradients of about 10 kV/mm are measurable.

5.2.6.2 Comparison with Doppler Reflectometry

In Figure 5.21 an E_r profile measured in the L-mode phase of the reference discharge (see Section 3.2) is shown. The time window is taken from a stable phase right before the L-H transition. The blue circles are data from the HES diagnostics, acquired in the time window 2 to 2.5 s and the blue line is a cubic spline fit to the data. The red symbols are E_r measurements from two independent DR systems acquired in the same time window. All three diagnostics are in excellent agreement over the complete radial range they cover, i.e. the region of the outer E_r gradient. No radial shift was applied to either of the E_r profiles.

5.2.6.3 Comparison with Langmuir Probe Data

A comparison of SOL-E_r mapped to the OMP is shown in Figure 5.22a. The blue circles are E_r measurements acquired by HES and the orange line is the inferred E_r at the OMP from the target profiles of the outer divertor measured by the Langmuir probes (LP).

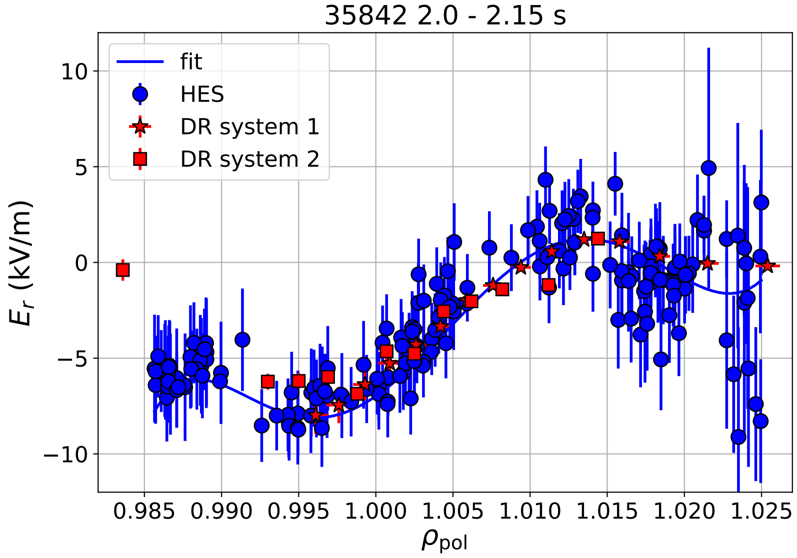

Figure 5.21: E_r profiles measured with HES and two independent DR systems during a stable L-mode phase. The three profiles agree very well in the radial range of the outer E_r gradient.

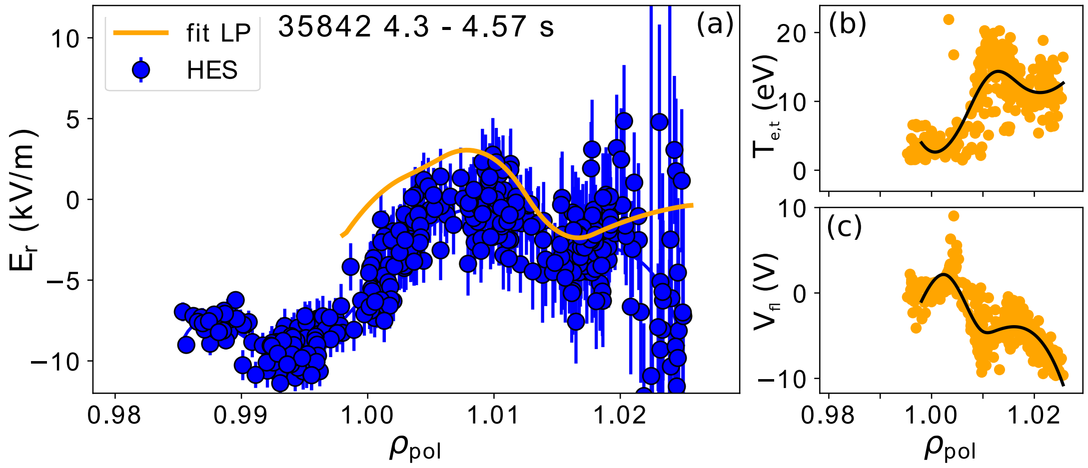

Figure 5.22: (a) SOL-E_r profiles at the OMP measured with HES (blue data) and reconstructed from target profiles (orange line), which were measured with LPs. The E_r profiles are from a stable L-mode phase with SP sweeps. The SOL-E_r profiles of the two diagnostics agree well within their uncertainties. (b) Corresponding electron target temperature and (c) floating potential profile measured with the LPs at the outer divertor. For the reconstruction of the E_r profile the experimental data were fit with cubic splines (black line).

For the determination of the upstream E_r from the target profiles Equation 2.44 was employed.

The data were acquired in the time window 4.3 – 4.57 s, a stable L-mode phase of the reference discharge # 35842. In this phase strike point sweeps (see Section 3.1.4) were performed for a better radial coverage of the target profiles. The LP target profiles ($T_{e,\rm t}$ and $V_{\rm fl}$) were fit with cubic splines (see black lines in Figure 5.22b,c) and mapped to the OMP to determine the radial gradient. Neither of the two profiles was shifted radially. Within the uncertainties the E_r profiles of LP data and HES agree, although the former seems to deliver slightly higher values for E_r in the SOL. This difference could originate from the slight underestimation of E_r in the SOL by HES, as it was found with the synthetic diagnostics. However, the uncertainties in the LP measurements are also large. A more detailed comparison of experimental SOL-E_r profiles in different drift configurations shows that the SOL-E_r is well described by $-\nabla_r T_{e,\mathrm{OMP}}/e$ (see Section 7.3.1.2).

The good agreement between the new He II spectroscopy diagnostics and conventional E_r measurement systems shows that HES can measure E_r reliably in the edge of a confined fusion plasma up to the SOL in different confinement regimes.

6 Diagnostic Effects on Radial Electric Field Measurements

For a wide range of L-mode E_r profiles the two measurement techniques, Doppler reflectometry (DR) and He II spectroscopy (HES), agree well amongst each other. However, also systematic deviations are observed between the two E_r diagnostics, mainly in LSN unfavourable drift configuration plasmas. Since DR and HES E_r measurements are based on different principles, the question remains if differences found in the experimental E_r profiles from the two diagnostics are due to systematic dependences of the measurement technique on other parameters. This may hamper an unambiguous determination of E_r. For this reason, in this chapter a detailed comparison of E_r profiles from DR, HES and the synthetic diagnostics is presented to disentangle possible diagnostic effects on the measurement of E_r from physics effects influencing the measured E_r. It is shown that deviations between the measured E_r profiles mainly originate from a loss of alignment of the poloidal optical head of the HES diagnostics (see Section 6.1). Also possible additional plasma turbulence effects, influencing the measurement of E_r, are discussed (see Section 6.2). The conclusions on which experimental E_r measurement can be used under which circumstances are presented in Section 6.3.

6.1 Loss of LoS Alignment During Experimental Campaign 2019/2020

The adjustment procedure of the in-vessel optical components was described in Section 4.3.2.1. Before each experimental campaign a calibration of the LoS geometry is performed, which is repeated after the experimental campaign to check for possible changes. In the experimental campaign 2019/2020 it was found in the post geometry calibration that the poloidal optical head (CNR) must have tilted during the campaign, see Figure 6.1. In the figure the grey lines depict the poloidal LoS geometry before the experimental campaign and the black lines after the experimental campaign. The reason for this tilt and the exact time point of the loss of alignment are unclear, but there are indications (presented in the next section) that the CNR head has been tilted from the very beginning of the experimental campaign 2019/2020, i.e. for all discharges from # 36794 to 38201, which are most of the presented discharges in this work.

The changed LoS geometry has a twofold impact on the measurements of v_θ: first, the poloidal LoS are misaligned with respect to the poloidal plane and, second, the LoS also do not intersect vertically with the injected He gas cloud. The first contribution due to of the misalignment is small and the changed projection of the LoS onto the poloidal plane is taken into account during the data evaluation. A deviation of at most 1.5 % from the actual v_θ accounts for it. The second part implies that the projection of the parallel velocity of the He^+ particle onto the poloidal LoS is increased. This contribution to the

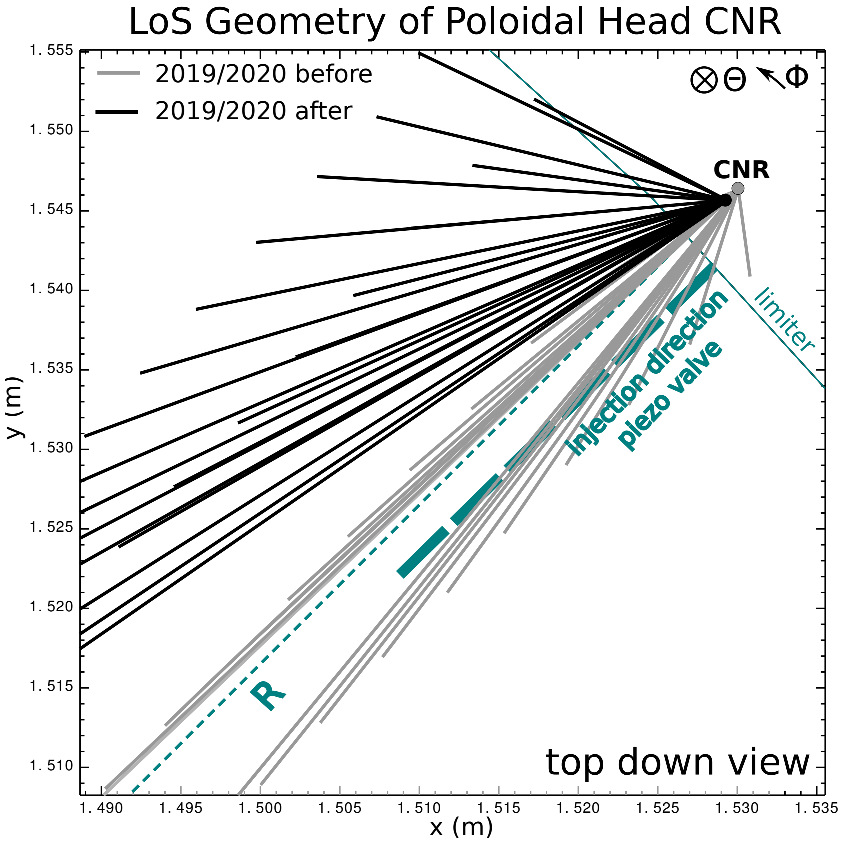

Figure 6.1: The poloidal optical head (CNR) got tilted during the experimental campaign 2019/2020 leading to a misalignment of the LoS geometry with respect to the injection direction of the piezo gas valve and with respect to the poloidal plane. In this toroidal top down view both LoS geometries are shown, the aligned LoS before the experimental campaign (grey) and the misaligned LoS after the experimental campaign (black).

measured v_θ is larger than the first contribution, but its assessment is more difficult. For its quantification the actual parallel velocity distribution of the He$^+$ particles in the gas cloud has to be known. For this reason, the synthetic HES diagnostics, which calculates the He$^+$ velocity distribution, see Section 5.2.5, was employed to quantify the impact of the changed LoS geometry on v_θ and, thus, the deduced E_r profiles.

6.2 Diagnostic Comparison in Different Drift Configurations

In the following, experimental L-mode E_r profiles in favourable and unfavourable drift configuration in LSN and USN plasmas are compared. The chosen L-mode windows are the same as used later in this work to study the impact of the drift configuration on E_r and the L-H transition and are described in more detail in Chapter 7. In favourable drift configuration they are always the last stable L-mode phases before the L-H transition, in unfavourable drift configuration they are at comparable heating power.

6.2.1 Comparison in LSN Plasmas

6.2.1.1 Favourable Drift Configuration

Figure 6.2a shows two L-mode E_r profiles from the region around the separatrix acquired with two different diagnostics, one Doppler reflectometry system (DR 1, stars) and HES (circles). The profiles are in good agreement, although small deviations in $E_{r,\mathrm{min}}$ of $E_{r,\mathrm{HES}} - E_{r,\mathrm{DR}} \approx -2.3\,\mathrm{kV/m}$ and $1.3\,\mathrm{kV/m}$ in $E_{r,\mathrm{max}}$ are observed, with HES always giving the larger values for $|E_{r,\mathrm{max}}|$ and $|E_{r,\mathrm{min}}|$. The E_r gradient across the separatrix, which connects confined plasma and SOL and is called the 'outer gradient', is found to be slightly steeper with DR ($\approx 2.5\,\mathrm{kV/m^2}$), because for the DR E_r measurement $E_{r,\mathrm{min}}$ and $E_{r,\mathrm{max}}$ are radially located closer to each other than for HES. This deviation can be explained by the limitation of the radial resolution of the HES diagnostics and becomes clear from Figure 6.2b. It shows two E_r profiles calculated with the synthetic HES diagnostics together with the two experimentally measured E_r profiles shown before. The DR E_r profile was given as input E_r profile to the synthetic diagnostics (black solid line) and the following two different output profiles were simulated: The profile shown in grey color in the figure was calculated using the LoS geometry as it was determined before the experimental campaign 2019/2020 (referred to as LoS geometry 'before'). The black coloured output profile was calculated with the LoS geometry of the tilted poloidal optical head, which was determined after the experimental campaign 2019/2020 (referred to as LoS geometry 'after').

The black E_r profile of the synthetic diagnostics is in very good agreement with the one measured by HES in the region of the outer E_r gradient. This leads to the conclusion that the poloidal optical head (CNR) of the HES diagnostics must have been tilted from the beginning of the experimental campaign 2019/2020, since the evaluated plasma discharge # 36983 was performed at the start of this experimental campaign. Partially there seems to be a slight underestimation of the absolute values of E_r by the synthetic diagnostics in the confined region and also in the SOL compared to the actually measured values. This could have two reasons: First, the input E_r profile is wrong, which is possible, since also DR has limitations in its resolution. However, the comparison of the two experimental profiles and the profiles of the synthetic diagnostics shows that the actual E_r profile is very close to the one determined by DR. The second reason could be that the parallel velocity of the He^+ particles is not correctly captured by the model of the synthetic diagnostics and underestimates v_{He}. Since a part of v_{He} is captured by the poloidal LoS, this underestimation would also lead to a deviation in the synthesized poloidal rotation and, thus, the measured E_r.

Certainly, plasma physics effects can also lead to a deviation of the two experimentally measured E_r profiles. For HES only the three leading terms of the radial force balance (Equation 2.32) are considered when deducing E_r from the HES measurements. Second, while with HES the background $E \times B$ flow is measured, DR detects the complete perpendicular fluid velocity $u_\perp$ (see Equation 3.2). For the reconstruction of E_r from the measurements it is assumed that the turbulence phase velocity, v_{ph}, is small. The strength and direction of v_{ph} hereby depend on features of the local turbulence and its direction can change from ion to electron diamagnetic drift direction and vice versa [146, 147]. Assuming the remaining differences between the reproduced E_r measurement by the synthetic diagnostics and the actually measured E_r by HES are not due to uncertainties of v_{He} in the model of the synthetic diagnostics, but originate from a non-negligible v_{ph}, which is detected by DR, then $v_{\mathrm{ph}} > 0$ in the confined region, i.e. to positive E_r, and, thus, points in the ion diamagnetic drift direction. However, gyro-kinetic simulations in the edge region of the confined plasma in AUG find a turbulence behaviour for which v_{ph} would point in the electron diamagnetic drift direction [148]. Furthermore, $|v_{\mathrm{ph}}|$ is predicted to be $\mathcal{O}(100\,\mathrm{m\,s^{-1}})$, which is too small to be resolved by the two E_r diagnostics.

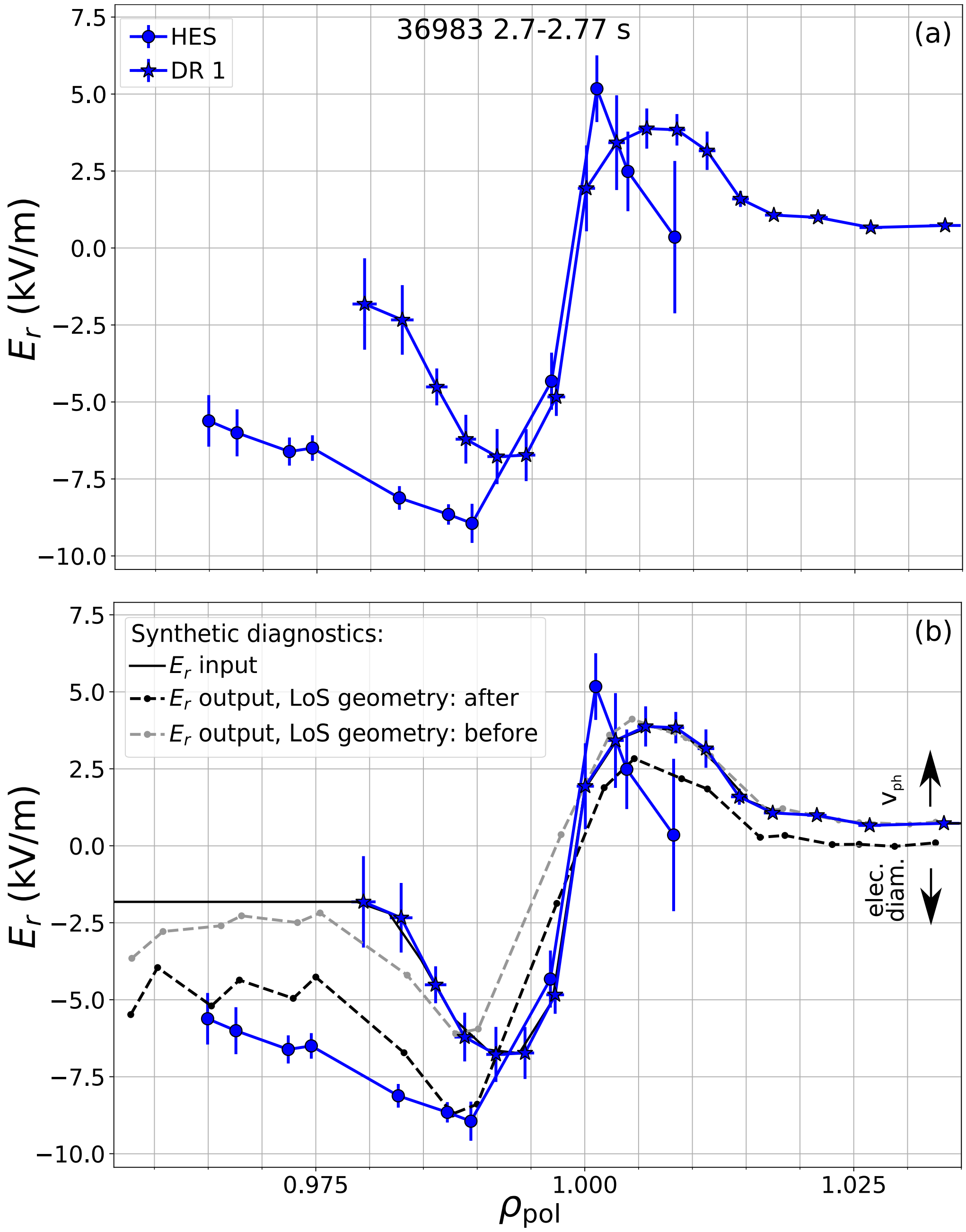

Figure 6.2: *LSN Favourable Drift Configuration* (a) Comparison of edge E_r profiles measured by DR (stars) and HES (circles): The two profiles agree well in this configuration, although HES gives always more extreme values for $|E_{r,\mathrm{min}}|$ and $|E_{r,\mathrm{max}}|$ compared to DR. A steeper E_r gradient across the separatrix is observed with DR. (b) Comparison with the synthetic diagnostics: The overall shape of the HES E_r profile can be reconstructed with the synthetic diagnostics, using the DR E_r profile as input for the modelling (black solid line) and the LoS geometry of the tilted poloidal optical head (labelled 'after').

6.2.1.2 Unfavourable Drift Configuration

Figure 6.3a shows E_r profiles acquired with DR and HES in the LSN, reversed I_p/B_ϕ discharge # 37375. The LSN unfavourable drift configuration is the only one in which the reconstructed E_r profiles from the HES diagnostics deviate strongly from DR E_r profiles. While the E_r profiles from the two DR systems (labelled DR1 and DR2) agree, the HES E_r profile seems to be shifted upwards by about 5 kV/m compared to them. Despite this, relative changes, like the E_r evolution in a discharge, are found to be the same for both measurement techniques (HES and DR) (see e.g. [50]). A comparison of the experimental E_r profiles with E_r profiles reconstructed from the synthetic diagnostics is shown in Figure 6.3b. Again, the DR E_r profile was given as input E_r profile to the synthetic diagnostics (black solid line) and from this, two E_r profiles were reconstructed using the two LoS geometries determined before (grey) and after (black) the experimental campaign 2019/2020.

The comparison reveals that for both LoS geometries ('before' and 'after') the radial resolution of the HES diagnostics is too low to detect the E_r well, since too few LoS cover the E_r well region. However, with DR the E_r well is detected. Also for this discharge the reconstructed profile using the LoS geometry as measured after the experimental campaign fits better to the experimental HES data, although large discrepancies of up to 5 kV/m between HES and the synthetic diagnostics are present in the SOL. Various uncertainties in the input parameters to the model, especially in the SOL, could lead to an underestimation of the parallel velocity of the He^+ particles (see Section 5.2.5 for more details), which projection on the poloidal LoS impacts the synthesized poloidal velocity. This is especially crucial for the non-ideal geometry of the tilted optical head.

Comparing the two output profiles of the synthetic diagnostics, it is notable that the tilting of the poloidal optical head ('after') leads to an even more positive E_r profile than it would have been observed with HES and the LoS geometry determined before the experimental campaign. This is the opposite trend to the LSN favourable drift configuration (see Figure 6.2b), where the reconstructed E_r profile with the LoS geometry 'after' is found to be more negative than with the LoS geometry 'before'. The reason for this is that in both configurations the field line pitch angle is positive, thus, the contribution of the parallel flow of the He^+ particles to the poloidal LoS is always poloidally upward (see Figure 2.7). However, since the sign of the $E \times B$ drift flips due to the reversal of B_ϕ, v_θ decreases or increases correspondingly.

Accounting for this diagnostic effect the comparison suggests that the underlying E_r profile measured by HES and DR is the same and the two measured profiles do not deviate by a constant offset, as it first appears. As mentioned in the subsection before, further existing deviations between the measured HES and the synthetic diagnostics using the DR E_r profile could arise from a non-negligible v_ph. In this drift configuration the remaining deviations in E_r are such that $v_\mathrm{ph} > 0$, which in a reversed I_p/B_ϕ discharge means that v_ph would points in the electron diamagnetic drift direction, i.e. to negative E_r.

6.2.2 Comparison in USN Plasmas

Figure 6.4 shows a comparison of measured HES and DR E_r profiles and the reconstructed E_r profiles of the synthetic diagnostics in USN L-mode plasmas. In both drift config-

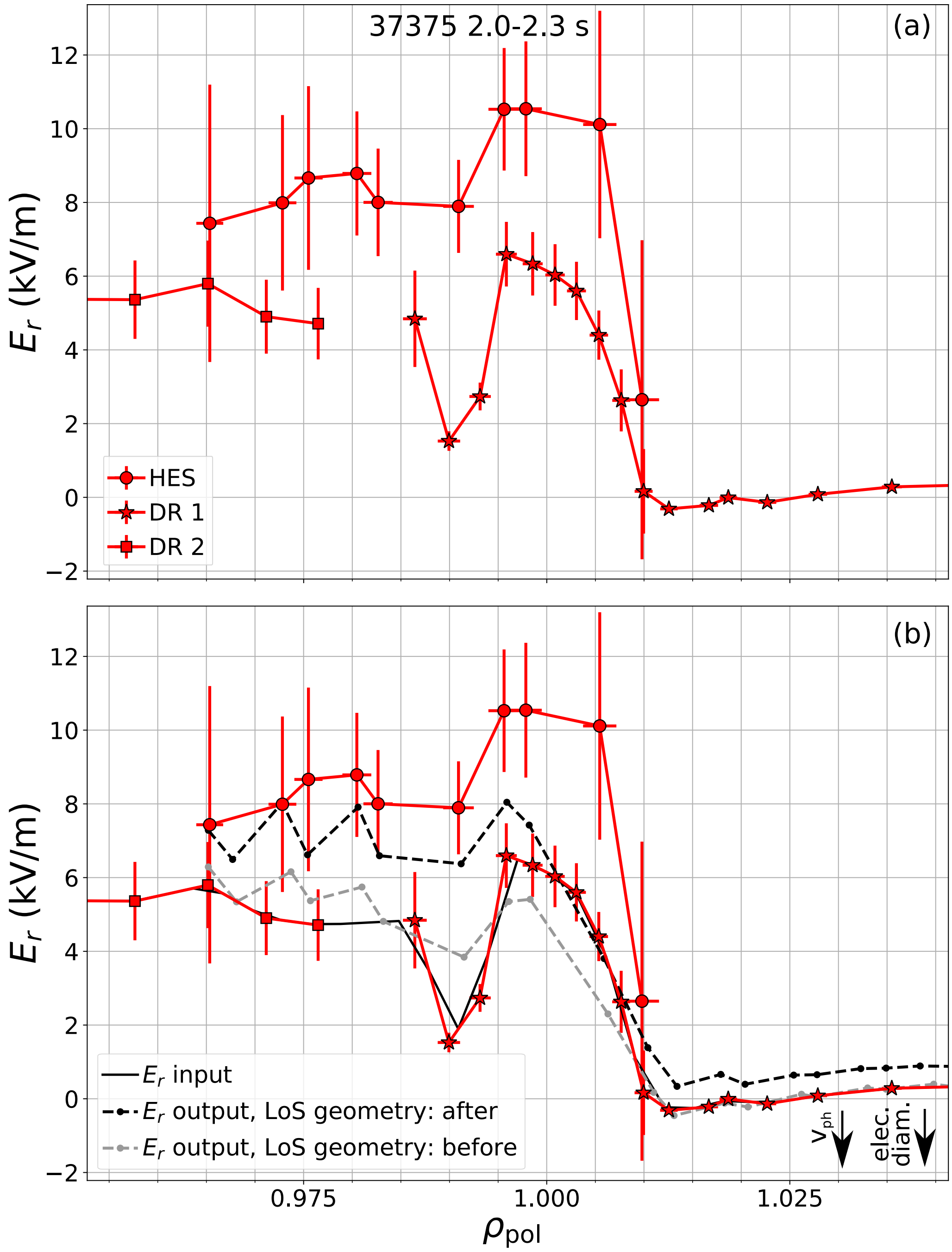

Figure 6.3: *LSN Unfavourable Drift Configuration* (a) Comparison of edge E_r profiles measured by DR (stars) and HES (circles): The L-mode E_r profile measured by HES seems to be shifted upward by about 5 kV/m compared to the DR E_r profile. This deviation can be explained by a comparison with the synthetic diagnostics (b): The effect of the tilted poloidal optical head is that the experimentally determined HES E_r profile can be brought into agreement with the E_r profile from the synthetic diagnostics, using the DR E_r profile as input profile for the modelling and the LoS geometry as determined after the experimental campaign.

urations, favourable (Figure 6.4a) and unfavourable (Figure 6.4b), the experimentally measured profiles agree very well, with small deviations in $E_{r,\min}$ and the gradients of E_r. For this set of discharges only one DR system was measuring the region around the E_r well, therefore, no data in the SOL are available for a comparison with HES.

Generally, the experimental profiles of the two diagnostics agree well with each other in both drift configurations. There are small differences in the radial positioning of the different E_r profiles, which are within the radial uncertainties of the equilibrium reconstruction. A comparison with the synthetic diagnostics shows that with the changed LoS geometry of the poloidal optical head ('after'), the measured HES E_r profile can be brought in even better agreement with the DR profile. Since the latter is given as input E_r profile to the synthetic diagnostics, it can be considered the true E_r profile.

It should also be noted that the tilted LoS geometry has the same effect on the HES E_r for both, favourable and unfavourable drift configuration, namely the measured HES E_r profile is more negative compared to the input DR E_r profile. This is consistent with the explanation before: in USN favourable configuration not only the direction of the $E \times B$ drift changes due to the reversal of B_ϕ, but also the field line pitch angle becomes negative (see Figure 2.7). Hence, the parallel He^{1+} velocity points poloidally downward. For USN unfavourable drift configuration the directions of the $E \times B$ drift and the field line geometry are identical to the LSN favourable drift configuration.

Remaining small deviations between the E_r profiles in the confined region can again originate from the afore mentioned contribution of v_{ph} to the DR measurement. However, here it is argued that this effect is likely not responsible for these deviations between DR and HES E_r measurements, since a systematic dependence of the sign of v_{ph} with the sign of B_ϕ, but not with the drift configuration (favourable and unfavourable), is found. In USN plasmas the existing discrepancies in E_r between the two diagnostics would suggest that v_{ph} points in the electron diamagnetic drift direction for the favourable and in the ion diamagnetic drift direction for the unfavourable drift configuration. Thus, the signs of v_{ph} in USN favourable/unfavourable drift configuration are opposite to the signs of v_{ph} in LSN favourable/unfavourable drift configuration, which, in turn, implies that the turbulence behaviour rather changes with $\mathrm{sign}(B_\phi)$, than with the drift configuration. Latest gyro-kinetic simulations on micro-instabilities in L-mode plasmas at the edge region of the confined plasma suggest a change of the plasma turbulence rather with the drift configuration than with a sole change of $\mathrm{sign}(B_\phi)$ [149]. This would also be in accordance with the behaviour of macroscopic plasma quantities, like P_{LH}, which changes with the drift configuration, but not with $\mathrm{sign}(B_\phi)$ only.

6.3 Consequences for Further Comparisons

The comparison of L-mode edge E_r profiles measured by DR and HES shows that deviations in the measured E_r profiles between the two diagnostics mostly originate from the misaligned LoS geometry. A deviation of the two experimental profiles due to a measurable contribution of the turbulence's v_{ph} to the DR measurements, as sometimes argued [50, 75], is unlikely, since it is found that differences in the measured E_r profiles between the two diagnostics show a dependence on the sign of B_ϕ, but not on the drift configuration.

It was shown that the tilting of the optical head must have been present already since the beginning of the experimental campaign 2019/2020, which means that the undesired effects on E_r measured by HES are present in most of the presented discharges, namely all which have a discharge number between 36794 and 38201. However, these deviations in E_r are normally smaller than 2 kV/m except for the LSN unfavourable drift configuration.

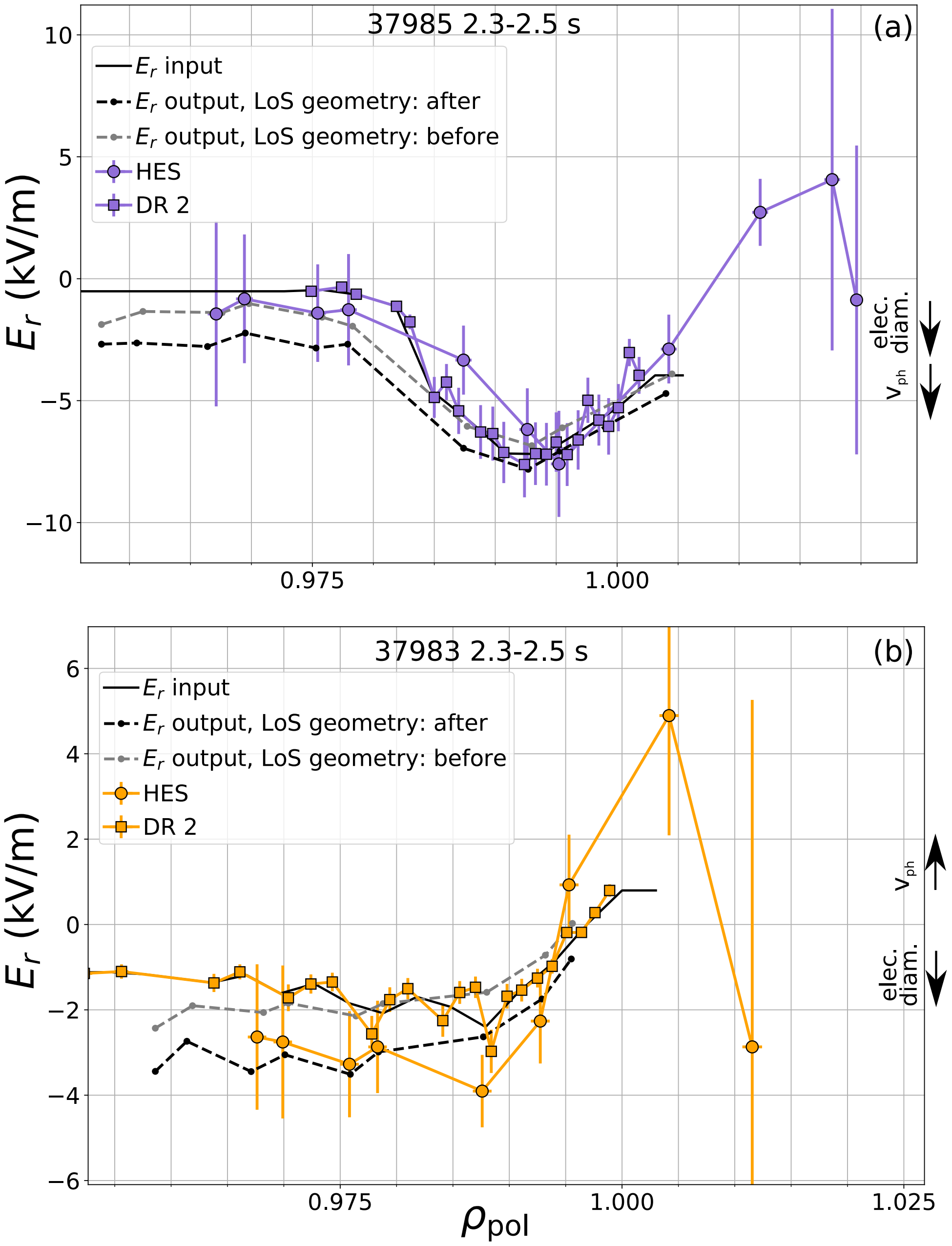

Figure 6.4: *USN favourable and unfavourable drift configuration* Comparison of measured E_r profiles of HES and DR shows good agreement in favourable drift configuration (a) and reasonable agreement in unfavourable drift configuration (b). In both drift configurations the HES E_r profile in the confined region can also be reconstructed by the synthetic diagnostics using the DR E_r profile as input for the modelling and the actual LoS geometry ('after').

Thus, the two diagnostics measuring E_r agree generally well. The larger deviations in the measured E_r profiles in the LSN unfavourable drift configuration can mainly be attributed to a positive E_r together with a change in the $E \times B$ drift direction. It was also found that deviations in the gradients of the measured E_r profiles can be explained by a more limited resolution of the HES diagnostics compared to the DR diagnostics, especially if no fine resolution by an R_{aus} scan (see Section 3.1.2) was applied to the plasma in the HES measurement phase. However, it has been found that relative changes in E_r measured within a discharge, or even within one specific drift configuration, agree qualitatively and quantitatively between the two diagnostics.

Therefore, the following approach is used when analysing E_r profiles from different discharges: For a detailed quantitative comparison of two different discharges in different drift configurations only DR E_r measurements are considered. If the focus is on the qualitative behaviour of E_r within one drift configuration, HES measurements are used.

It should be also noted that the effect of the contribution of the parallel velocity on v_θ becomes less important the larger $v_{E\times B}$ is. Therefore, deviations between the two diagnostics in I-mode are smaller and become even smaller in H-mode.

7 H-mode Access in Different Drift Configurations

The multi-machine scaling of the H-mode power threshold, P_{LH}, gives the most important dependencies of P_{LH} on global plasma parameters for the high-density branch (see Equation 2.56). However, there are some further dependences found to influence P_{LH} in different tokamaks, which are not included in the scaling. The most prominent, since it is observed on all machines, is the reversal of the $\nabla B \times B$ drift direction, which leads to an increase of P_{LH} by approximately a factor of 2, as can be seen in Figure 7.1.

7.1 Density Dependence of P_{LH} and P_{IH}

Figure 7.1 shows the density dependence of P_{LH} and P_{IH}. For the plot several discharges in favourable and unfavourable drift configuration from the experimental campaigns 2018/2019 and 2019/2020 were analysed. The discharges were heated with ECRH or NBI and they all have a toroidal magnetic field strength of $|B_{\phi}| = 2.5\,\mathrm{T}$ at the magnetic axis. The plasma current was $|I_{\mathrm{p}}| = 0.8\,\mathrm{MA}$ for the LSN and $|I_{\mathrm{p}}| = 1\,\mathrm{MA}$ for the USN plasmas. This difference in I_{p} has, in the high-density branch, no effect on P_{LH} [73]. Figure 7.1a shows the net input power, P_{net}, against the line-averaged electron density, $\bar{n}_e$, at the transition to H-mode as determined according to Section 3.2 and Figure 7.1b shows the loss power, P_{loss}, which corrects P_{net} for the main chamber radiation, $P_{\mathrm{rad,main}}$.

For both drift configurations a scan of P_{LH} with density, ranging from 2 to $6 \times 10^{19}\,\mathrm{m}^{-3}$, was investigated. Both drift configurations show for the ECRH discharges, the typical parabolic dependency of P_{LH} with $\bar{n}_e$. This is found for both calculated quantities P_{net} and P_{loss}, although for the latter an overall reduction of 300 to 500 kW due to main chamber radiation is observed. The P_{LH} values of one drift configuration agree with each other, regardless whether LSN or USN plasmas were investigated. Also, within one drift configuration, the absolute values agree well with former P_{LH} studies at AUG (see [73] and [53]). In unfavourable drift configuration P_{LH} is higher than in favourable drift configuration, but a large scatter is observed with $P_{\mathrm{LH}}^{\mathrm{unfav}} \approx 1.1\,P_{\mathrm{LH}}^{\mathrm{fav}}$ to $3.5\,P_{\mathrm{LH}}^{\mathrm{fav}}$. This could be explained by a shift of the density minimum, $\bar{n}_{e,\mathrm{min}}$, which is about $4 \times 10^{19}\,\mathrm{m}^{-3}$ in favourable drift configuration [73], to higher values in unfavourable drift configuration. In the so-called low-density branch (see Section 2.4.2) the power threshold depends strongly on the employed heating scheme and its efficiency on ion heating. Indeed, the NBI heated discharges appear to have a lower P_{LH} than their ECRH counterparts in unfavourable drift configuration and this deviation of NBI and ECRH P_{LH} is already observed at $\bar{n}_e \approx 5 \times 10^{19}\,\mathrm{m}^{-3}$ in unfavourable drift configuration. However, $\bar{n}_{e,\mathrm{min}}$ in unfavourable drift configuration can still not be determined due to too few data. There is also one data point in the figure, taken from a low density ($\bar{n}_e \approx 2.4 \times 10^{19}\,\mathrm{m}^{-3}$) discharge in unfavourable drift configuration, which was heated with ECRH only and does not transit

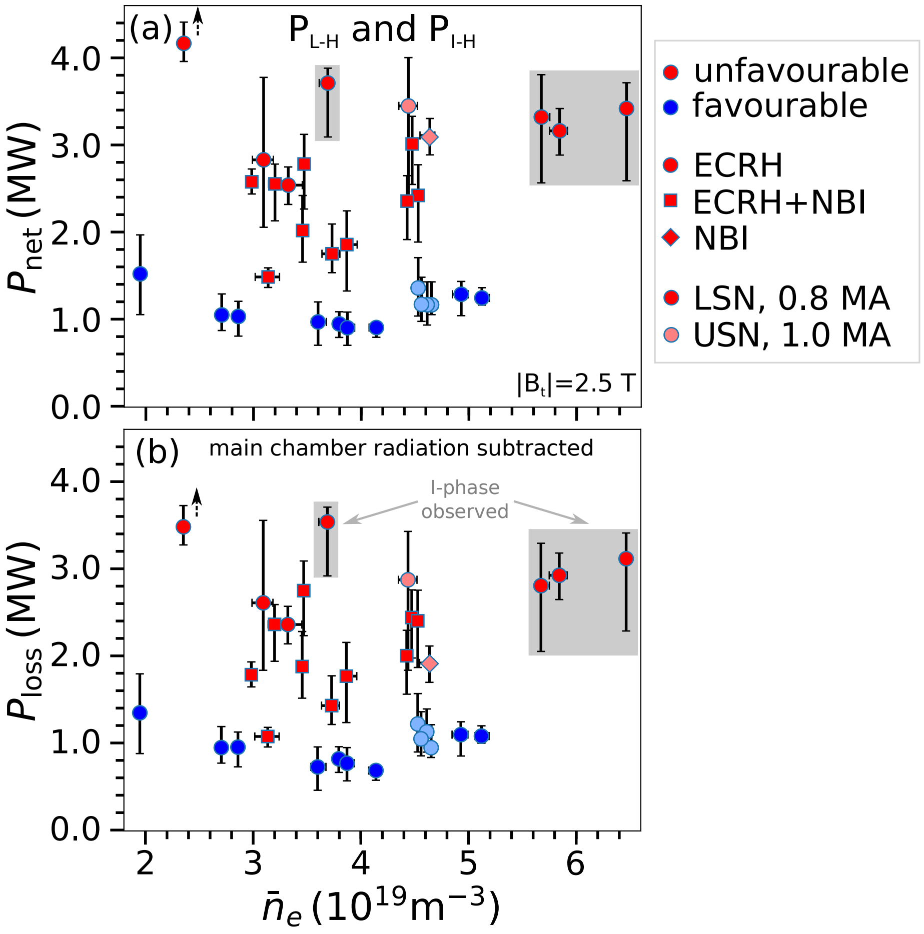

Figure 7.1: *Density dependence of the H-mode power threshold in favourable and unfavourable drift configuration* (a) Net input power before L-H transition (P_{LH}) or I-H transition (P_{IH}) versus line-averaged electron density, $\bar{n}_e$. (b) Loss power, i.e. P_{LH} or $P_{\mathrm{IH}} - P_{\mathrm{rad,main}}$, versus $\bar{n}_e$. The H-mode power threshold is higher in unfavourable compared to favourable drift configuration on average by a factor of 2. The density minimum is $\bar{n}_{e,\mathrm{min}} \approx 4 \times 10^{19}\,\mathrm{m}^{-3}$ in favourable drift configuration at AUG, but can not be determined in unfavourable drift configuration.

into I- nor H-mode. This gives a lower boundary for P_{LH}, what is indicated by the upwards facing arrow.

In unfavourable drift configuration the plasma was normally in I-mode before the transition to H-mode. For this reason the terms P_{LH} and P_{IH} are used, although both describe the power threshold needed to enter H-mode. Interestingly, in unfavourable drift configuration there are a few cases where transitions into an improved confinement regime were observed with the signature of an I-phase. This transient regime with L-H dithers is normally observed at the L-H transition in favourable drift configuration. The cases with an I-phase in unfavourable drift configuration are marked in Figure 7.1. As of yet it is not clear which conditions or parameters determine whether an I-mode or an I-phase occur in unfavourable drift configuration, however, the two confinement regimes have not been observed to appear simultaneously. Figure 7.1 suggests that I-modes occur rather at low to middle densities and NBI heating, while I-phases tend to appear at higher densities and with ECRH in unfavourable drift configuration.

Previous confinement studies at AUG in unfavourable drift configuration focused on the I-mode regime itself and the transition from L- to I-mode, see e.g. [52] and [53]. There, it was observed that a critical $Q_{i,\mathrm{edge}}$ is needed for the L-I transition, which points again to the importance of the ion heat channel in the transition to an improved confinement regime and, $Q_{i,\mathrm{edge}}$, is also closely linked to E_r via the main ion diamagnetic pressure gradient term $(\nabla_r p_i)/(en_i)$. On the other hand, the L-I transition only shows a very weak dependence on B_ϕ, while the I-H transition exhibits an almost linear dependence on B_ϕ. In favourable drift configuration the almost linear dependence of P_{LH} on B_ϕ is related to a critical $v_{E\times B}$ shear observed at the L-H transition [74]. This supports the theory that a certain edge $E\times B$ shearing is needed for turbulence suppression and the access to H-mode. In turn, the absence of the B_ϕ dependence in the I-mode access would suggest that the $E\times B$ shearing mechanism is not a key element to the I-mode. This is also supported by edge E_r measurements from He II spectroscopy acquired in L-H and L-I-H transition experiments, which are presented in the following section.

7.2 Evolution of E_r in the Transition from L- to H-mode

7.2.1 Favourable Drift Configuration

Figure 7.2 shows the time evolution of global and edge plasma quantities during an L-H transition for a LSN plasma in favourable drift configuration (discharge # 36983). The discharge was density feed-back controlled to $\bar{n}_e \approx 3\times10^{19}\,\mathrm{m}^{-3}$. Except for this lower density, the design of the presented discharge # 36983 is similar to the reference discharge # 35842, which was introduced in Section 3.2. In particular, long and stable ECRH phases with a beam blip at the end of each phase for CXRS measurements were applied. The ECRH power was stepwise increased to trigger the L-H transition. The lower density makes that this discharge is already on the low-density branch of the n_e-P_{LH} diagram (see Figure 2.4). For this reason also the development of the L-H transition and of E_r are in some points different to the reference discharge, which is explained in the following.

The E_r profiles across the separatrix (Figure 7.2d) as well as the evolution of the E_r minimum (Figure 7.2c) were measured with the HES diagnostics. Further time traces, shown in Figure 7.2a, are the applied heating power P_{net}, $P_{\mathrm{ECRH}}, P_{\mathrm{NBI}}$ and the power radiated in the main chamber, $P_{\mathrm{rad,main}}$. The edge ion and electron temperatures, $T_{i,e,\mathrm{edge}}$, measured at $\rho_{\mathrm{pol}} \approx 0.95$, are shown in Figure 7.2b. It also depicts the measured mean electron core and edge densities, $\bar{n}_{e,\mathrm{core}}$ and $\bar{n}_{e,\mathrm{edge}}$, respectively and the stored plasma energy W_{MHD}. Signals monitoring the L-H transition, namely $\dot{B}_\theta$ measurements from Mirnov coils and shunt current measurements in the outer and inner lower divertor, $I_{\mathrm{SOL,a/i}}$, are plotted in Figure 7.2c.

The L-H transition occurs directly after the first beam blip, at 2.78 s, at a power of about $P_{\mathrm{LH}} = 1.1\,\mathrm{MW}$. Then the plasma develops only slowly into an ELM-y H-mode and signatures of I-phase and H-mode alternate throughout the discharge, with the first type-I ELM detected at about 3 s. This slow increase in confinement of the plasma can be seen in the weak and only gradual increase of density and W_{MHD}. $T_{e,\mathrm{edge}}$ shows a continuous, irregular variation which correlates with the alternation of the confinement regime and the overall trend is that both $T_{e,\mathrm{edge}}$, and $T_{i,\mathrm{edge}}$ increase from L- to H-mode.

In the entire L-mode phase the E_r profiles show little variation, with $E_{r,\mathrm{min}}$ values from -7 to $-10\,\mathrm{kV/m}$ in the confined region and $E_{r,\mathrm{max}}$ values from 3 to $6\,\mathrm{kV/m}$ in the SOL. In the I-phase and H-mode the outer E_r gradient, i.e. the gradient between E_r well and SOL, steepens and $E_{r,\mathrm{min}}$ decreases to $-16\,\mathrm{kV/m}$ with the first heating step and up to -20 to $-28\,\mathrm{kV/m}$ at a later stage. The latter are typical H-mode values at AUG [45]. It should be noted that the H-mode E_r profiles are are not ELM-synchronized since the ELM frequency is too high, but averaged values over the acquisition time of 2.45 ms. At the same time as $E_{r,\mathrm{min}}$ decreases $E_{r,\mathrm{max}}$ increases from an average of $4.5\,\mathrm{kV/m}$ in L-mode via $7\,\mathrm{kV/m}$ in I-phase to $10\,\mathrm{kV/m}$ in H-mode. Hereby, the position of $E_{r,\mathrm{max}}$ moves further outside into the SOL from $\rho_{\mathrm{pol}} \approx 1.0005$ in L-mode to $\rho_{\mathrm{pol}} \approx 1.005$ in H-mode, while the position of $E_{r,\mathrm{min}}$ remains relatively constant at around $\rho_{\mathrm{pol}} = 0.988$.

The same general features in the time evolution of E_r across the separatrix, and, in particular, of $E_{r,\mathrm{min}}$ during the L-H transition in favourable drift configuration are also found in USN plasmas.

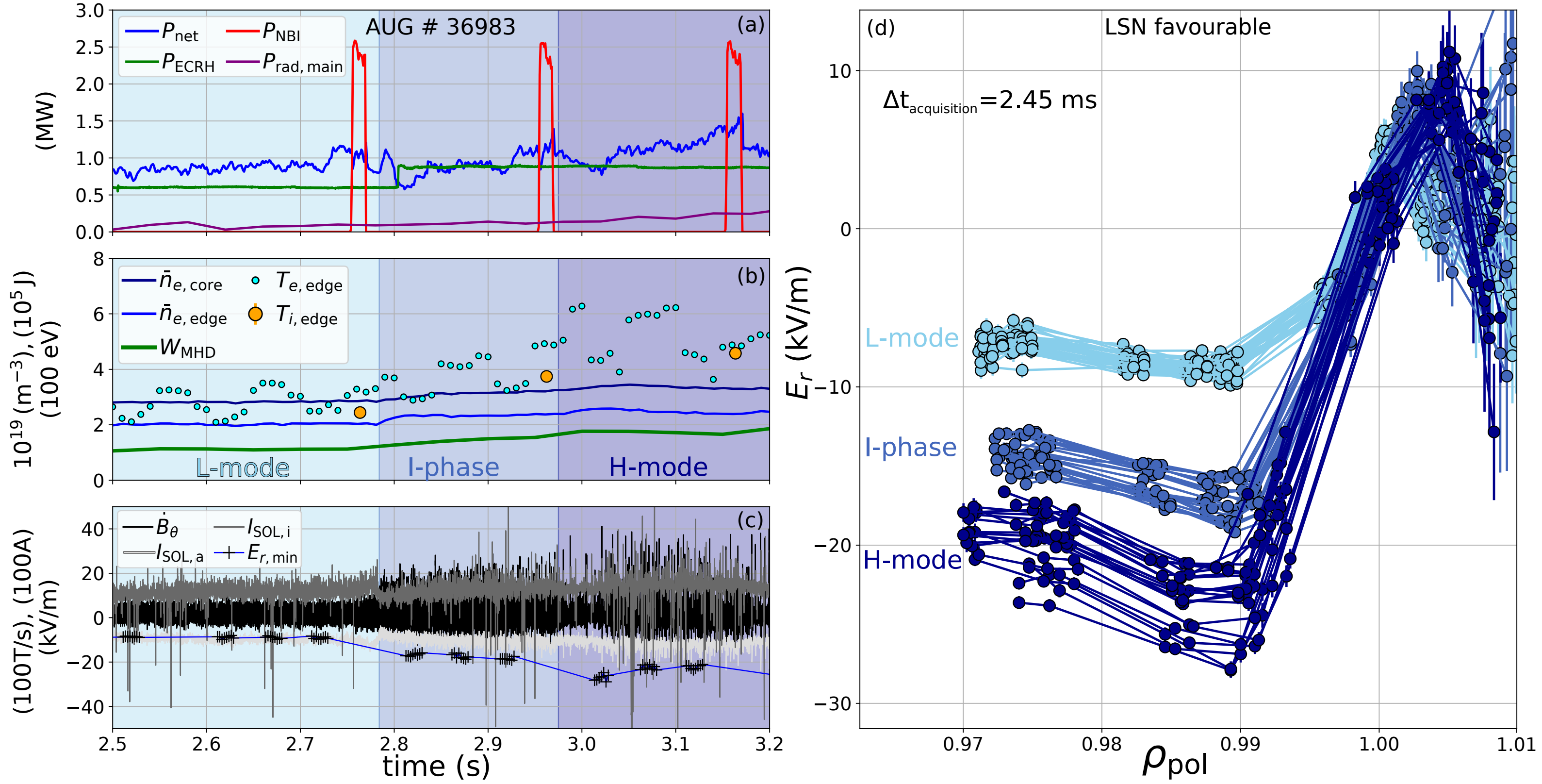

Figure 7.2: *L-H transition in favourable drift configuration with ECRH.* Time traces of important edge and global plasma quantities during the L-H transition (a-c) and edge E_r measurements by HES in the different confinement regimes (d). The time traces show that when the input power is increased (a) in discharge # 36983, the plasma enters the transient I-phase at 2.78 s (indicated by the divertor shunt current and Mirnov coil measurements (c)) and soon after H-mode. The edge temperatures and the density as well as the stored energy (b) rise, while at the same time $E_{r,\text{min}}$ decreases. The edge radial electric is constant during the complete L-mode phase and a steepening of the E_r gradient across the separatrix only starts when the plasma enters I-phase.

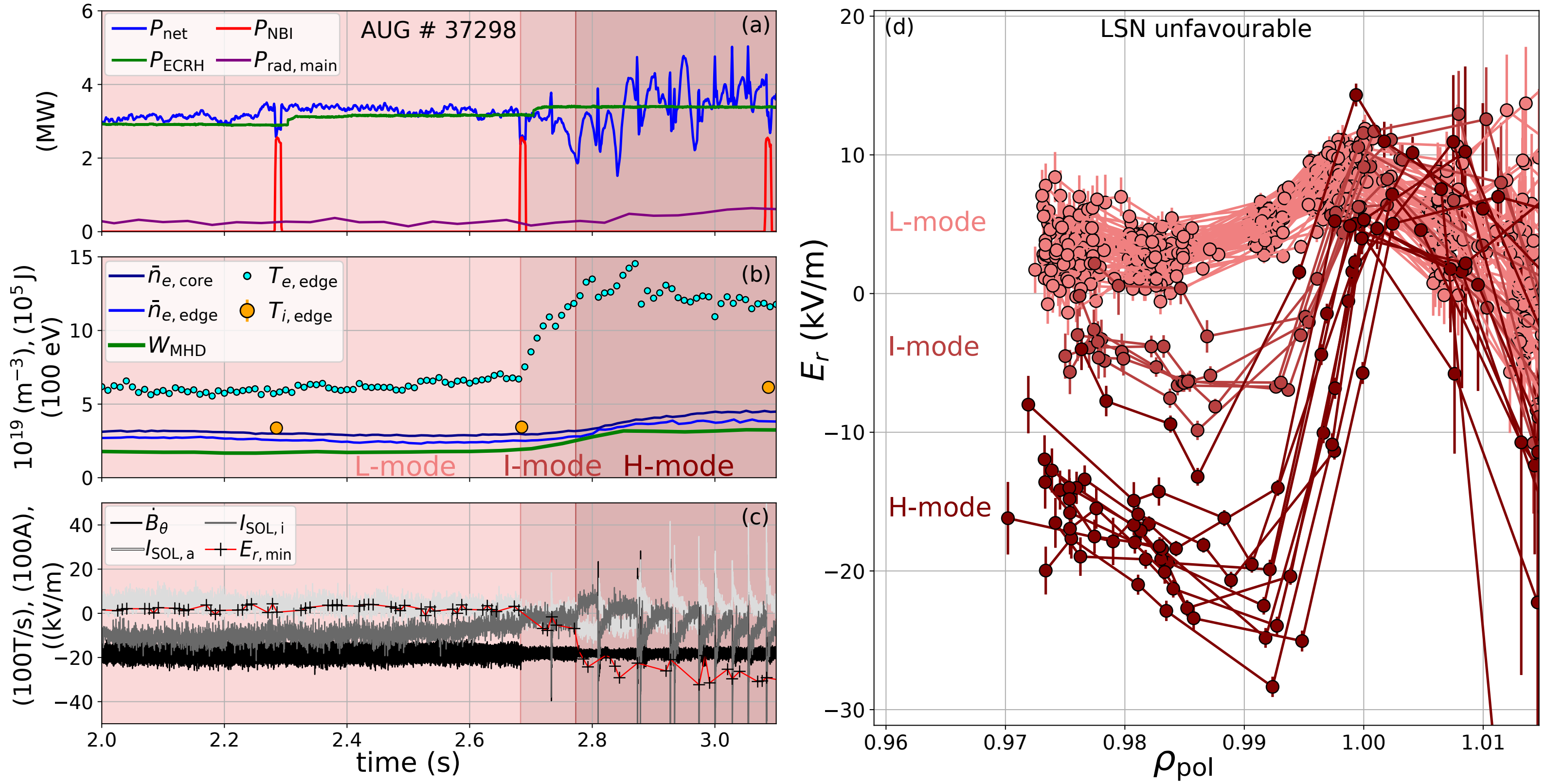

Figure 7.3: *L-I-H transition in unfavourable drift configuration with ECRH.* Time traces of important edge and global plasma quantities during the L-I-H transition (a-c) and edge E_r measurements by HES in the different confinement regimes (d). The time traces show that when the input power is increased (a) in discharge # 37298, the plasma enters I-mode at 2.68 s and H-mode at 2.77 s (also indicated by the divertor shunt current and Mirnov coil measurements (c)). While the edge temperatures increase already during I-mode, and, with this, also the stored energy (b), the electron density only starts to increase when H-mode is accessed. The edge radial electric (d) is constant during the complete L-mode phase and a steepening of the E_r gradient across the separatrix only starts when the plasma enters I-mode with a further increase in H-mode.

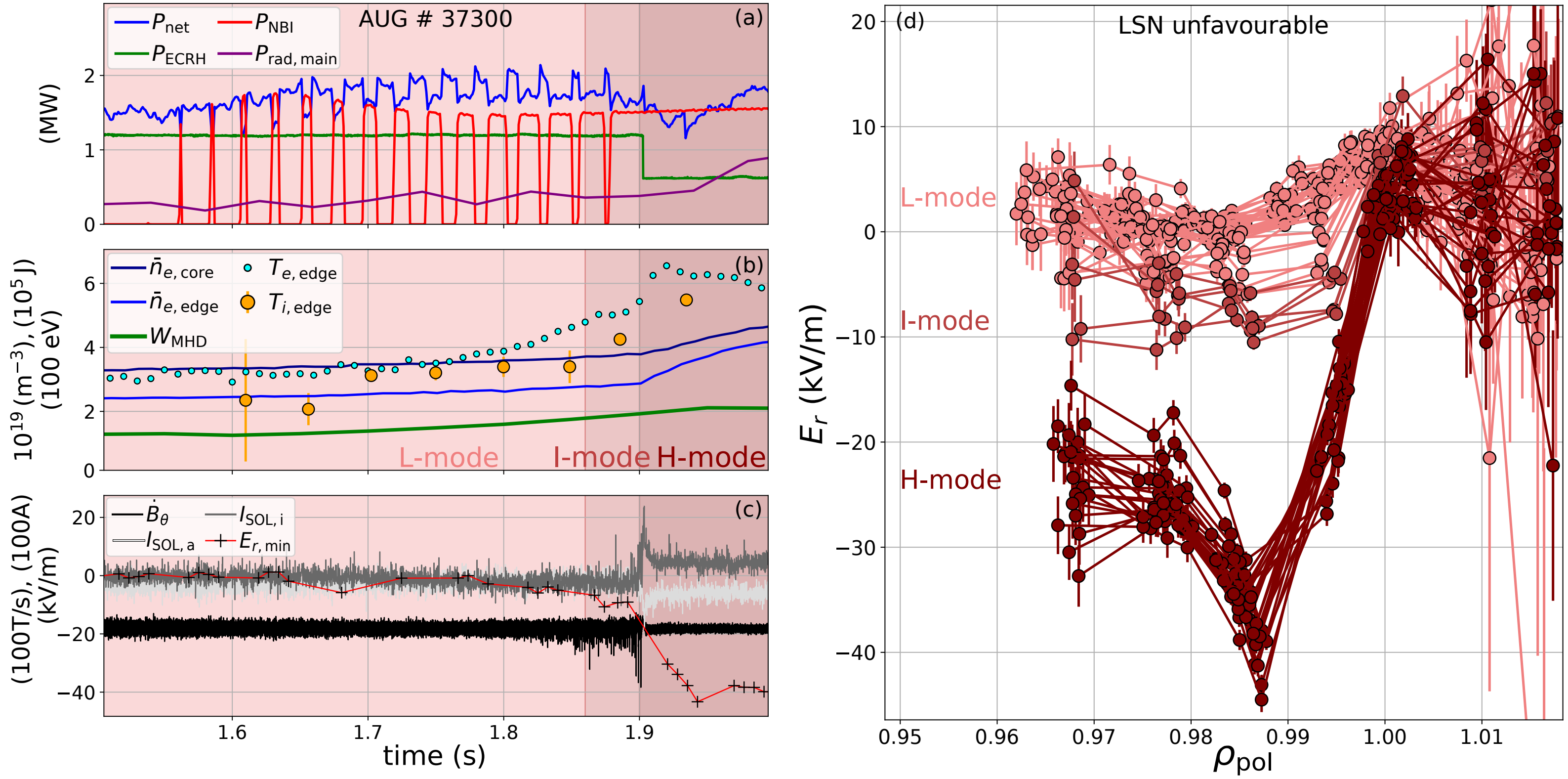

Figure 7.4: *L-I-H transition in unfavourable drift configuration with NBI.* Time traces of important edge and global plasma quantities during the L-I-H transition (a-c) and edge E_r measurements by HES in the different confinement regimes (d). The time traces show that with an input power of about 1.8 MW (a) the plasma enters I-mode in discharge # 37300 and H-mode at about 1.6 MW. As also indicated by the divertor shunt current and Mirnov coil measurements (c), while the transition from I- to H-mode is sharp, the one from L- to I-mode is rather smooth and, in the latter, the edge temperatures and the stored energy (b) increase steadily but faster during I-mode. The electron density (b) starts to increase strongly when H-mode is accessed. The edge radial electric and its gradient (d), as the other edge and global parameters, are weak, but constant in the beginning of the L-mode phase and then start to eventually develop, by a steepening of the E_r gradient, into I-mode, while in H-mode directly much stronger gradients are observed.

7.2.2 Unfavourable Drift Configuration

Figures 7.3 and 7.4 show two discharges with transitions from L-mode via I-mode to H-mode (L-I-H transition) in LSN unfavourable drift configuration. While discharge # 37298 is purely heated with ECRH, discharge # 37300 has a heating mix of ECRH and NBI. Except for this, the discharges have the same plasma parameters. Furthermore, discharge # 37298 is the equivalent in unfavourable drift configuration to the above shown discharge # 36983 in LSN favourable drift configuration.

In # 37298 (Figure 7.3) the I-mode starts at around 2.68 s and is soon after followed by the H-mode at around 2.77 s. For both transitions an input heating power of approximately 3 MW is needed, which is more than a factor of 2 higher than P_{LH} in favourable drift configuration for otherwise same plasma parameters (see Figure 7.1). Interestingly, P_{net} at the I-H transition tends to be lower compared to P_{net} at the L-I transition, which was already observed in earlier I-mode studies at AUG [53]. This can be attributed to a lower Ohmic power in the I-mode, due to improved energy confinement, and a stronger change of W_{MHD} at the L-I transition. Both terms contribute to P_{net} via Equation 2.50.

The HES measurements show that the $E_{r,\mathrm{min}}$ values of the L-mode are positive, between 0 and 5 kV/m, although these values are measured a bit too high by HES according to Section 6.2.1.2. A positive E_r in the confined plasma region hints to a substantial contribution of $v_i \times B$ to E_r, see Equation 2.34, since $(\nabla_r p_i)/(en_i)$ is always negative at the plasma edge. This observation will be discussed in more detail in Section 7.4.1. The outer E_r gradient is weak in L-mode and only starts to increase during I-mode. This observation is restricted to low density plasmas only. In high density plasmas ($\bar{n}_e$ above the density minimum of P_{LH}) a steepening of both the inner and the outer E_r gradient is observed already in L-mode. However, as presented later in Section 7.3.2, this steepening of the two E_r gradients is caused by an increase of E_r at the pedestal top, i.e. $\rho_{\mathrm{pol}} \approx 0.95$, and in the SOL ($E_{r,\mathrm{max}}$) and not by a decrease of $E_{r,\mathrm{min}}$. Only in I-mode $E_{r,\mathrm{min}}$ decreases until it reaches a value of approximately -10 kV/m. Then the transition to H-mode occurs. This $E_{r,\mathrm{min}}$ value is about the same as the L-mode values reached in favourable drift configuration at the L-H transition and hints to the importance of $v_{E\times B}$ for the access to H-mode in both drift configurations.

In H-mode the E_r profile develops strongly and $E_{r,\mathrm{min}}$ values of -15 to -25 kV/m are reached in this investigated time window of discharge # 37298. Interestingly, the SOL E_r values tend to get smaller in H-mode compared to L- and I-mode, which would not be expected from the estimate $E_{r,\mathrm{sol}} \approx \nabla_r T_{e,\mathrm{OMP}}/e$ (see Section 2.2.5). In fact $\nabla_r T_{e,\mathrm{OMP}}/e$ increases from L- to H-mode (not shown), whereas Langmuir probe measurements at the outer divertor show that the target profiles of $T_{e,\mathrm{tar}}$ and V_{sh} decrease (see Figure 7.5). Thus, E_r at the sheath entrance, which is $-\nabla_r V_{\mathrm{sh}}$, is smaller in H-mode compared to I- and L-mode. This, in sheath-limited SOL plasma regimes, corresponds to a lower E_r at the OMP [37] and would point to a transition from conduction-limited in L- to sheath-limited regime in H-mode in this discharge. However, this observation is again inconsistent with the SOL T_e measurements, which exhibit a strong decrease along the field lines from the OMP to the divertor target and suggest that the plasma is in the conduction-limited regime even in H-mode.

In the case of discharge # 37300 the development of E_r during the L-I-H transition is similar as for discharge # 37298, indicating that the applied heating has no direct impact on it. The main difference between the NBI and the ECRH heated discharges is that in

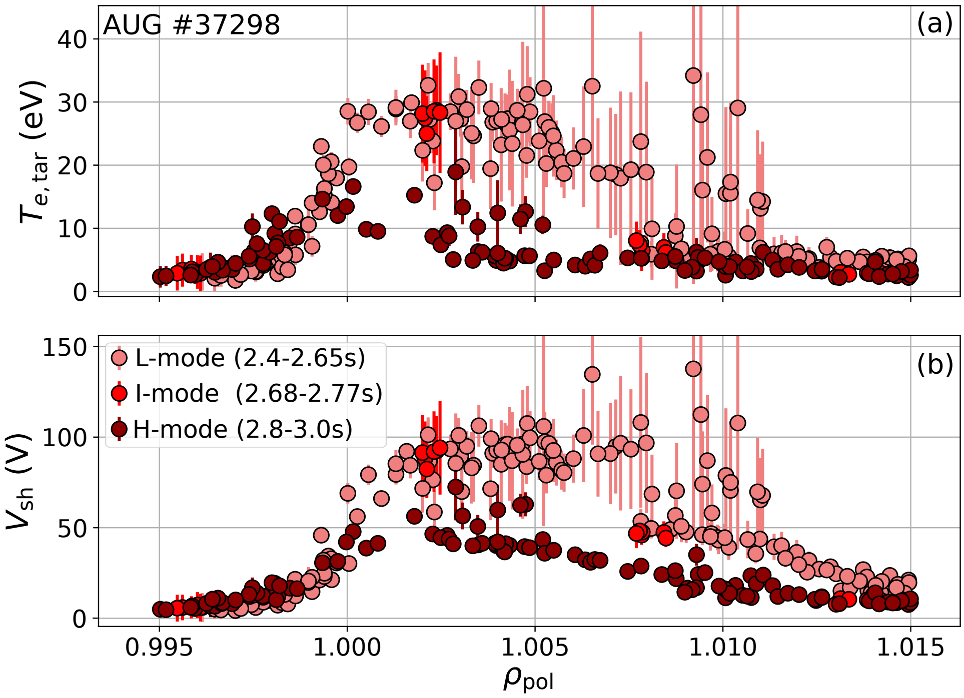

Figure 7.5: *Outer divertor target profiles during different confinement regimes.* Radial profiles of the electron temperature (a) and plasma potential at the sheath entrance (b) of the outer divertor. Both quantities as well as their respective radial gradients decrease from L- to I- to H-mode, indicating that also the SOL E_r at the sheath entrance decreases.

the first, # 37300 the L-I and I-H transitions already occurs at $P_{\mathrm{net}} = 1.8 - 2$ MW, which is more than 1 MW lower than for the ECRH heated discharge # 37298. This has been observed already in former I-mode studies and indicates an important role of the edge ion heat flux, $Q_{i,\mathrm{edge}}$, also in the transition from L- to I-mode [53]. As reported in [53], $Q_{i,\mathrm{edge}}$ and $T_{i,\mathrm{edge}}$ are the same at the L-I transition for both ECRH and NBI discharges. Due to the direct heating of the ions by NBI, it requires less power to be applied to the plasma to reach the same $Q_{i,\mathrm{edge}}$ and $T_{i,\mathrm{edge}}$ as for ECRH. In both discharges $T_{i,\mathrm{edge}} \approx 320$ eV and $Q_{i,\mathrm{edge}} = 0.9$ MW at the L-I transition, while for the discharge in favourable drift configuration both $T_{i,\mathrm{edge}}$ and $Q_{i,\mathrm{edge}}$ are lower at the L-H transition, with values of about 220 eV and $Q_{i,\mathrm{edge}} = 0.60$ MW, respectively.

Also in discharge # 37300 $E_{r,\mathrm{min}}$ is positive in L-mode and $E_{r,\mathrm{max}}$, which is located at the separatrix, is about 5-10 kV/m. In this discharge the I-mode itself and also the WCM develop smoothly when entering I-mode and a sharp transition between L- and I-mode can not be determined in a way as it can be done for the I-H transition. This has been observed for several other discharges with L-I-H transitions and is also reflected in the development of the E_r profiles. In the presented discharge $E_{r,\mathrm{min}}$ starts to decrease at 1.85 s until it again reaches values of about -10 kV/m. Then the plasma enters H-mode at 1.91 s and the $E_{r,\mathrm{min}}$ values decrease concurrently down to $-30 - -45$ kV/m. At the same time $n_{e,\mathrm{edge}}$ and $T_{i,\mathrm{edge}}$ increase. The $E_{r,\mathrm{max}}$ values in the SOL reduce slightly during H-mode, which could, in this case, also be related to a reduction of ECRH, which occurs almost at the same time as the I-H transition.

Corresponding observations in the evolution of E_r in unfavourable drift configuration are also made in USN plasmas.

7.3 Comparison of L-modes in Different Drift Configurations

7.3.1 LSN Plasmas

In this section, L-mode phases of several discharges, # 36983, 37375, 37298, 35753 and 35758, in favourable and unfavourable drift configuration are compared. All the discharges have similar parameters, namely $|I_\mathrm{p}| = 800\,\mathrm{kA}$, $|B_\phi| = 2.5\,\mathrm{T}$ at the magnetic axis, $q_{95} = -5$ and are heated with ECRH only (except for beam blips needed for the CXRS measurements). First the discharges and general observations about their performance are described.

7.3.1.1 Discharges

As shown in Figure 7.2, in the favourable drift configuration discharge # 36983 the plasma enters H-mode after a beam blip at $t_\mathrm{LH} = 2.78\,\mathrm{s}$ with $P_\mathrm{LH} = 1.1\,\mathrm{MW}$ and an edge ion heat flux of $Q_{i,\mathrm{edge}} = 0.60\,\mathrm{MW}$. These values are typical for AUG in D plasmas with $\bar{n}_e = 3.0 \times 10^{19}\,\mathrm{m}^{-3}$ [58, 73].

The two discharges # 37375 (see Figure 7.6) and # 37298 (see Figure 7.3) in unfavourable drift configuration were performed for a comparison with discharge # 36983. Although for the two discharges an identical D gas puff rate of 0.7×10^{21} el/s was used, # 37375 had a lower density of $\bar{n}_e = 2.35 \times 10^{19}\,\mathrm{m}^{-3}$ compared to # 37298 with $\bar{n}_e = 3.0 \times 10^{19}\,\mathrm{m}^{-3}$ (see figures 7.6 and 7.3). The reasons for this different behaviour are unclear, but various factors can have an impact on the plasma fuelling efficiency, like wall conditioning (# 37298 was performed after boronisation, # 37375 not) or gas fuelling [150]. The lower density and, hence, a reduced heat transfer from electrons to ions, p_{ei}, causes that # 37375 does not reach the critical $Q_{i,\mathrm{edge}}$ of 0.7 MW, which is needed to enter I-mode and, subsequently, H-mode [53]. For this reason, # 37375 with its low density stays in L-mode throughout, although the ECRH power, P_ECRH, is increased to 4 MW. Power balance calculations for this discharge have shown that $Q_{i,\mathrm{edge}}$ saturates at 0.59 MW, because p_{ei} saturates with increasing T_e according to Equation 3.6. In # 37298 the transition from L- to I-mode occurs at 2.682 s and soon after, at 2.773 s, the transition from I- to H-mode, with $P_\mathrm{LI} = 3.0\,\mathrm{MW}$ and $Q_{i,\mathrm{edge}} = 0.91\,\mathrm{MW}$ (see also Figure 7.3). These values of P_LH and $Q_{i,\mathrm{edge}}$ are, again, in agreement with former observed values for the L-I transition on AUG [53].

A second pair of discharges with ECRH power ramps in unfavourable drift configuration, # 35753 and 35758, was performed to study the evolution of E_r and the path to the L-I-H transition at different densities. The nominal densities were $\bar{n}_e = 2.5$, 4.0 and $6.0 \times 10^{19}\,\mathrm{m}^{-3}$, which spans the densities from the low-density branch through $\bar{n}_{e,\mathrm{min}}$ and into high-density branch of P_LH (see Figure 7.1). As for the other low density discharges described before, neither I- nor H-mode was reached at $\bar{n}_e = 2.5 \times 10^{19}\,\mathrm{m}^{-3}$, although the ECRH power was raised to 4.0 MW. This can be attributed again to a low p_{ei} at this low density, but additionally also the radiated power increased almost linearly with the input power in the low density part of discharge # 35753.

At the two higher densities the main chamber radiation was lower and did not increase with the input power in L-mode. At medium density the plasma enters an improved

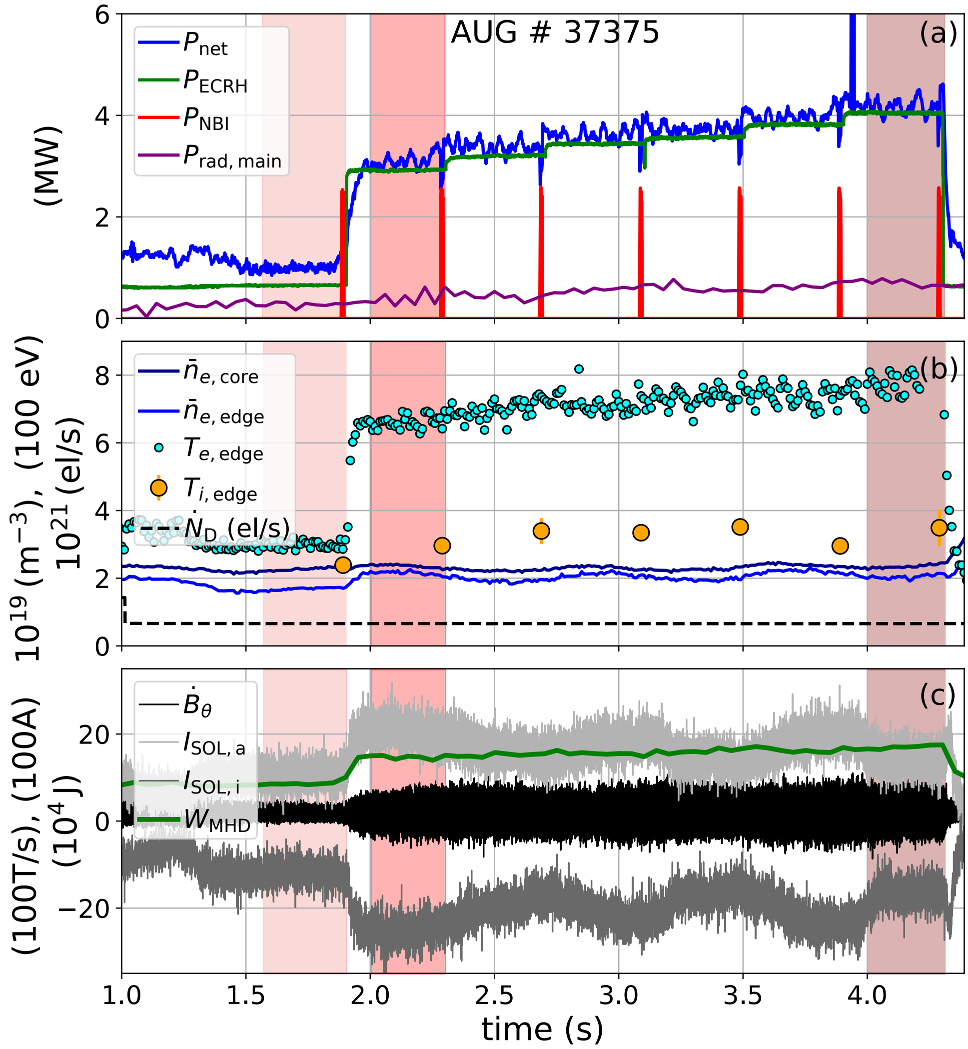

Figure 7.6: *Time evolution of a low density, ECRH heated discharge in unfavourable drift configuration.* (a) Input power and radiated power. (e) Averaged core and edge electron density, edge electron and ion temperature, measured at $\rho_{\mathrm{pol}} = 0.95$ and deuterium gas puff rate. (c) Plasma stored energy, inner and outer divertor shunt current measurements and poloidal magnetic field measurements from the Mirnov coil located at the lower divertor. The time traces indicate that the plasma stays in L-mode throughout the discharge, although an ECRH power of up to 4.0 MW was applied. The time windows shaded in red are used in the following for comparisons of L-mode plasmas in favourable and unfavourable drift configuration.

confinement regime at a net input power $P_{\mathrm{net}} \approx 3.3\,\mathrm{MW}$. However, this improved confinement regime does not have the signatures of an I-mode, like the WCM or a sole rise of temperature, but rather the signatures of an I-phase, with a small concomitant increase of the edge electron density. As described in Section 3.3, the I-phase is a transient phase of improved confinement between L- and H-mode and is normally found in favourable drift configuration. In the last couple of years, however, a few examples of I-phases in unfavourable drift configuration have been observed, besides the ones described here, e.g. in an USN plasma or in a He plasma [122,151]. At high density there are again signs of an I-phase visible, when the plasma enters H-mode at $P_{\mathrm{LH}} \approx 3.8\,\mathrm{MW}$. I-phase occurrences at L-H transitions in unfavourable drift configuration are also marked in Figure 7.1.

First, edge kinetic and E_r profiles of different time windows of discharge # 37375, marked in red shades in Figure 7.6, will be compared to corresponding L-mode phases of # 36983 and 37298.

7.3.1.2 Same Heating Power and Same Plasma Density

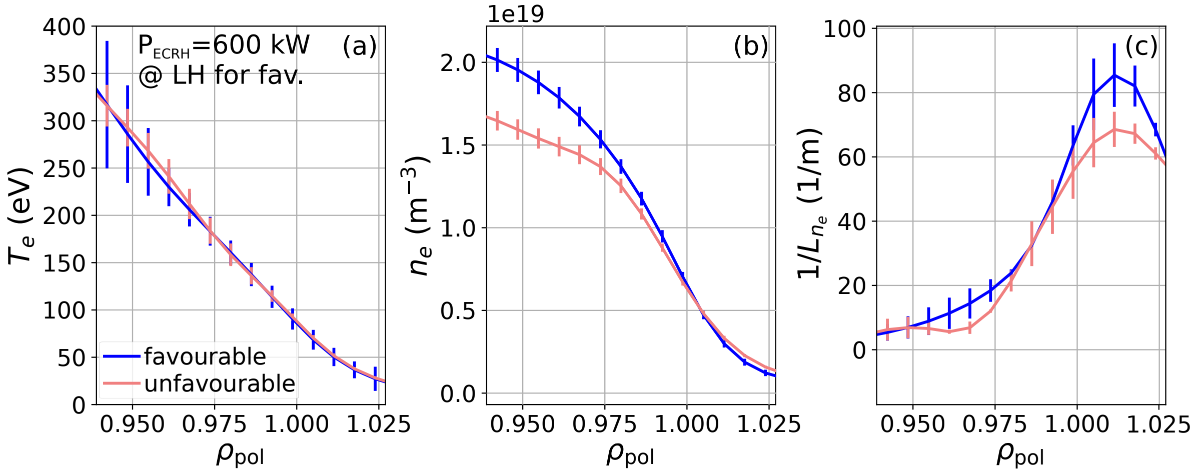

Figure 7.7: *L-mode electron profiles in LSN favourable and unfavourable drift configuration at same ECRH power and comparable plasma density.* (a) Electron temperature, (b) electron density and (c) normalized electron density gradient. All three electron profiles are in good agreement at the region around the separatrix, with only slight lower values of n_e and $1/L_{n_e}$ in unfavourable drift configuration.

Edge Kinetic and E_r Profiles Figures 7.7a and 7.7b show electron temperature and density profiles, T_e and n_e, from the very edge of the confined plasma to the near SOL. The profiles are averaged from 1.60-1.90 s for discharge # 37375 (unfavourable) and from 2.70-2.77 s for discharge # 36983 (favourable). For the latter this is the last L-mode phase before the L-H transition. During these two time windows 600 kW of ECRH were applied and the plasma was fuelled with a D gas puff rate of 0.7×10^{21} el/s.

Care was taken in the alignment of the profiles, following the approach described in Section 3.4.2, by using the two-point model which gives $T_{e,\mathrm{sep}} = 78\,\mathrm{eV}$ at the separatrix, independent of the drift configuration. The T_e and n_e profiles generated with IDA also contain the He I beam data (see Section 3.1.1) and the equilibrium was reconstructed using IDE (see Section 3.1.5). Despite this, there is still a radial uncertainty of 3 to 4 mm remaining in the exact positioning of the n_e profile in favourable drift configuration, as will be shown later in this section.

The comparison of the two discharges shows that at the same heating power the edge T_e profiles are the same in favourable and unfavourable drift configuration. Also the edge n_e profiles are in good agreement, but, as mentioned in the description of the discharges, the density in unfavourable drift configuration is slightly lower. For this reason the normalized edge density gradient $1/L_{n_e} := -(\nabla_r n_e)/n_e$ is calculated, which is plotted in Figure 7.7c. The comparison shows that the maximal edge density gradient is lower in unfavourable than in favourable drift configuration. However, $\max(1/L_{n_e})$ is already located outside the separatrix, at $\rho_{\mathrm{pol}} \approx 1.01$. In the confined region $1/L_{n_e}$ is nearly the same for both drift configurations, although there is a tendency of a slightly higher $1/L_{n_e}$

in the favourable drift configuration. It should be also mentioned that this quantity enters in the determination of E_r, in the case $n_e = n_i$ (see Equation 2.32).

If the paradigm of a critical $v_{E\times B}$ shear flow needed to enter H-mode held (see Section 2.4.1.1), then a reduced $1/L_{n_e}$ at the same heating power in unfavourable drift configuration compared to favourable drift configuration could explain the observation of an increased P_{LH}: More heating power would be needed to set the same L-mode edge E_r gradient, since the lower $1/L_{n_e}$ has to be balanced by an increased ion temperature gradient, $-1/L_{T_i}$. Such a mechanism had been found to be responsible for the reduction of P_{LH} when switching from carbon to tungsten as first wall material [55, 152]. However, the only small differences in $1/L_{n_e}$ at the same heating power between the two drift configurations can not explain the by a factor of 2 increased P_{LH} in unfavourable drift configuration, especially since also the edge T_i gradients are comparable at the same heating power between the two drift configurations (see Figure 7.8a).

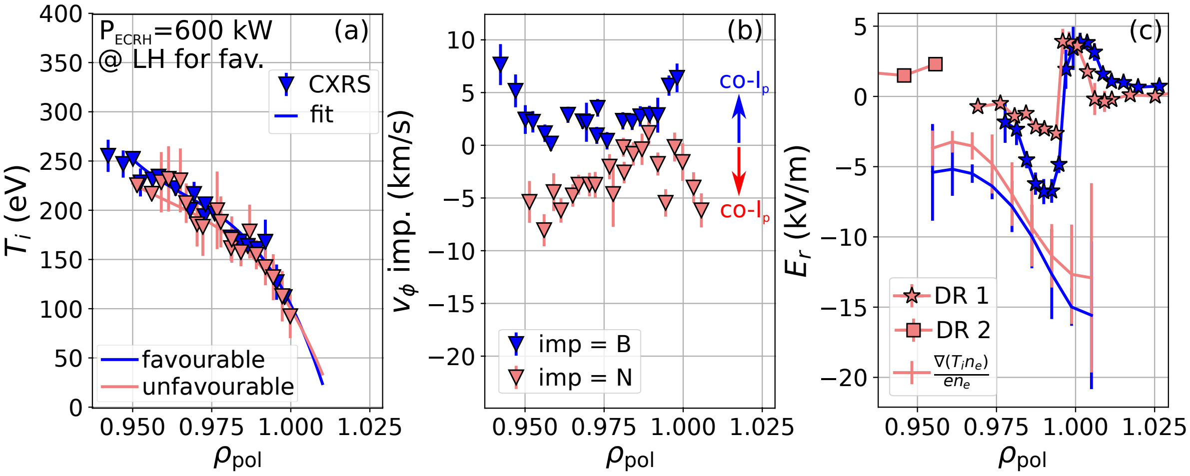

Figure 7.8: *L-mode ion and E_r profiles in LSN favourable and unfavourable drift configuration at same heating power and comparable plasma density.* (a) Edge ion temperature, (b) impurity ion toroidal rotation and (c) measured radial electric field across the separatrix together with a proxy of the main ion pressure gradient, assuming $n_i = n_e$. The ion temperatures and their gradients (not shown) are, within the error bars, the same for both drift configurations. The impurity rotations are mirror-inverted, but in both cases directed co-current. The experimental E_r profiles deviate from each other mainly in the confined region, where $E_{r,\mathrm{min}}$ in favourable configuration is lower than in unfavourable drift configuration. Both E_r profiles do not agree with the main ion pressure gradient term in the confined plasma, suggesting that other contributions to E_r are also important.

The edge ion temperature profile, T_i, measured by CXRS during a beam blip of 12 ms length is shown for both drift configurations in Figure 7.8a. Within the measurement uncertainties the T_i profiles in favourable and unfavourable drift configuration agree. No radial shift was applied to the T_i data and for the mapping to the OMP the IDE equilibria were used. The experimental data were fit with cubic splines. As usually observed, the edge T_i profiles are flatter than the edge T_e profiles, as at $\rho_{\mathrm{pol}} = 0.95$, $T_{i,95} \approx 230 - 250\,\mathrm{eV}$ $= 0.80 - 0.90\,T_{e,95}$ and $T_{i,\mathrm{sep}} \approx 100\,\mathrm{eV} = 1.3\,T_{e,\mathrm{sep}}$ at the separatrix. These ratios are found for both drift configurations.

Figure 7.8b shows the impurity intrinsic toroidal rotation at the plasma edge measured by CXRS ($v_{\phi,\mathrm{imp}}$) for favourable and unfavourable drift configuration. The same radial alignment as for the T_i profiles was applied. As expected from neoclassical theory, Section 2.2.4, $v_{\phi,\mathrm{imp}}$ changes sign with B_ϕ and is positive in favourable and negative in unfavourable drift configuration. However, this means that for both configurations the intrinsic edge plasma rotation is co-current, since also I_p is reversed. The $v_{\phi,\mathrm{imp}}$ profiles are in both cases relatively flat and exhibit values of about 5 km/s (favourable) and −5 km/s (unfavourable) at $\rho_\mathrm{pol} = 0.95$. Further outward the values decrease for favourable increase for unfavourable drift configuration to about 0 km/s and then they increase for favourable and decrease for unfavourable again towards the separatrix to $v_{\phi,\mathrm{imp}} \approx 6\,\mathrm{km/s}$ in the favourable and to about −2 km/s in the unfavourable drift configuration. In detail the $v_{\phi,\mathrm{imp}}$ profiles deviate from each other, with the dip (hill) in $v_{\phi,\mathrm{imp}}$ being broader (narrower) in favourable (unfavourable) drift configuration. However, the scatter of the experimental data points is considerable, which could lead to an artificial structure in the profiles.

The deviation in the absolute values of $v_{\phi,\mathrm{imp}}$ between the two different drift configurations may be influenced by the fact that in favourable drift configuration the investigated impurity was boron (B) and in unfavourable drift configuration it was nitrogen (N), which can lead to slightly different rotation velocities at the plasma edge ($\approx 2\,\mathrm{km/s}$,) even if the main ion rotation is the same. Even though the effect of beam torque is minimized by the short duration of the beam blip, a small effect due to the non-zero torque of the beam cannot be excluded even more as the toroidal rotation was not time-resolved during the beam blip [153] and in favourable drift configuration the torque input is co-current, whereas it is counter-current in unfavourable drift configuration.

Taken together, the differences in the impurity toroidal edge rotation between the two drift configurations are, except for the sign, small and in both cases its contribution to E_r would be, according to Equation 2.32, positive and at most 2 kV/m.

In Figure 7.8c the E_r profiles as measured by DR are presented for the corresponding time intervals and drift configurations. The E_r profiles differ from each other, with the E_r profile in unfavourable drift configuration (lightred) being more positive than the one in unfavourable drift configuration blue) in the confined region. In the favourable drift configuration an $E_{r,\mathrm{min}}$ value of about −6.8 kV/m is reached at $\rho_\mathrm{pol} = 0.99$. The $E_{r,\mathrm{max}}$ value of 3.9 kV/m is found just outside the separatrix at $\rho_\mathrm{pol} = 1.001$ and then E_r decreases to 1.3 kV/m at $\rho_\mathrm{pol} = 1.01$. For the E_r profile in unfavourable drift configuration only an $E_{r,\mathrm{min}}$ of about −2.7 kV/m is reached at $\rho_\mathrm{pol} = 0.994$, while the $E_{r,\mathrm{max}}$ value of 4.0 kV/m is already reached inside the separatrix at $\rho_\mathrm{pol} = 0.996$. Then in the SOL E_r also decays faster to 0 kV/m at already $\rho_\mathrm{pol} = 1.006$.

According to the measurement the outer E_r gradient, i.e. the one connecting the confined plasma with the SOL, is of the same strength in both drift configurations, namely $(\mathrm{d}E_r/\mathrm{d}R)_\mathrm{max} = 2 - 2.5\,\mathrm{MV/m^2}$. Furthermore, it seems to be located at the same radial position, although this radial localization depends critically on the used n_e profiles which themselves have radial uncertainties. This is discussed in more detail below. The inner E_r gradient differs between the two cases and is shallower for the unfavourable compared to the favourable drift configuration.

Figure 7.8c also includes an approximation of the ion diamagnetic term, $(\nabla_r p_i)/(en_e)$, for which it is assumed that $n_i = n_e$. This term would give a minimal value of −15 kV/m for the favourable and −13 kV/m for the unfavourable drift configuration, where the differences between the two profiles originate mainly from the different n_e profiles (see Figure 7.7b,c). Within the uncertainties, however, the $(\nabla_r p_i)/(en_e)$ terms agree for the two drift configurations. It is found that $\min((\nabla_r p_i)/(en_e)) \approx 2\,E_{r,\min}$ in both drift configurations. This suggests that besides the $(\nabla_r p_i)/(en_e)$ term also the contribution of $v_i \times B$ becomes important to E_r (see Equation 2.34). This will be discussed in more detail in Section 7.4. Furthermore, the comparison shows that the radial position of the $(\nabla_r p_i)/(en_e)$ minimum is reached at or outside the separatrix, which is also not in line with the experimental E_r measurements, where the $E_{r,\min}$ position is found to be close to, but inside the separatrix.

The minimum of the $(\nabla_r p_i)/(en_e)$ terms would only be positioned inside the separatrix if the n_e profiles were shifted further inside. This, however, would cause that also the E_r profiles measured by DR would need to be shifted inwards by nearly the same amount, since the DR measurement position depends almost linearly on the n_e profile position [154]. It was, however, found for the discharge in favourable drift configuration that, depending on the diagnostics used for the T_e and n_e profiles, the n_e gradient across the separatrix can be different. This translates into a radial shift of the DR E_r profile as shown in Figure 7.9, which is discussed in the following.

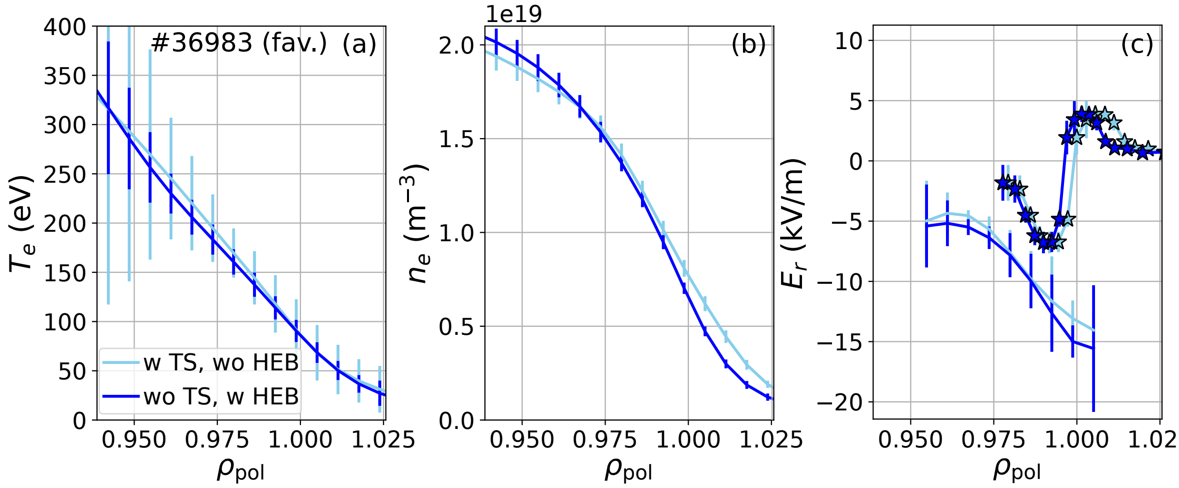

Figure 7.9: *Comparison of edge electron and E_r profiles in LSN favourable drift configuration.* (a) Edge electron temperature and (b) edge electron density profiles, created by integrated data analysis of either ECE, Li I beam and He I beam data (dark blue) or ECE, Li I beam and Thomson scattering data (light blue). (c) Resulting edge E_r profiles by DR employing the respective n_e profiles. The temperature profiles are in excellent agreement, whereas the density profiles deviate from each other at $\rho_{\rm pol} < 0.95$ and $\rho_{\rm pol} > 0.99$. This leads to an apparent radial shift in the DR E_r profiles of about 4 mm at the separatrix.

Discussion of Radial Uncertainties The dark blue profiles in Figure 7.9 show the IDA edge T_e and n_e profile and the DR E_r profiles, which were presented before in Figure 7.7a,b and Figure 7.8c. The IDA profiles employ besides ECE and lithium-beam also data from the He I beam, whereas the profiles in lightblue use Thomson scattering data instead of HEB data. The T_e profiles are almost identical, but the n_e gradient of the n_e profile using TS data is lower. This leads to an apparent outward-shift of the E_r profile by about 4 mm. Thus, the zero-crossing of the light-blue E_r profile is almost located at the separatrix. The difference to $(\nabla_r p_i)/(en_e)$ is as described above and not resolved.

It is unclear which of the two resulting n_e profiles and, thus, E_r profiles is the correct one, but the DR E_r profile employing the n_e profile with TS data was also used for the comparison with the HES diagnostics (see Figure 6.2). Only with this DR E_r profile the HES E_r profile could be reproduced by the synthetic diagnostic without applying a radial shift to the experimental HES data. If the DR E_r profile with HEB n_e data were used, the HES E_r profile would have needed to be shifted inwards.

In order to reduce the uncertainties in the radial alignment of the different profiles, it is planned for the near future to combine the HES and HEB diagnostics, so that T_e, n_e and E_r can be measured simultaneously on the same lines of sight.

In Figure 7.10a the n_e profile employing TS data is shown in comparison with the L-mode edge n_e profile in unfavourable drift configuration from discharge # 37375. For the unfavourable drift configuration the same n_e profile as already presented in Figure 7.7b is shown, since for this discharge both the edge T_e and n_e profiles agree using either TS or HEB data.

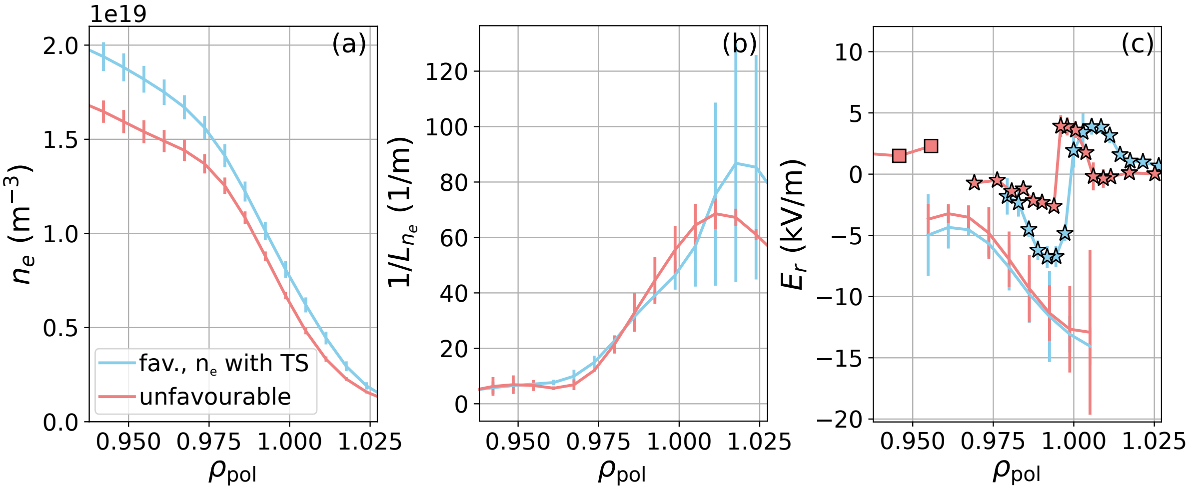

Figure 7.10: *L-mode electron and E_r profiles in LSN favourable and unfavourable drift configuration using electron TS data.* Radial electron edge density profiles (a) and their normalized edge density gradients (b). (c) Main ion pressure gradient term and DR E_r profiles using the respective n_e profiles. Using the n_e profiles with TS data, n_e deviates more in the two drift configurations, with n_e being higher in favourable drift configuration. In contrast, the $1/L_{n_e}$ and the $(\nabla_r p_i)/(en_e)$ profiles agree better between the two drift configurations than for the profiles employing HEB data (see Figure 7.7). For the E_r profiles bigger deviations between the two drift configurations in the SOL are observed, where E_r is higher in the entire near SOL in favourable drift configuration and also decays slower.

Comparing these two n_e profiles one would conclude that the edge n_e data in unfavourable and favourable drift configuration still do not agree. The n_e profile in favourable drift configuration is higher than the one in unfavourable drift configuration over the complete radial range from $\rho_{\mathrm{pol}} = 0.94$ to 1.025. However, the $1/L_{n_e}$ profiles, shown in Figure 7.10b, and the $(\nabla_r p_i)/(en_e)$ term[1], shown in 7.10c, are now in even better agreement between the two different drift configurations.

Using the n_e profile with the flatter gradient for the reconstruction of the E_r profile in favourable drift configuration leads to a stronger deviation from the E_r profile in unfavourable drift configuration. The radial position of $E_{r,\mathrm{min}}$ is now for both configurations

---

[1] For its calculation the same T_i profiles as shown in Figure 7.8a were used.

at $\rho_{\mathrm{pol}} = 0.994$, but$E_{r,\mathrm{max}}$ in favourable drift configuration is only reached in the SOL at $\rho_{\mathrm{pol}} = 1.004$. As a consequence the SOL-E_r is larger for favourable drift configuration than for unfavourable drift configuration, which would be in accordance to SOL modelling predictions. On the other hand, the E_r gradient across the separatrix does not change strongly and is still about $(\mathrm{d}E_r/\mathrm{d}R)_{\mathrm{max}} = 2 - 2.5\,\mathrm{MV/m^2}$.

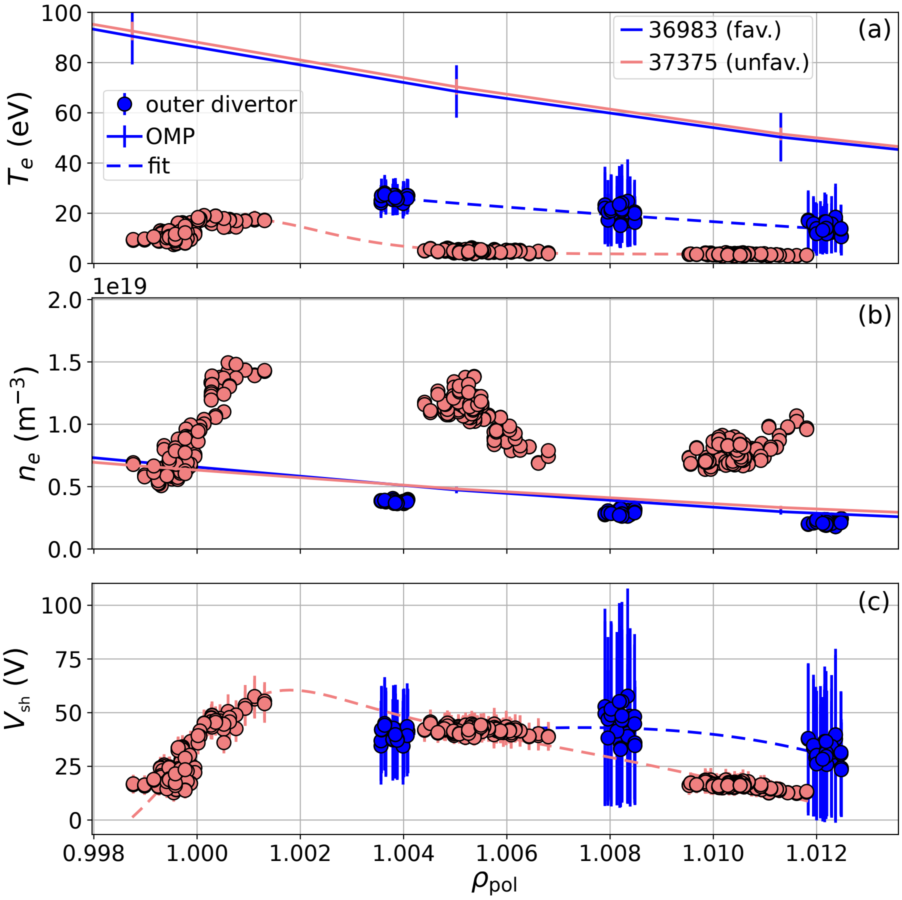

Figure 7.11: *Outer divertor target profiles in LSN favourable and unfavourable drift configuration L-modes.* (a) Electron temperature, (b) electron density and (c) sheath potential. Due to the reversal of the drift directions in the SOL, T_e is lower and n_e is higher in unfavourable drift configuration compared to favourable drift configuration. Comparison of the target with the upstream T_e and n_e profiles (also shown in (a) and (b)) indicates that in both drift configurations the plasma is in the high recycling (conduction-limited) regime. The sheath potential is strongly different between the two drift configurations, which would also lead to different E_r profiles at the sheath entrance.

Divertor Profiles Figure 7.11a and 7.11b show target-T_e and n_e profiles of the outer divertor in favourable (blue) and unfavourable (lightred) drift configuration. The profiles were measured with Langmuir probes (LPs). Also shown in the figure are the respective T_e and n_e profiles at the outer mid-plane (OMP), which were already presented in Figure 7.7. The strong reduction of T_e along the field lines with a concomitant increase of n_e towards the divertor target indicates that the SOL plasma is in the so-called conduction-limited or high recycling regime. This, in turn, implies that the two-point model is valid and can be applied for the determination of the separatrix temperature at the OMP [37].

As expected from the reversal of the magnetic field, and, thus, the drift directions [37,155,156], the particle transport towards the outer divertor is increased in unfavourable drift configuration compared to favourable drift configuration. Consequently, $T_{e,\text{target}}$ is lower in unfavourable compared to favourable drift configuration. In favourable drift configuration, $T_{e,\text{OMP}} \approx 3T_{e,\text{target}}$ and $\nabla_r T_{e,\text{OMP}} \approx 3\nabla_r T_{e,\text{target}}$, while in unfavourable drift configuration $T_{e,\text{OMP}} > 3T_{e,\text{target}}$, but $\nabla_r T_{e,\text{OMP}} < 3\nabla_r T_{e,\text{target}}$. In unfavourable drift configuration, where the target profiles are fully resolved, $T_{e,\text{target}}$ peaks at the separatrix, while the maximum value of n_e is reached a bit further outside in the SOL, at about $\rho_{\text{pol}} = 1.001$. This is observed regularly and also theoretically predicted due to diffusive processes and the field line geometry [37].

The plasma potential at the sheath entrance, V_{sh}, reconstructed from the LP measurements according to Equation 2.46 is shown in Figure 7.11c. Although the absolute values are similar in both drift configurations, with V_{sh} between 0 and 60 eV, the profile shapes differ strongly. While in unfavourable drift configuration the peak of V_{sh} is narrow and occurs close to the separatrix, at around $\rho_{\text{pol}} = 1.002$, in favourable drift configuration the peak is broader and exhibits its maximum at $\rho_{\text{pol}} \approx 1.007$.

It should be noted that in discharge # 36983 no strike point sweeps (see Section 3.1.4) were programmed, thus, the divertor profiles are incomplete. However, a comparison of # 36983 with discharges of similar overall plasma parameters (n_e, I_{p} and P_{ECRH}) and strike point sweeps has shown that $T_{e,\text{target}}$ does not exceed 30 eV and that the maximum value of V_{sh} is indeed reached at around $\rho_{\text{pol}} = 1.007$.

The $T_{e,\text{target}}$ and V_{sh} profiles were fit with cubic splines or, if possible, with a combination of an exponential decay and the error function, which is also commonly used to fit the divertor heat flux profiles [157]. Two estimates of the SOL E_r at the OMP were calculated and are shown in Figure 7.12 together with the measured DR E_r profiles which were already presented in Figure 7.8. For the first estimate it is assumed that $E_r = -\nabla_r V_{\text{sh}}$, i.e. the plasma potential at the outer mid-plane equals the plasma potential at the sheath entrance, V_{sh}. This equality normally holds for SOL plasmas in the sheath-limited regime. The second estimate is $E_r = -\nabla_r T_{e,\text{OMP}}$, which is true if the SOL plasma is in the conduction-limited regime.

The E_r profiles reconstructed from V_{sh} neither agree amongst each other for the two drift configurations nor with the measured DR E_r profiles. In favourable drift configuration $-\nabla_r V_{\text{sh}}$ is negative and increases to positive values with increasing ρ_{pol}, while the actual E_r profile is positive and decreases with higher ρ_{pol}. In unfavourable drift configuration $-\nabla_r V_{\text{sh}}$ is higher than 5 kV/m from $\rho_{\text{pol}} = 1.002$ and, thus, larger than the actual E_r. Further inside, towards the separatrix, $-\nabla_r V_{\text{sh}}$ exhibits a strong negative gradient and reaches values of −33 kV/m at the separatrix. This strong change of $-\nabla_r V_{\text{sh}}$ is due to the peaking of the plasma potential, not at, but slightly outside the separatrix (see Figure 7.11c). As mentioned before, due to different effects some target quantities peak not directly at the separatrix, but further outside [37]. Therefore, a negative radial shift of V_{sh} to lower ρ_{pol} values is not justified.

In contrast, $-\nabla_r T_{e,\text{OMP}}$ is the same for both drift configurations and it agrees very well with the experimentally determined E_r at the separatrix. The decay of the experimental E_r in the SOL is in both cases faster than the decay of $-\nabla_r T_{e,\text{OMP}}$ and the two profiles only start to agree again at $\rho_{\text{pol}} \approx 1.025$. It should be noted that the theoretical prediction of E_r $-\nabla_r T_{e,\text{OMP}}$ is only valid in the SOL, but for a better comparison with $E_{r,\text{max}}$, which

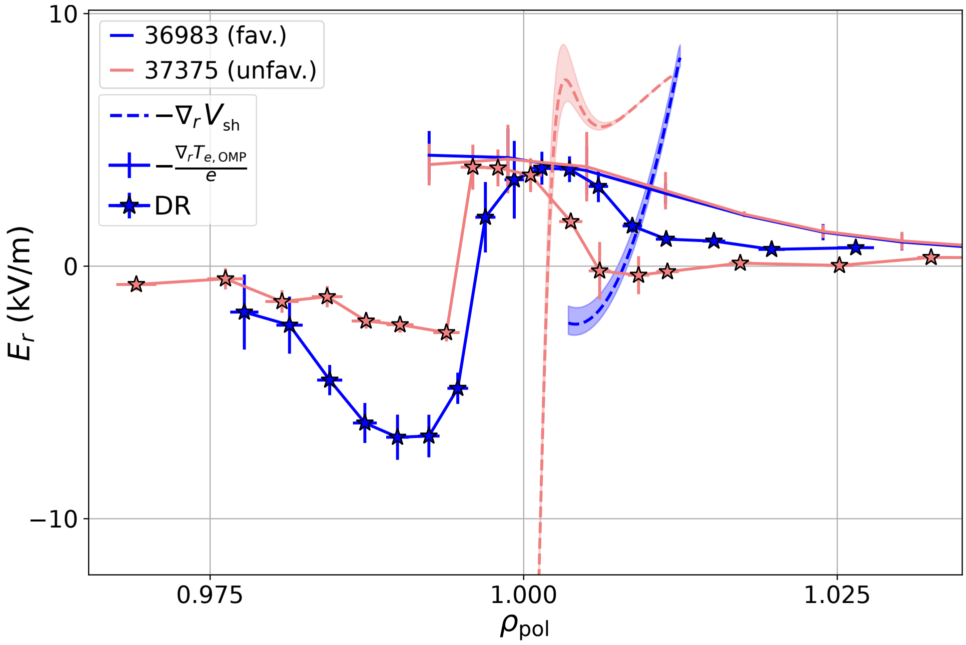

Figure 7.12: *SOL E_r profiles in LSN favourable and unfavourable drift configuration L-modes at same heating power and plasma density.* Comparison of the measured DR E_r profiles (stars) with their respective $-\nabla_r V_{sh}$ (dashed line) and $-\nabla_r T_{e,\mathrm{OMP}}$ (solid line) terms. In both drift configurations E_r deviates strongly from $-\nabla_r V_{sh}$, but agrees well with $-\nabla_r T_{e,\mathrm{OMP}}$. This indicates that the SOL plasma is in the conduction-limited regime for both drift configurations.

is located inside the separatrix for the unfavourable drift configuration, and to also account for radial uncertainties, $-\nabla_r T_{e,\mathrm{OMP}}$ is shown up to $\rho_{\mathrm{pol}} \approx 0.99$ in Figure 7.12.

In conclusion, the good agreement of the experimental E_r with $-\nabla_r T_{e,\mathrm{OMP}}$ supports again that the SOL is in the conduction-limited regime in both drift configurations. It also shows that indeed the upstream E_r can be estimated from the upstream T_e profile. Small differences in the measured E_r profiles from the estimates suggest that there are still other contributions, arising from the parallel force balance as argued in, which have to be taken into account to correctly determine E_r at the OMP from the other SOL quantities [38]. Most importantly, no significant difference in the measured SOL E_r profiles and the outer E_r gradient is observed between the two drift configurations at same heating powers. Thus, the strong difference in P_{LH} between the two drift configurations can not be explained by a direct and sole impact of the reversal of SOL flows on the SOL E_r as suggested by SOL modelling results [63, 158].

7.3.1.3 Different Heating Power and Same Plasma Density

In this section L-mode phases of different heating power in unfavourable drift configuration are compared. For this purpose the three time ranges marked in Figure 7.6 from discharge # 37375 are chosen. In these time windows the plasma was heated with $P_{\mathrm{ECRH}} = 0.60$, 2.9 and 4.0 MW, respectively. Also discharge # 37298, 2.0-2.3 s, with $P_{\mathrm{ECRH}} = 2.9$ MW is used in the comparison. As stated in Section 7.3.1.1 these two discharges have similar plasma parameters, although the resulting density is slightly higher for discharge # 37298 than for discharge # 37375. For # 37298 the chosen time window is the last constant L-mode phase before the L-I transition. The edge kinetic electron and ion profiles as well

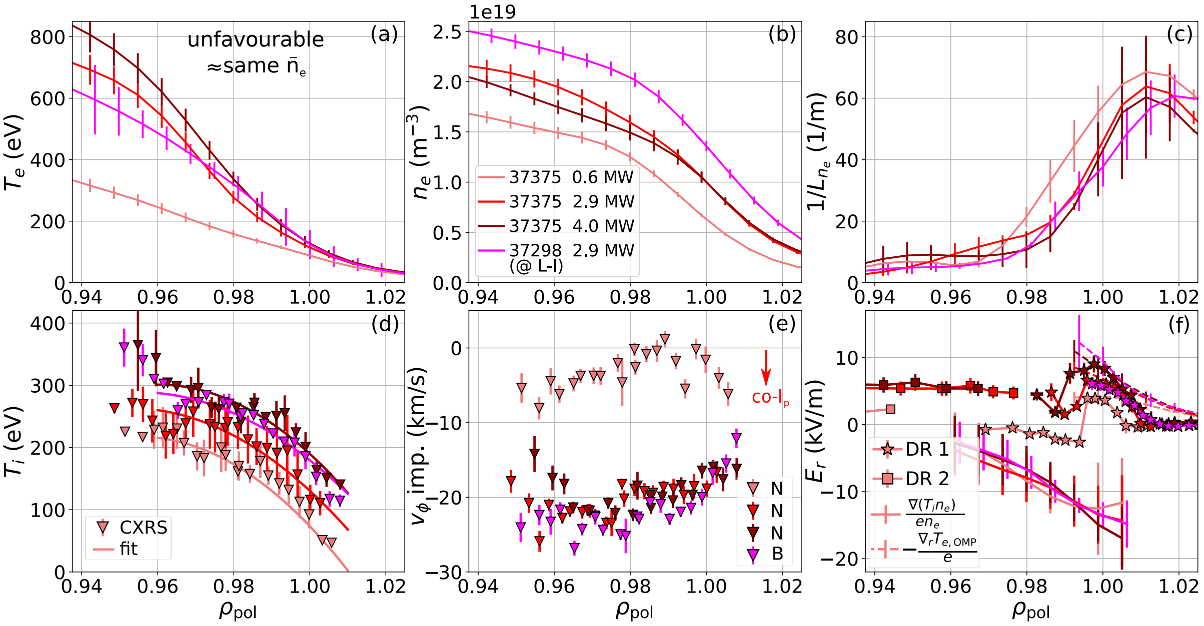

Figure 7.13: *Edge kinetic profiles of L-modes at different heating powers and same plasma density in LSN unfavourable drift configuration.* Experimental radial profiles of the edge (a) electron temperature, (b) electron density, (c) normalized electron density gradient, (d) ion temperature, (e) toroidal impurity rotation and (f) radial electric field. With increasing ECRH power the electron temperature and also the edge electron density increase, while the normalized edge density gradient decreases. The edge ion temperature increases with increasing P_{ECRH}, the intrinsic toroidal impurity rotation becomes more co-current and E_r shifts upwards, so that $E_{r,\text{min}}$ becomes positive. The experimental E_r profiles also strongly deviate from their respective $\nabla_r(T_i n_e)/(e n_e)$ terms in the confined region (solid lines), whereas they are in agreement with $-\nabla_r T_{e,\text{OMP}}$ in the SOL (dashed lines).

as the toroidal impurity rotation and the E_r profiles from DR are shown for all four time slices in Figure 7.13.

As it is expected T_e increases strongly with increasing P_{ECRH} at the plasma edge (see Figure 7.13a). At the separatrix an electron temperature of 130 eV is reached for the highest heating power, a value which is, in favourable drift configuration, only observed in H-modes. Figure 7.13b shows that n_e also increases slightly with increasing heating power, which can be ascribed to higher particle recycling from the plasma wall by ECRH [150]. The normalized electron density gradient has the trend of slightly decreasing with increasing heating power as shown in Figure 7.13c.

The edge ion temperature and its gradient increase with increasing heating power as can be seen in Figure 7.13d. The slightly higher density in # 37298 compared to # 37375 causes, via an increase of the electron-ion energy exchange term p_{ei}, that at the same $P_{\text{ECRH}} = 2.9$ MW the T_i profile and its gradient are steeper and, thus, the minimum in $(\nabla_r p_i)/(e n_e)$ is slightly more negative as well (this is shown in Figure 7.13f).

The impurity's intrinsic toroidal rotation is shown in Figure 7.13e. For all four cases it is negative, and, thus, in the co-current direction. However, while for the lowest heated case it is small, between 0 and −10 km/s, for the three other cases it exhibits values of −20 to −25 km/s. For the lowest heating power $v_{\phi,\text{imp}}$ exhibits a maximum at around $\rho_{\text{pol}} \approx 0.99$. For the higher heating powers $v_{\phi,\text{imp}}$ increases gradually towards the separatrix and the

SOL, where it reaches $-10\,\mathrm{km/s}$ at about $\rho_{\mathrm{pol}} = 1.01$. Although the investigated impurity was nitrogen in discharge # 37375 and boron in # 37298, their v_ϕ profiles do not show any difference outside the measurement uncertainties.

The E_r profiles for all four cases measured with DR are compared to $(\nabla_r p_i)/(en_e)$ in the confined region and $-\nabla_r T_{e,\mathrm{OMP}}$ in the SOL (see Figure 7.13f). The experimental SOL E_r profiles are in reasonable agreement with $-\nabla_r T_{e,\mathrm{OMP}}$. In the confined region the experimental E_r profiles deviate strongly from $(\nabla_r p_i)/(en_e)$. $(\nabla_r p_i)/(en_e)$ is, within the uncertainties, constant with increasing heating power, whereas $E_{r,\min}$ increases with increasing heating power and even becomes positive for the cases with high heating power. Furthermore, values of $(\nabla_r p_i)/(en_e) \approx -20\,\mathrm{kV/m}$ at the separatrix are found, which, in favourable drift configuration, are typical values of H-mode plasmas.

For a more detailed description of the four experimental E_r profiles and their dependencies, a magnified picture of them is shown in Figure 7.14a. The E_r profile with $P_{\mathrm{ECRH}} = 0.6\,\mathrm{MW}$ (lightred) has already been presented in Section 7.3.1.2. It exhibits $E_{r,\min} \approx -2.5\,\mathrm{kV/m}$ and $E_{r,\max} \approx 4.0\,\mathrm{kV/m}$. As soon as the heating power is increased to 2.9 MW E_r in the near SOL raises to $6\,\mathrm{kV/m}$, which is expected (see also Section 2.2.5). In the confined region, however, an even higher upward shift of $E_{r,\min}$ is observed, so that $E_{r,\min}$ is positive with a value of about $1.9\,\mathrm{kV/m}$. In discharge # 37298 (2.9 MW) the radial probing range of the DR systems changed due to the slightly higher electron density. Thus, the E_r well could not be detected. However, in the SOL E_r profile (magenta) agrees very well with the corresponding E_r profile from discharge # 37375 (red). When the heating power is further increased to 4 MW no more development of the E_r profile in the confined region is found, which is in line with the observation that $Q_{i,\mathrm{edge}}$ saturates and $\min((\nabla_r p_i)/(en_e))$ does not decrease further. This means that in the confined plasma region no more power is transferred into the ion channel. $E_{r,\max}$ and the SOL E_r still increase due to increasing P_{ECRH} and the values are in agreement with $-\nabla_r T_{e,\mathrm{OMP}}$ (see Figure 7.13d). This is also in line with measurements of the electron heat flux to the outer divertor (q_e) and $T_{e,\mathrm{target}}$, which also increase with increasing P_{ECRH}. The profiles are shown in Figure 7.15.

From the experimental E_r data it seems that the inner E_r gradient steepens with increasing heating power, from a maximal value of about $-0.3\,\mathrm{MV/m^2}$ to $-1.3\,\mathrm{MV/m^2}$. Since there is a gap in experimental data due to the transition from one DR to the other system, this value for the steepest part of the inner E_r gradient is not determined with high accuracy. In contrast the outer E_r gradient weakens slightly with increasing heating power from $2.0\,\mathrm{MV/m^2}$ to about $1.5\,\mathrm{MV/m^2}$.

The same trends in the evolution of the E_r profiles with changing heating power at low density are also observed with the He II spectroscopy, but due to diagnostics effects (see Chapter 6), the absolute values differ.

Figure 7.14b shows again the $v_{\phi,\mathrm{imp}}$ profiles multiplied with B_θ. This term enters in the radial force balance (see Equation 2.32). In all cases $v_\phi B_\theta$ is positive and varies for the low heating power L-mode between 0 and $2\,\mathrm{kV/m}$. For the high heating power L-modes $v_{\phi,\mathrm{imp}} B_\theta = 6 - 8\,\mathrm{kV/m}$. Interestingly, this relative change of $v_{\phi,\mathrm{imp}} B_\theta$ between low- and high-heated L-modes corresponds to the relative change of the actual E_r in the confined region measured with DR (see Figure 7.14a). Neoclassical calculations performed on these cases and presented in Section 7.4.1 show good agreement between experimental data and predicted neoclassical flows.

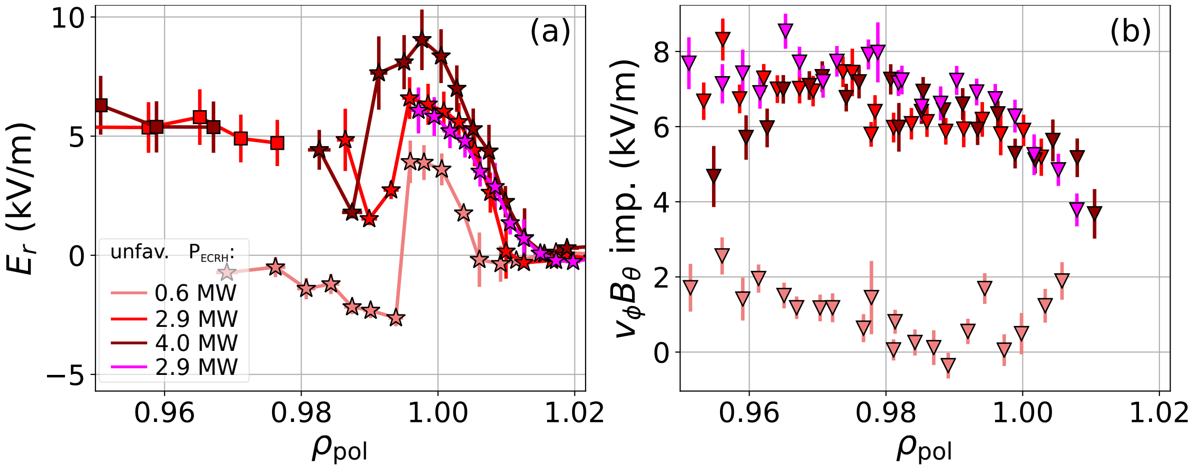

Figure 7.14: *Comparison of E_r profiles in L-modes of different heating powers and same plasma density in LSN unfavourable drift configuration.* (a) Experimental E_r profiles and (b) measured impurity rotation multiplied with the poloidal magnetic field. A positive upward shift of $4-6\,\mathrm{kV/m}$ is seen in E_r and in $v_{\phi,\mathrm{imp}}B_\theta$ for higher P_{ECRH}.

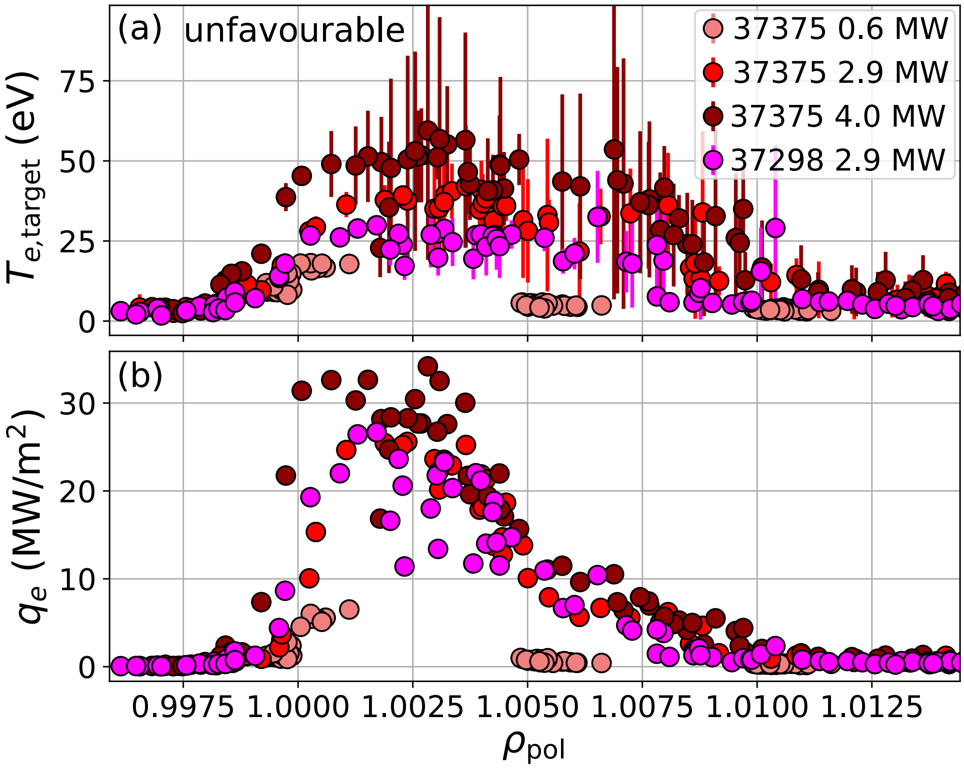

Figure 7.15: *Outer divertor profiles of L-modes at different heating powers and same plasma density in LSN unfavourable drift configuration.* Radial profiles of (a) electron target temperature and (b) electron heat flux to the outer target. Both quantities increase with increasing P_{ECRH}.

7.3.1.4 Same Heating Power and Different Plasma Density

In Figure 7.16 a comparison of n_e, T_e, T_i, toroidal impurity rotation and E_r profiles at the plasma edge for the two discharges # 35753 and # 35758 is shown. The profiles are all taken from stable L-mode phases with $P_{\mathrm{ECRH}} = 3.0\,\mathrm{MW}$. The only difference between the discharges are their plasma densities of $\bar{n}_e = 2.5$, 4.0 and $6.0 \times 10^{19}\,\mathrm{m}^{-3}$.

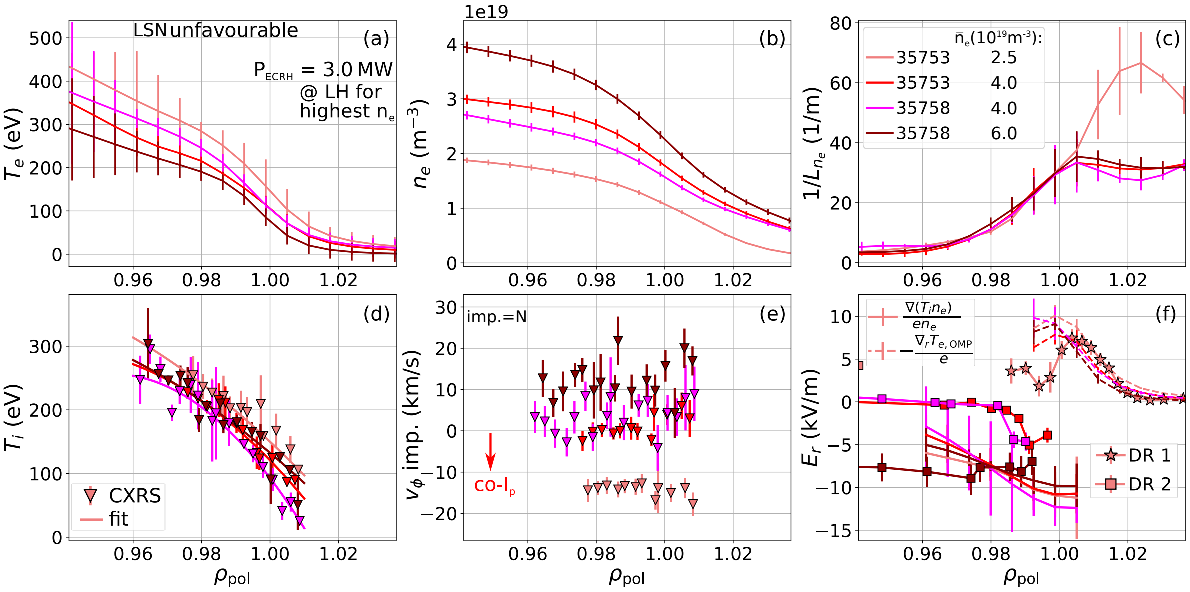

Figure 7.16: *L-mode kinetic profiles at different plasma densities and same heating power in LSN unfavourable drift configuration.* Measured radial profiles of the edge (a) electron temperature, (b) electron density, (c) normalized electron density gradient, (d) ion temperature, (e) toroidal impurity rotation and (f) radial electric field. With increasing plasma density the electron temperature decreases at constant P_{ECRH}, leading to a constant electron pressure at the separatrix of about 280 Pa . The normalized edge density gradient and the edge ion temperature stay constant for the different L-modes. The intrinsic toroidal impurity rotation becomes more positive with increasing plasma density and finally flips sign into the counter-current direction. The E_r profile shifts downwards by about the same amount as $v_\phi B_\theta$ contributes to it. $\nabla_r(T_i n_e)/(e n_e)$ (solid line) agrees with the experimental E_r profile in the confined region only for the highest plasma density, while $-\nabla_r T_{e,\mathrm{OMP}}$ (dashed line) agrees with the experimental E_r profile in the SOL (comparison possible only for lowest plasma density).

With increasing plasma density the edge electron temperature decreases over the complete radial range. This can be expected, since the power per plasma particle decreases with constant heating power and increasing density. It is found that the electron pressure at the separatrix is the same for all four cases, $p_{e,\mathrm{sep}} \approx 280\,\mathrm{Pa}$. The normalized electron density gradient profile is the same inside the separatrix for all four L-modes. The T_i profiles do not show any systematic dependence on n_e. T_i and $\nabla_r T_i$ are, within the measurement uncertainties, the same. The fact that T_i does not decrease with increasing n_e indicates that there are competing mechanism. On the one hand the power per plasma particle decreases linearly with increasing density at constant heating power, but on the other hand the energy exchange term between ions and electrons increases almost quadratically with increasing n_e (see Equation 3.6).

A strong difference is found in the edge $v_{\phi,\mathrm{imp}}$. In both discharges the investigated impurity was nitrogen (N). All $v_{\phi,\mathrm{N}}$ profiles are relatively flat. While at the lowest density $v_{\phi,\mathrm{N}} = -13\,\mathrm{km/s}$ and co-current, it increases with medium density to values of about 0 -10 km/s and changes its direction to counter-current. At the highest density values larger than 10 km/s are observed. A co-current toroidal rotation adds positively to E_r, while a counter-current v_ϕ adds negatively. Thus, $E_{r,\mathrm{min}}$ should decrease with increasing density. This is indeed found in the measured DR E_r profiles, shown in Figure 7.16f, where $E_{r,\mathrm{min}} \approx 1.8\,\mathrm{kV/m}$ for the lowest density and it is about $-8\,\mathrm{kV/m}$ for the highest density. This means that the change in v_ϕ agrees, within the measurement uncertainties, with the change in E_r. In detail $\mathit{\Delta} v_{\phi,\mathrm{N}} B_\theta = 7 \pm 2\,\mathrm{kV/m}$ and $\mathit{\Delta} E_{r,\mathrm{min}} = 9 \pm 2\,\mathrm{kV/m}$ between highest and lowest density.

Shown in Figure 7.16f are also, for comparison, $(\nabla_r p_i)/(en_e)$ in the confined region and $-\nabla_r T_{e,\mathrm{OMP}}$, in the SOL. For the medium and highest density cases $(\nabla_r p_i)/(en_e)$ and the measured E_r start to agree, while for the lowest density case a clear discrepancy is observed. The measured E_r and $-\nabla_r T_{e,\mathrm{OMP}}$ agree very well for the lowest density, while for the other densities the DR profiles do not allow for a comparison. According to the experimental data the inner E_r gradient seems to decrease with increasing density and is almost $0\,\mathrm{MV/m^2}$ for the highest density case. However, for the lowest density case the inner E_r gradient could not be measured, because there is a gap in the detection range of the two different DR systems. For the higher density cases one of the DR systems could measure the E_r well, but neither of the two could detect the outer E_r gradient. Therefore, Figure 7.17 shows the E_r data from the HES diagnostics. Although the absolute values deviate slightly from the DR E_r data (this was discussed in detail in Section 6.2) the trend of a lower $E_{r,\mathrm{min}}$ with higher density is also found in the HES data.

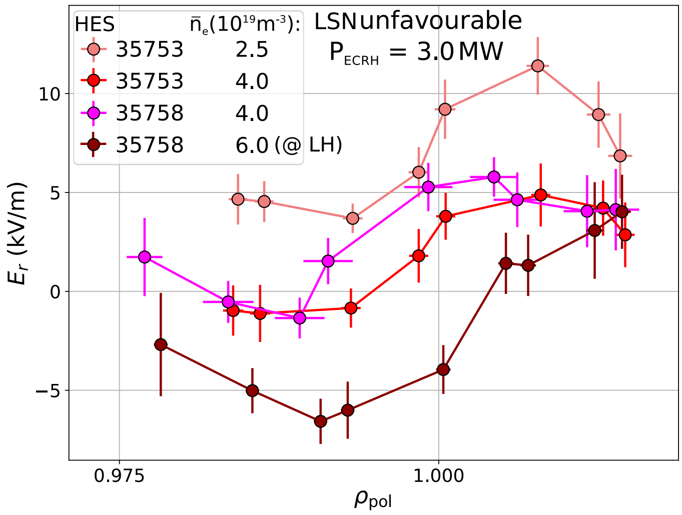

Figure 7.17: *Comparison of E_r profiles in L-modes of different plasma density and same ECRH power in LSN unfavourable drift configuration.* The E_r measurements by HES show that the values of E_r decrease equally in the confined plasma region and in the SOL with increasing density. Thus, the outer E_r gradient is almost constant at same heating power over a wide density range, regardless whether it is an L-mode window right before an L-H transition or not.

Additionally, the HES data suggest that the SOL E_r reduces by about the same amount as in the confined region $E_{r,\mathrm{min}}$. Consequently, the outer E_r gradient does not change between L-modes of different plasma density. In turn, this would mean that the SOL E_r does not agree with $-\nabla_r T_{e,\mathrm{OMP}}$ at higher densities, since the latter has a constant value of about $8\,\mathrm{kV/m}$ at the separatrix (see Figure 7.16f). On the other hand, the reduction of the SOL E_r at the OMP is consistent with the dependencies at the divertor. The SOL plasma is in the high-recycling regime, i.e. the increase of the electron density at the outer target is accompanied by a decrease of the electron temperature. Indeed the maximum of $T_{e,\mathrm{tar}} \approx 50\,\mathrm{eV}$ for the lowest density and it reduces to $\max(T_{e,\mathrm{tar}}) = 10 - 15\,\mathrm{eV}$ for the higher densities.

Taking together the results from Section 7.3.1.3 and Section 7.3.1.4, E_r in the confined region increases with increasing T_e (or T_i) and decreases with increasing n_e in L-modes. These dependencies are found for both LSN favourable and unfavourable drift configuration, although in unfavourable drift configuration a larger L-mode window can be studied with larger variations in n_e and T_e (T_i). The dependencies of E_r and also of $v_{\phi,\mathrm{imp}}$ on n_e and T_e (T_i) hint to the importance of the electron and ion collisionalities, ν_e^* and ν_i^*, which are proportional to n_e/T_e^2 and n_i/T_i^2, respectively. Indeed it has been found at AUG that the toroidal impurity and main ion edge rotation correlate with $\nu_{i,\mathrm{edge}}^*$ in NBI heated H-modes [21]. To elucidate the correlation between collisionality, the intrinsic plasma rotation and E_r at the plasma edge, neoclassical calculations of the main ion rotation profiles have been performed and compared to experimental data. This is presented in Section 7.4.

7.3.2 USN Plasmas

In this section L-mode profiles of discharges in USN favourable and unfavourable drift configuration will be compared. All discharges were run at $I_\mathrm{p} = 1.0\,\mathrm{MA}$, $|B_\phi| = 2.5\,\mathrm{T}$ on the magnetic axis and they were density feedback controlled to $\bar{n}_e = 4.5 \times 10^{19}\,\mathrm{m}^{-3}$. This value is slightly above the density minimum of P_LH at AUG (see Figure 7.1).

7.3.2.1 Same ECRH Power and Same Plasma Density

Discharges The here investigated two discharges, # 37983 and 37985, are identical, except that # 37983 is in unfavourable drift configuration, i.e. $B_\phi < 0$, and # 37985 is in favourable drift configuration, i.e. $B_\phi > 0$. Both discharges were heated with ECRH, which was stepwise increased from 0.4 to 1.9 MW to trigger a confinement transition. The heating trajectory was similar as for other investigated discharges (see e.g. Figure 7.6), with an NBI blip of 12 ms length at the end of each ECRH step for CXRS measurements. In favourable drift configuration the L-H transition occurred at $P_\mathrm{net} \approx 1.1\,\mathrm{MW}$. In unfavourable drift configuration the L-I transition occurred at $P_\mathrm{net} = 1.7 - 1.8\,\mathrm{MW}$, while there was not enough heating power to trigger the transition from I- to H-mode.

Edge Profiles In Figure 7.18 the edge kinetic electron and ion profiles and the respective E_r profiles for the time window 2.3 – 2.5 s are plotted for discharges # 37983 and 37985. For favourable drift configuration this is the last stable L-mode phase before the plasma transitions into H-mode. $P_\mathrm{ECRH} = 0.2\,\mathrm{MW}$, but $P_\mathrm{net} \approx 1.0\,\mathrm{MW}$ for both discharges, due to a large contribution of Ohmic power.

As described in Section 7.3.1, the electron profiles were aligned by calculating the separatrix temperature with the two-point model. The ion temperature, impurity rotation and also the E_r profiles measured by HES were not shifted. For the localization of the DR E_r profiles the respective n_e profiles, shown in Figure 7.18b, were used. Still, in both drift configurations an uncertainty in the radial alignment of about 3 mm remains when considering the measurements of all different edge diagnostics.

The edge electron profiles, T_e, n_e and also $1/L_{n_e}$ are almost identical for both drift configurations. Due to the high density and low heating power, $T_{e,\mathrm{sep}}$ is relatively low, at 50 eV. The edge T_i profile in favourable drift configuration is slightly higher than in

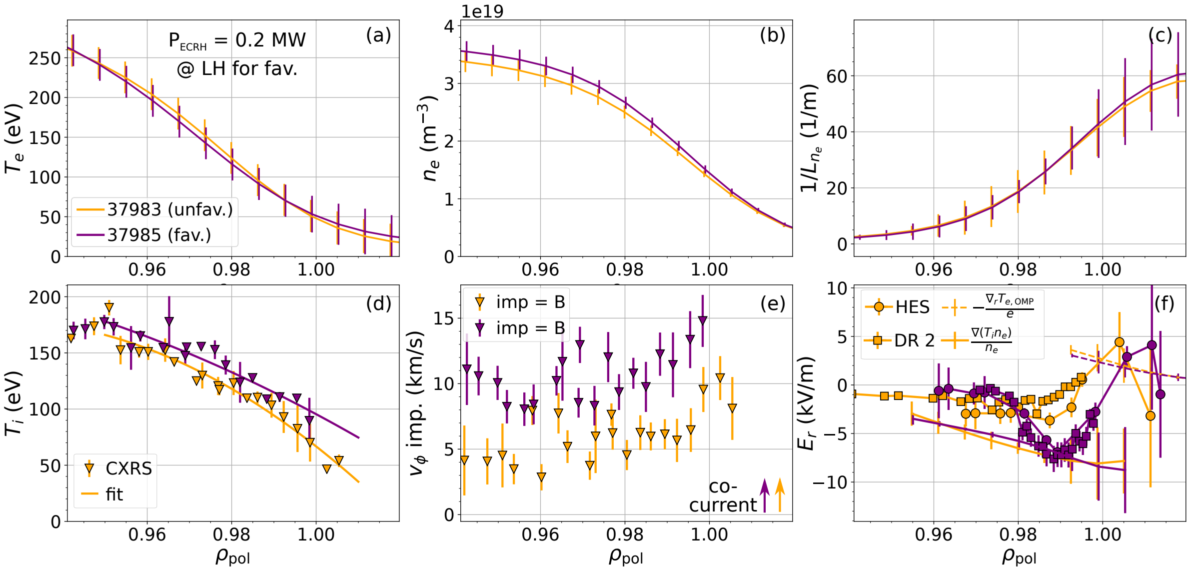

Figure 7.18: *Edge kinetic profiles of L-modes in USN favourable and unfavourable drift configuration at same ECRH power and plasma density.* Experimental radial profiles of the edge (a) electron temperature, (b) electron density, (c) normalized electron density gradient, (d) ion temperature, (e) toroidal impurity rotation and (f) radial electric field. The edge electron profiles are almost identical for both drift configurations, while the ion temperature and impurity rotation profiles show slightly higher values for favourable compared to unfavourable drift configuration. In both cases the intrinsic impurity edge rotation is co-current. The E_r well is more developed in favourable compared to unfavourable drift configuration, leading to a steeper inner E_r gradient. The outer E_r gradient is comparable, because $E_{r,\max}$ is found closer to the separatrix in unfavourable drift configuration compared to favourable drift configuration. The SOL E_r agrees reasonably well with $-\nabla_r T_{e,\mathrm{OMP}}$ (dashed lines), whereas E_r in the confined region agrees with $\nabla_r(T_i n_e)/(e n_e)$ (solid line) only for the favourable drift configuration.

unfavourable drift configuration. Again, the T_i profile is flatter than the T_e profile, leading to a T_i/T_e ratio at the separatrix of about 1.4 in unfavourable and to 1.8 in favourable drift configuration. The toroidal impurity rotation is positive and, thus, co-current for both drift configurations. The scattered experimental data suggest a relatively flat profile, with a slight increase of the rotation towards the separatrix. The measured v_ϕ is higher by 3 to 5 km/s for the favourable compared to the unfavourable drift configuration. The biggest difference is found in the edge E_r profiles. In favourable drift configuration E_r exhibits a clear well with an $E_{r,\min}$ of about −8 kV/m at $\rho_{\mathrm{pol}} = 0.99$. The inner and outer E_r gradient are approximately equally steep and the $E_{r,\max}$ of about 4 kV/m is clearly located in the SOL, at $\rho_{\mathrm{pol}} = 1.01$. In unfavourable drift configuration almost no inner E_r gradient exists, since the profile is relatively flat inside of $\rho_{\mathrm{pol}} = 0.985$, the position of $E_{r,\min}$. $E_{r,\min}$ differs slightly between the two E_r diagnostics[2] and is approximately −2.5 kV/m. An outer E_r gradient exists but it is not as steep in unfavourable drift configuration as in favourable drift configuration. At $\rho_{\mathrm{pol}} \approx 1.004$ an $E_{r,\max}$ of 4.5 kV/m is reached. The observations of a less developed E_r well in unfavourable compared to favourable drift configuration, at otherwise similar edge and global plasma parameters,

---

[2] This can be attributed to the misalignment of the poloidal optical head, see Chapter 6.

are consistent with experimental E_r measurements in LSN favourable and unfavourable drift configurations (see Section 7.3.1.2).

Plotted in Figure 7.18f are also $-\nabla_r T_{e,\mathrm{OMP}}/e$ and $(\nabla p_i)/(en_e)$. The experimental SOL E_r data are in reasonable agreement with $\nabla_r T_{e,\mathrm{OMP}}$. However, deviations in the shape of the HES E_r and $-\nabla_r T_{e,\mathrm{OMP}}/e$ are visible. This deviation might be ascribed to resolution limitations of the HES diagnostics, but higher resolved SOL E_r measurements from DR are not available for these discharges. Good agreement is found between the experimental E_r in the confined region and $(\nabla p_i)/(en_e)$ for favourable drift configuration, although the experimental inner E_r gradient is steeper than the one given by $(\nabla p_i)/(en_e)$. In unfavourable drift configuration $(\nabla p_i)/(en_e)$ is the same as in favourable drift configuration, but the experimental E_r is not as negative. As shown later in Section 7.4.2 the experimental data and predictions by neoclassical theory can be brought into agreement in unfavourable drift configuration if $E_r = (\nabla p_i)/(en_i) + v_i \times B$ is considered. However, then the experimental E_r data in favourable drift configuration do not fit to neoclassical theory any more.

7.3.2.2 Different ECRH Power and Same Plasma Density

Discharges In this section stable L-mode time windows of the unfavourable drift configuration discharges # 37983 and 37980 are compared. Discharge # 37983 was already introduced in the previous section, an ECRH heated discharge with an L-I transition at $P_{\mathrm{net}} \approx 1.8\,\mathrm{MW}$. Discharge # 37980 is identical to # 37983, except that the ECRH power was raised. P_{ECRH} was stepwise increased from 1.7 MW to 3.2 MW. The plasma was in I-mode throughout the discharge, except for the last power step, where an I-H transition was triggered with $P_{\mathrm{net}} = 3.5\,\mathrm{MW}$. The edge profiles for four different stable time phases of 200 ms length (L-mode, right before L-I transition, I-mode and right before I-H transition) were analysed and are shown in Figure 7.19.

Edge Profiles Naturally, the edge electron temperature increases and its gradient steepens with increasing heating power, but $T_{e,\mathrm{sep}}$ starts to saturate at a value of 100 eV during I-mode. As expected, the n_e profile does not change and, consequently, also $1/L_{n_e}$ stays the same. Due to the higher plasma density, compared to the investigated LSN plasmas, the energy exchange between electrons and ions is more efficient, such that also T_i increases with increasing P_{ECRH}. Corresponding to a smaller ∇T_i than ∇T_e, T_i is lower than T_e at $\rho_{\mathrm{pol}} = 0.95$, but (slightly) higher than T_e at the separatrix. For higher heating power $\nabla_r T_i$ steepens, which leads to a strong decrease of the minimum of $(\nabla p_i)/(en_e)$ from $-8\,\mathrm{kV/m}$ in L-mode, via $-20\,\mathrm{kV/m}$ at the L-I transition to $-30\,\mathrm{kV/m}$ at the I-H transition. The impurity rotation, measured on fully ionized boron, increases with increasing heating from 5 km/s to 15 – 20 km/s during L-mode. Interestingly, $v_{\phi,\mathrm{imp}}$ starts to develop a dip during I-mode, which is located at $\rho_{\mathrm{pol}} = 0.97 - 0.98$. Such a dip in the edge $v_{\phi,\mathrm{imp}}$ is regularly observed in H-mode plasmas at AUG [45].

The edge E_r measurements by HES and DR are shown in Figure 7.19f. $E_{r,\mathrm{max}}$, located at around $\rho_{\mathrm{pol}} = 1.005$ increases with increasing heating power, from about 4 kV/m in L-mode, via 8 – 9 kV/m at the L-I transition to about 12 kV/m at the I-H transition. The experimental SOL E_r measurements agree well with $-\nabla_r T_{e,\mathrm{OMP}}/e$ for all four cases. During L-mode $E_{r,\mathrm{min}}$ is constant at about $-3\,\mathrm{kV/m}$, but both E_r gradients, particularly

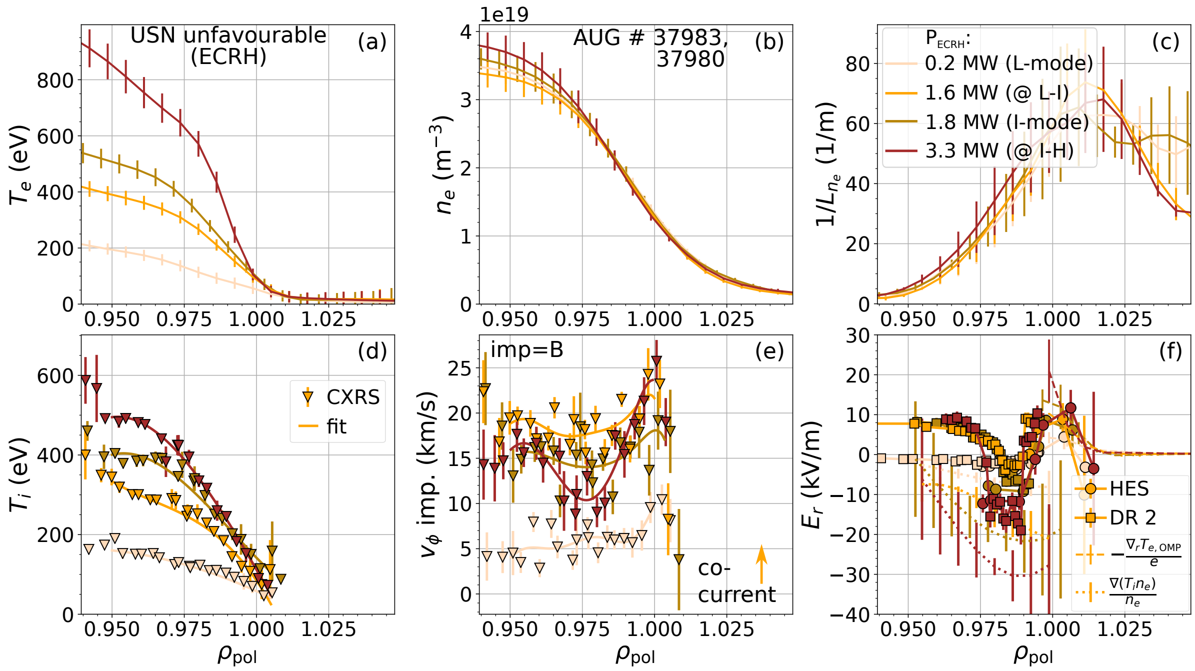

Figure 7.19: *Edge kinetic profiles of L- and I-modes in USN unfavourable drift configuration at different ECRH power and same plasma density.* Measured radial profiles of the edge (a) electron temperature, (b) electron density, (c) normalized electron density gradient, (d) ion temperature, (e) toroidal impurity rotation and (f) radial electric field. With increasing heating power the plasma transits from L- to I-mode. Accordingly, the edge temperature profiles (T_e and T_i) start to increase and their gradients steepen, while n_e stays constant. The toroidal impurity rotation increases in the co-current direction during L-mode, while it starts to develop a dip at around $\rho_{\mathrm{pol}} = 0.975$ during I-mode. Similarly, the gradients of the E_r profiles steepen with increasing heating power during L-mode, but $E_{r,\mathrm{min}}$ only decreases during I-mode. The SOL E_r increases with increasing P_{ECRH} and agrees reasonably well with $-\nabla_r T_{e,\mathrm{OMP}}$ (dashed line) for L- and I-mode, whereas $\nabla_r(T_i n_e)/(e n_e)$ (dotted line) is more negative than E_r in the confined region.

the inner one, steepen strongly. Only after the transition into I-mode also $E_{r,\mathrm{min}}$ decreases until it reaches a value of about $-12\,\mathrm{kV/m}$ at the I-H transition.

7.3.2.3 Different NBI Power and Same Plasma Density

Discharge In discharge # 37991 (unfavourable drift configuration), an NBI ramp was employed to trigger the L-I-H transition. This NBI ramp was designed as a modulation of the neutral beams, similar as depicted in Figure 7.4. Other parameters, like I_{p} and B_ϕ were the same as for the other USN plasmas and also the density was feedback controlled to $\bar{n}_e = 4.5 \times 10^{19}\,\mathrm{m}^{-3}$. In Figure 7.21 ion temperature, impurity rotation and E_r profile measurements are shown for three L-modes of different heating powers ($P_{\mathrm{NBI}} = 1.3, 2.3$ and $3.0\,\mathrm{MW}$). With about 3.0 MW of NBI the plasma entered I-mode.

Edge Profiles Similar as for the ECRH plasmas T_i increases and its gradient steepens with increasing heating power, although between the T_i profiles of 2.3 MW and 3.0 MW no difference is visible. The toroidal rotation, measured on fully ionized boron, increases

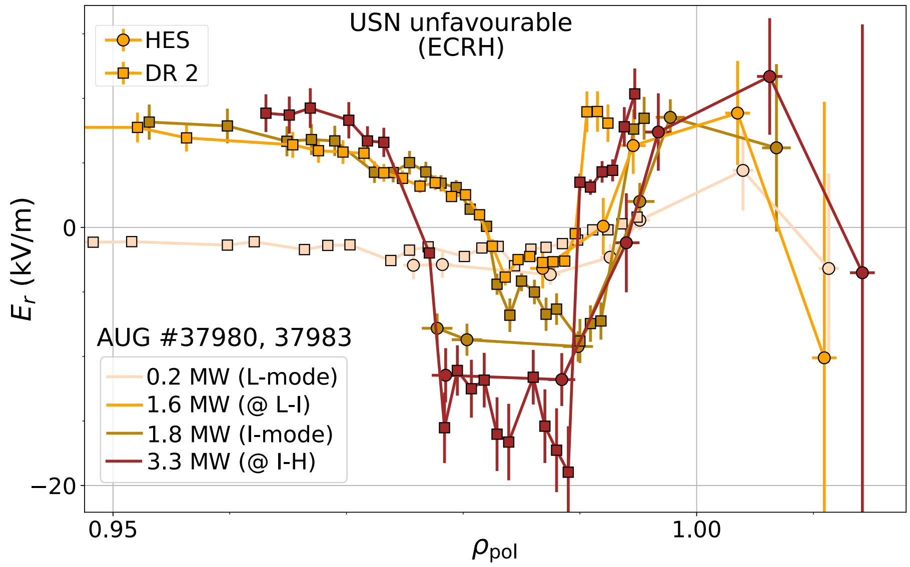

Figure 7.20: *Comparison of E_r profiles at different ECRH power and same plasma density in USN unfavourable drift configuration.* The gradients of the E_r profiles steepen with increasing heating power during L-mode, but $E_{r,\min}$ only decreases during I-mode until it reaches a value of about $-15\,\mathrm{kV/m}$ at the transition to H-mode.

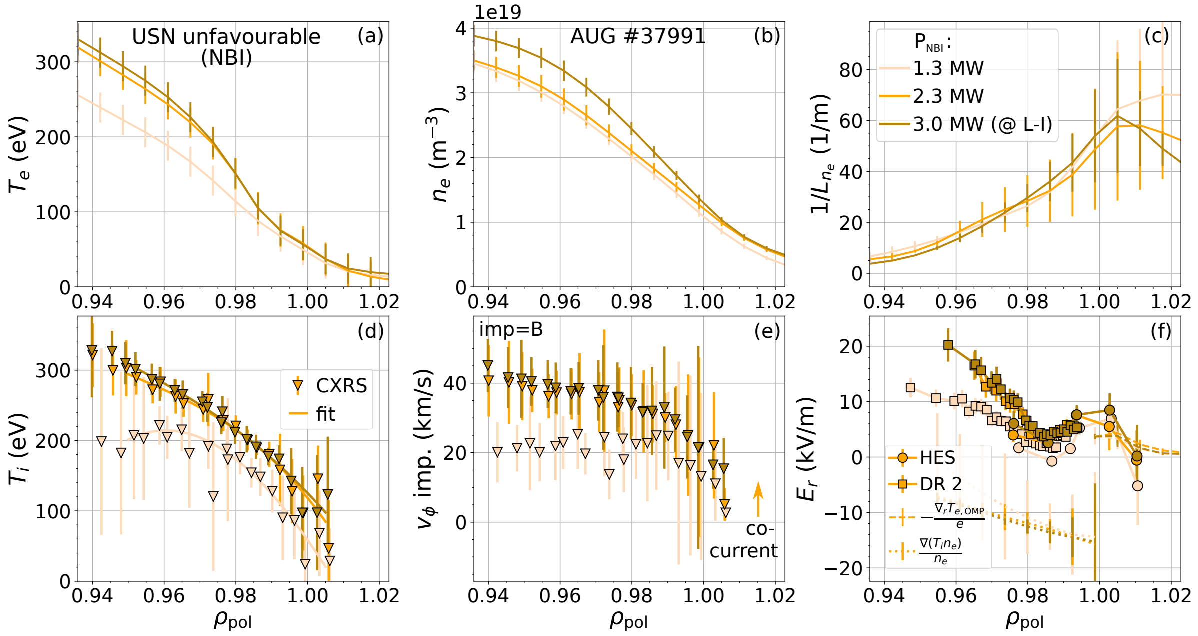

Figure 7.21: *L-mode edge kinetic profiles in USN unfavourable drift configuration at different NBI power and same plasma density.* Measured radial profiles of the edge (a) electron temperature, (b) electron density, (c) normalized electron density gradient, (d) ion temperature, (e) toroidal impurity rotation and (f) radial electric field. With increasing P_{NBI} T_e, T_i, n_e and $v_{\phi,\mathrm{imp}}$ increase, while $1/L_{n_e}$ stays constant. The experimental E_r data show that with increasing P_{NBI} the inner E_r gradient steepens strongly and the outer E_r gradient only slightly. E_r is positive and $E_{r,\min}$ does not decrease with increasing P_{NBI}. Thus, the experimental E_r profile deviates strongly from $\nabla_r(T_i n_e)/(e n_e)$ (dotted line), which is negative. In the SOL, $-\nabla_r T_{e,\mathrm{OMP}}$ (dashed line) is slightly lower than the experimental E_r data measured by HES.

from 20 km/s for the lowest heating to about 40 km/s for the higher heating powers at $\rho_{\mathrm{pol}} = 0.95$. Also here the two profiles with 2.3 MW and 3.0 MW of NBI are the same within the measurement uncertainties. A comparison with Figure 7.19e shows that the profile shape and absolute values of $v_{\phi,\mathrm{imp}}$ deviate between ECRH and NBI heated plasmas. While, at comparable heating power, $v_{\phi,\mathrm{imp}} \approx 15 - 20$ km/s at $\rho_{\mathrm{pol}} = 0.95$ for ECRH, the external torque input by NBI increases $v_{\phi,\mathrm{imp}}$ to about 40 km/s. Also, the shape of the $v_{\phi,\mathrm{imp}}$ L-mode profiles is different between the different heating schemes: For ECRH the edge $v_{\phi,\mathrm{imp}}$ profile is relatively flat and increases by about 5 km/s towards the separatrix, whereas with NBI heating the $v_{\phi,\mathrm{imp}}$ profiles decrease continuously over the edge region towards the separatrix to 15 – 20 km/s.

These different edge rotation profiles obtained with NBI also affect the L-mode E_r profiles. The strong rotation causes a high $E_{r,\mathrm{min}}$ value of 0 kV/m for $P_{\mathrm{NBI}} = 1.3$ MW and $E_{r,\mathrm{min}} \approx 4$ kV/m for $P_{\mathrm{NBI}} = 2.3$ and 3.0 MW. In contrast to the ECRH case, $E_{r,\mathrm{max}}$, located in the SOL at $\rho_{\mathrm{pol}} = 1.003$, shows no increase with heating power and exhibits values between 5 and 8 kV/m. Consequently, the outer E_r gradient decreases with increasing heating power. The NBI heated plasmas exhibit a strong inner E_r gradient. In the case of 3.0 MW NBI heating an E_r value of 20 kV/m is observed at $\rho_{\mathrm{pol}} = 0.96$. The measurements also suggest that the inner E_r gradient increases with increasing heating power, although for the lowest heated L-mode the inner E_r gradient could not be resolved. For comparison also $(\nabla_r p_i)/(en_i)$ is shown in the figure, which does not agree with the experimental E_r profiles. $(\nabla_r p_i)/(en_i)$ exhibits its minimum at the separatrix with values of -14 kV/m (low NBI) to -18 kV/m (high NBI). Also the gradient of $(\nabla_r p_i)/(en_i)$ is not as steep as the measured inner E_r gradient, which points to the importance of $v_{\phi,i}$ in the formation of the edge E_r profile.

7.3.3 LSN versus USN Plasmas

Figure 7.22 shows E_r profiles measured with DR and HES in a LSN (blue) and an USN (violet) plasma both in favourable drift configuration. The LSN discharge is the reference discharge # 35842 (see Section 3.2) and the USN discharge is # 37985, which was already presented in Section 7.3.2. Both plasmas have a comparable density of $\bar{n}_e = 4 \times 10^{19}\,\mathrm{m}^{-3}$, $|B_\phi| = 2.5$ T on the magnetic axis and were heated with ECRH close to P_{LH}. The only difference is that the plasma current was 0.80 MA for # 35842 and 1.0 MA for # 37985. The plasma conditions, however, can be considered equal for the two discharges, since plasmas in the high density branch show no dependence of P_{LH} on the plasma current [57] which could be explained by a phenomenological model recently [159]. Indeed P_{LH} is about 1.0 MW for both discharges and the E_r profiles are in very good agreement.

In both cases an $E_{r,\mathrm{min}}$ of -7 to -8 kV/m is observed at $\rho_{\mathrm{pol}} \approx 0.995$. The outer E_r gradients are the same, the measured $E_{r,\mathrm{max}}$ values differ, but not outside the error bars. In LSN $E_{r,\mathrm{max}} \approx 2$ kV/m at $\rho_{\mathrm{pol}} \approx 1.01$ and in USN $E_{r,\mathrm{max}} \approx 4$ kV/m at $\rho_{\mathrm{pol}} \approx 1.02$, which is no significant difference regarding the uncertainties. The inner E_r gradient seems to be a bit steeper for the LSN plasma, but within the radial uncertainties of the DR measurements it agrees with the inner E_r gradient of the USN plasma[3]. In the Figure also the two main determining terms of E_r in the confined region, $(\nabla_r p_i)/(en_i)$ (dotted), and in the SOL, $-\nabla_r T_{e,\mathrm{OMP}}/e$ (dashed), are shown. The experimental data agree with $(\nabla_r p_i)/(en_i)$ at $E_{r,\mathrm{min}}$ but further inside they start to deviate. $(\nabla_r p_i)/(en_i)$ exhibits a

---

[3] The radial uncertainties of the DR measurements are not shown in this plot for reasons of clarity.

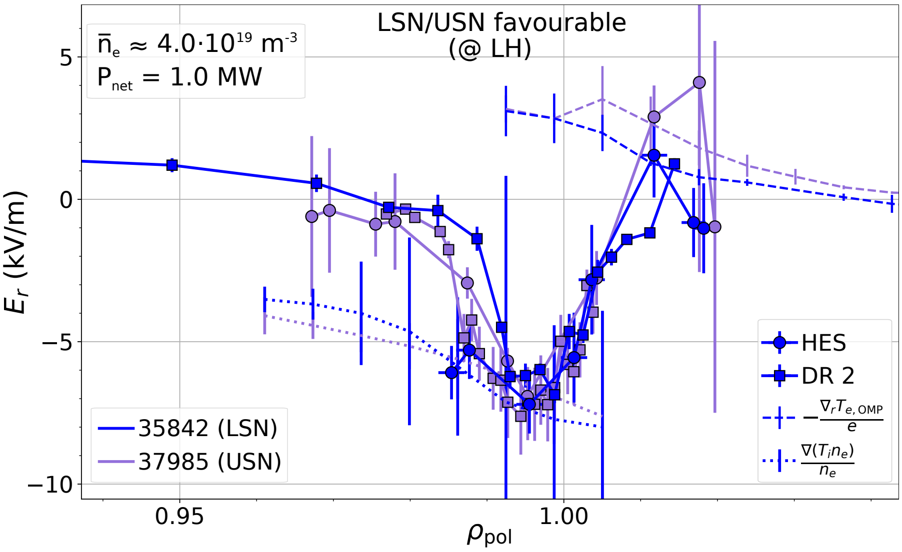

Figure 7.22: *Comparison of E_r profiles in LSN and USN favourable drift configuration L-modes of comparable plasma parameters.* The experimental E_r profiles (measured with HES and DR) are in very good agreement for the same drift configuration, independent of whether it is a LSN or an USN plasma. Furthermore, the experimental SOL E_r profiles agree with $-\nabla_r T_{e,\mathrm{OMP}}/e$, as it is predicted for conduction-limited plasmas. Also, as observed before for L-modes in the high density branch, the experimental E_r profiles agree with $\nabla_r(T_i n_e)/(e n_e)$ in the confined plasma region.

less steep gradient than the measured E_r profile. The SOL E_r and $-\nabla_r T_{e,\mathrm{OMP}}/e$ also agree reasonably well.

For the chosen USN and LSN cases in favourable drift configuration the E_r profiles are very comparable.

7.4 Comparison to Neoclassical Theory

In the following a comparison of the above presented L-mode profiles with neoclassical (NC) calculations is shown. Since NC theory is only valid on closed flux surfaces, the calculations stop at the separatrix and can only be compared to experimental data in the confined plasma. For the NC calculations the local NC code NEOART was used [160]. NEOART solves, for a given impurity, the set of linear coupled equations of the parallel velocity in all collision regimes for each charge state [140]. Hereby, NEOART includes the collisions of the considered impurity ion with the main plasma ions and all other impurities. Experimental n_e, T_e, T_i, $v_{\phi,\mathrm{imp}}$ and n_{imp} are given as input to the code, which calculates the NC poloidal main ion and impurity rotation profile ($v_{\theta,i}$ and $v_{\theta,\mathrm{imp}}$), the differential of the toroidal main ion rotation ($v_{\phi,i}$) to a given $v_{\phi,\mathrm{imp}}$ and the main ion density (n_i).

In all the calculations it was assumed that T_i equals the temperature of the investigated impurity (N or B), measured with CXRS. Furthermore, it was assumed that besides the main ion species (D) only this one impurity is present in the plasma. To calculate the charge state distribution of the investigated impurity ($\sum_Z n_{\mathrm{imp},Z}$) from n_{imp}, the corona ionisation equilibrium is solved in the code [33], for which the density of each charge state ($n_{\mathrm{imp},Z}$) is a function of T_e. The corona ionisation equilibrium is valid for low transport plasmas, which might not fully apply in the plasma edge. From the charge state distribution the main ion density profile can be calculated as $n_i = n_e - \sum_Z Z n_{\mathrm{imp},Z}$. Since the actual impurity density at the plasma edge can not always be experimentally assessed, two assumptions were made and compared. For the first case it was assumed that the impurity density is the one of the fully ionized impurity, e.g. $n_\mathrm{N} = n_{\mathrm{N}^{7+}}$. The latter can be assessed experimentally from the CXRS radiance measurements (see Section 3.1.2). For this purpose, measurements of the beam-based CXRS were used together with the CHICA code [83]. For the second approach a constant impurity concentration was assumed over the investigated radial range, i.e. $n_\mathrm{imp} = 0.01\, n_e$. It was found that n_i is not sensitive to these two different assumptions on n_imp. For this reason the latter was used in the presented NC calculations.

7.4.1 LSN Plasmas

7.4.1.1 Same Heating Power and Same Plasma Density

Figure 7.23 shows the NC predictions of $v_{\phi,i}$, $v_{\theta,\mathrm{imp}}$ and $v_{\theta,i}$ for the two L-mode time windows in LSN favourable (blue) and unfavourable (lightred) drift configuration presented in Section 7.3.1.2. Both L-modes have a plasma density of about $\bar{n}_e = 3 \times 10^{19}\,\mathrm{m}^{-3}$ and same P_ECRH of 0.6 MW. The experimental n_e, T_e, T_i, and $v_{\phi,\mathrm{imp}}$ profiles (see Figures 7.7 and 7.8) were given as input profiles for the NC calculations. For completeness the measured toroidal impurity rotations and their fits, which are an input to the NC code, are shown in Figure 7.23a. As stated before, in the favourable drift configuration the measured impurity was B, while in unfavourable drift configuration, the measured impurity was N, which was considered in the NC calcualtions.

The intrinsic toroidal rotation of the main ions is, in absolute values, larger than the intrinsic toroidal impurity rotation. In favourable drift configuration it exhibits a value of 11 km/s at $\rho_\mathrm{pol} = 0.95$ and increases at the very edge, between $\rho_\mathrm{pol} = 0.98$ and 1, to about 25 km/s. In unfavourable configuration the $v_{\phi,\mathrm{i}}$ profile looks the same as in favourable drift configuration, but, due to the reversal of I_p and, thus, B_θ, it is reversed and the values are between -15 and -25 km/s. In both drift configurations the intrinsic toroidal main ion rotation is co-current.

The predicted neoclassical poloidal impurity rotation is negative for favourable and positive for unfavourable drift configuration. This sign change is expected since besides I_p also B_ϕ is reversed. The absolute values increase from about 1 km/s at $\rho_\mathrm{pol} = 0.95$ to about 3 km/s at the separatrix in both drift configurations. The values agree reasonably well with experimental edge $v_{\theta,\mathrm{imp}}$ data, which were measured with CXRS. However, the experimental data do not show any structure, also because the uncertainties are large. The data scatter around 0 km/s. The neoclassical main ion poloidal rotation is, as $v_{\theta,\mathrm{imp}}$, negative for favourable and positive for unfavourable drift configuration, although inside of $\rho_\mathrm{pol} = 0.94$, the calculations indicate a sign flip and $v_{\theta,i}$ becomes positive (negative) for the favourable (unfavourable) drift configuration. In the region of interest ($\rho_\mathrm{pol} = 0.95 - 1$) $v_{\theta,i}$ is in the electron diamagnetic drift direction in both drift configurations. The predicted absolute values of $v_{\theta,i}$ are smaller than 0.3 km/s, which translates into a contribution to E_r of less than 0.6 kV/m.

In Figure 7.24 the predicted E_r profiles ($E_{r,\mathrm{pred}}$) using the radial force balance (see Equation 2.34) with the main ion rotations calculated by NEOART are plotted for

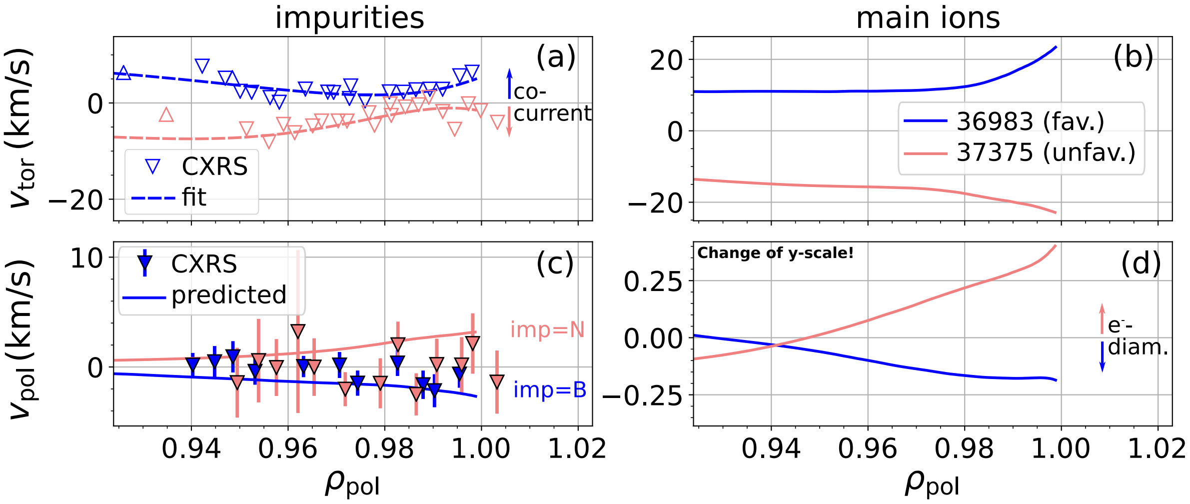

Figure 7.23: *Neoclassical rotations of L-mode plasmas in LSN favourable and unfavourable drift configuration with same ECRH power and same plasma density.* (a) Measured toroidal impurity rotation profiles. Predicted (b) toroidal main ion rotation, (c) poloidal impurity rotation and (d) poloidal main ion rotation profiles, using the edge kinetic profiles shown in Figures 7.7 and 7.8. Except for a change in sign, due to a reversal of B_ϕ and B_θ, the predicted intrinsic main ion rotation and the neoclassical poloidal rotations are the same for favourable and unfavourable drift configuration. The neoclassical poloidal rotation is also in agreement with experimental $v_{\theta,\mathrm{imp}}$ data from CXRS for both drift configurations. The neoclassical poloidal main ion rotation is by more than a factor of 10 smaller than the impurity rotation (note the different y-scale). Thus, it accounts for at maximum 0.6 kV/m to E_r.

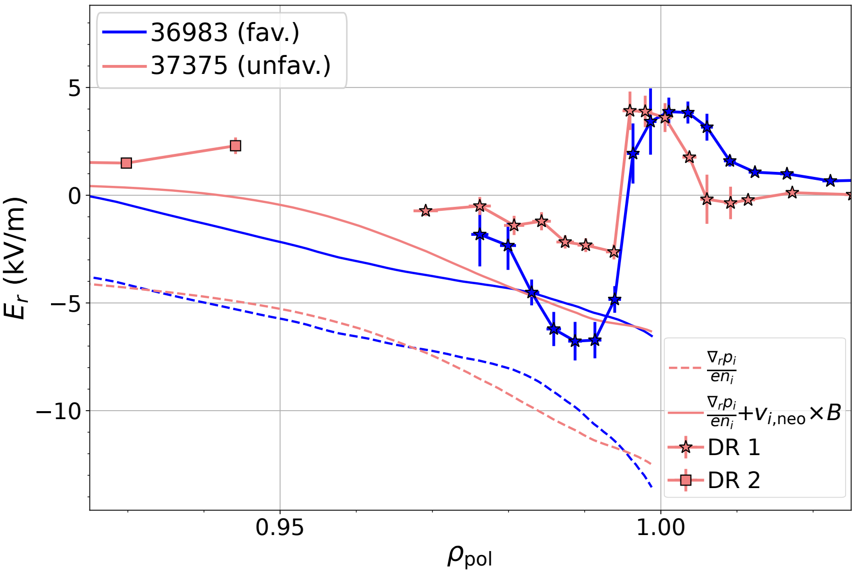

Figure 7.24: *Comparison of E_r profiles with neoclassical predictions in LSN favourable and unfavourable drift configuration L-modes of same ECRH power and same plasma density.* Only if the main ion rotations, calculated with NC theory, are taken into account in the prediction of E_r, the experimental L-mode E_r profiles can be reproduced. This holds especially for favourable drift configuration (blue). In unfavourable drift configuration (light red) larger deviations are observed.

both drift configurations. Also shown are the respective main ion diamagnetic term $(\nabla_r p_i)/(en_i)$, using now n_i instead of n_e, and the experimental DR E_r profiles. The experimental E_r profiles were already presented in Section 7.3.1.2.

As the figure shows, $(\nabla_r p_i)/(en_i)$ and $E_{r,\mathrm{pred}}$ in favourable drift configuration are the same as in unfavourable drift configuration. However, $(\nabla_r p_i)/(en_i)$ does not match the experimental data in either drift configuration and only if the contribution of $v_i \times B$ is taken into account, $E_{r,\mathrm{pred}}$ fits the experimental data in favourable drift configuration. While $(\nabla_r p_i)/(en_i) \approx -9\,\mathrm{kV/m}$, $\min(E_{r,\mathrm{pred}}) \approx -6\,\mathrm{kV/m}$. This value agrees well with $E_{r,\mathrm{min}} \approx -6.8\,\mathrm{kV/m}$ in favourable drift configuration. For unfavourable drift configuration $(\nabla_r p_i)/(en_i) \approx -11\,\mathrm{kV/m}$ and $\min(E_{r,\mathrm{pred}}) \approx -6\,\mathrm{kV/m}$, which still disagrees with $E_{r,\mathrm{min}} \approx -2.7\,\mathrm{kV/m}$ in unfavourable drift configuration. The deviation could indicate that in LSN unfavourable drift configuration the poloidal rotation is non-neoclassical. However, the uncertainties in the predictions need to be discussed before arriving at any conclusion.

The profile shape of $E_{r,\mathrm{pred}}$ differs from the experimental E_r profiles in both drift configurations. The experimental $E_{r,\mathrm{min}}$ is located at $\rho_{\mathrm{pol}} = 0.99 - 0.995$, where both $(\nabla_r p_i)/(en_i)$ and the $E_{r,\mathrm{pred}}$ profile still decrease towards the separatrix. They do not exhibit a minimum in the confined region. In Section 7.3.1.2 it was already shown that the minimum value of $(\nabla_r T_i n_e)/(en_e)$, the proxy for $(\nabla_r p_i)/(en_i)$, is even found outside the separatrix. Also the inner gradient of $E_{r,\mathrm{pred}}$ is not as steep as experimentally observed for the favourable drift configuration. This can be resolved with an alternative fit of the edge T_i profile allowing for steeper gradients.

7.4.1.2 Discussion of Uncertainties

In a sensitivity study it was found that the T_i profile has a strong impact on the predicted E_r profile. The normalized ion temperature gradient, $1/L_{T_i}$, is a quantity which not only contributes to $(\nabla_r p_i)/(en_i)$, but also enters in the predictions of the neoclassical rotations according to Equations 2.41 and 2.43. For this reason the T_i fits were varied within the experimental uncertainties to study the impact of the T_i profile shape on the resulting $E_{r,\mathrm{pred}}$. For each drift configuration one stiff T_i profile fit with a relatively flat T_i gradient at the the separatrix was produced and one more flexible with a steeper T_i gradient.

Favourable Drift Configuration For the favourable drift configuration the two corresponding T_i profiles are plotted in Figure 7.25a, while the resulting predicted E_r profiles are presented in Figure 7.25b. For a better comparison also the experimental data are again shown in both plots.

The figure suggests that with the steeper T_i gradient the measured E_r profile can be reproduced by the neoclassical calculations ($E_{r,\mathrm{pred}}$) qualitatively and quantitatively. From the flat to the steep T_i profile $\nabla_r T_i$ changes from $-2.5\,\mathrm{keV/m}$ to $-6\,\mathrm{keV/m}$ at $\rho_{\mathrm{pol}} = 0.995$ This translates into a decrease of $E_{r,\mathrm{pred}}$ from $-5\,\mathrm{kV/m}$ to $-7\,\mathrm{kV/m}$ at $\rho_{\mathrm{pol}} = 0.995$. With the steeper T_i gradient profile the inner E_r gradient can be reproduced also quantitatively by the NC calculations. Interestingly, even an E_r well develops in $E_{r,\mathrm{pred}}$. This can be attributed to a sign change of the slope of the T_i profile very close to the separatrix, but can also be considered an artefact of the less constrained T_i fit.

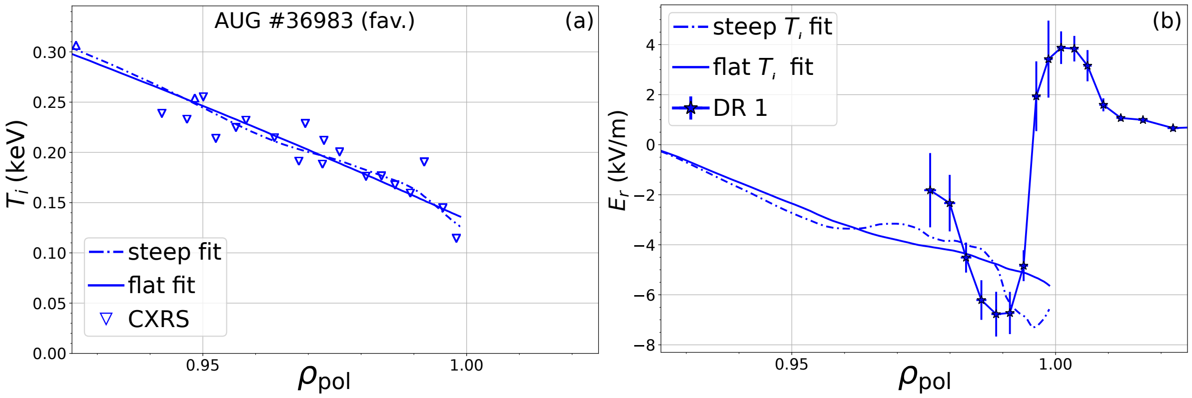

Figure 7.25: *Comparison of E_r and neoclassical predictions in LSN favourable drift configuration for two different T_i profiles.* (a) Experimental T_i data fitted with cubic splines of high (solid line) and low (dashed-dotted line) stiffness. (b) Resulting predicted E_r profiles. If the T_i data are fit with cubic splines of lower stiffness, allowing for a steeper T_i gradient at the separatrix, the inner E_r gradient as observed in the experimental E_r profile can be reproduced quantitatively by the NC calculations.

There still exists a radial deviation between $E_{r,\text{pred}}$ and the experimental E_r. $E_{r,\text{pred}}$ seems to be shifted further outside by about 1.5 mm compared to the experimental E_r profile. This deviation is within the radial uncertainties, but with a different n_e profile, the two E_r profiles can be brought into even better agreement. It was shown in Section 7.3.1.2 that the edge n_e exhibits a higher separatrix value if the TS data instead of the HEB data are used for the IDA electron profile reconstruction. This translates into a radial outward shift of the DR E_r profile in this region (see Figure 7.9c). Therefore, a second pair of neoclassical calculations was performed with this n_e profile, using again the two T_i profiles with flat and steep T_i gradients.

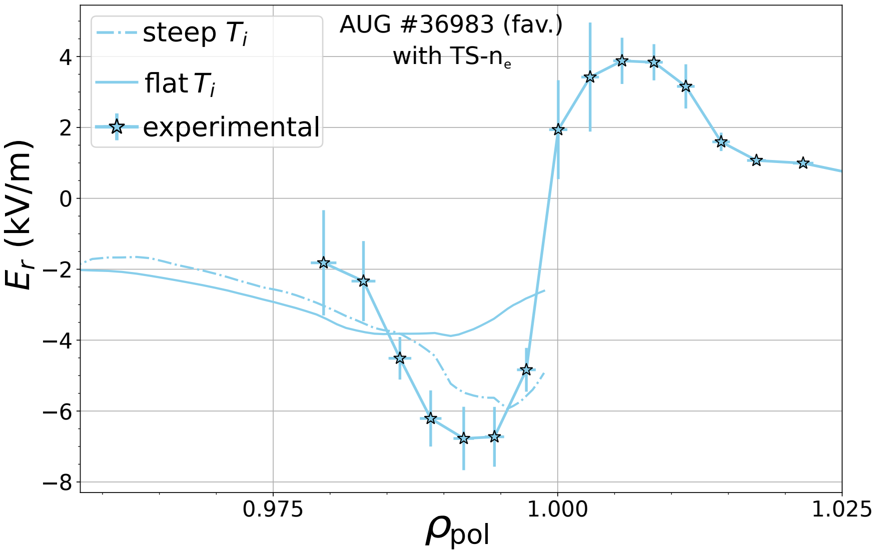

Figure 7.26: *Comparison of E_r and neoclassical predictions in LSN favourable drift configuration for a different n_e profile.* Predictions of E_r using the n_e profile with TS data (see Figure 7.9) in the NC rotation calculations. If also the steeper T_i profile is used (see Figure 7.25a), the experimental E_r profile can be reproduced even without applying a radial outward shift to the predicted E_r profile.

Figure 7.26 shows the two corresponding $E_{r,\mathrm{pred}}$ profiles together with the respective DR E_r profile. Also in this case the E_r profile calculated with the steep gradient T_i profile fits better to the experimental data compared to the flat T_i profile. With the steep T_i profile the inner E_r gradient can be reproduced better, while for the flat T_i profile the inner E_r gradient is flat. The different n_e profile causes that the predicted E_r values are slightly higher compared to the corresponding $E_{r,\mathrm{pred}}$ profiles shown in Figure 7.25b. For the flat T_i profile this leads to a strong deviation of the predicted $E_{r,\mathrm{min}}$ (about $-4\,\mathrm{kV/m}$) from the experimental $E_{r,\mathrm{min}}$ ($-6.8\,\mathrm{kV/m}$). Only with the steep T_i profile the predicted E_r profile agrees also quantitatively with the experimental data.

Unfavourable Drift Configuration The same study has been done for the unfavourable drift configuration. The two used input T_i profiles are shown in Figure 7.27a together with the experimental data. The resulting predicted E_r profiles are presented with the respective DR E_r profile in Figure 7.27b. In this drift configuration the predicted E_r profile using the flat T_i profile (solid line) exhibits constantly lower values than the measured E_r profile. The difference is about $-3\,\mathrm{kV/m}$. Like in the favourable drift configuration, the steep T_i profile (dashed-dotted line) leads to an even more negative predicted $E_{r,\mathrm{min}}$, a steeper inner E_r gradient and the formation of an E_r well. $E_{r,\mathrm{min}}$ is then about $-10.3\,\mathrm{kV/m}$ at $\rho_{\mathrm{pol}} \approx 0.995$, which is four times deeper than the measured $E_{r,\mathrm{min}}$.

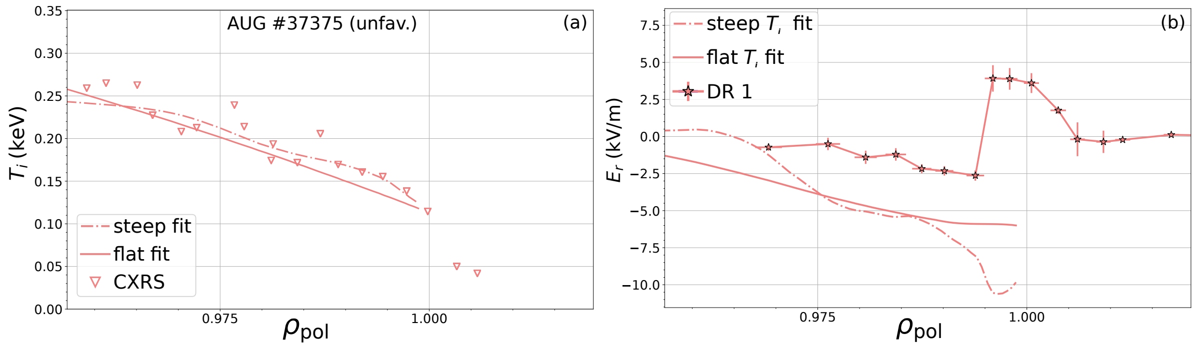

Figure 7.27: *Comparison of E_r and neoclassical predictions in LSN unfavourable drift configuration for two different T_i profiles.* (a) Experimental T_i data fitted with cubic splines of high (solid line) and low (dashed-dotted line) stiffness. (b) Resulting predicted E_r profiles. The experimental E_r profile can not be reproduced by NC predictions with either T_i profile as input for the NC calculations. As observed in favourable drift configuration, the steeper T_i gradient leads to a decrease of the minimum of $E_{r,\mathrm{pred}}$ and a steeper inner E_r gradient. This reconstructed E_r profile fits even less to the experimental data than the predicted E_r profile using the flat T_i profile.

In conclusion this means that a variation of the T_i profile within the measurement uncertainties can not reconcile the experimental E_r data with local NC theory in LSN unfavourable drift configuration. This is, however, not the case in USN plasmas, as will be shown in Section 7.4.2. In LSN unfavourable drift configuration either the T_i profile would need to be flatter than the experimental data suggest or the toroidal impurity rotation would need to be different than the experimentally determined one, in order to still fit the local NC calculations. For this purpose, a NC calculation was performed which uses the experimental E_r profile as input and predicts the $v_{\phi,\mathrm{i}}$ profile under the assumption of a neoclassical poloidal velocity employing the radial force balance equation. This is shown in the following.

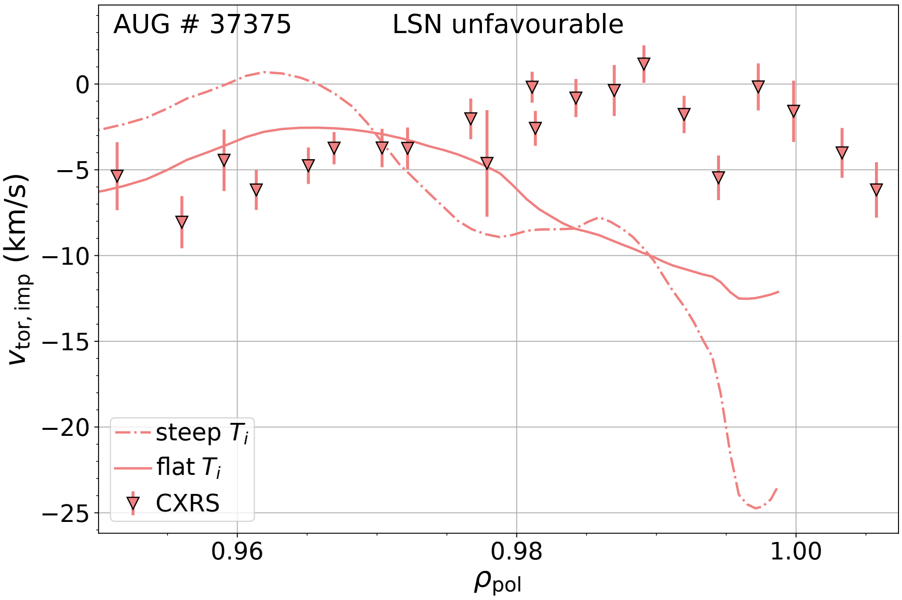

Figure 7.28: *Comparison of the toroidal impurity rotation and neoclassical predictions using the experimental E_r profile in LSN unfavourable drift configuration.* The $v_{\phi,\mathrm{imp}}$ profiles (solid and dashed-dotted line) were calculated from the experimental E_r profile via the radial force balance, assuming the neoclassical poloidal rotations as calculated by NEOART for the steep and the flat T_i profiles (see Figure 7.27). The predicted $v_{\phi,\mathrm{imp}}$ profiles deviate from the experimentally measured ones for $\rho_{\mathrm{pol}} > 0.98$.

A comparison of the predicted $v_{\phi,\mathrm{imp}}$ profiles giving once the flat T_i fit as input for the NC calculation (solid line) and once the steep T_i fit (dotted-dashed line) are shown in Figure 7.28. Also the experimental data are given for comparison. Up to $\rho_{\mathrm{pol}} \approx 0.98$ the experimental data and the predicted $v_{\phi,\mathrm{imp}}$ still fit and values of roughly -5 km/s are observed. For higher ρ_{pol} values, i.e. closer to the separatrix, the two profiles start to deviate by more than 10 km/s. Such a deviation is outside of the CXRS measurement uncertainties. Furthermore, the shape of the profiles is different. The experimental $v_{\phi,\mathrm{imp}}$ data increase towards the separatrix to about 0 km/s, whereas the values of the predicted toroidal rotation profiles decrease to -12 km/s for the flat T_i gradient profile and to -25 km/s for the steep T_i profile. In conclusion this means that in LSN unfavourable drift configuration the experimental edge measurements can not be brought into quantitative agreement with local NC predictions. As shown in the next section relative changes of the experimental $v_{\phi,\mathrm{imp}}$ and E_r are correctly reproduced by NC theory also in LSN unfavourable drift configuration.

7.4.1.3 Different Heating Power and Same Plasma Density

NC edge rotation profiles of the four different L-mode time windows introduced in Section 7.3.1.3 are presented in Figure 7.29. In these four L-modes in unfavourable drift configuration the plasma density was about $3.0 \times 10^{19}\,\mathrm{m}^{-3}$ and P_{ECRH} was varied from 0.6 to 4.0 MW. For the NC calculations flat, i.e. stiff T_i profile fits (see Section 7.4.1.2) were used. The measured toroidal intrinsic impurity rotation is co-current and decreases with increasing P_{ECRH}. The same is found for the toroidal intrinsic main ion rotation, although in absolute values it is larger than $v_{\phi,\mathrm{imp}}$. For $P_{\mathrm{ECRH}} = 0.6$ MW it is between -15 and -25 km/s and for the high-powered cases (2.9 and 4.0 MW) $v_{\phi,\mathrm{i}}$ is between -30

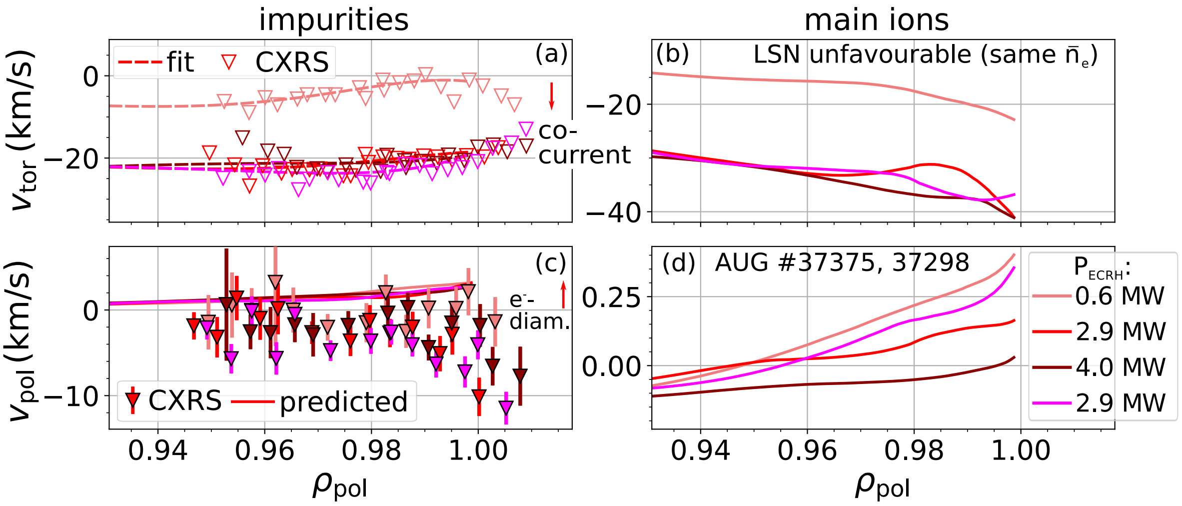

Figure 7.29: *Neoclassical rotations of L-mode plasmas in LSN unfavourable drift configuration of different ECRH power and same plasma density.* (a) Measured toroidal intrinsic impurity rotation profile (input) and (b) predicted toroidal intrinsic main ion rotation, (c) predicted neoclassical poloidal impurity rotation and (d) predicted neoclassical poloidal main ion rotation. The rotation profiles were calculated with NEOART giving the edge kinetic profiles shown in Figure 7.13 as input. The intrinsic plasma rotation is co-current for both impurities and main ions and decreases with increasing P_{ECRH}. The neoclassical poloidal impurity rotation is constant, independent of heating power, and positive. This is different to the experimental data, which show a small, but negative poloidal impurity rotation. The neoclassical poloidal main ion rotation is about a factor of 10 smaller than the impurity rotation (note the different y-scale) and decreases with increasing P_{ECRH}. For the highest power $v_{\theta,i}$ is negative and, thus, in the ion diamagnetic drift direction.

and -40 km/s. The neoclassical poloidal impurity edge rotation is positive and small. It is about the same for all four cases and does not exceed 3 km/s. v_θ of the main ions is even smaller and it decreases with increasing P_{ECRH} from about 0.3 km/s to 0 km/s at $\rho_{\mathrm{pol}} = 0.995$. For the highest P_{ECRH} of 4.0 MW $v_{\theta,i}$ is negative for $\rho_{\mathrm{pol}} < 0.995$. This means that the neoclassical $v_{\theta,i}$ changes from electron to ion diamagnetic drift direction when increasing P_{ECRH} from 0.6 to 4.0 MW.

Also the experimental $v_{\theta,\mathrm{imp}}$ values measured by CXRS are small, but they tend to be negative and, thus, point in the ion diamagnetic direction. This is opposite to NC theory predictions which exhibit a positive $v_{\theta,\mathrm{imp}}$, i.e. in the electron diamagnetic drift direction. Although the differences between the experimental and the NC $v_{\theta,\mathrm{imp}}$, are small, they have a big impact on the resulting E_r profile, since v_θ is multiplied with the local B_ϕ strength, which is about 2 T. This is shown in Figure 7.30b-f, where four different reconstructions of edge E_r profiles are shown for each of the four L-mode cases of same $\bar{n}_e$ but different P_{ECRH}. The square and star symbols in the plots depict the experimental E_r profiles measured by DR, which have already been introduced in Section 7.13. Furthermore, the plots contain the respective $(\nabla_r p_i)/(en_i)$ profiles (dashed lines) and the E_r profiles using v_θ and v_ϕ as predicted by NEOART (solid lines). Lastly, also the E_r profiles reconstructed from CXRS are shown (triangle symbols with dashed lines), which use the experimentally measured $v_{\theta,\mathrm{imp}}$ and $v_{\phi,\mathrm{imp}}$ profiles in the radial force balance equation of the impurities.

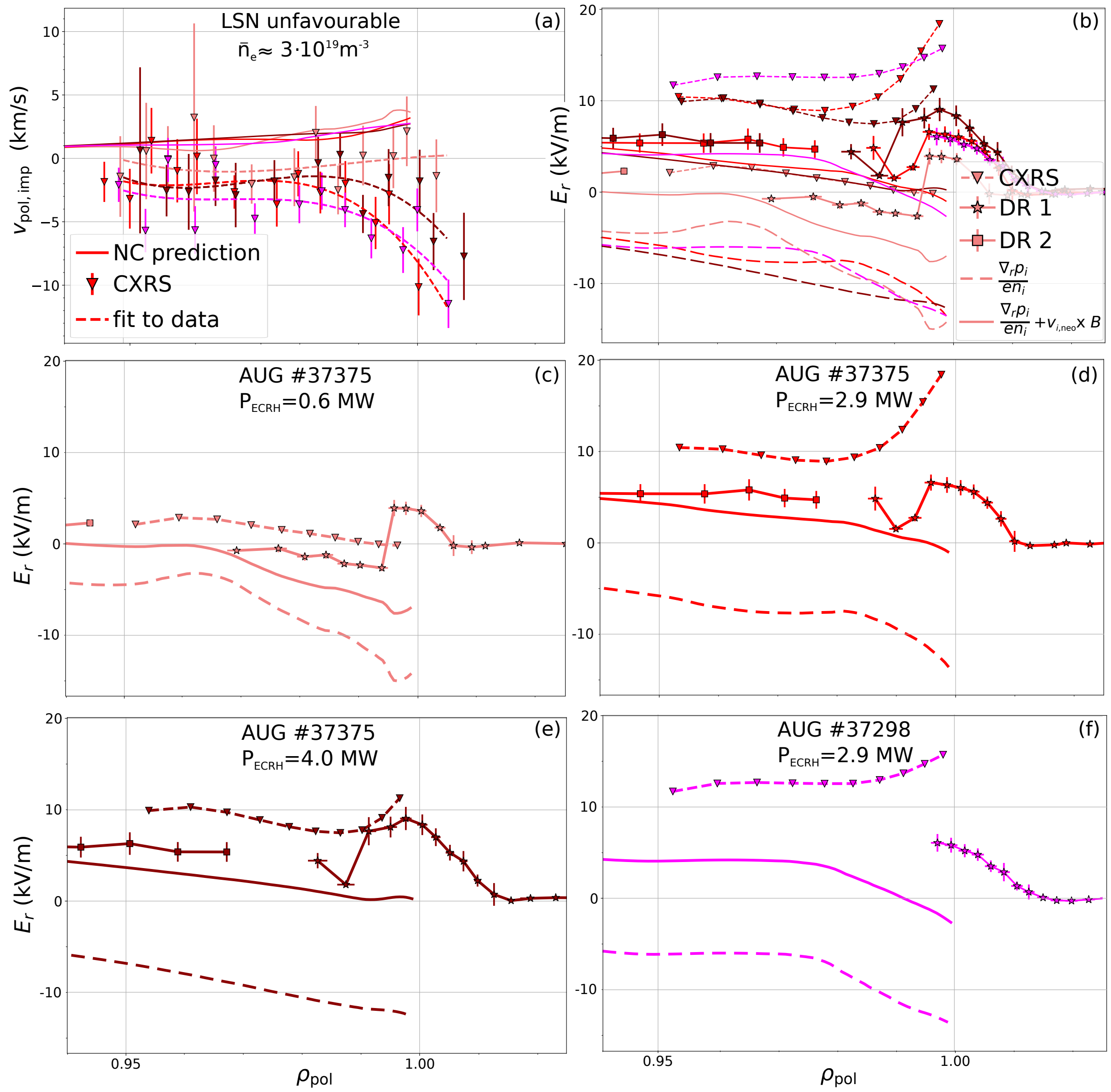

Figure 7.30: *Comparison of E_r profiles in LSN unfavourable drift configuration L-modes of comparable plasma density and different ECRH power.* (a) NC predictions and CXRS measurements of $v_{\theta,\rm imp}$ and (b) overview of E_r profiles from DR, CXRS, NEOART and $(\nabla_r p_i)/(en_i)$. Experimental and predicted E_r profiles of low-density L-modes with (c) $P_{\rm ECRH} = 0.6\,\rm MW$, (d) $P_{\rm ECRH} = 2.9\,\rm MW$, (e) $P_{\rm ECRH} = 4.0\,\rm MW$ and (e) $P_{\rm ECRH} = 2.9\,\rm MW$ (slightly higher $\bar{n}_e$.) For all four L-mode windows the $(\nabla_r p_i)/(en_i)$ profiles deviate strongly from the DR E_r profiles and can only be brought into reasonable agreement with the experimental data if the contribution of $v_i \times B$ to E_r is taken into account. However, the E_r profiles reconstructed from measured impurity velocities by CXRS are slightly higher than the measured DR E_r profiles, while the E_r profiles employing NC velocities are slightly more negative than the DR E_r profiles. Thus, $v_{\theta,\rm imp}$ profiles deduced from the DR E_r profiles would lay in between the $v_{\theta,\rm imp}$ profiles predicted by NC theory and the measured CXRS $v_{\theta,\rm imp}$ profiles.

In Figure 7.30a $v_{\theta,\rm imp}$ is shown again for the four L-mode cases as predicted by NC theory (solid lines) and as measured by CXRS (triangle symbols). The fits to the experimental data (dashed lines) were used to reconstruct E_r from CXRS. An overview of the different E_r profiles calculated from experimental data or reconstructed from theoretical predictions is shown in Figure 7.30b. In the Figures 7.30c-f the E_r profiles of each L-mode case are presented separately for clarity and to better distinguish the details. It can be seen that for all four L-mode cases the CXRS E_r is more positive than the DR E_r, while $E_{r,\mathrm{pred}}$ from NC theory is more negative than the DR E_r profiles. The deviations between CXRS E_r and DR E_r are the smallest for the L-mode with the lowest ECRH power, while for the L-modes with $P_{\mathrm{ECRH}} = 2.9$ and $4.0\,\mathrm{MW}$ the deviations between the experimental $E_{r,\mathrm{min}}$ and $E_{r,\mathrm{pred}}$ are very small. A comparison of the DR E_r profiles with $(\nabla_r p_i)/(en_i)$ shows poor agreement for all four L-mode profiles, with the latter being much more negative than the experimental E_r. Also the minimum of $(\nabla_r p_i)/(en_i)$ does not exhibit the trend of an increase with increasing P_{ECRH} as found for $E_{r,\mathrm{min}}$ of the DR measurements. This trend can only be reproduced by the E_r profiles from CXRS and from NC theory, which take the contribution of $v_i \times B$ into account.

The data quality of the DR measurements is generally high in L-modes and it was also shown in Chapter 6 that DR and HES L-mode E_r profiles agree in all drift configurations if geometry effects are taken into account in the HES measurements. Thus, assuming that the E_r profile by DR is the true E_r profile, it can be deduced backwards that the actual edge v_θ profile lays in between the NC prediction and the experimental CXRS measurements.

7.4.1.4 Same Heating Power and Different Plasma Density

Here NC calculations for the L-modes introduced in Section 7.3.1.4 are presented. These four L-modes were all in unfavourable drift configuration and their nominal plasma densities were $\bar{n}_e = 2.5$, 4.0 and $6.0 \times 10^{19}\,\mathrm{m}^{-3}$. The heating power was the same, with $P_{\mathrm{ECRH}} \approx 3.0\,\mathrm{MW}$.

In Figure 7.31 the toroidal main ion rotation and the poloidal impurity and main ion rotation are shown as calculated with NEOART. For completeness also the toroidal impurity rotation is shown, which was given as input for the NC calculations. With increasing plasma density the toroidal intrinsic impurity and main ion rotations increase, until they even become positive and, thus, are counter-current. $v_{\phi,\mathrm{imp}}$ is always a bit more positive than $v_{\phi,i}$ and while $v_{\phi,\mathrm{imp}}$ varies between 10 and 15 km/s for the highest plasma density, $v_{\phi,i} = -10 - 10\,\mathrm{km/s}$. Thus, it accounts for less than 3.5 kV/m to E_r.

The neoclassical poloidal rotations $v_{\theta,\mathrm{imp}}$ and $v_{\theta,i}$ are both predicted to be positive outside of $\rho_{\mathrm{pol}} = 0.96$ and, thus, in the electron diamagnetic drift direction. $v_{\theta,i}$ is again much smaller than $v_{\theta,\mathrm{imp}}$, by about a factor of 5, and it does not exceed a value of about 1.4 km/s for any of the cases. Thus, its contribution to $E_r$is negative, but, in absolute terms, at most 2.8 kV/m. There is no systematic dependence of v_θ on the plasma density visible, although $v_{\theta,i}$ tends to increase more towards the separatrix for the high density L-modes compared to the lowest density L-mode.

The experimental $v_{\theta,\mathrm{imp}}$ data agree relatively well with the NC predictions for the medium and low plasma density cases and radial values smaller than $\rho_{\mathrm{pol}} = 0.985$. For the high density case and for ρ_{pol} values larger than 0.985 the experimental $v_{\theta,\mathrm{imp}}$ data deviate from the NC predictions, because they seem to get slightly negative. $v_{\theta,\mathrm{imp}}$ would then point in the ion diamagnetic drift direction. This negative $v_{\theta,\mathrm{imp}}$ would lead to a more positive E_r profile close to the separatrix than observed with DR. However, it was decided to not reconstruct E_r profiles from CXRS for this set of L-modes since the scatter of the experimental $v_{\theta,\mathrm{imp}}$ data is large and no clear profile shape is visible. Consequently, the

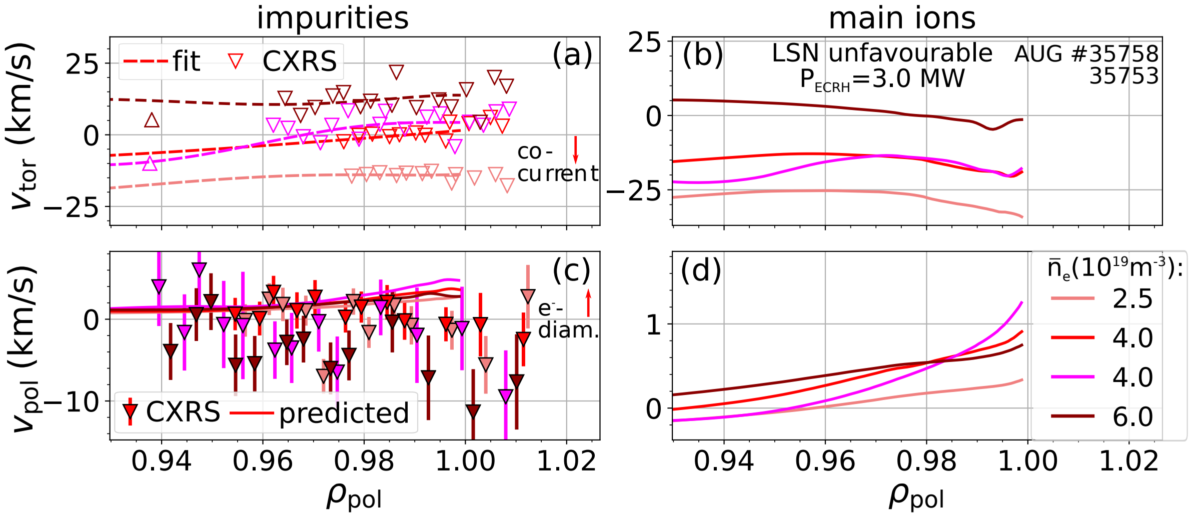

Figure 7.31: *Neoclassical rotations of L-mode plasmas in LSN unfavourable drift configuration of same ECRH power and different plasma density.* (a) Toroidal intrinsic impurity rotation profile (input), (b) predicted toroidal intrinsic main ion rotation, (c) predicted neoclassical poloidal impurity rotation and (d) predicted neoclassical poloidal main ion rotation. The rotation profiles were calculated with NEOART giving the edge kinetic profiles shown in Figure 7.16 as input. The intrinsic impurity and main ion plasma rotations change from co- to counter-current when increasing the plasma density. The neoclassical poloidal rotations are small, positive and do not show a significant dependence on the plasma density. The experimental data from CXRS rather suggest a negative poloidal impurity rotation, which decreases slightly with increased density. The neoclassical poloidal main ion rotation is about a factor of 5 smaller than the impurity rotation (note the different y-scale).

shape of the resulting CXRS E_r profiles would be biased strongly by the fit constraints of $v_{\theta,\mathrm{imp}}$.

Therefore, in Figure 7.32 only the DR E_r profiles and the predicted E_r profiles, using the rotation profiles as predicted by NEOART, are shown four the four L-mode cases together with their respective $(\nabla_r p_i)/(en_i)$ terms. Again the experimental E_r profiles can be better reproduced if the contribution of $v_i \times B$ is taken into account besides $(\nabla_r p_i)/(en_i)$, even if they can not be reproduced exactly in a quantitative way with the calculated NC rotations. Especially for the lowest density L-mode there is a strong upward shift of $E_{r,\mathrm{pred}}$ compared to $(\nabla_r p_i)/(en_i)$, which is due to the large values of $|v_\phi|$ ($|v_\theta|$ is comparably small for all considered cases and does not show strong differences between the different L-mode cases). However, this upward shift is not enough to get good agreement between $E_{r,\mathrm{pred}}$ and the experimental DR E_r profile. The differences there are still large. For the highest density $(\nabla_r p_i)/(en_i)$, $E_{r,\mathrm{pred}}$ and the experimental $E_{r,\mathrm{min}}$ are in good agreement since $|v_\phi|$ is very small. Inside of $\rho_{\mathrm{pol}} = 0.975$ the experimental E_r profile is still better reproduced by $E_{r,\mathrm{pred}}$ than by $(\nabla_r p_i)/(en_i)$. For the medium density cases there is one for which $E_{r,\mathrm{pred}}$ fits more and one for which $E_{r,\mathrm{pred}}$ fits less to the experimental E_r profile. This result strongly depends on the quality of the experimental input data (mainly T_i) and the resulting fits of the input profiles. It can be seen in Figure 7.32 and Figure 7.31d that for these two medium density cases already $(\nabla_r p_i)/(en_i)$ and $v_{\theta,i}$ differ from each other.

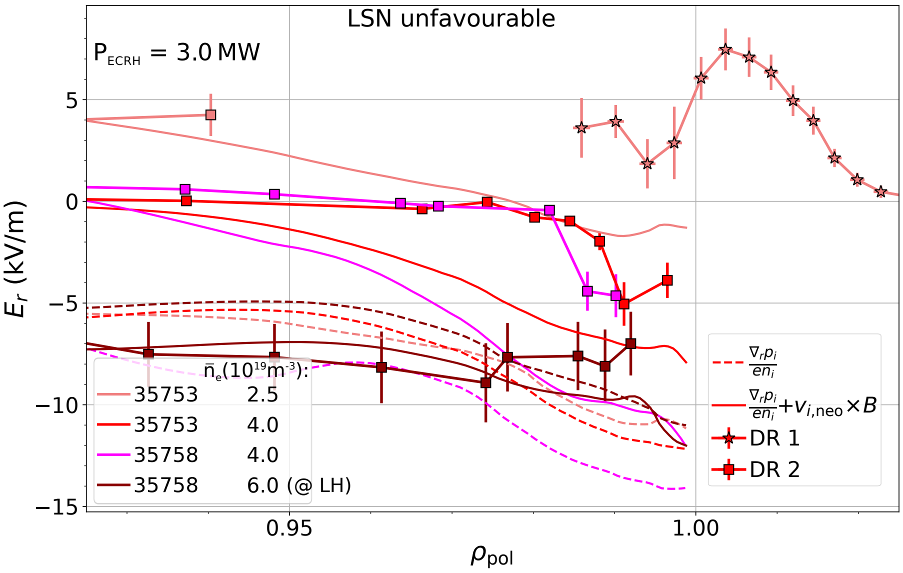

Figure 7.32: *Prediction of E_r with NC theory in LSN unfavourable drift configuration* For the L-mode with highest density the predicted E_r profile using NC rotation profiles and the experimental E_r measured by DR agree. For medium and low density L-modes, the absolute values and the shape of E_r can not be reproduced with the local NC calculations. Still, relative changes observed in the experimental E_r profiles when changing the plasma density are better reproduced with $E_{r,\rm pred}$, which takes the contribution of $v_i \times B$ to E_r into account, than with $(\nabla_r p_i)/(e n_i)$ only.

For the low and medium density cases the experimentally observed steep inner E_r gradient is not reproduced by $E_{r,\rm pred}$. As shown in Section 7.4.1.2 a steeper inner gradient could be achieved for $E_{r,\rm pred}$ by using a less stiff fit of the T_i data, allowing for steeper T_i gradients. However, then the absolute values of $E_{r,\rm pred}$ are even more negative and deviate even stronger from the experimentally observed E_r values.

E_r profiles based on CXRS measurements would again, as for the L-mode cases shown in the section before, lead to even higher E_r profiles in the confined plasma region.

7.4.2 USN Plasmas

In this section L-mode rotation and E_r profiles of USN plasmas in favourable and unfavourable drift configuration are compared with NC predictions from NEOART.

7.4.2.1 Same Heating Power and Same Plasma Density

In Figure 7.33 experimental and NC results of the edge impurity and main ion rotation profiles are shown for the two L-modes which were already presented in Section 7.3.2.1. Both L-modes were heated with $P_{\rm ECRH} = 0.2\,\rm MW$ ($P_{\rm net} \approx 1.0\,\rm MW$) and had the same plasma density (feedback controlled to $\bar{n}_e = 4.5 \times 10^{19}\,\rm m^{-3}$), but a different drift configuration.

In both drift configurations $v_{\phi,\rm imp}$ and $v_{\phi,i}$ are positive and since the signs of $I_{\rm p}$ and, thus, B_θ are kept the same in USN discharges (see also Figure 2.7), both L-mode plasmas exhibit an intrinsic rotation which is co-current. $v_{\phi,i}$ is by about 3 km/s larger than $v_{\phi,\rm imp}$

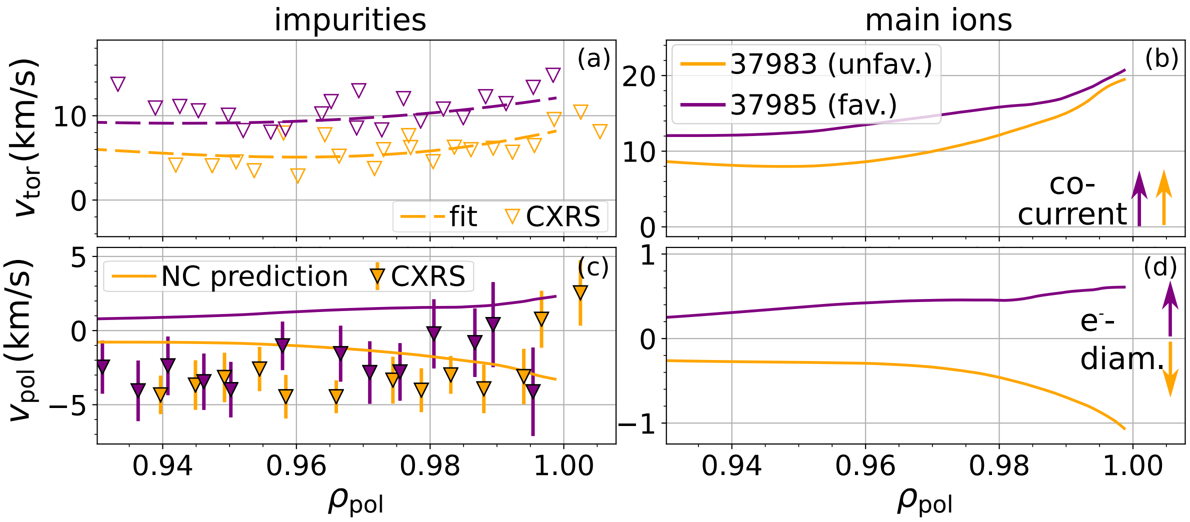

Figure 7.33: *Neoclassical rotation profiles of L-modes in USN favourable and unfavourable drift configuration of same ECRH power and plasma density.* (a) Toroidal intrinsic impurity rotation profile (input), (b) predicted toroidal intrinsic main ion rotation, (c) predicted neoclassical poloidal impurity rotation and (d) predicted neoclassical poloidal main ion rotation. The rotation profiles were calculated with NEOART giving the edge kinetic profiles shown in Figure 7.18 as input. The intrinsic impurity and main ion plasma rotations are both co-current, with v_ϕ being by about 3 km/s larger in favourable compared to unfavourable drift configuration. The neoclassical poloidal rotations are small for both impurities and main ions and of about the same magnitude for both drift configurations. However, v_θ is positive for favourable and negative for unfavourable drift configuration and, thus, in the electron diamagnetic drift direction for both configurations. In unfavourable drift configuration the predicted NC poloidal rotation agrees with the experimental data, while in favourable drift configuration $v_{\phi,\mathrm{imp}}$ is negative and, thus, in the ion diamagnetic drift direction.

in both drift configurations. Additionally, $v_{\phi,\mathrm{imp}}$ and $v_{\phi,i}$ are by about 3 km/s larger in favourable than in unfavourable drift configuration, although towards the separatrix the two $v_{\phi,i}$ profiles get closer and reach a value of about 20 km/s.

As expected the NC poloidal impurity velocity is small for both drift configurations and reaches its maximum (minimum) value of 3 km/s (−3 km/s) for favourable (unfavourable) drift configuration at the separatrix. The magnitude of the main ion rotation is in both drift configurations by a factor of 2 − 3 smaller than the magnitude of the impurity rotation. In favourable drift configuration v_θ from NC theory is positive, while it is negative in unfavourable drift configuration. Thus, in both cases the NC prediction of v_θ points in the electron diamagnetic drift direction, which leads to a decrease of E_r in either drift configuration.

A comparison of $v_{\theta,\mathrm{imp}}$ from NEOART with experimental data shows relatively good agreement in unfavourable drift configuration, although the experimental data tend to be more negative than the NC prediction inside of $\rho_{\mathrm{pol}} = 0.97$. In favourable drift configuration the experimental data do not agree with the NC prediction and are even in opposite direction. Like in unfavourable drift configuration, the experimental $v_{\theta,\mathrm{imp}}$ profile is negative in favourable drift configuration. Thus, in favourable drift configuration $v_{\theta,\mathrm{imp}}$ is in the ion diamagnetic drift direction, which would lead to an increase of E_r.

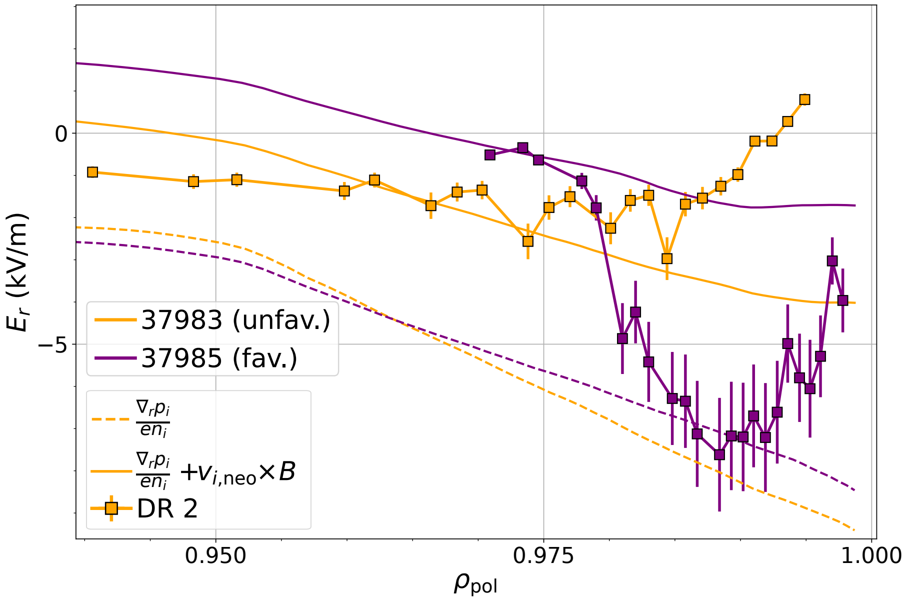

Figure 7.34: *Comparison of E_r profiles with neoclassical predictions in USN favourable and unfavourable drift configuration L-modes of same ECRH power and plasma density.* The DR E_r profile in favourable drift configuration is more negative than the E_r profile in unfavourable drift configuration for otherwise same plasma parameters. In favourable drift configuration the experimental E_r agrees with $(\nabla_r p_i)/(e n_i)$, but disagrees with $(\nabla_r p_i)/(e n_i) + v_{i,\mathrm{NEO}} \times B$, which leads to an increase of $E_{r,\mathrm{pred}}$ by about 6 kV/m. In unfavourable drift configuration $(\nabla_r p_i)/(e n_i)$ is more negative than the experimental E_r profile, but $E_{r,\mathrm{pred}}$ can be brought into agreement with the experimental data if the NC predicted rotations are taken into account in the calculations of $E_{r,\mathrm{pred}}$.

In Figure 7.34 the predicted and measured E_r profiles for both L-modes are shown. The experimental DR E_r profiles have been presented before in Section 7.3.2.1. As discussed there, in favourable drift configuration the measurement reveals a more negative E_r and stronger E_r gradients than observed in unfavourable drift configuration, for otherwise same plasma parameters. The $(\nabla_r p_i)/(e n_i)$ terms are approximately the same for both drift configurations. In favourable drift configuration $(\nabla_r p_i)/(e n_i)$ agrees from $\rho_{\mathrm{pol}} = 0.965$ up to $E_{r,\mathrm{min}}$ (located at about $\rho_{\mathrm{pol}} = 0.987$) with the experimental E_r profile, while in unfavourable drift configuration $(\nabla_r p_i)/(e n_i)$ is much more negative than the experimental E_r profile. If the NC main ion poloidal rotation and the toroidal main ion rotation are taken into account in determining E_r from the radial force balance in unfavourable drift configuration, then the experimental E_r and the predicted E_r profile are in excellent agreement inside of $\rho_{\mathrm{pol}} = 0.98$. This radial value is also the location of $E_{r,\mathrm{min}}$ seen in the experimental data. The absence of a minimum in $E_{r,\mathrm{pred}}$ can have two reasons. First, a stiff fit for the T_i data was used, which does not produce strong changes of the T_i slope. However, a less stiff fit of the experimental data, allowing for steeper T_i gradients, can better reproduce the E_r profile shape, as shown in Section 7.4.1.2. Second, influences of the SOL-E_r which extend into the confined plasma region are not taken into account in NC theory.

In favourable drift configuration the consideration of $v_i \times B$ in the radial force balance leads to an increase of $E_{r,\mathrm{pred}}$ by about 6 kV/m. This produces a strong deviation of $E_{r,\mathrm{pred}}$ from the experimental E_r profile, which was in good agreement with $(\nabla_r p_i)/(e n_i)$. $E_{r,\mathrm{pred}}$ and the experimental E_r profile could, thus, only be brought into agreement if

$v_i \times B \approx 0\,\mathrm{kV/m}$. This would be the case if either $v_{\phi,i}$ were lower or $v_{\theta,i}$ were higher, such that the two velocities cancel each other out in $v_i \times B$. A more positive v_θ would, however, be in contradiction to the experimental v_θ data measured with CXRS, which are negative for the favourable drift configuration (see Figure 7.33c). Also, a less stiff fit of the experimental T_i data, leading to steeper T_i gradients and a more negative $(\nabla_r p_i)/(en_i)$ (see Section 7.4.1.2) could help to produce a slightly more negative $E_{r,\mathrm{pred}}$ than presented in Figure 7.34. However, $E_{r,\mathrm{pred}}$ will always be slightly more positive in favourable compared to unfavourable drift configuration, due to the higher measured $v_{\phi,\mathrm{imp}}$ values in favourable compared to unfavourable drift configuration (see Figure 7.33a,b), which is opposite to the dependency of the measured E_r profiles on the drift configuration.

Even if in USN favourable drift configuration the experimental E_r and $E_{r,\mathrm{pred}}$, reconstructed from NC predictions of the main ion edge rotation profiles, can not be brought into agreement, it is shown in the next two sections that $v_i \times B$ can explain observed differences in L- and I-mode E_r profiles in USN unfavourable drift configuration plasmas.

7.4.2.2 Different ECRH Power and Same Plasma Density

In this section NC calculations for the four L-mode phases in USN unfavourable drift configuration from Section 7.3.2.2 are presented. The resulting edge poloidal and toroidal rotation profiles are shown in Figure 7.35. The NC calculations for the lowest heating power L-mode case were already presented in the previous section.

The intrinsic impurity and main ion rotations are co-current for all four cases, where the main ion rotation is about two times higher than the impurity rotation. The impurity intrinsic rotation behaves not systematically with P_ECRH, whereas the predicted main ion intrinsic rotation increases along with P_ECRH. This increase is, however, not linear in P_ECRH but depends on the electron (ion) edge collisionality (see Figure 7.42), which depends on T_e (T_i) and, thus, can be influenced by P_ECRH. Local NC theory predicts a poloidal rotation (for impurities and ions) which is in the electron diamagnetic drift direction and increases in size with increasing P_ECRH. The only exception is the poloidal main ion rotation inside $\rho_\mathrm{pol} = 0.975$ of the L-mode with highest P_ECRH. For this case $v_{\theta,i}$ is positive and, thus, points in the ion diamagnetic drift direction. Also the experimental CXRS data show small $v_{\theta,\mathrm{imp}}$ which agree with the NC prediction up to $\rho_\mathrm{pol} = 0.98$. For larger radii the experimental data tend to be more positive than their respective NC prediction, although no clear statement on a possible deviation can be made since the scatter in the experimental data can be large.

The predicted E_r profiles calculated with the NC rotation profiles are shown together with the experimental E_r profiles from DR and the respective $(\nabla_r p_i)/(en_i)$ terms in Figure 7.36. It can be seen again that the experimental E_r profiles and $(\nabla_r p_i)/(en_i)$ deviate strongly from each other. If, however, $v_i \times B$ is considered in the prediction of E_r, the experimental profiles and $E_{r,\mathrm{pred}}$ can be bought into agreement, at least close to $E_{r,\mathrm{min}}$. For radial values very close to the separatrix, $\rho_\mathrm{pol} > 0.99$ the experimental E_r and $E_{r,\mathrm{pred}}$ deviate since contributions to E_r from the SOL are not taken into account. However, for values lower than $\rho_\mathrm{pol} \approx 0.975$ $E_{r,\mathrm{pred}}$ and the experimental E_r also do not agree, when a steep inner E_r gradient is present. This steep E_r gradient can not be reproduced with the NC rotation profiles, which are predicted to be relatively flat and do not exhibit strong gradients or a micro-structure as would be needed to bring the experimental data and

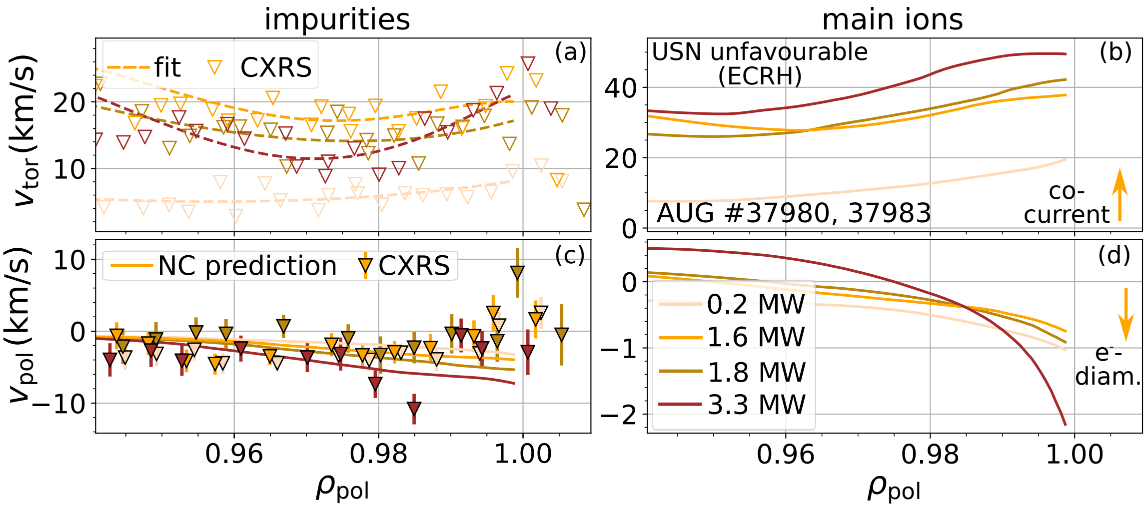

Figure 7.35: *Neoclassical rotation profiles of L-modes in USN unfavourable drift configuration with different ECRH power and same plasma density.* (a) Toroidal intrinsic impurity rotation profile (input), (b) predicted toroidal intrinsic main ion rotation, (c) predicted neoclassical poloidal impurity rotation and (d) predicted neoclassical poloidal main ion rotation. The rotation profiles were calculated with NEOART giving the edge kinetic profiles shown in Figure 7.18 as input. The intrinsic impurity and main ion plasma rotations are both co-current and increase with increasing P_{ECRH}. The neoclassical poloidal rotations are small for both impurities and main ions and of about the same magnitude for both drift configurations. However, v_θ is positive for favourable and negative for unfavourable drift configuration and, thus, in the electron diamagnetic drift direction for both configurations. In unfavourable drift configuration the predicted NC poloidal rotation agrees with the experimental data, while in favourable drift configuration $v_{\phi,\mathrm{imp}}$ is negative and, thus, in the ion diamagnetic drift direction.

the predictions of E_r into agreement. The experimental data and the NC predictions can also not be reconciled with less stiff fits of the T_i data, as it was possible for LSN L-mode plasmas (see Section 7.4.1.2).

7.4.2.3 Different NBI Power and Same Plasma Density

In Figure 7.37 the NC predictions for the edge rotation L-mode profiles of the NBI heated discharge # 37991 are shown. This discharge and the respective L-mode time windows were already introduced in Section 7.3.2.3.

Since these L-modes are heated with NBI and not with ECRH, the toroidal plasma rotation is not purely intrinsic any more. The shape of the edge rotation profile is different compared to all presented edge rotation profiles before. The values of the impurity and main ion rotations are almost the same, with $v_{\phi,i}$ being slightly higher than $v_{\phi,\mathrm{imp}}$. For both ion species the toroidal rotation is positive and thus, co-current and it increases with increasing P_{NBI}.

The predicted NC poloidal rotations point for both species in the electron diamagnetic drift direction. The main ion rotation is by a factor of 3 – 4 smaller than the impurity rotation and does not even reach values of $|v_{\phi,i}| = 1.0\,\mathrm{km/s}$. $v_{\theta,\mathrm{imp}}$ stays approximately constant with increasing P_{NBI}, whereas $v_{\theta,i}$ increases slightly with increasing P_{NBI}. The experimental $v_{\theta,\mathrm{imp}}$ data are again in good agreement with the predicted $v_{\theta,\mathrm{imp}}$ for $\rho_{\mathrm{pol}} <$

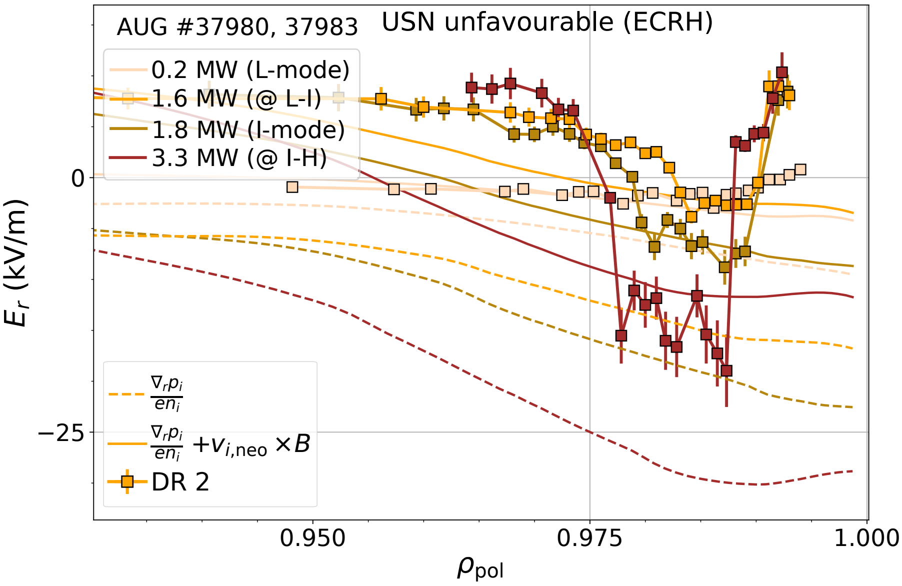

Figure 7.36: *Comparison of E_r profiles with neoclassical predictions in USN unfavourable drift configuration plasmas heated with ECRH.* The DR E_r profile in favourable drift configuration is more negative than the E_r profile in unfavourable drift configuration for otherwise same plasma parameters. In favourable drift configuration the experimental E_r agrees with $(\nabla_r p_i)/(en_i)$, but disagrees with $(\nabla_r p_i)/(en_i) + v_{i,\mathrm{NEO}} \times B$, which leads to an increase of $E_{r,\mathrm{pred}}$ by about 6 kV/m. In unfavourable drift configuration $(\nabla_r p_i)/(en_i)$ is more negative than the experimental E_r profile, but $E_{r,\mathrm{pred}}$ can be brought into agreement with the experimental data if the NC predicted rotations are taken into account in the calculations of $E_{r,\mathrm{pred}}$.

0.98. Towards the separatrix the predictions and the experimental data start to deviate from each other, where the latter start to increase and reach positive values. However, also the quality of the experimental $v_{\theta,\mathrm{imp}}$ data decreases towards the separatrix and there, the uncertainties become large such that within the uncertainties the experimental and the NC $v_{\theta,\mathrm{imp}}$ profiles are not significantly

In Figure 7.38 the respective E_r profiles for the three L-mode plasmas are shown. Again, the experimental DR E_r data and the predicted E_r profiles agree quantitatively better if $v_i \times B$ is taken into account around $E_{r,\mathrm{min}}$. $(\nabla_r p_i)/(en_i)$ deviates strongly from the experimental E_r data. The trend of a steepening of the experimental inner E_r gradient with increasing P_{NBI} is also observed in $E_{r,\mathrm{pred}}$. However, still deviations are found and the strength of the inner E_r gradient is underestimated in $E_{r,\mathrm{pred}}$ compared to the experimental data for all three L-mode cases. It was also tested to fit the T_i profiles with a less stiff fit in order to produce steeper T_i gradients. However, the resulting gradients of $E_{r,\mathrm{pred}}$ did not match the experimental E_r gradients and were still shallower.

7.4.3 Validity of Local Neoclassical Theory

As stated before, NEOART employs local neoclassical theory to determine the neoclassical poloidal and toroidal fluid velocities. For NC theory the main ion distribution function is assumed to be purely Maxwellian, because other contributions are of the order of $L_{p_i}/r_{\mathrm{L,pol}} \approx L_{T_i}/r_{\mathrm{L,pol}}$ smaller [19, 23]. L_{p_i} is hereby the characteristic length of the ion pressure gradient, L_{T_i} the characteristic length of the ion temperature gradient and $r_{\mathrm{L,pol}}$

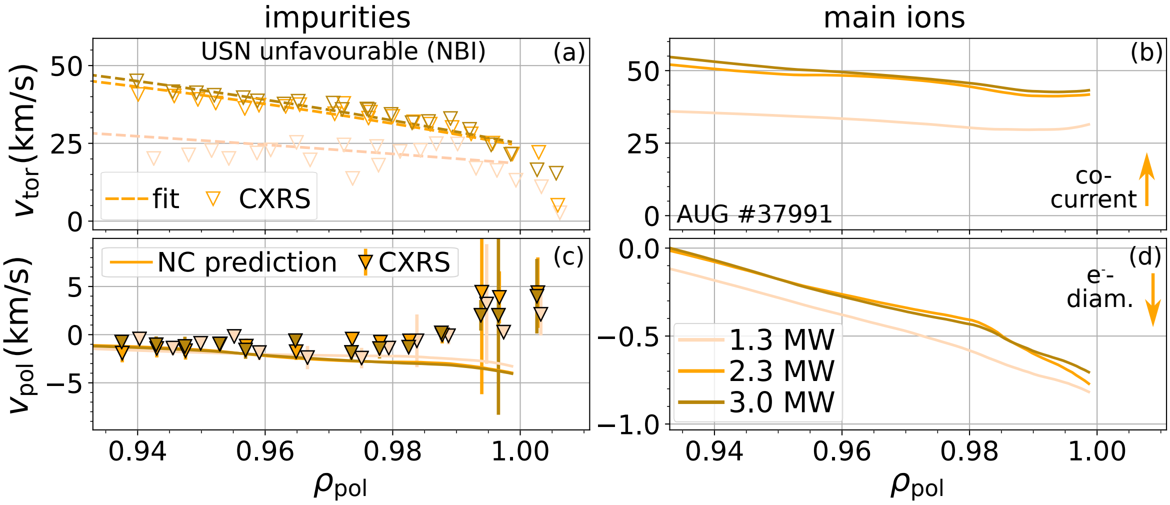

Figure 7.37: *Neoclassical rotation profiles of L-modes in USN unfavourable drift configuration with different NBI power and same plasma density.* (a) Toroidal impurity rotation profile (input), (b) predicted toroidal intrinsic main ion rotation, (c) predicted neoclassical poloidal impurity rotation and (d) predicted neoclassical poloidal main ion rotation. The rotation profiles were calculated with NEOART giving the edge kinetic profiles shown in Figure 7.18 as input. The intrinsic impurity and main ion plasma rotations are both co-current, with v_ϕ being by about 3 km/s larger in favourable compared to unfavourable drift configuration. The neoclassical poloidal rotations are small for both impurities and main ions and of about the same magnitude for both drift configurations. However, v_θ is positive for favourable and negative for unfavourable drift configuration and, thus, in the electron diamagnetic drift direction for both configurations. In unfavourable drift configuration the predicted NC poloidal rotation agrees with the experimental data, while in favourable drift configuration $v_{\phi,\mathrm{imp}}$ is negative and, thus, in the ion diamagnetic drift direction.

the poloidal ion Larmor radius, defined as $r_{\mathrm{L,pol}} = (\sqrt{2m_i k_{\mathrm{B}} T_i})/(ZeB_\theta)$. In the core of fusion plasmas $r_{\mathrm{L,pol}}/L_{p_i} \ll 1$, but this relation does not necessarily hold in the plasma edge region, especially in H-modes, where the ion temperature and density profiles exhibit strong gradients and, thus, the kinetic profiles vary within the ion orbit width. For such cases L_{p_i} and L_{T_i} are small and $r_{\mathrm{L,pol}}/L_{p_i} \ll 1$ does not hold any more and the scale separation used for local NC theory is not always justified. Consequently, global effects have to be taken into account [161].

As shown in [162] global effects can have a strong impact on the resulting NC edge ion velocity profiles at the OMP. For the study presented in [162] local and global NC calculations with the PERFECT code [161, 163] were compared for typical JET H-mode D/He plasmas. The predicted radial toroidal rotation profiles do not change strongly between local and global simulations for main ions and impurities, but the poloidal velocity profiles flip sign at the plasma edge for both ion species. Such a change in v_θ will also change the resulting E_r profiles predicted with the NC poloidal and toroidal rotation profiles.

Therefore, for all here investigated L-mode plasmas the ratio $r_{\mathrm{L,pol}}/L_{p_i}$ was calculated. For the L-mode plasmas $r_{\mathrm{L,pol}}/L_{p_i} \leq 0.5$ over the complete radial range up to the separatrix and, thus, local NC theory could still be valid. However, in the I-mode plasmas, for which L_{T_i} gets small, $r_{\mathrm{L,pol}}/L_{p_i}$ reached values of up to 0.9 at the separatrix. For these plasma

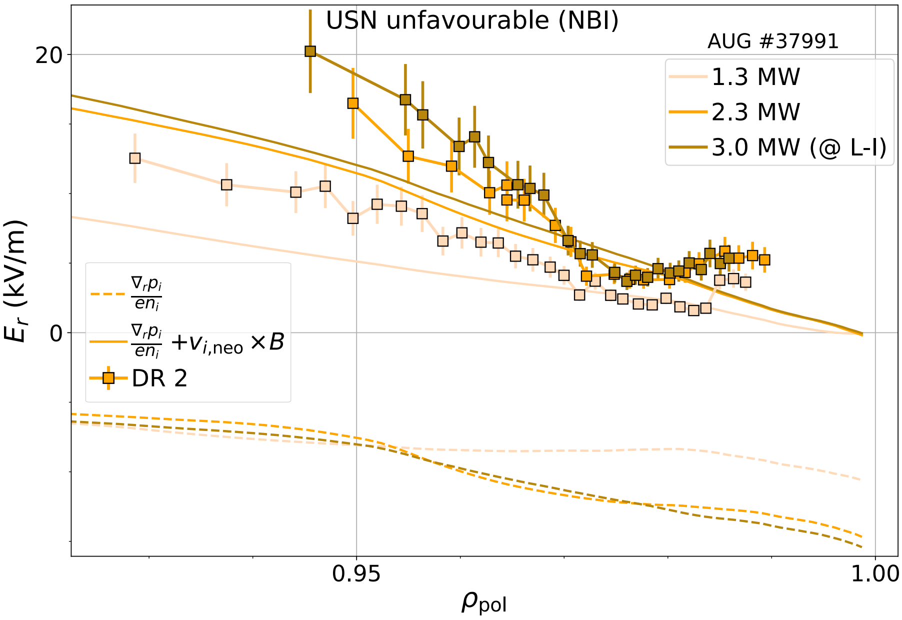

Figure 7.38: *Comparison of E_r profiles with neoclassical predictions in USN unfavourable drift configuration heated with NBI.* The DR E_r profile in favourable drift configuration is more negative than the E_r profile in unfavourable drift configuration for otherwise same plasma parameters. In favourable drift configuration the experimental E_r agrees with $(\nabla_r p_i)/(e n_i)$, but disagrees with $(\nabla_r p_i)/(e n_i) + v_{i,\mathrm{NEO}} \times B$, which leads to an increase of $E_{r,\mathrm{pred}}$ by about 6 kV/m. In unfavourable drift configuration $(\nabla_r p_i)/(e n_i)$ is more negative than the experimental E_r profile, but $E_{r,\mathrm{pred}}$ can be brought into agreement with the experimental data if the NC predicted rotations are taken into account in the calculations of $E_{r,\mathrm{pred}}$.

phases local NC theory is likely not applicable any more and global NC calculations have to be applied. A comparison of local and global NC calculations for these L- and I-mode plasmas and their impact on the resulting predicted rotation and E_r profiles will be the subject of future work.

It should be also mentioned that turbulent effects such as Reynolds stress can add contributions to E_r and, thus, to v_ϕ and v_θ, especially in L-mode where the turbulence level is high. Such contributions can leading to a deviation from NC predictions.

7.5 E_r Profiles at the Confinement Transition

In the following, experimental edge E_r profiles in different drift configurations are compared, which were acquired right before the L-H, L-I or I-H transition.

7.5.1 Favourable Drift Configuration at Different Densities

In the LSN discharge series # 36981 – 36984 P_LH was determined for the nominal plasma densities $\bar{n}_e = 2$, 3 and $4 \times 10^{19}\,\mathrm{m}^{-3}$. Except for the different plasma density all other parameters were identical and $I_\mathrm{p} = 0.8$ MA and $B_\phi = -2.5$ T at the magnetic axis. All four discharges were heated with ECRH. Discharge # 36983 has been investigated in detail before (see Sections 7.3.1.2 and 7.4.1.1) and time traces of this discharge are shown in Figure 7.2. The plasmas entered H-mode at $P_{\mathrm{LH}} = 1.5$, 1.0 and 0.9 MW for the lowest, medium and the highest density, respectively.

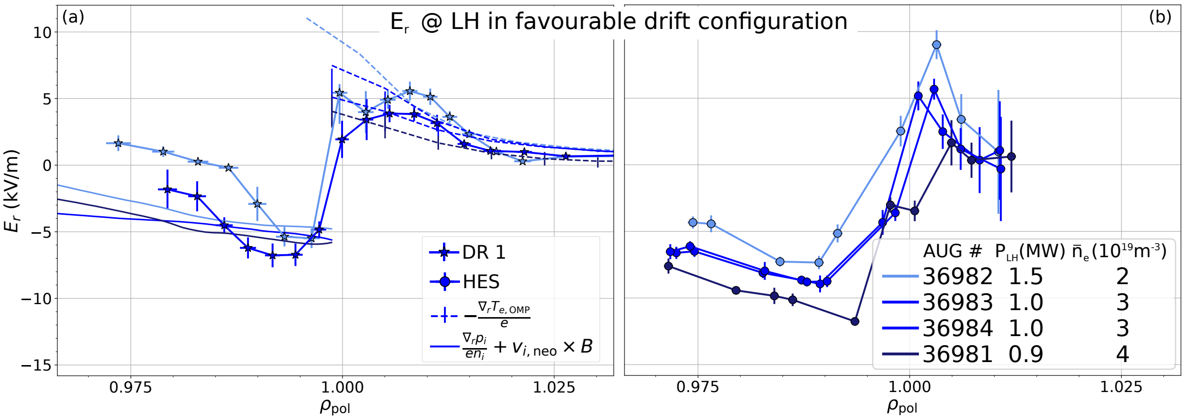

Figure 7.39: *Comparison of E_r profiles at the LH transition in favourable drift configuration at different densities.*

In Figure 7.39a the edge E_r profiles acquired by DR (stars) are shown together with the NC predictions of E_r (solid lines) and $-\nabla_r T_{e,\mathrm{OMP}}/e$ (dashed lines), which predict E_r in the confined plasma and in the SOL, respectively. Only for the lowest two densities it was possible to detect the edge E_r profile with the DR system. Therefore, Figure 7.39b shows the respective E_r profiles measured with HES for all four L-mode cases. The absolute values of the HES E_r profiles differ from their respective DR E_r profiles and they also differ from other HES E_r profiles at similar plasma densities, e.g. from the reference discharge # 35842 (see Figure 7.22). The reason is that for this series of discharges the poloidal head of the HES diagnostics was already de-aligned (see Chapter 6). Modelling of the HES E_r profiles with the synthetic diagnostics (see Section 5.2.5) using the DR E_r profiles as input leads to excellent agreement between the two E_r diagnostics.

The E_r profile shapes look all very similar for the different densities, but with both E_r systems it is observed that $E_{r,\mathrm{min}}$ and $E_{r,\mathrm{max}}$ decrease by about the same amount with increasing plasma density. Since the position of $E_{r,\mathrm{min}}$ and also $E_{r,\mathrm{max}}$ vary only little, the outer E_r gradient stays constant within the measurement uncertainties. The decrease of $E_{r,\mathrm{max}}$ with increasing density is also observed for the $-\nabla_r T_{e,\mathrm{OMP}}/e$ term. The experimental E_r profiles also agree quantitatively with $-\nabla_r T_{e,\mathrm{OMP}}/e$. In the confined region $E_{r,\mathrm{min}}$ agrees with the predicted E_r profile from NC theory, which would also indicate a slight decrease of $E_{r,\mathrm{min}}$ with increasing plasma density, however, not quite as large as observed experimentally.

In the lowest density E_r profile and in all E_r profiles measured by HES, positive spikes in E_r are observed close to the separatrix, which are, however, not significant. As of yet it is unclear whether these spikes are artefacts or real, but SOLPS modelling of SOL plasmas including particle drift effects also predict spikes in the E_r profiles [164, 165].

The observed $E_{r,\mathrm{min}}$ values in LSN favourable drift configuration agree within the measurement uncertainties with former experimental studies at AUG, where a critical $E_{r,\mathrm{min}}$ of about -13.6 ± 4 kV/m was found at the L-H transition for a large range of plasma densities [74, 166], with otherwise comparable parameters of I_{p} and B_ϕ. However, the here presented $E_{r,\mathrm{min}}$ values tend to be less negative and also show a dependence on plasma density. The experimentally observed $E_{r,\mathrm{min}}$ values in [74] were all measured with CXRS. Therefore, the experiments used NBI heating which unavoidably acts as particle source.

Thus, equally low plasma densities as presented in the current work were not accessible. Significantly higher $E_{r,\mathrm{min}}$ and P_{LH} values are, however, according to the present study only observed for the very low densities, which are outside the observation range of [74].

In [166] the focus was on low density plasmas heated with ECRH. Due to a limited number of available DR E_r measurements at the L-H transition, the $E_{r,\mathrm{min}}$ value was approximated with the minimum of the ion diamagnetic term, which in this work was found to be lower than the actual $E_{r,\mathrm{min}}$ value. Furthermore, in [166] the L-H transition was defined as the end of the oscillatory I-phase, whereas in the here presented study it is defined as the transition from L-mode to I-phase (see Section 3.3). As can be seen in Figures 3.1 and 7.2 $T_{i,\mathrm{edge}}$ increases and E_r decreases during I-phase, reaching $E_{r,\mathrm{min}}$ values of about $-15\,\mathrm{kV/m}$ which is also observed in [166].

In the previous L-H transition studies the $E_{r,\mathrm{min}}$ value was used as an approximation of the E_r gradients, assuming a constant radial extension. From this it could be concluded that a constant $E_{r,\mathrm{min}}$ value implies constant E_r gradients at the L-H transition. As it is shown now in this work with the highly resolved L-mode E_r profiles by DR and HES this assumption can not be made. A constant outer E_r gradient at the L-H transition is observed in these four plasmas despite the systematic decrease of $E_{r,\mathrm{min}}$ with increasing $\bar{n}_e$. A statement about the behaviour of the inner E_r gradient at the L-H transition can not be made here since it was not experimentally accessible.

7.5.2 Favourable versus Unfavourable Drift Configuration

7.5.2.1 Low Density Branch

In Figure 7.40 the experimental and predicted E_r profiles of the low density discharges # 36983 (favourable drift configuration) and # 37298 (unfavourable drift configuration) are compared. They transit into H-mode (favourable) or I-mode (unfavourable) directly after the here investigated time windows at $P_{\mathrm{LH}} = 1.0\,\mathrm{MW}$ and $P_{\mathrm{LI}} = 3.0\,\mathrm{MW}$, respectively. Their respective edge profiles have been introduced and discussed in Sections 7.3.1.2 and 7.3.1.3.

Due to the slightly higher plasma density in the unfavourable drift configuration discharge, the DR E_r profile only covers the SOL region, but the E_r profile in the confined region was reconstructed from the HES measurements and the synthetic diagnostics. It can be seen that in the SOL the E_r profile is slightly higher in unfavourable drift configuration compared to favourable drift configuration. In the confined plasma region this discrepancy is even larger, although the outer E_r gradient agrees within the uncertainties ($\pm 3\,\mathrm{kV/m}$) for the two drift configurations. Due to lack of experimental data no statement about the inner E_r gradient can be made.

The predicted E_r profiles employing NC rotation profiles agree within $2\,\mathrm{kV/m}$ with the measured experimental E_r data, although a more detailed comparison of these E_r profiles (with a discussion of uncertainties) is given in Sections 7.4.1.1 – 7.4.1.3. The $-\nabla_r T_{e,\mathrm{OMP}}/e$ profiles are in reasonable agreement with the experimental SOL E_r data and they also show the trend of a slightly higher E_r in unfavourable compared to favourable drift configuration, which can be related to the higher input power.

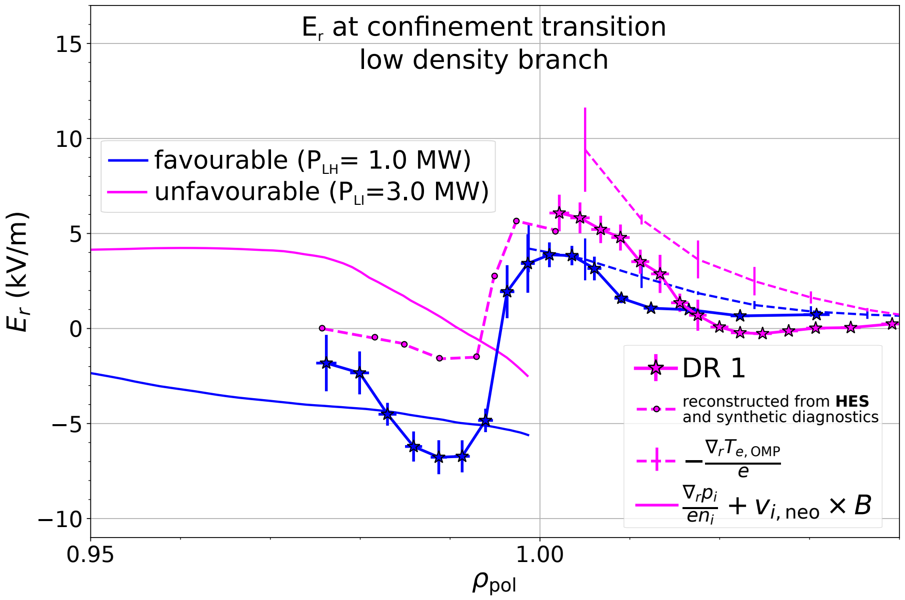

Figure 7.40: *E_r profiles at the confinement transition in favourable and unfavourable drift configuration of low density plasmas.*

7.5.2.2 High Density Branch

In Figure 7.41 three E_r profiles, acquired in a stable L-mode or I-mode phase right before the transition into I-mode or H-mode, are shown for discharges in favourable and unfavourable drift configuration. All three profiles have been introduced before in Section 7.3.2. The discharges were operated at a plasma density of about $4.5 \times 10^{19}\,\mathrm{m}^{-3}$, and are, therefore, located in the high-density branch of P_{LH}. The L-H transition in favourable drift configuration occurred with $P_{\mathrm{net}} = 1.0\,\mathrm{MW}$. In unfavourable drift configuration the L-I transition was achieved with $P_{\mathrm{net}} = 1.8\,\mathrm{MW}$ and the I-H transition with $P_{\mathrm{net}} = 3.3\,\mathrm{MW}$.

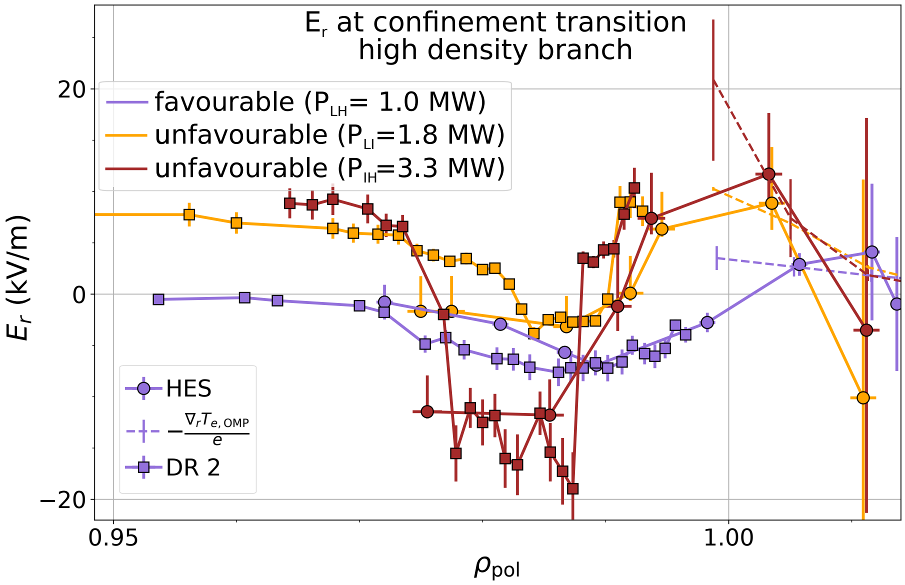

Figure 7.41: *E_r profiles at the confinement transition in favourable and unfavourable drift configuration of high density plasmas.*

The E_r profiles were acquired with the DR and HES diagnostics. Due to the different plasma density in these discharges, also the inner E_r gradient could be resolved by DR.

The E_r profiles of the two diagnostics agree with each other for all three time window. Also, the measured inner and outer E_r gradients are of comparable strength for each of the three E_r profiles. However, a comparison of the three E_r profiles amongst each other shows that they are all different. In favourable drift configuration $E_{r,\mathrm{min}}$ is at about $-8\,\mathrm{kV/m}$ at the L-H transition and, thus, in between the $E_{r,\mathrm{min}}$ values of $-3\,\mathrm{kV/m}$ and $-12\,\mathrm{kV/m}$ measured at the L-I and I-H transition in unfavourable drift configuration. However, the E_r profile at the L-H transition in favourable drift configuration exhibits the flattest inner and outer E_r gradients. The E_r values in the SOL agree with their respective $-\nabla_r T_{e,\mathrm{OMP}}/e$ terms and the lowest $E_{r,\mathrm{max}}$ is found for the favourable drift configuration.

It is also interesting to note that $E_{r,\mathrm{min}}$ and $E_{r,\mathrm{max}}$ are located further outside in favourable compared to unfavourable drift configuration. By now, these radial shifts seem to be real, but they will be investigated in more detail in the near future. For this purpose it is considered to combine the He beam (measurement of n_e and T_e from the He I emission line) and the HES diagnostics (E_r from He II), such that these three quantities are measured simultaneously at the same position in the plasma vessel. Thus, an absolute value of the radial measurement position can be achieved.

7.6 Discussion of Experimental Results

7.6.1 Power Threshold

In Section 7.1 evidence was presented that the H-mode power threshold (P_{LH}) is about 2 – 3 times higher in unfavourable compared to favourable drift configuration for otherwise similar plasma parameters. However, in unfavourable drift configuration a minimum in P_{LH} is not observed as is clearly observed in favourable drift configuration. In favourable drift configuration the occurrence of the minimum in P_{LH} can be understood in terms of e-i coupling (see Section 2.4.2.1) it remains unclear why in unfavourable drift configuration the minimum of P_{LH} is not visible. Possibly the mechanism forming the E_r well, which is modified between the two drift configurations, also influences P_{LH}.

7.6.2 Plasma Behaviour

L-H transitions were observed in unfavourable drift configuration which did not exhibit an I-mode, but rather showed the signatures of an I-phase (they are indicated in Figure 7.1). As of yet the requirements or conditions under which an I-mode or an I-phase develops during the L-H transition are not clear. However, in a larger set of unfavourable drift configuration discharges at AUG the transient I-phase regimes were only observed at relatively high densities in unfavourable drift configuration [151].

7.6.3 E_r in L-mode

7.6.3.1 Evolution

The E_r profile generally follows the development of $(\nabla_r p_i)/(en_i)$ in the transition from L- to H-mode for either drift configuration (see Section 7.2). A significant decrease of $E_{r,\mathrm{min}}$

in the confined plasma region and with it the development of an E_r well with strong E_r gradients is, however, only observed in a regime of improved confinement, like the I-phase or the I-mode. Hereby it could not be experimentally addressed whether the steepening of the $(\nabla_r p_i)/(en_i)$ profile and of the E_r gradients is a cause or a consequence of the confinement improvement.

In L-mode, deviations of the experimentally measured E_r profiles from their respective $(\nabla_r p_i)/(en_i)$ terms are observed. As soon as $(\nabla_r p_i)/(en_i)$ is relatively small, which is the case for L-mode plasmas, the importance of the $v_i \times B$ contribution to E_r increases. This is especially the case for L-mode plasmas of low density, high ECRH power or in NBI heated L-mode plasmas. In these plasmas E_r can not be approximated by $(\nabla_r p_i)/(en_i)$ any more.

In these plasmas it is found that the evolution of E_r with external parameters, like heating power, depends critically on the dependence of $v_i \times B$ and $(\nabla_r p_i)/(en_i)$ on these parameters. In low density plasmas with ECRH heating it was found that $E_{r,\mathrm{min}}$ increases with heating power, because $v_{\phi,i}B_\theta$ increases (due to the decrease of edge collisionality), whereas $(\nabla_r p_i)/(en_i)$ develops weakly (low e-i coupling). In contrast at high density, $(\nabla_r p_i)/(en_i)$ is the dominant contribution to E_r and E_r develops accordingly with $(\nabla_r p_i)/(en_i)$. $v_i \times B$ plays only a minor role. In these conditions (pure ECRH heating) a transition into H-mode is only observed in the high-density plasmas, which hints to an important role of $(\nabla_r p_i)/(en_i)$ and E_r in the H-mode access.

A large contribution of $v_i \times B$ to E_r does not necessarily hinder the development of relatively strong E_r gradients in L-mode. As was seen in NBI heated plasmas in unfavourable drift configuration, steep inner E_r gradients build-up. In NBI heated plasmas v_ϕ exhibits strong edge gradients, which influence via $v_i \times B$ the E_r profile. Thus, the formation and evolution of the E_r profile in L-mode depends critically on the evolution of the $(\nabla_r p_i)/(en_i)$ term and the evolution and shape of $v_i \times B$.

7.6.3.2 Collisionality Dependence and Relation to SOL Flows

As discussed before the intrinsic toroidal impurity and main ion edge rotations $v_{\phi,\mathrm{imp}}$ and $v_{\phi,i}$ (the latter is inferred from local NC theory) are found to be collisionality-dependent (see Figure 7.42a), as is E_r across the separatrix (represented by $E_{r,\mathrm{min}}$ and $E_{r,\mathrm{max}}$ in Figure 7.42b). v_ϕ increases with increasing ion collisionality ($\nu^*_{i,\mathrm{edge}}$), i.e. it becomes less co-current, and E_r decreases with increasing $\nu^*_{i,\mathrm{edge}}$. Since $v_{\phi,i}$ contributes to E_r via $v_{\phi,i}B_\theta$, a correlation between $v_{\phi,i}$ and $E_{r,\mathrm{min}}$, as it is found experimentally (see Figure 7.42c), is expected. However, the observation that $E_{r,\mathrm{max}}$ also correlates with these two quantities suggests that there is an interaction between SOL quantities and the edge rotation of the confined plasma.

Such an observation was already done at the Alcator C-Mod tokamak, where it was found that the SOL flows set the boundary condition for the intrinsic toroidal edge rotation [167]. At Alcator C-Mod measurements of the intrinsic v_ϕ in favourable and unfavourable drift configuration suggested that the intrinsic v_ϕ follows transport driven SOL flows of the high field side. This leads to a co-current intrinsic toroidal edge rotation at the outer mid-plane in favourable and to a counter-current intrinsic toroidal edge rotation in unfavourable drift configuration. In the case of Alcator C-Mod it is concluded that the contribution of $v_{\phi,i}B_\theta$ to E_r would lead to a stronger E_r (i.e. $E_{r,\mathrm{min}}$ more

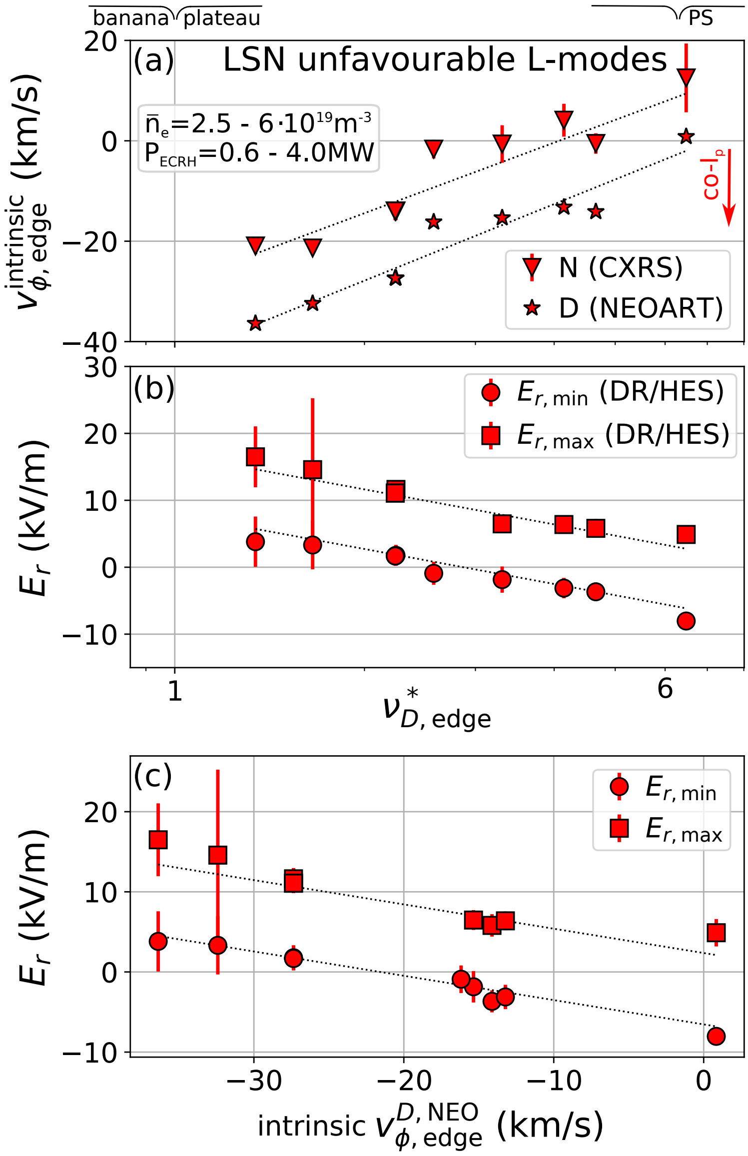

Figure 7.42: (a) The intrinsic toroidal edge v_ϕ and (b) E_r across the separatrix show a dependence on the edge ion collisionality. (c) $v_{\phi,i}$ and E_r correlate because $v_{\phi,i}B_\theta$ is one of the main contributions to E_r. The edge collisionality of deuterium (main ion species) was evaluated at $\rho_{\mathrm{pol}} = 0.98$. The intrinsic toroidal edge $v_{\phi,\mathrm{imp}}$ was measured with CXRS and evaluated at $\rho_{\mathrm{pol}} = 0.98$. The main ion rotation was inferred from neoclassical calculations, using NEOART. The minimum value of E_r in the confined plasma region ($E_{r,\min}$) and the maximum value of E_r in the SOL ($E_{r,\max}$) are determined with Doppler reflectometry (DR) or, if no data are available, with He II spectroscopy (HES). The dotted black lines are linear fits to the data using the same slopes for $E_{r,\min}$ and $E_{r,\max}$, with a different offset.

negative) in favourable and to a weaker E_r (i.e. $E_{r,\min}$ more positive) in unfavourable drift configuration.

The same dependence is not observed at AUG. As the present work shows, in which the intrinsic $v_{\phi,\mathrm{imp}}$ was measured in both LSN and USN plasmas in favourable and unfavourable drift configuration, the inferred intrinsic $v_{\phi,i}$ is always co-current in L-mode plasmas of $\nu_{i,\mathrm{edge}}^*$ in the plateau regime. Only for one case in LSN favourable drift configuration, an L-mode of very high edge ion collisionality, for which $\nu_{i,\mathrm{edge}}^*$ is already in the Pfirsch-Schlüter (PS) regime, $v_{\phi,i}$ is found to be counter-current (see Figure 7.42a). For all other plasma configurations of comparable $\nu^*_{i,\mathrm{edge}}$ in the PS-regime $v_{\phi,i}$ is deduced to be co-current.

As soon as $v_{\phi,i}$ is co-current, $v_{\phi,i}B_\theta$ is positive and leads to an increase of E_r. However, a more positive E_r does not imply that the respective E_r gradients are weaker. As it was shown in this work, depending on the shape of the actual rotation and diamagnetic ion pressure gradient profiles the complete edge E_r profile can be shifted upwards, leaving the inner and outer E_r gradients unchanged (see Section 7.3.1.3). In some other cases the inner E_r gradient was found to steepen in L-mode either due to steepening of the gradient in the $v_i \times B$ profile (see Section 7.3.2.3) or the gradient of the $(\nabla_r p_i)/(en_i)$ profile (see Section 7.3.2.2). Also the outer E_r gradient is not necessarily constant in L-modes as Figure 7.42 would suggest, because a variation of the radial position of $E_{r,\mathrm{max}}$ and $E_{r,\mathrm{min}}$ is possible, leading to a stronger or a weaker outer E_r gradient. Therefore, it is not sufficient to deduce the strength of the E_r gradients solely from the minimum value of the edge E_r profile as has been done in several studies before [74, 152, 166]. As it is discussed in the following section, the shape of the L-mode edge E_r profiles is also substantially different between plasmas in favourable and unfavourable drift configuration.

7.6.3.3 Favourable and Unfavourable Drift Configuration

E_r profiles were presented featuring L-mode pairs in favourable and unfavourable drift configuration, but same plasma density and heating power. The edge kinetic electron and ion profiles and their respective gradients show little difference between the two drift configurations, thus, $(\nabla_r p_i)/(en_i)$ is found to be the same within the measurement uncertainties. Small differences were found in the toroidal rotation profiles, where $v_{\phi,i}$ was always slightly more co-current if B_ϕ was reversed (i.e. in LSN unfavourable and in USN favourable drift configuration). This is in contrast to the measured E_r profiles, which were always found to exhibit a more negative $E_{r,\mathrm{min}}$ and a stronger inner E_r gradient in favourable compared to unfavourable drift configuration. In general, for same plasma parameters the E_r profiles are the edge profiles which differ most from each other between favourable and unfavourable drift configuration.

Not only $E_{r,\mathrm{min}}$ is more positive in unfavourable compared to favourable drift configuration, but also its position is found to be further inside the plasma, at about $\rho_{\mathrm{pol}} \approx 0.98$ in unfavourable compared to $\rho_{\mathrm{pol}} \approx 0.99$ in favourable drift configuration (see Figures 7.10c and 7.18f). Also $E_{r,\mathrm{max}}$ is located further inside in unfavourable drift configuration, where it can be found even in the confined plasma region. Thus, the outer E_r gradient is found to be weaker or of comparable strength in unfavourable compared to favourable drift configuration, depending on the exact positions of $E_{r,\mathrm{min}}$ and $E_{r,\mathrm{max}}$. The inner E_r gradient is always found to be steeper in favourable compared to unfavourable drift configuration for otherwise identical plasma parameters.

If the paradigm of the suppression of edge turbulence by a large enough shear in $v_{E\times B}$ velocity holds, the observed differences in the E_r profiles between the two drift configurations could explain the differently high H-mode power thresholds for the two drift configurations. In this theoretical framework, more heating power would be needed in unfavourable drift configuration in order to reach a steep enough E_r gradient to suppress the edge turbulence. However, in unfavourable drift configuration it is not always found that the edge E_r gradients steepen as soon as the input power is increased, but it can be even the opposite effect as was discussed earlier. Furthermore, it is also not observed that similarly steep edge E_r gradients (neither the inner nor the outer E_r gradient) are reached at the respective confinement transition for plasma pairs in favourable and unfavourable drift configuration. This can be seen from Figures 7.40 and 7.41.

These experimental observations leave room for doubts about the importance of the E_r gradients on turbulence suppression and the formation of an edge transport barrier and, thus, on the access to H-mode. For this reason it is planned to do gyro-kinetic calculations on these L-mode plasmas to see whether the measured $E \times B$ shearing rate $\gamma_{E\times B}$ is able to suppress the theoretically predicted turbulent transport at the plasma edge.

7.6.3.4 Comparison to Theory

For both drift configurations it was found that the SOL-E_r measured at the OMP is in good agreement with $-\nabla_r T_{e,\mathrm{OMP}}/e$. This equality is predicted by theory for plasmas, which SOL transport is in the conduction-limited regime. This is the case for all investigated L-mode plasmas (see e.g. Figure 7.11). However, in detail deviations between the experimental E_r and $-\nabla_r T_{e,\mathrm{OMP}}/e$ profiles are found. $E_{r,\max}$ normally agrees quantitatively with $-\nabla_r T_{e,\mathrm{OMP}}/e$, but the profile shapes are often different, with the experimental SOL E_r profiles exhibiting a faster radial decay in into the far SOL than $-\nabla_r T_{e,\mathrm{OMP}}/e$ (see e.g. Figure 7.12). Furthermore, the observed dependence of $E_{r,\max}$ on collisionality is not seen in $-\nabla_r T_{e,\mathrm{OMP}}/e$, whereas a corresponding change of the outer divertor target electron profiles with collisionality is observed (see Figure 7.11). This suggest a more complex interaction between upstream and target SOL quantities and their impact on E_r at the OMP than assumed so far and should be studied with more complex simulations of the SOL, like SOLPS, which can also include drift effects [168].

In the confined plasma region the experimental E_r profiles of the different investigated L-mode plasmas were compared to predictions from neoclassical theory (see Section 7.4). For this purpose the main ion toroidal and poloidal edge rotation profiles as well as the main ion density were computed from experimental edge kinetic profiles using the local NC code NEOART. By employing the radial force balance equation (see Equation 2.34), an E_r profile was inferred from the NC calculations.

It was found that with local NC theory the experimentally observed $E_{r,\min}$ values can be reproduced to a large extent in both drift configurations. Also, relative changes of the L-mode E_r profiles in one specific drift configuration are captured correctly by the neoclassical predictions. However, experimental L-mode E_r profiles of plasma configurations in which B_ϕ is in the normal direction (i.e. $B_\mathrm{t} < 0$, the standard configuration of AUG) are reproduced better by the local NC calculations than L-mode E_r profiles of plasmas in which B_ϕ is reversed. In LSN these are the favourable drift configuration plasmas, but in USN these are plasmas in unfavourable drift configuration. In detail deviations between the experimental E_r profiles and the NC predictions are found. The differences in the experimental E_r profiles between favourable and unfavourable drift configuration L-modes of otherwise same plasma parameters are not reproduced by the NC predictions. The predictions would suggest identical edge E_r profiles for the two drift configurations. Also, the measured inner E_r gradients which are steep are regularly underestimated by the local NC predictions. This discrepancy can not be resolved within the experimental uncertainties, even if the fits of the experimental kinetic edge profiles, which are given as input to the NC calculations, are chosen in a way to allow for steeper gradients in the resulting predicted NC E_r profiles.

A reason for the discrepancy between experiment and theory could be that for the here presented NC calculations local NC theory was applied, which is at the limit of validity in the edge plasma close to the separatrix (see Section 7.4.3). Thus, a global NC code should be tested for predicting the toroidal and poloidal edge rotation profiles. In a theoretical study conducted on JET H-mode plasmas the comparison of global and local NC calculations revealed that especially the poloidal edge rotation is different [162]. As mentioned in Section 7.4.1.3, E_r is very sensitive to v_θ and small variations in v_θ can change the E_r profile substantially. For this reason it is planned in the near future to use perform global NC calculations to predict the edge rotation profiles in the here presented L-mode plasmas and compare them to the local NC calculations and the experimental data.

It should be mentioned that a discrepancy between the experimental data and the NC predictions can also hint to large turbulent transport, as it is often observed in L-modes [89]. Non-collisional transport may also cause $\nabla_r \mathit{\Gamma} \neq 0$, which perturbs the NC flow equilibrium on a flux surface.

8 The Isotope Effect of the L-H Transition

A dependence of the H-mode power threshold (P_{LH}) on the main ion plasma species was found already in early isotope experiments [64]. For hydrogenic species P_{LH} scales with the inverse of the main ion mass A_i. Thus, in hydrogen (H) plasmas P_{LH} is about two times larger than in deuterium (D) plasmas. The H-mode power threshold for pure helium (He) plasmas varies for different machines between 1 to $1.8 \times P_{\text{LH}}(\text{D})$ [14, 64, 70]. At AUG it was observed that $P_{\text{LH}}(\text{He}) \approx P_{\text{LH}}(\text{D})$ [55].

In order to elucidate the underlying mechanism leading to a changed P_{LH} for the different ion species, experimental measurements of the edge radial electric field (E_r) and calculations of the total edge ion heat flux ($Q_{i,\text{edge}}$) were performed in pure D, He and H plasmas, in H plasmas with He doping and in mixed HD plasmas. The results of these experiments are presented in the following.

8.1 Investigations in Pure D, H and He Plasmas

The presented measurements are all taken from discharges which were designed similar to the reference discharge (see Section 3.2), but applied to D, H and He plasmas. They have same global parameters, namely $B_\phi = -2.5\,\text{T}$ and $I_\text{p} = 0.8\,\text{MA}$ at the magnetic axis and $q_{95} = -5$, and were heated with either ECRH or NBI. All discharges were fuelled feed-forward and $\bar{n}_e$ was chosen to be close to the density minimum, $\bar{n}_{e,\text{min}}$, which is about $4 \times 10^{19}\,\text{m}^{-3}$ at AUG for all three ion species [55, 73]. Please note that not all plasmas have the exact same $\bar{n}_e$ (this can be seen e.g. in Figure 8.1), because different gas fuelling rates are needed for the different ion species to reach the same plasma density. In H plasmas the fuelling rate is about 2 times larger than in D plasmas, which is connected to increased L-mode particle transport in H compared to D [169]. In He plasmas the pumping efficiency of the cryo-pumps is strongly reduced, thus, only a tiny amount of He fuel is needed [170].

The time point of the L-H transition was chosen as described in Section 3.3. The plasmas show alike behaviour, independent of the main ion species, with a dithering I-phase at the transition from L- to H-mode as shown for a pure D plasma in Figure 3.1.

The purity of the H plasmas is a bit lower than of D plasmas due to remaining deuterium from previous experiments. It is given in terms of relative hydrogen content defined as

$$f_\text{H} = n_\text{H}/(n_\text{D} + n_\text{H}), \tag{8.1}$$

with n_H and n_D being the hydrogen and deuterium ion density, respectively. At AUG it is measured as a radially averaged value with the neutral particle analyser (NPA) [171]. In all here presented pure H experiments $f_\text{H} \approx 0.95$. It should also be noted that for a pure He plasma the He concentration c_{He}, defined as

$$c_{\mathrm{He}} = n_{\mathrm{He}}/n_e, \tag{8.2}$$

is 50 %, since He has a charge number $Z_{\mathrm{He}} = 2$.

8.1.1 Power Threshold

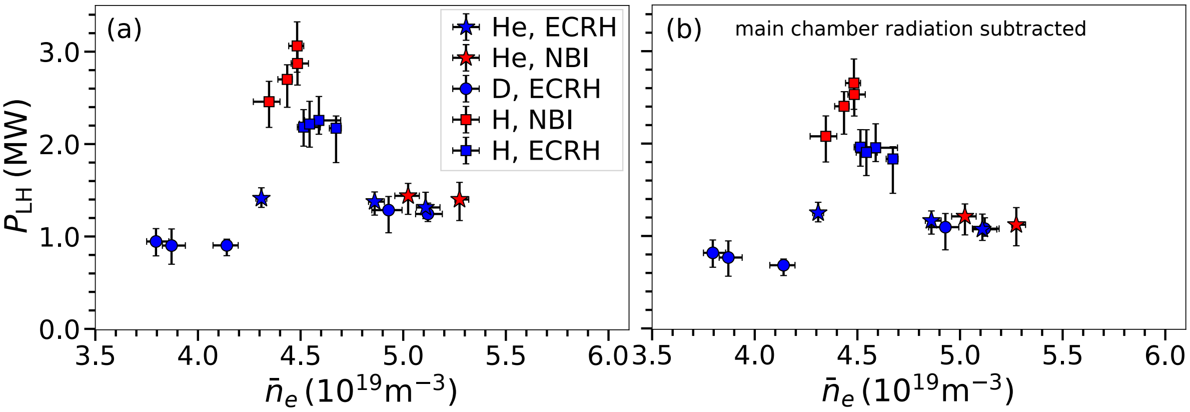

Figure 8.1: (a) H-mode power threshold and (b) loss power at the L-H transition of deuterium, hydrogen and helium plasmas plotted against the average electron density. For comparable densities and similar plasma parameters, P_{LH} of hydrogen is a factor of 2 – 3 higher than of deuterium, with NBI heated H plasmas exhibiting a higher threshold than ECRH heated H plasmas. P_{LH} of helium is a factor of 1 to 1.2 higher than P_{LH} of deuterium at AUG. For D and He plasmas no difference in P_{LH} with heating power is found.

Figure 8.1a shows P_{LH} of the investigated pure He, H and D plasmas plotted against their line-averaged electron density $\bar{n}_e$. P_{LH}(D) is between 0.9 and 1.2 MW for the investigated plasma parameters. P_{LH}(H) is at least two times higher than P_{LH}(D), where the higher values of 3.2 MW are observed in NBI and the lower values of about 2.3 MW in ECRH heated H plasmas. A possible explanation for this difference is given in detail in Section 8.2.1.1 and is related to a critical $Q_{i,\mathrm{edge}}$ at the LH transition. The data in Figure 8.1 also suggest that P_{LH}(He) is at most increased by 20 % compared to P_{LH}(D). A dependence of P_{LH} on the heating mechanism is neither observed for He nor for D plasmas in the investigated density range. As can be seen in Figure 8.1b the main chamber radiation is of the order of 200-400 kW for all discharges and, thus, reduces the overall P_{LH} values, but not the relative changes between P_{LH} of the different plasma species.

Please note, the impression gained from Figure 8.1 that there is a maximum in P_{LH} is due to the fact that P_{LH} values of plasmas with different main ion species and slightly varying $\bar{n}_e$ are compared and is not a contradiction to the existence of $\bar{n}_{e,\mathrm{min}}$. If for each of the three different main ion species a complete density scan would be done, then P_{LH} of the respective ion species would again show a parabolic dependence on $\bar{n}_e$ (with different offsets), exhibiting its minimum at $\bar{n}_e \approx 4 \times 10^{19}\,\mathrm{m}^{-3}$, as shown in Figure 2.4b.

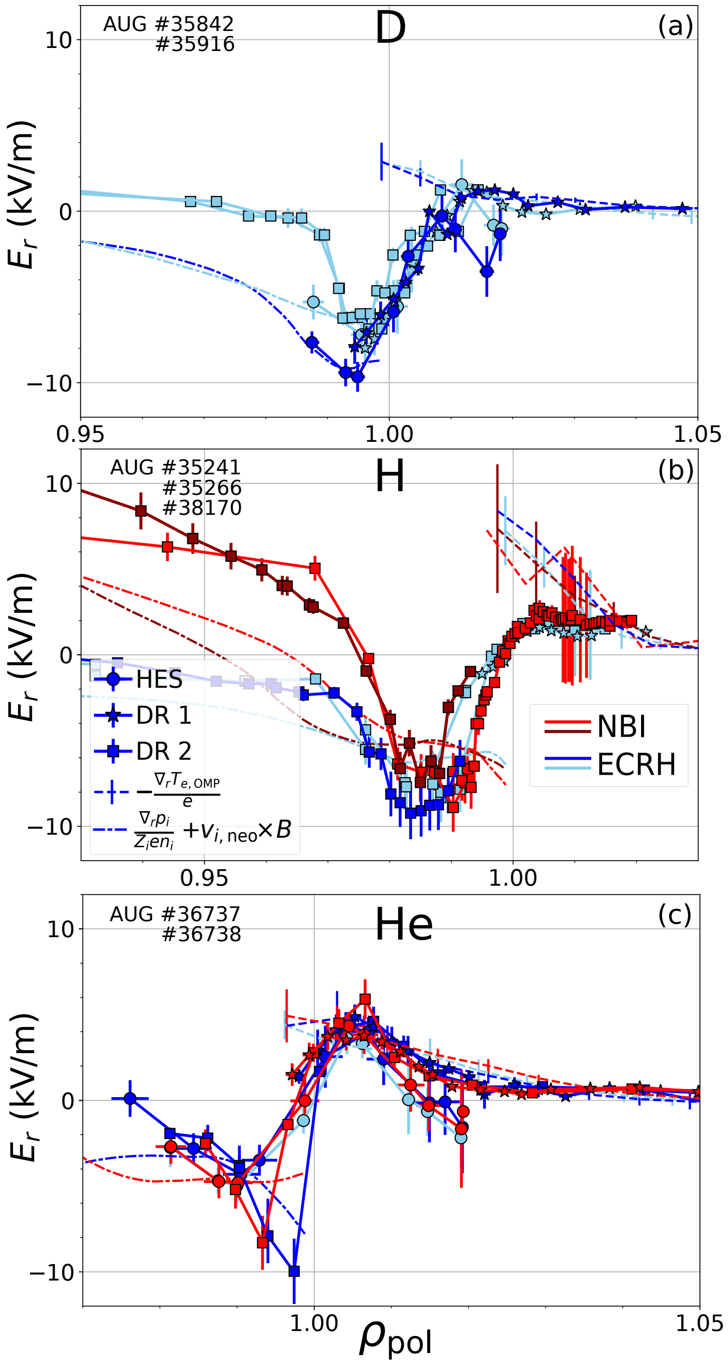

Figure 8.2: *Edge radial electric field profiles at the L-H transition.* (a) Deuterium, (b) hydrogen and (c) helium plasmas. At similar plasma parameters the outer E_r gradient across the separatrix is of comparable strength. In hydrogen the inner E_r gradient varies depending on the employed heating scheme and is stronger for NBI than for ECRH plasmas. For all three plasmas species the $E_{r,\mathrm{min}}$ value in the confined plasma region agrees with E_r deduced from the radial force balance with neoclassically predicted rotation profiles (dashed-dotted lines). $E_{r,\mathrm{max}}$ in the SOL agrees with $-\nabla_r T_{e,\mathrm{OMP}}/e$ (dashed lines) for He and D plasmas, but not for H plasmas.

8.1.2 Edge Radial Electric Field

Figure 8.2 presents edge E_r profiles of pure D, He and H plasmas, measured during the last stable L-mode phase before the L-H transition. For D and He plasmas the presented E_r

profiles are taken from the He II spectroscopy (HES) and the Doppler reflectometry (DR) diagnostics, while for H plasmas only DR E_r profiles are available. For these discharges the E_r profiles of the HES diagnostics did not have to be corrected for geometry effects as described in Chapter 6. The DR profiles were aligned using the approach described already in Section 7.3, whereas the HES E_r profiles were not shifted radially. The experimental E_r profiles are also compared to NC predictions (dashed-dotted lines in Figure 8.2) by calculating the NC main ion rotations for the respective main ion species (D, H, He) with the local NC code NEOART (for further details see Section 7.4).

In D plasmas (Figure 8.2a) $E_{r,\mathrm{min}}$ has a value between -7.0 and $-10\,\mathrm{kV/m}$, depending on the exact plasma density. In the SOL $E_{r,\mathrm{max}}$ is about $2.0\,\mathrm{kV/m}$, which is found to agree well with $-\nabla_r T_{e,\mathrm{OMP}}/e$. The strength of the outer E_r gradient agrees well between the two diagnostics and they give a maximum value of about $1.0\,\mathrm{MV/m^2}$ for it. The inner E_r gradient is found to be a bit steeper at the L-H transition than the outer E_r gradient and reaches absolute values of 1.5 to $2.0\,\mathrm{MV/m^2}$. This difference is, however, within the uncertainties of the experimentally determined E_r gradients, which are $\pm 0.5\,\mathrm{MV/m^2}$. The experimental $E_{r,\mathrm{min}}$ values are in agreement with the ones deduced from neoclassical (NC) calculations, but as already seen before (see Section 7.4), the inner E_r gradient is found to be stronger in the experiment than as it is predicted by NC theory. Interestingly, the equilibrium reconstruction suggests that the E_r profiles in D plasmas are still negative at the separatrix, reaching positive values only at about $\rho_{\mathrm{pol}} = 1.01$. This is different to the E_r profiles in H and He plasmas, where the measurements indicate the zero-crossing of the outer E_r gradient to be located at or very close to the separatrix. Given the radial uncertainties of about 5 mm at the separatrix attributed to the equilibrium reconstruction [172], this may not be a significant difference.

In H plasmas (Figure 8.2b) the experimentally measured $E_{r,\mathrm{min}}$ varies between -6.0 and $-8.0\,\mathrm{kV/m}$ and agrees with its respective neoclassical predictions. The E_r values in the SOL are slightly higher than in D plasmas with $E_{r,\mathrm{max}}$ between 2.0 and $4.0\,\mathrm{kV/m}$. These higher SOL E_r values are reasonable since more heating power is applied to the plasma at the L-H transition in H plasmas compared to D plasmas, which leads to a higher ∇T_e in the edge/SOL of the plasma. However, the measured SOL E_r values in the radial range $\rho_{\mathrm{pol}} = 1.00$ to 1.02 are for all four H plasma cases (NBI and ECRH) lower than their respective $-\nabla_r T_{e,\mathrm{OMP}}/e$ term.

For both heating schemes the E_r profiles in H plasmas seem to be shifted radially further inside compared to D plasmas. With this, the position of $E_{r,\mathrm{min}}$ is at about $\rho_{\mathrm{pol}} \approx 0.985$ in H plasmas compared to $\rho_{\mathrm{pol}} \approx 0.995$ in D plasmas and also the position of $E_{r,\mathrm{max}}$ in the SOL is shifted to lower ρ_{pol} values. The outer E_r gradient is of comparable strength for ECRH and NBI heated plasmas and with a maximum value of $2.0\,\mathrm{MV/m^2} \pm 0.5\,\mathrm{MV/m^2}$ slightly stronger in H than in D plasmas. A bigger difference is found in the inner E_r gradient between NBI and ECRH heated H plasmas. The maximum absolute value of the inner E_r gradient might not be so different (about $1.5\,\mathrm{MV/m^2}$ for NBI and $1.0\,\mathrm{MV/m^2}$ for ECRH), but the radial extension of this steep gradient region is larger for NBI than for ECRH plasmas. At $\rho_{\mathrm{pol}} \approx 0.97$ $E_r \approx -2.0\,\mathrm{kV/m}$ for ECRH, and about $4.0\,\mathrm{kV/m}$ for NBI heated H plasmas, while $E_{r,\mathrm{min}}$ is approximately the same independent of the external heating. This trend is also reproduced by NC calculations and can be attributed to differences in the toroidal edge rotation profiles. Indeed the $v_{\phi,\mathrm{imp}}$ profiles are found to be strongly different between NBI and ECRH heated H plasmas, as shown later in this section, whereas the experimental edge T_i profiles and $(\nabla_r p_i)/(e n_i)$ are the same within the measurement uncertainties.

In He plasmas (Figure 8.2c) differences between the HES and DR E_r profiles are observed around $\rho_{\mathrm{pol}} = 0.995$. These can not be attributed to the known resolution effects of the HES diagnostics (see Chapter 6), because a radial plasma sweep (see Section 3.1.2) was applied in the measurement phase, which increases the radial resolution of the HES diagnostics. The HES measurements deliver a less negative $E_{r,\mathrm{min}}$ of about $-5.0\,\mathrm{kV/m}$, whereas DR gives an $E_{r,\mathrm{min}}$ of -8.0 to $-10\,\mathrm{kV/m}$. Also the position of $E_{r,\mathrm{min}}$ is different. According to HES $E_{r,\mathrm{min}}$ is located at about $\rho_{\mathrm{pol}} = 0.99$, whereas for DR it is located at $\rho_{\mathrm{pol}} \approx 0.995$. The NC predictions agree in one case better with the HES and in the other case better with the DR measurements, but it has to be noted that the uncertainties on these reconstructed E_r profiles are large. As of yet, it is unclear for which reason the two E_r diagnostics disagree in these plasma conditions (He as main ion), since they are normally in good agreement. This will be investigated systematically in the future.

In the SOL the two measurement techniques agree very well. It is found that $E_{r,\mathrm{max}}$ is about $6.0\,\mathrm{kV/m}$ in He plasmas, which is much higher compared to the values in H and particularly in D plasmas at comparable density. Furthermore, the SOL-E_r is in excellent agreement with $-\nabla_r T_{e,\mathrm{OMP}}/e$ over the complete radial extent in the SOL. This agreement can maybe be related to the low pumping efficiency of He by cryogenic pumps located in the lower divertor of AUG [170]. This leads to a high particle recycling at the divertor target, which is the nature of the conduction-limited regime.

The outer E_r gradient is, depending on the employed E_r diagnostics, of equal steepness (HES) or steeper (DR) than the outer E_r gradient in D and H plasmas. As for P_{LH}, no significant difference is found in the E_r profiles between ECRH and NBI heated He plasmas. This can be likely attributed to a similar $v_{\phi,i}$ profile and is supported by measurements of $v_{\phi,\mathrm{imp}}$ in these L-mode phases, which do not show a significant difference between NBI and ECRH cases.

In total it is found that T_i at the plasma edge is, within the measurement uncertainties, the same at the L-H transition for pure D, H and He plasmas. Also the outer E_r gradient is found to be comparable at the L-H transition for all three plasma species. On average it changes by about $10\,\mathrm{kV/m}$ within $1.5\,\mathrm{cm}$. In contrast the inner E_r gradient is found to be different at the L-H transition in NBI compared to ECRH heated H plasmas. In order to further investigate this difference, edge ion profiles of three different hydrogen L-mode phases with comparable plasma density and same heating power ($P_{\mathrm{heat}} = 2.0\,\mathrm{MW}$), but one heated with NBI and two with ECRH, are shown in Figure 8.3.

As can be seen in Figure 8.3a T_i is slightly higher in the NBI compared to the ECRH case, but its gradient is slightly weaker. Therefore, the edge ion pressure gradient is, within the experimental uncertainties, the same (see Figure 8.3c, dotted line). The toroidal impurity rotation profiles, measured on N VII with CXRS, are different, with $v_{\phi,\mathrm{imp}}$ being positive and increasing towards the plasma core for the NBI heated case. For the ECRH case $v_{\phi,\mathrm{imp}}$ is close to zero, or slightly negative, and increases only close at the separatrix to positive values. This difference in the rotation profiles leads to a more pronounced inner E_r gradient in the NBI compared to the ECRH plasmas, as shown experimentally in Figure 8.3b.

These measurements are in contradiction to former observations made at the DIII-D tokamak and at AUG, where it was found that P_{LH} and the critical $Q_{i,\mathrm{edge}}$ at the L-H transition increase with input torque [58,70]. In these works it was argued, based on $v_{\phi,\mathrm{imp}}$ measurements at one radial position at the plasma edge, that an increased co-current external torque input increases $v_{\phi,\mathrm{edge}}$ in the co-current direction and, thus, weakens E_r,

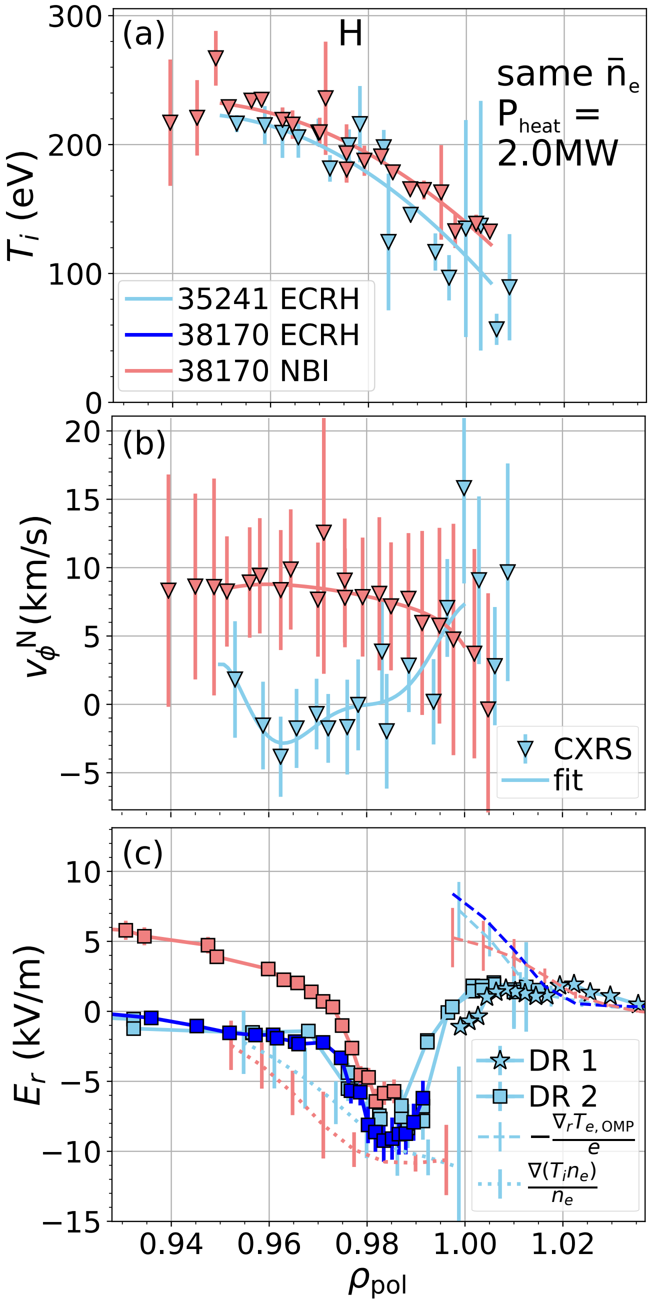

Figure 8.3: *Edge profiles in hydrogen plasmas of same plasma density and heating power.* (a) Ion temperature, (b) nitrogen impurity toroidal rotation and (c) measured radial electric field, $(\nabla_r p_i)/(en_i)$ and $-\nabla_r T_{e,\mathrm{OMP}}/e$ for two L-modes heated with 2.0 MW of NBI (lightred) and ECRH (blue), respectively. Although the edge ion temperature is slightly higher for the NBI case, the resulting $(\nabla_r p_i)/(en_i)$ profile (dotted line) is the same as for the ECRH case. The rotation profiles are strongly different, leading via $v_i \times B$ to a stronger inner E_r gradient for the NBI compared to the ECRH case.

i.e. reduces the E_r gradients. As a consequence, more heating power and a higher critical $Q_{i,\mathrm{edge}}$ is needed to trigger the L-H transition, due to a reduced $\boldsymbol{E}\times\boldsymbol{B}$ shear. However, the experiments at the DIII-D tokamak and at AUG were conducted in the low-density branch of P_{LH}. As discussed in Chapter 7, the interaction between $v_i \times B$ and $(\nabla_r p_i)/(en_i)$ is quite complex and can lead to substantial differences in the development of the edge E_r profiles in L-mode plasmas located in the low-density branch of P_{LH} (for which indeed an upward shift of $E_{r,\mathrm{min}}$ with increasing edge rotation was observed) compared to the development of E_r in plasmas of the high-density branch (for which a steepening of the E_r gradients with increasing heating power was observed). Therefore, in Section 8.2.1 a different explanation for the higher P_{LH} of NBI compared to ECRH H plasmas will be given, which holds for the here presented L-H transition experiments of the high-density branch. This explanation still assumes that a critical $Q_{i,\mathrm{edge}}$ is needed to enter H-mode, as observed at AUG [58], but it is independent of the plasma edge rotation.

8.2 Investigations in Mixed Main Ion Species Plasmas

This part of the study has been published in [173] and is motivated by recent findings at the JET tokamak, where a reduction of $P_{\mathrm{LH}}(\mathrm{H})$ by up to 40 % was observed in NBI heated H plasmas when a He concentration of less than10 % was added. Furthermore, a non-linear dependence of P_{LH} on the relative hydrogen content, f_{H}, was found in ion cyclotron resonance heated (ICRH) mixed hydrogen-deuterium (HD) plasmas [69]. A doubling of P_{LH} was found at JET between $f_{\mathrm{H}} = 0.0$ and 0.2, and another increase of P_{LH} by about 20 % for $f_{\mathrm{H}} = 0.9$.

8.2.1 H Plasmas with He Doping

A series of discharges (# 35241 – 35245 and # 35266) was performed in which subsequently an increasing amount of He was puffed into pure H plasmas ($f_{\mathrm{H}} \approx 0.95$). In this way c_{He} was gradually increased from below 1 % to almost 20 %. Both ECRH and NBI power ramps were used to trigger the L-H transition in these plasmas. The time point of the L-H transition was taken as defined in Section 3.3 and the presented experimental kinetic profile measurements were collected from the last stable L-mode phase right before the transition into I-phase.

8.2.1.1 Power Threshold and Edge Ion Heat Flux

Figure 8.4a displays $P_{\mathrm{LH}}(\mathrm{H})$ plotted against c_{He}. The figure shows that there is no dependence of P_{LH} on c_{He}. This holds for both the NBI and the ECRH discharges, although for the former only the range of $c_{\mathrm{He}} \approx 1 - 5\,\%$ was investigated, whereas for the latter a fine scan of c_{He} up to 10 % was performed. $\bar{n}_e$ varied in these discharges from 4.4 to $5.8 \times 10^{19}\mathrm{m}^{-3}$, i.e. the discharges are performed in the high-density branch close to $\bar{n}_{e,\mathrm{min}}$. The highest densities were reached in the discharges with the largest c_{He}, since the He gas was puffed additionally to the constant H gas puff.

n_{He} was calculated from plume-corrected CXRS measurements [174]. The volume average of the c_{He} profile up to $\rho_{\mathrm{tor}} = 0.9$ was taken, as no strong gradients in the c_{He} profile were observed. For CXRS measurements small amounts of nitrogen (N) were injected into the plasma, but not during the very first power ramp, such that a N-free reference is available. The low-Z impurity content was monitored with CXRS [83], which delivered nitrogen and boron (B) concentrations below 0.1 %. Also the tungsten (W) concentration was below the detection limit of 0.2×10^{-5} in all discharges. This is in accordance with

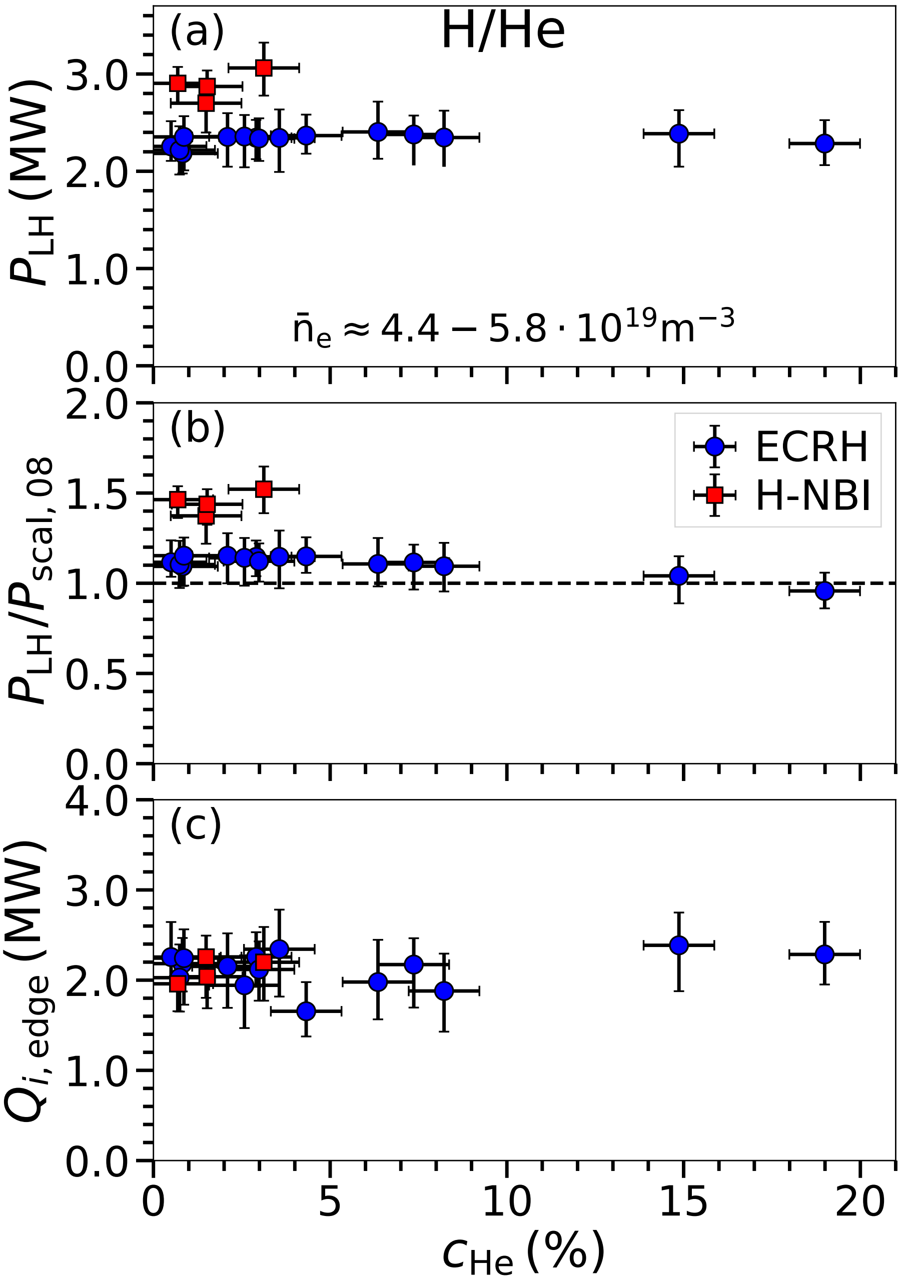

Figure 8.4: (a) H-mode power threshold, (b) divided by the H-mode power threshold in pure D plasmas derived from the multi-machine scaling of the high-density branch and (c) edge ion heat flux at the L-H transition in H plasmas with He doping versus the volume-averaged He concentration. No significant decrease of P_{LH} with increasing He concentration is found, this holds for NBI and ECRH heated plasmas. $Q_{i,\mathrm{edge}}$ is found to be constant at the L-H transition, independent of the applied external heating.

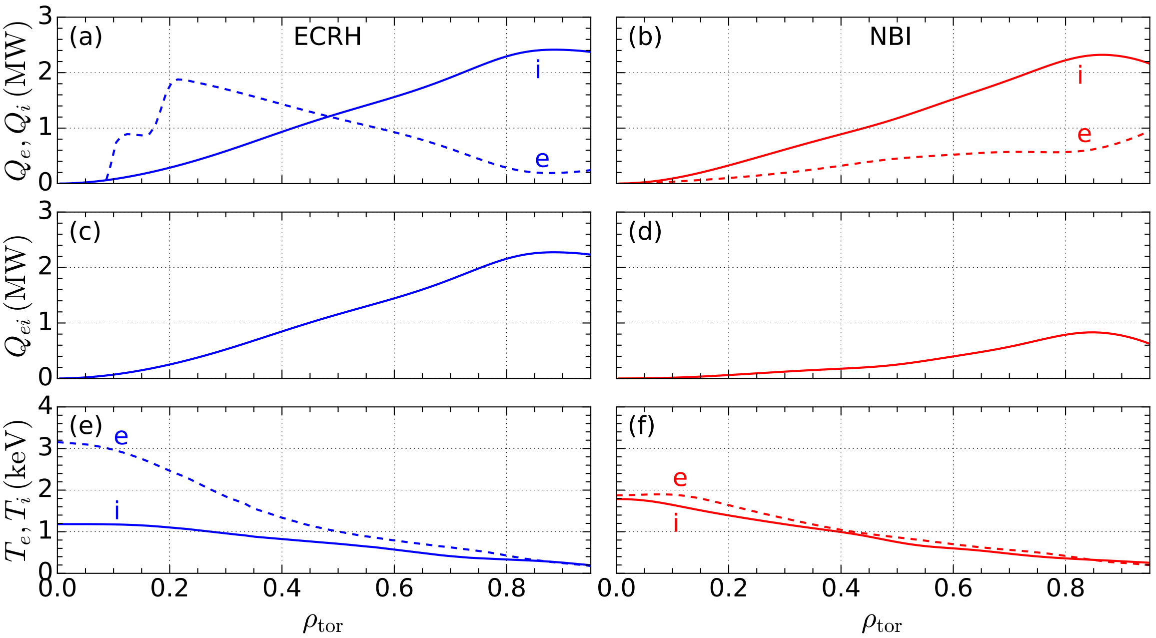

Figure 8.5: Radial profiles of (a),(b) the surface-integrated ion (solid) and electron (dashed) heat flux, (c), (d) the surface-integrated heat flux due to equipartition and (e),(f) the input ion (solid) and electron (dashed) temperature profiles for an ECRH (blue) and a NBI (red) heated H discharge at the L-H transition, respectively. The bigger difference in $(T_e - T_i)$ for ECRH compared to NBI H plasmas makes that for the same $Q_{i,\text{edge}}$, $Q_{e,\text{edge}}$ is lower in ECRH compared to NBI plasmas. This leads to a lower P_{LH} in ECRH compared to NBI H plasmas.

Z_{eff} measurements from visible Bremsstrahlung [175], which give radially averaged Z_{eff} values of 1.2 to 1.3 for all the presented discharges except for the discharges with He concentrations above 10 % to 20 %. For the latter, Z_{eff} increases from 1.5 up to 1.7.

Since the density increases slightly with increasing c_{He} in these experiments, P_{LH} was normalized to its respective value of $P_{\text{scal,08}}$ (see Equation 2.56), in order to account for the density dependence of P_{LH} (see Section 2.4.2). The resulting data points are shown in Figure 8.4b. Note, the fact that at the density minimum $P_{\text{LH}}(\text{H})$ matches $P_{\text{scal,08}}$, which is computed for D plasmas, has been also reported earlier in [73] and will be discussed in Section 8.2.2. Although the absolute values between the observed P_{LH} and the scaling do not agree, the density dependencies of H and D plasmas in the high density branch are well reproduced by the scaling [73]. Thus, taking the ratio $P_{\text{LH}}/P_{\text{scal,08}}$ adequately accounts for variations in the plasma density also in the conditions of the present experiments. However, as can be seen in Figure 8.4b, no significant decrease of $P_{\text{LH}}(\text{H})/P_{\text{scal,08}}$ with increasing c_{He} is found. This observation, namely that $P_{\text{LH}}(\text{H})$ stays constant with c_{He} up to 20 %, is in line with former observations at AUG. Then a decrease of $P_{\text{LH}}(\text{H})$ to $P_{\text{LH}}(\text{He})$ was only seen for $c_{\text{He}} > 30\,\%$ [55].

As already mentioned in Section 8.1 higher values of $P_{\text{LH}}(\text{H})$ are found for NBI heated hydrogen discharges compared to ECRH heated hydrogen discharges. An explanation for this increase of P_{LH} by up to 500 kW is found in the power balance of these discharges. This is shown in Figure 8.4c, where $Q_{i,\text{edge}}$ at the L-H transition is plotted against c_{He}. $Q_{i,\text{edge}}$ was calculated as described in Section 3.4.1, using the experimentally determined He, N and B densities and the measured n_e, T_e and T_i profiles. Figure 8.4c shows that

$Q_{i,\mathrm{edge}}$ stays constant at a value of 2.2 MW, independent of the He concentration and the applied external heating. In contrast, $Q_{e,\mathrm{edge}}$ is found to be systematically lower for the ECRH than the NBI heated discharges at the L-H transition, what directly translates into a lower P_{LH}. This observation is counter-intuitive to the fact that NBI partly heats the ions directly, while ECRH, which exclusively heats the electrons, needs a strong electron-ion heat exchange, p_{ei}, to be able to transfer energy into the ion channel. However, the observation that $Q_{e,\mathrm{edge}}$ is smaller with ECRH than with NBI heating can in fact be explained by a large p_{ei} and its resulting heat flux, Q_{ei}, being the dominant contribution to Q_i. Indeed it is known that p_{ei} can influence heat transport in hydrogen significantly [176].

From Equation 3.6 it can be seen that in H plasmas p_{ei} is larger than in D and He plasmas due to its Z_i/A_i dependence.[1] Moreover, at the L-H transition $(T_e - T_i)/T_e^{3/2}$ is in a regime where p_{ei} increases with increasing T_e. Thus, at constant density, a reduction of $(T_e - T_i)$ leads to a reduction of p_{ei}. Figure 8.5 shows profiles of Q_i (solid line) and Q_e (dashed line) for an ECRH (blue) and a NBI (red) heated discharge (Figure 8.5a,b) and their corresponding Q_{ei} (Figure 8.5c,d). Q_{ei} is calculated using experimental electron density profiles and the experimental electron and ion temperature profiles depicted in Figure 8.5e,f, respectively. The radial profile of the T_e/T_i ratio depends on the energy deposition profile of the respective heating scheme. ECRH heats the electrons directly in the plasma center, hence $(T_e - T_i)$ is large. Since Q_{ei} is the only contribution to Q_i, this leads to a strong reduction of $Q_{e,\mathrm{edge}}$. In contrast, NBI heats both electrons and ions and, additionally, it exhibits a broad heat deposition profile. This leads to a decrease of $(T_e - T_i)$ over the whole radial range, thus, to a lower Q_{ei} and, consequently, to a higher $Q_{e,\mathrm{edge}}$.

At AUG it has been observed that $Q_{i,\mathrm{edge}}$ is critical for the L-H transition [58], which is found to be constant in these discharges. Thus, the lower $Q_{e,\mathrm{edge}}$ in the ECRH compared to the NBI heated discharges leads to a lower P_{LH}. This finding provides an explanation for a higher P_{LH} in H plasmas in NBI compared to ECRH discharges, which is based on a critical $Q_{i,\mathrm{edge}}$ at the L-H transition, and does not rely on differences in the toroidal rotation as found in [70]. As stated before, p_{ei} is smaller in D and He plasmas than in H plasmas, due to its Z_i/A_i dependence. Therefore, the dominant contribution to Q_i, Q_{ei} becomes smaller and is more comparable between NBI and ECRH plasmas, ultimately leading to the same P_{LH} for NBI and ECRH heated D and He plasmas. Interestingly, the observation that a critical $Q_{i,\mathrm{edge}}$ is needed at the L-H transition also implies that in plasmas where Q_{ei} is the dominant contribution to Q_i, e.g. all plasmas heated with ECRH only, the transport properties of the plasma core influence the condition for the H-mode access.

These AUG P_{LH} studies can be directly related to the conditions during ITER PFPO-1, where H-mode operation in H plasmas at the density minimum is foreseen with dominant electron heating. The experiments suggest that admixture of He to H plasmas will not lower $P_{\mathrm{LH}}(\mathrm{H})$. On the other hand the findings underline again the importance of $Q_{i,\mathrm{edge}}$ for the H-mode access. This gives more confidence to use the existing scaling of the density minimum, which is based on the assumption of a critical edge ion heat flux at the L-H transition, for extrapolation of the density minimum to ITER [58, 177].

---

[1] In H plasmas $Z_i/A_i = 1$, in D and He plasmas $Z_i/A_i = 1/2$.

8.2.2 Hydrogen-Deuterium Plasmas

In another sequence of L-H transition discharges, the relative hydrogen content, f_H, was scanned by gradually changing the H/D ratio of the gas fuelling and setting one of the two NBI heating systems on hydrogen and the other on deuterium. The discharges were again designed similar as for the other L-H transition experiments, with an ECRH or a NBI heating ramp, at otherwise constant plasma parameters. Two different series of HD plasma scans were performed. In the first $\bar{n}_e$ was in the high-density branch of P_LH, in the second $\bar{n}_e$ was in the low-density branch of P_LH.

8.2.2.1 High-Density Branch

Power Threshold and Edge Ion Heat Flux Figure 8.6a shows P_LH plotted against $f_\mathrm{H} = n_\mathrm{H}/(n_\mathrm{H} + n_\mathrm{D})$. Also at AUG a non-linear dependence of P_LH on f_H is observed. Differently from JET P_LH remains constant at the level of pure D ($\approx 1.0\,\mathrm{MW}$) up to $f_\mathrm{H} \approx 0.5$, for both ECRH and NBI heated plasmas. Starting from $f_\mathrm{H} \approx 0.5$ P_LH increases gradually up to the level of pure H ($P_\mathrm{LH} = 2.3 - 2.8\,\mathrm{MW}$), where again slightly higher values are observed for NBI compared to ECRH heated HD plasmas.

The line-averaged density in the experiments varied from 3.5 to $4.7 \times 10^{19}\mathrm{m}^{-3}$. To account for the density variation, the measured P_LH values were divided by their respective $P_\mathrm{scal,08}$ values (see Equation 2.56). This is shown in Figure 8.6b. As can be seen in the figure the non-linear dependence of P_LH on f_H does not change, but the absolute values show that the scaling overestimates $P_\mathrm{LH}(\mathrm{D})$ by almost a factor of 2 and the experimentally found value of $P_\mathrm{LH}(\mathrm{H})$ is roughly at the level of $P_\mathrm{scal,08}(\mathrm{D})$. This observed reduction of P_LH at AUG can be attributed to two effects, which also apply to ITER and, therefore, are favourable for ITER P_LH predictions. First, the multi-machine scaling was determined for the high-density branch, i.e. for densities higher than the density minimum. The present experiments were conducted close to the density minimum of P_LH and there the scaling overestimates P_LH slightly (see also Figure 5 in [73]). Second, the multi-machine scaling was mostly deduced from P_LH data in carbon wall tokamaks (about 11 % of the selected data were from a metal wall device, namely Alcator C-Mod with a molybdenum wall) [57]. In 2007 AUG was equipped with a first wall and divertor surface completely made from tungsten and since then a reduction of $P_\mathrm{LH}(\mathrm{D})$ by up to 30 % compared to the carbon wall was observed [73]. This reduction of P_LH is also seen at JET starting from its operation with a beryllium/tungsten (ITER-like) wall [178].

Also $Q_{i,\mathrm{edge}}$ was calculated at the L-H transition for a subset of discharges, for which kinetic electron and ion profiles were available. For the calculation of $Q_{i,\mathrm{edge}}$, only one impurity species was assumed to be present, which was the measured impurity N, and the mixed HD plasma was assumed as a single species plasma with an equivalent ion mass of A_eqiv, defined as:

$$1/A_\mathrm{eqiv} \coloneqq \frac{A_\mathrm{H} n_\mathrm{D} + A_\mathrm{D} n_\mathrm{H}}{A_\mathrm{D} A_\mathrm{H}(n_\mathrm{D} + n_\mathrm{H})}. \tag{8.3}$$

For HD plasmas with a relative hydrogen content of f_H, $1/A_\mathrm{eqiv} = \frac{1}{2}(1 + f_\mathrm{H})$. For pure D plasmas $A_\mathrm{eqiv} = 2$ and for pure H plasmas $A_\mathrm{eqiv} = 1$. For pure HD plasmas, i.e. no impurities present, $p_{ei} \propto A_\mathrm{eqiv}$ at constant n_e, T_e and T_i.

The resulting $Q_{i,\mathrm{edge}}$ values at the L-H transition are plotted against f_H in Figure 8.6c. The behaviour of $Q_{i,\mathrm{edge}}$ with f_H is the same as of P_LH. In particular, $Q_{i,\mathrm{edge}}(\mathrm{H}) \approx 2Q_{i,\mathrm{edge}}(\mathrm{D})$,

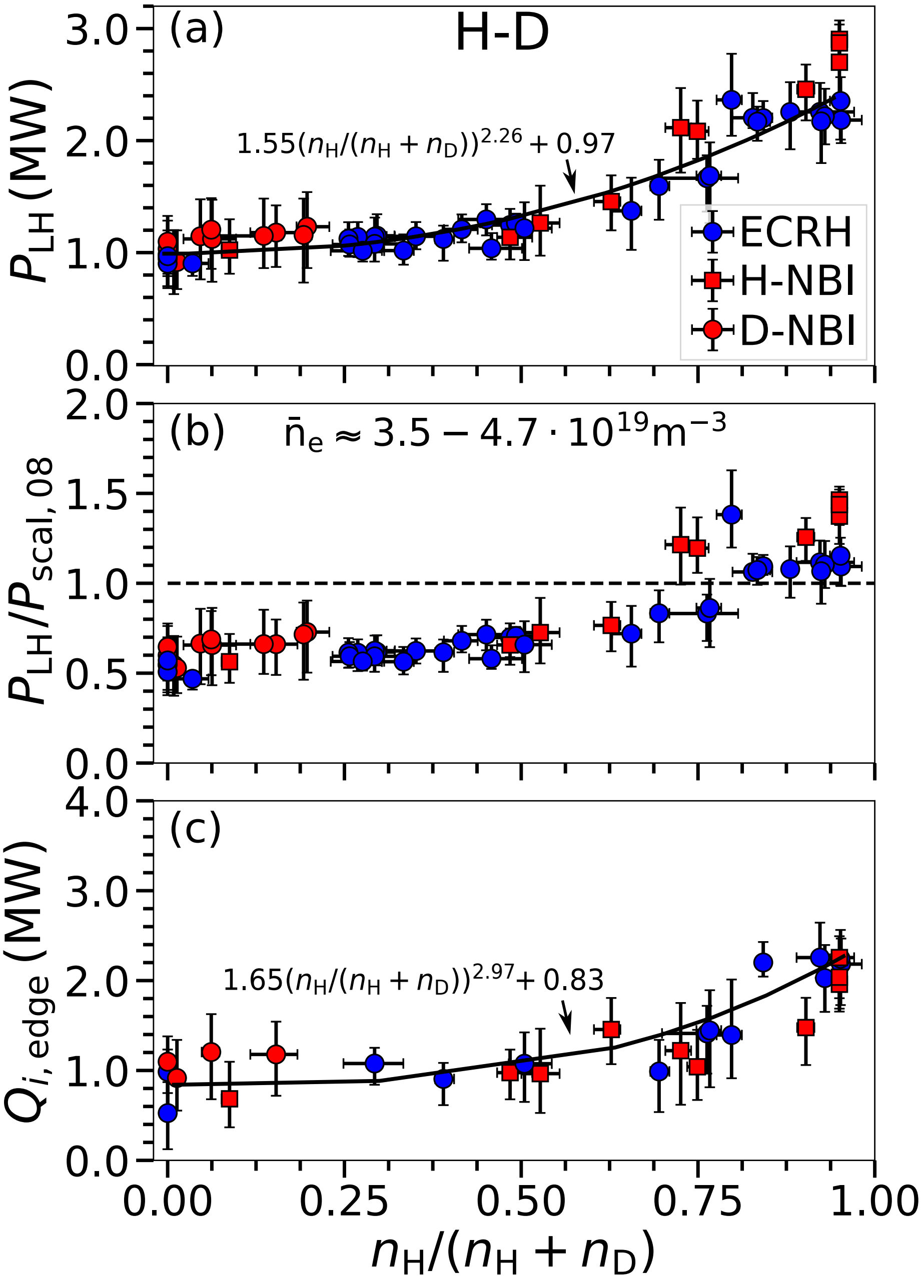

Figure 8.6: (a) H-mode power threshold, (b) divided by the H-mode power threshold in pure D plasmas derived from the multi-machine scaling and (c) edge ion heat flux at the L-H transition in mixed hydrogen-deuterium plasmas versus the relative hydrogen content. P_{LH} as well as $Q_{i,\mathrm{edge}}$ show a similar behaviour, which is non-linear against $n_{\mathrm{H}}/(n_{\mathrm{H}}+n_{\mathrm{D}})$. Starting from $n_{\mathrm{H}}/(n_{\mathrm{H}}+n_{\mathrm{D}}) = 0.5$ P_{LH} and $Q_{i,\mathrm{edge}}$ increase, until both are two times as high in a pure H compared to a pure D plasmas.

as has been also observed in former AUG L-H transition experiments [56]. Furthermore, no difference in $Q_{i,\mathrm{edge}}$ is found between ECRH and NBI heated discharges, as it is observed for P_{LH} in HD plasmas with $f_{\mathrm{H}} > 0.5$.

Edge Profiles at Same Heating Power Figure 8.7 shows edge kinetic electron, ion and E_r profiles for a sub-series of the above presented discharges in HD plasmas. All discharges have comparable density and were heated with the same amount of $P_{\mathrm{ECRH}} = 600\,\mathrm{kW}$, but have different hydrogen content (darkblue: $f_{\mathrm{H}} = 0$, bright green:$f_{\mathrm{H}} = 0.95$.) The edge electron temperature (Figure 8.7a) is the same for all discharges and exhibits a separatrix value of $T_{e,\mathrm{sep}} \approx 50\,\mathrm{eV}$ at this heating power. Also the edge density and its normalized gradient, $1/L_{n_e}$, (Figures 8.7b,c) are about the same for different values of f_{H}. However, the particle fuelling rate ($\dot{N}$) was increased with increasing f_{H}, such that $\dot{N}_{\mathrm{H}} \approx 1.8\dot{N}_{\mathrm{D}}$ at $f_{\mathrm{H}} = 0.95$. This increase of the particle source hints to an increased particle transport in H compared to D L-mode edge plasmas, as it is observed at other machines [179] and can be explained by the peculiar mass-dependence of edge turbulence [65].

T_i and its gradient are, within the experimental uncertainties, also the same for all investigated discharges of varying f_{H} (see Figure 8.7d). This is an indication for an additionally increased ion heat transport in H compared to D plasmas, since, as discussed in the section before, the heat transfer p_{ei} from electrons to ions is by a factor of 2 higher in H compared to D plasmas for otherwise same plasma parameters due to its Z_i/A_i dependence. Indeed it is found in these plasmas of same heating power that $Q_{i,\mathrm{edge}}(f_{\mathrm{H}}) = (1 + f_{\mathrm{H}})Q_{i,\mathrm{edge}}(\mathrm{D})$. Since

$$Q_i = -\chi_i n_i \nabla T_i, \tag{8.4}$$

with χ_i being the ion heat diffusivity, it follows that $\chi_{\mathrm{H}} \approx 2\chi_{\mathrm{D}}$ in these ECRH heated L-modes of same plasma density $\bar{n}_e$.

The intrinsic toroidal impurity rotation, measured on nitrogen, is slightly positive and, thus, co-current (see Figure 8.7e). It shows only a slight dependence on f_{H}. Interestingly, $v_{\phi,\mathrm{N}}$ tends to be a bit lower ($0 - 10\,\mathrm{km/s}$) for an approximate 50/50 mixture of hydrogen and deuterium ($f_{\mathrm{H}} = 0.4 - 0.6$). In these plasmas N can be considered the only impurity. For dominant D and dominant H plasmas, for which the respective other hydrogenic species can be considered a second impurity, $v_{\phi,\mathrm{N}} \approx 10 - 20\,\mathrm{km/s}$.

The experimental E_r profiles, measured with DR or HES, are shown in Figure 8.7f. They all agree well with their respective $(\nabla_r p_i)/(en_i)$ term in the confined plasma region with $E_{r,\mathrm{min}} \approx -10\,\mathrm{kV/m}$. In the SOL, the experimental E_r values tend to be slightly lower than $-\nabla_r T_{e,\mathrm{OMP}}/e$, even exhibiting negative values. However, the outer E_r gradients are, within the measurement uncertainties, the same for all discharges, independent of f_{H}. The inner E_r gradients were only measured for the extreme cases, pure D and H plasmas, but these also show, taking into account the radial uncertainties of the DR measurements, the same strength. Only for $\rho_{\mathrm{pol}} < 0.97$ the measured E_r profiles deviate from each other outside the measurement uncertainties, with H exhibiting higher E_r values than D. Whether this difference in E_r is connected to a different main ion rotation could not be assessed in this experiment, since no CXRS measurements are available for the pure H plasma.

Edge Profiles at the L-H Transition Edge kinetic electron and ion profiles as well as E_r profiles taken right before the L-H transition are shown in Figure 8.8 for the different HD plasmas of varying f_{H}. In all here investigated HD plasmas $P_{\mathrm{ECRH}} > 600\,\mathrm{kW}$ at the L-H transition, except for the pure D plasmas. Thus, both the edge T_e and T_i values, measured at $\rho_{\mathrm{pol}} = 0.95$, are higher at the L-H transition than in the cases for which $P_{\mathrm{ECRH}} = 600\,\mathrm{kW}$. Also n_e increases slightly with higher heating power, while $1/L_{n_e}$ stays constant. The higher T_e and T_i values also lead to an increased $Q_{i,\mathrm{edge}}$ at the L-H transition compared to the values at $P_{\mathrm{ECRH}} = 600\,\mathrm{kW}$. The exact values of $Q_{i,\mathrm{edge}}$ at the L-H transition were already presented before in Figure 8.6c and indicate that $\chi_{i,\mathrm{H}} \geq 2\chi_{i,\mathrm{D}}$ at the L-H transition, as already reported in [56].

The $v_{\phi,\mathrm{N}}$ profiles are constant with increasing heating power for f_{H} between 0.4 and 0.6, but exhibit a slight decrease with increasing P_{ECRH} for all other relative hydrogen ratios. This observation is consistent with E_r measurements in the pure H plasma. They show that the values of the E_r profiles inside of $\rho_{\mathrm{pol}} = 0.97$ are slightly decreased at the L-H transition ($P_{\mathrm{ECRH}} \approx 1.6\,\mathrm{MW}$) compared to the values found for the E_r profiles with $P_{\mathrm{ECRH}} = 600\,\mathrm{kW}$ (see Figure 8.7f). Furthermore, the experimental E_r profiles reveal that the outer E_r gradient is slightly steeper at the L-H transition for all mixed HD plasmas, i.e. $f_{\mathrm{H}} > 0$, compared to the pure D plasma case. In the confined region $E_{r,\mathrm{min}}$ is constant at about $-10\,\mathrm{kV/m}$ and agrees for all cases with $(\nabla_r p_i)/(e n_i)$. In the SOL $E_{r,\mathrm{max}}$ increases with heating power, but also its position moves further inside the plasma, being positive already inside but close to the separatrix. In the cases of $f_{\mathrm{H}} > 0$, E_r in the SOL also fits better to $-\nabla_r T_{e,\mathrm{OMP}}/e$. According to the DR measurements the inner E_r gradients between pure D and H plasmas are the same at the L-H transition.

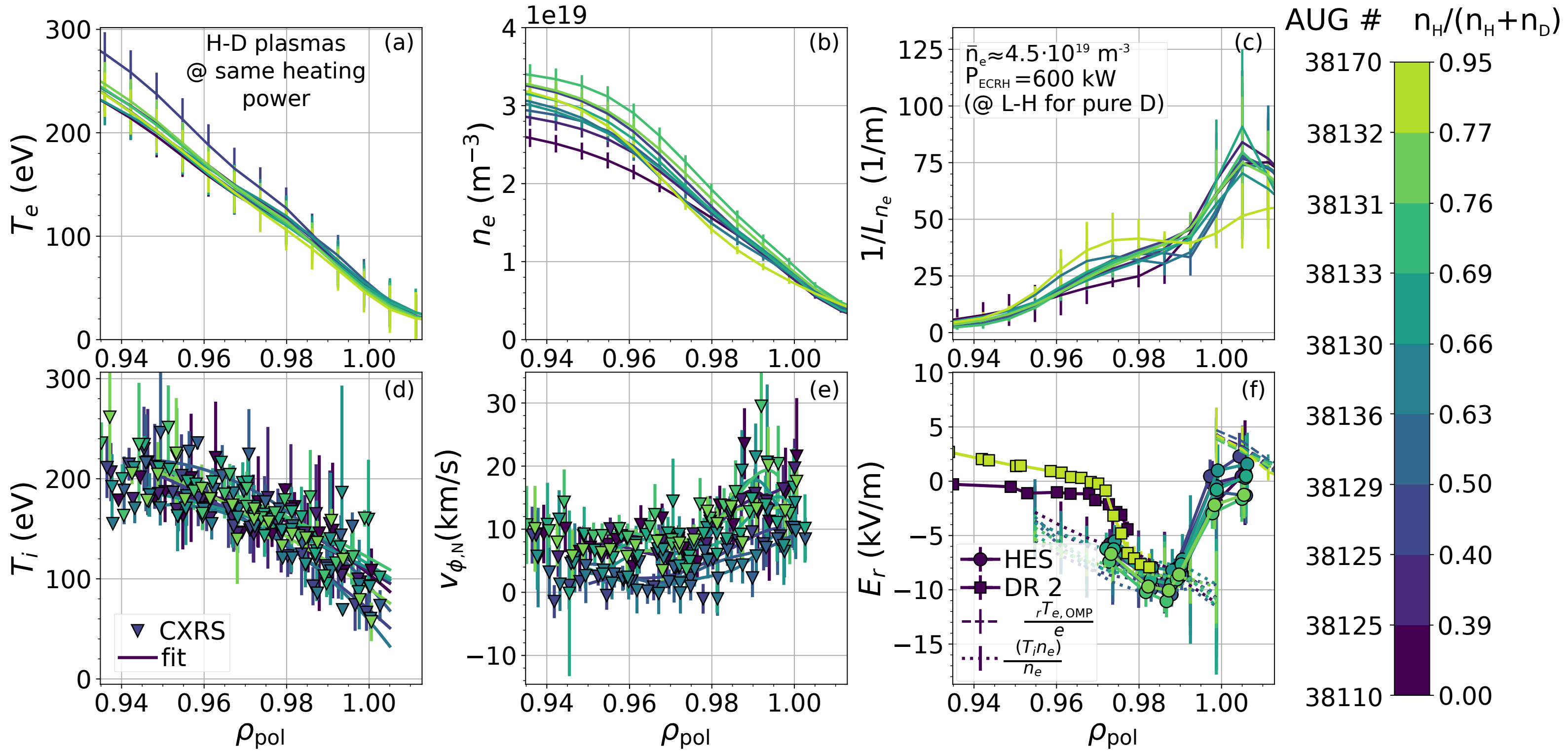

Figure 8.7: Radial profiles of the edge (a) electron temperature, (b) electron density, (c) normalized electron density gradient, (d) ion temperature, (e) toroidal rotation of nitrogen, (f) radial electric field for L-modes of same ECRH power and similar plasma density, but different relative hydrogen content. There are no significant differences in the edge profiles found between dominant H and dominant D plasmas, which implies that the particle and energy transport is increased in H compared to D.

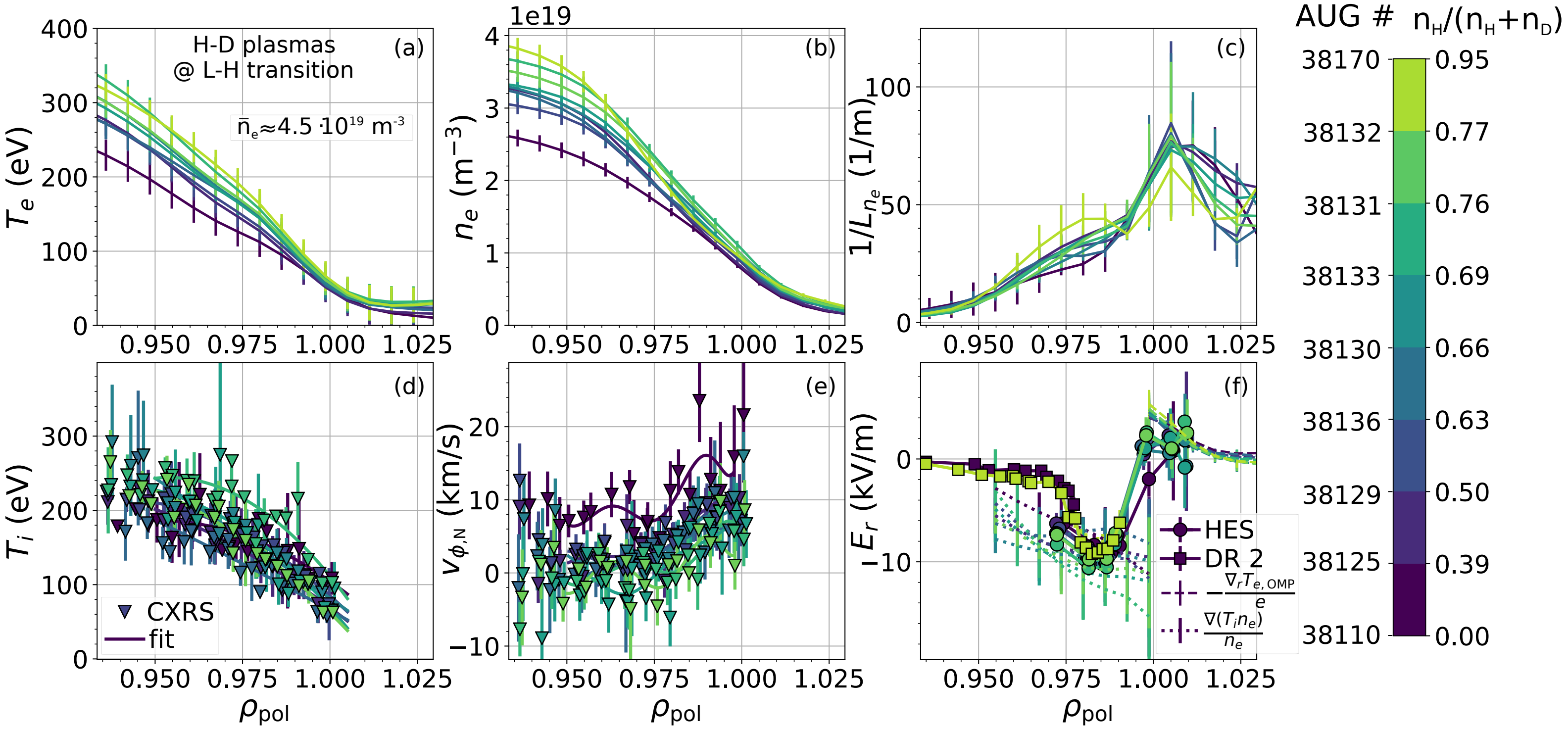

Figure 8.8: Radial profiles of the edge (a) electron temperature, (b) electron density, (c) normalized electron density gradient, (d) ion temperature, (e) toroidal rotation of nitrogen, (f) radial electric field at the L-H transition in ECRH heated plasmas with different relative hydrogen content. With increasing hydrogen content the edge electron pressure increases at the L-H transition. For the normalized edge density gradient and T_i no systematic dependence on the relative hydrogen content is found. At the L-H transition the toroidal rotation of nitrogen is found to be higher and the outer E_r gradient flatter for pure D plasmas compared to mixed HD plasmas.

H-L Back Transition In the same subset of discharges also back transitions from H- to L-mode (H-L back transition) were studied. The H-L back transitions were induced by gradually ramping down the ECRH power. The time point of the H-L back transition (t_{HL}) is defined as the time point at which the plasma exits I-phase and enters L-mode. P_{HL} is then the net power at t_{HL}. The measured P_{HL} values, plotted against f_{H}, are shown together with the respective P_{LH} values (grey) in Figure 8.9a. As the figure shows there is no difference visible between P_{LH} and P_{HL} for any f_{H}. However, the density is increased in H-mode compared to L-mode. Considering the linear, positive dependence of P_{LH} on $\bar{n}_e$ in the high-density branch (see Section 2.4.2), the power needed to exit H-mode is lower than the one to enter H-mode. This hysteresis in P_{LH} was first observed at AUG and is reported in [58, 73]. For this reason the P_{LH} and P_{HL} data were also divided by the respective value of $P_{\mathrm{scal,08}}$, to account for the density dependence. This is shown in Figure 8.9b, which indicates that at the same f_{H} P_{HL} tends to be below P_{LH}. However, the absence of hysteresis with respect to P_{net} for any f_{H} together with the fact that these plasmas were feed-forward, i.e. a constant gas puff level was applied throughout the discharge, indicates that for the same gas puff level P_{LH} and P_{HL} are the same.

In Figure 8.9c values of $E_{r,\mathrm{min}}$, determined with HES, are shown for a subset of discharges for which E_r measurements are available. Besides $E_{r,\mathrm{min}}$ at the L-H transition (grey data points), also $E_{r,\mathrm{min}}$, averaged over 50 ms right before the H-L back transition (filled symbols), as well as $E_{r,\mathrm{min}}$ averaged over 50 ms right after the H-L back transition (open symbols), are shown. It can be seen that before the H-L back transition $E_{r,\mathrm{min}}$ scatters, but average values (not ELM-synchronized) of −15 to −21 kV/m are found for both, NBI and ECRH heated plasmas. When the plasma is back in L-mode $E_{r,\mathrm{min}}$ average values of −10 to −12 kV/m are observed, which are also measured for the respective L-H transition. These measurements suggest that E_r is not the same at the L-H and H-L back transition and, thus, seemingly contradict former observations made at AUG in which it was found that $p_{e,\mathrm{edge}}$, measured at $\rho_{\mathrm{pol}} = 0.95$ is constant at the L-H and H-L back transition [180] and that during I-phase E_r follows the development of the main ion diamagnetic term $((\nabla_r p_i)/(en_i))$, because the toroidal and poloidal flows (v_ϕ and v_θ) are found to be on the neoclassical level and, thus, small [76, 77]. However, $p_{e,\mathrm{edge}}$ and E_r develop rather fast in a time window of about 5 ms before the H-L back transition and therefore, an averaging over 50 ms leads to wrong results, because the profiles are not stable in these time windows

In this plot time traces of P_{net}, $\dot{B}_\theta$, $I_{\mathrm{SOL,a}}$, $p_{e,\mathrm{edge}}$, and $E_{r,\mathrm{min}}$ are shown relative to the L-H transition (Figure 8.10a) and the H-L back transition (Figure 8.10b) for the same set of HD discharges. In this way the time resolution of the E_r profiles is given by the time resolution of the HES diagnostics, which is 2.45 ms. Figure 8.9 shows that in the pure D plasma ($f_{\mathrm{H}} = 0.0$, darkblue), the edge electron pressure, $p_{e,\mathrm{edge}}$, measured at $\rho_{\mathrm{pol}} = 0.95$, is about 0.80 kPa at the L-H transition. This value is in agreement with the critical $p_{e,\mathrm{edge}}$ value found in [180] for a plasma edge density, $n_{e,\mathrm{edge}}$, measured at $\rho_{\mathrm{pol}} = 0.95$, of about $2.6 \times 10^{19}\,\mathrm{m}^{-3}$. At the H-L back transition $p_{e,\mathrm{edge}}$ is slightly higher, at 1.0 kPa, but also $n_{e,\mathrm{edge}}$ is higher at about $3.4 \times 10^{19}\,\mathrm{m}^{-3}$ and in [180] it is shown that the critical $p_{e,\mathrm{edge}}$ increases with increasing $n_{e,\mathrm{edge}}$. Figure 8.9 also shows that the critical $p_{e,\mathrm{edge}}$ at the L-H and the H-L back transition increases slightly with increasing f_{H}, although this increase is not significant if the variation in $n_{e,\mathrm{edge}}$ is taken into account. As $p_{e,\mathrm{edge}}$ increases directly after the L-H transition, $E_{r,\mathrm{min}}$ decreases, i.e. the E_r well gets stronger. At the H-L back transition $p_{e,\mathrm{edge}}$ starts to decrease about 5 to 3 ms before t_{HL} and at the same time $E_{r,\mathrm{min}}$ starts to increase again, i.e. the E_r well gets weaker. Right at the H-L back transition

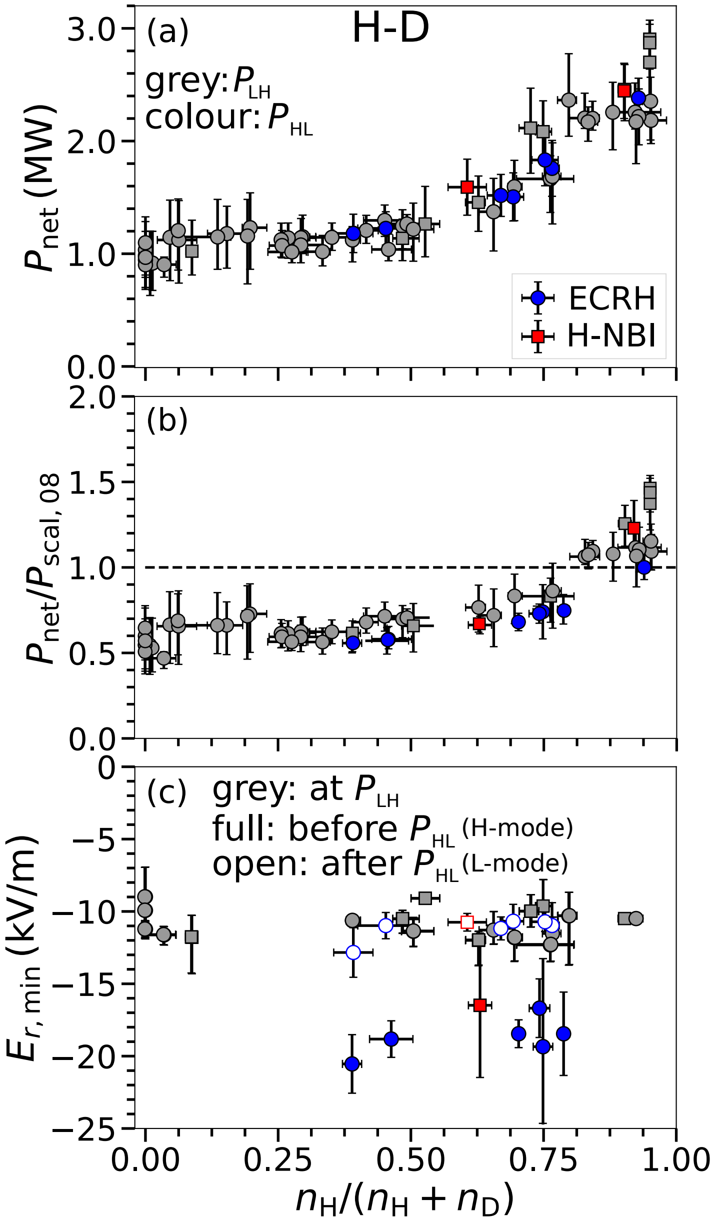

Figure 8.9: (a) H-mode power threshold (grey) and net power at H-L back transition (coloured), (b) divided by the H-mode power threshold in pure D plasmas derived from the multi-machine scaling and (c) minimum of the edge radial electric field at the L-H transition (grey) and before and after the H-L back transition (colour) in mixed hydrogen-deuterium plasmas versus the relative hydrogen content. P_{LH} shows no hysteresis in terms of P_{net} when plotted against $n_{\mathrm{H}}/(n_{\mathrm{H}}+n_{\mathrm{D}})$, only if also the density dependence of P_{LH} is taken into account. $E_{r,\mathrm{min}}$ can be considered a proxy of the E_r gradients in these plasma conditions. Its value, averaged over a time window of 50 ms, is deeper, i.e. more negative, before the H-L back transition, but reduces, i.e. is less negative, to the same L-mode values as observed before the L-H transition after the H-L back transition.

the same value of $E_{r,\mathrm{min}}$ is reached as at the L-H transition. Please note that not for all discharges HES E_r data right at the L-H and the H-L back transition are available, due to the timing of the on-off phases of the piezo valve with respect to the transition time points. However, the time points for which E_r data are available, $E_{r,\mathrm{min}}$ shows little variation in the H-mode and L-mode phases between the different discharges of varying f_H.

Interestingly, the time traces of $\dot{B}_\theta$ and $I_\mathrm{SOL,a}$, which both indicate the same time point as the L-H transition, show a slight variation in the end of the I-phase, and, thus, the time point of the H-L back transition. Dithers are seen longer in $I_\mathrm{SOL,a}$ than in $\dot{B}_\theta$, which would lead to a slightly later t_HL. However, it can be well possible that there is a latency in the excursions to occur in the $I_\mathrm{SOL,a}$, which is detected in the divertor plates, compared to $\dot{B}_\theta$, which is detected in magnetic coils located closer to the main plasma. For this reason, t_HL is considered the time point, in which the dithers are not visible in $\dot{B}_\theta$ any longer.

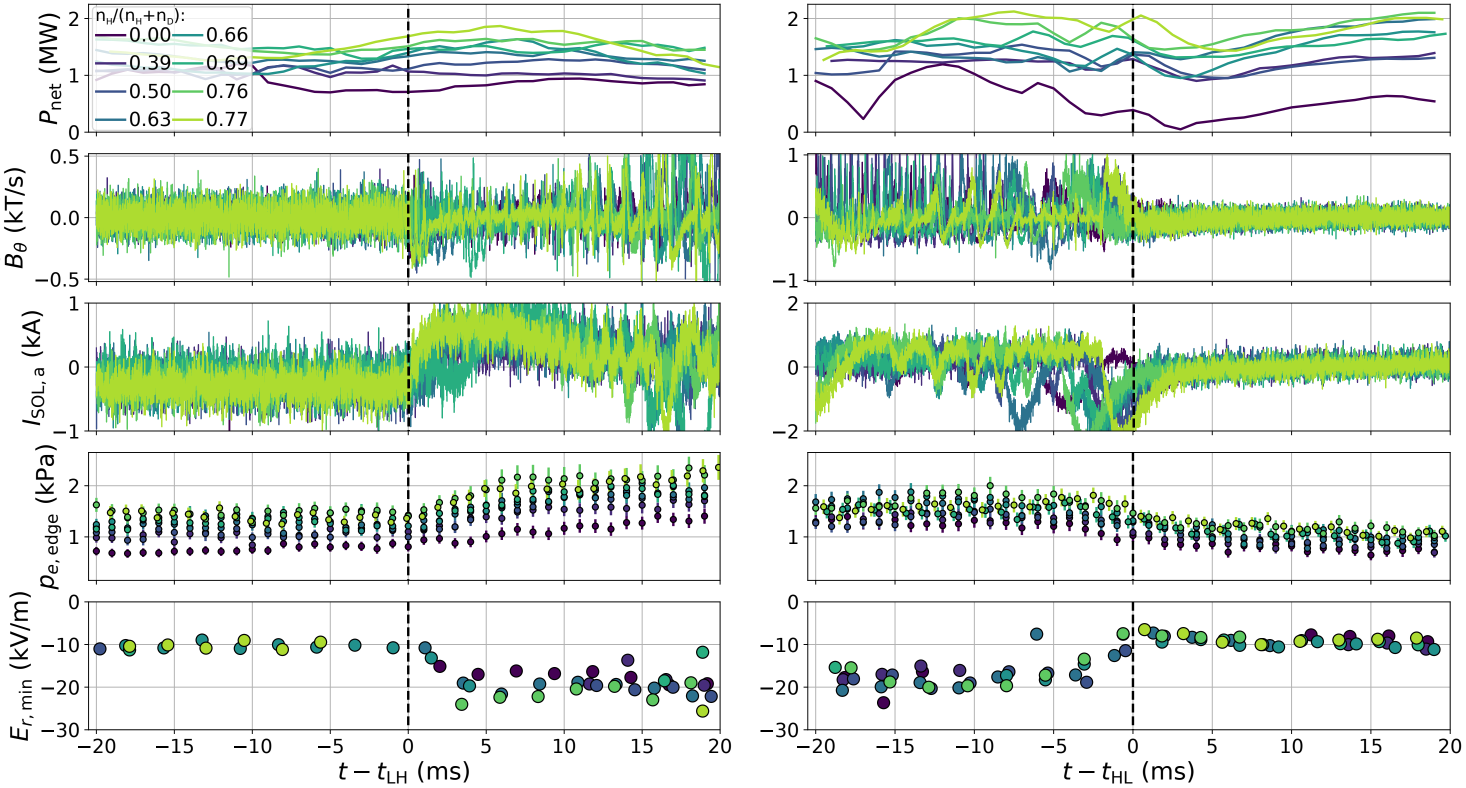

(a) L-H Transition **(b)** H-L Back Transition

Figure 8.10: Time traces of the net input power, the poloidal magnetic field fluctuations, the shunt current of the outer divertor, the edge electron pressure measured at $\rho_{\rm pol} = 0.95$ and the minimum of the edge radial electric field relative to the L-H transition (a) and the H-L back transition (b) for the HD discharges. The time traces show that at the L-H and the H-L back transition same values of $p_{e,\rm edge}$ and $E_{r,\rm min}$ are reached.

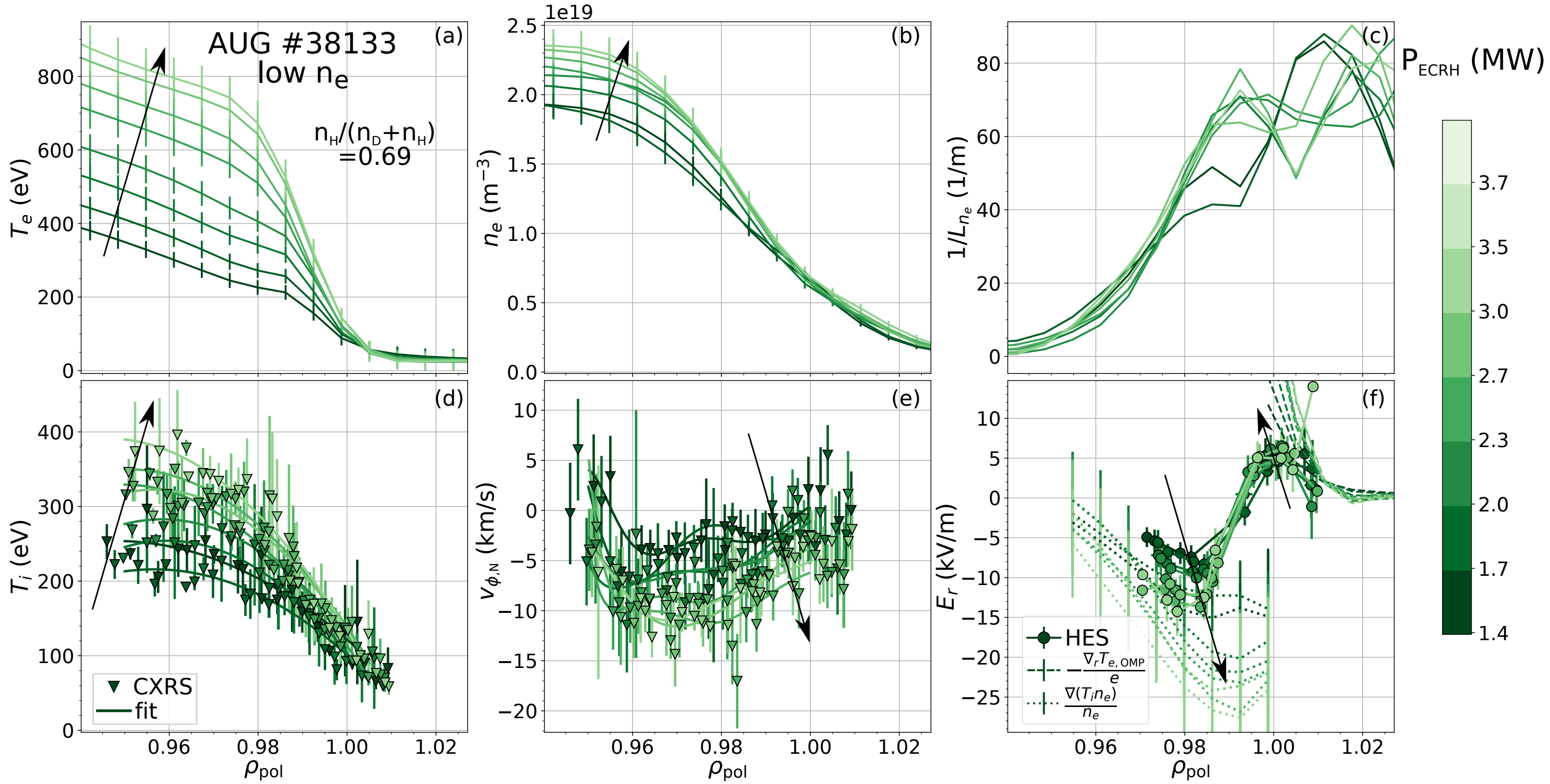

Figure 8.11: Radial profiles of the edge (a) electron temperature, (b) electron density, (c) normalized electron density gradient, (d) ion temperature, (e) toroidal rotation of nitrogen, (f) radial electric field of a low density, ECRH heated discharge with a relative hydrogen content of 0.69. With increasing ECRH power the edge electron and ion temperature develop a pedestal, whereas the density shows only a weak increase with P_{ECRH} and no development of a pedestal. This is indicative of an I-mode regime. The toroidal rotation of nitrogen and the minimum of E_r are found to decrease with increasing P_{ECRH} in I-mode and the outer E_r steepens as well. These developments are also indicated by the black arrows in the plots.

8.2.2.2 Low-Density Branch

In the first have of the above presented discharges ECRH power ramps at low density were performed. Thus, the development of the edge electron and ion profiles as well as of E_r could be studied for plasmas with $\bar{n}_e \leq 2.5 \times 10^{19}\,\mathrm{m}^{-3}$, i.e. they are in the low-density branch of P_{LH}. In none of these discharges an L-H transition could be triggered, although the ECRH power was raised up to 3.7 MW. However, an improved energy confinement regime with I-mode signatures (see Section 2.4.1.2) was observed, which is discussed in the following on one example, i.e. AUG discharge # 38133 ($f_{\mathrm{H}} = 0.69$). The I-mode existence window seems to be very small. It was only observed for discharges with $2.0 \times 10^{19}\,\mathrm{m}^{-3} < \bar{n}_e < 2.5 \times 10^{19}\,\mathrm{m}^{-3}$ and $f_{\mathrm{H}} \geq 0.6$.

The main criterion of the I-mode is the improved energy confinement with a simultaneously L-mode like particle transport. This leads to the development of a temperature edge pedestal, without a concomitant density pedestal (L-mode-like edge density profiles). Figure 8.11 shows the development of the edge kinetic electron and ion profiles as well as the E_r profile in the transition from L- to I-mode. This transition does not take place suddenly, but rather exhibits a gradual development from L- into I-mode. With increasing ECRH power T_e increases (Figure 8.11a), eventually forming a pedestal. Such a T_e pedestal formation was also observed in ECRH heated low-density L-modes in unfavourable drift configuration (see e.g. Figure 7.7), however, in contrast to these L-modes, the here presented discharge also shows a formation of a pedestal in the ion temperature, T_i, (see Figure 8.11d). The edge density increases slightly with increasing P_{ECRH} (see Figure 8.11b), which has been also observed in several L-modes, but it does not form a pedestal, since the normalized edge density gradient stays approximately the same (see Figure 8.11c).

Interestingly, the impurity toroidal edge rotation (measured on N) decreases with increasing P_{ECRH}, i.e. it gets less co-current and even becomes counter-current (see Figure 8.11d). Such a behaviour has been observed in I-modes in unfavourable drift configuration (see Figure 7.19), but has not been seen in low-density ECRH heated L-modes in unfavourable drift configuration (see Figure 7.8). The more co-current rotation leads via the radial force balance to a decrease of E_r in the confined region, which is observed in experimental E_r measurements by HES (see Figure 8.11f). At the same time in which $E_{r,\mathrm{min}}$ decreases in the confined plasma $E_{r,\mathrm{max}}$ increases. This leads to a steepening of the outer E_r gradient. Such a development of the edge E_r with increasing P_{ECRH} has never been observed in L-mode plasmas, in which the profiles do not change much with increasing P_{ECRH}, which was observed before. Thus, the development of E_r it is another indication that this discharge develops into the I-mode regime.

According to [181] further criteria for the I-mode are the existence of a weakly-coherent mode (WCM) and the absence of H-mode signatures in divertor signals. Both criteria are fulfilled for the here presented I-mode regime in favourable drift configuration. Figure 8.12 shows the WCM as seen in the spectrogram of the density fluctuations of one of the reflectometer frequency bands. The frequency of the WCM is rather low, at around 120 kHz, but lately it was also observed in pure hydrogen I-modes that the WCM is present at slightly lower frequencies than in deuterium plasmas [182]. In agreement with observations in pure hydrogen I-modes [183], the energy confinement improvement from L- to I-mode in the here presented I-modes is not as pronounced as in D plasmas.

It should be mentioned that such an I-mode regime (then denoted as improved L-mode) has been already observed before at AUG [48] and it was suggested that it occurs in regimes for which P_{LH} is high, e.g. in low-density H plasmas and in plasmas in unfavourable drift configuration. As of yet there are only few other examples reported in which an I-mode was found in favourable drift configuration, e.g. in [184].

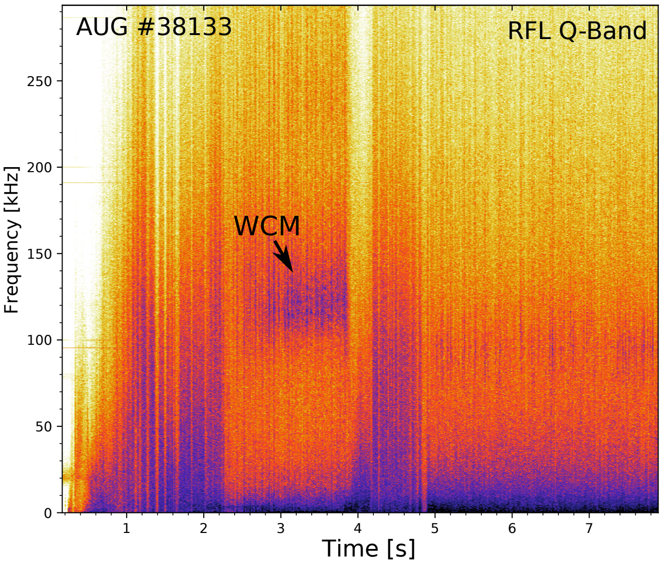

Figure 8.12: A weakly coherent mode (WCM) at a frequency of about 120 kHz is observed in ECRH heated, mixed HD plasmas with a plasma density between 2.0 and $2.5 \times 10^{19}\,\mathrm{m}^{-3}$ and a relative hydrogen content larger than 0.6. This presence of a WCM is an indication for the development of an I-mode in these plasmas conditions, which are plasmas in favourable drift configuration.

i

9 Summary and Outlook

It is widely accepted that the shear in the $E{\times}B$ velocity ($v_{E\times B}$) is the causing mechanism to reduce turbulent edge transport in a fusion plasma and, thus, lead to a confinement transition from L- to H-mode. The radial electric field E_r at the plasma edge exhibits a negative well with two gradients, the inner and the outer gradient, where the latter connects the confined plasma with the SOL. Previous experimental and modelling results have led to different conclusions on the leading role of the inner or the outer E_r gradient in the transition into H-mode. In particular, SOL modelling results have suggested that divertor conditions and magnetic configuration can modify E_r in the SOL and, thus, influence the outer E_r gradient. This, in turn, will impact the access conditions to H-mode. Indeed experimental observations are such that the power needed to enter H-mode (P_{LH}) is increased when the modelling results hint to a less steep outer E_r gradient. However, a lack of experimental data in these conditions has prevailed a confirmation of these predictions so far.

Besides the role of E_r in the access conditions to H-mode, another open question is which are the determining processes forming E_r in L-mode. Due to limited capabilities of E_r measurements in these conditions, investigations on the nature of E_r in L-mode have not been clarified as of yet.

To address these questions a new active spectroscopy diagnostics has been developed in the course of this thesis which is able to measure E_r from the plasma edge to the near SOL in all confinement regimes. In the experiments special focus was put on the characterisation of E_r in the SOL and the outer E_r gradient in L-mode conditions for which it is known that the H-mode power threshold changes strongly. Furthermore, the development of E_r at the confinement transitions was investigated and comparisons to neoclassical transport theory were undertaken.

9.1 Summary

The newly developed spectroscopic system consists of a piezo gas valve, which introduces neutral particles into the plasma, in-vessel optical components which detect the light emitted by the interactions of the introduced neutrals and the plasma particles and a spectrometer which spectrally resolves the collected light in order to deduce local plasma quantities.

The gas supply system of the piezo valve has been assembled in a way that it is safe to be operated with explosive gases like hydrogen. The piezo valve has been characterized in a laboratory set-up and the spectroscopic system was carefully calibrated in order to determine the measured plasma quantities with high accuracy.

Two spectroscopy methods were tested to measure the outer E_r gradient and E_r in the SOL in L-mode and in other confinement regimes. The first one is based on charge exchange reactions between plasma impurities and externally introduced hydrogen (or deuterium) neutrals. It was found that the signal-to-noise ratio is too low in L-mode to get useful measurements of impurity rotation, temperature and density and, consequently, E_r. Besides the too low impurity content in L-mode in the SOL, the characteristic line spectrum is disturbed by molecular lines of the injected hydrogen neutrals. The other, successful approach is the spectroscopy of singly ionized helium (He II spectroscopy or HES). The He neutrals, introduced by the piezo valve, get ionized and excited by the plasma electrons (electron impact excitation) and immediately adjust to the local radial electric field E_r. The existence of the excited He^{1+} ions is restricted to a region close to the separatrix ranging from $\rho_{\mathrm{pol}} \approx 0.97$ to 1.02. The SNR is high at a very low He gas injection rate ($\approx 1 \times 10^{19}$ el/s). This makes it possible to measure E_r in all confinement regimes with a temporal resolution of about 2.5 ms. Another advantage of the new system different to beam-based CXRS systems is that the diagnostics is independent of the neutral beam operation and, thus, does not introduce torque into the plasma.

In parallel a synthetic diagnostics was developed which includes the geometry of the gas cloud, the most important particle interactions and assesses the migration of the He^{1+} ions in the detection volume by a Monte-Carlo approach. The outputs are the measured quantities (He temperature, rotation, density and the radial electric field) as well as the line spectra. A comparison with the experimental data shows good agreement for all measured quantities. The synthetic diagnostics is used to interpret the HES data, for example it shows that the He^{1+} are not fully equilibrated with the ambient plasma. Furthermore, it was found that restrictions in the radial resolution and a complicated migration of the He^{1+} ions within the detection volume lead to a slight underestimation of both the maximal E_r value in the SOL and the E_r minimum in the confined plasma. The deviation is in both cases not large, about 1.5 kV/m in typical L-mode plasmas, but it prevents from a quantitative assessment of the E_r gradient directly from the measurement. Moreover, the synthetic diagnostics can be used in an iterative way to determine the underlying E_r profile from the measured data.

A careful comparison of L-mode E_r profiles from the HES diagnostics, the DR systems and the synthetic diagnostics was undertaken. It showed that imperfections of the alignment of the poloidal optical head of the HES diagnostics can lead to deviating results between the DR and the HES diagnostics. If these imperfections are taken into account, the E_r measurements are in excellent agreement. From this it is concluded that the phase velocity of the characteristic turbulence in L-mode is no larger than a few hundreds of m/s in the plasma edge.

Measurements of the edge E_r during the L-H transition showed that E_r follows mainly the evolution of the diamagnetic main ion pressure gradient $(\nabla_r p_i)/(en_i)$. This observation is true for all drift configurations and plasma species. It is found that as soon as $p_{i,\mathrm{edge}}$ increases, $E_{r,\mathrm{min}}$ decreases and the E_r gradients steepen. It is observed that right before the H-L back transition $E_{r,\mathrm{min}}$ changes in such a way that it reaches the same value as at the corresponding L-H transition. Since $E_{r,\mathrm{min}}$ is in these conditions a good approximation of the E_r gradients, it is concluded that the decrease of the E_r gradients and, thus, a reduction of the $E \times B$-velocity shear is responsible for the H-L back transition. Hence, the hysteresis observed in the power threshold is not present in the E_r gradients.

In L-modes in the standard drift configuration (LSN favourable), at plasma densities close to $\bar{n}_{e,\mathrm{min}}$, $E_{r,\mathrm{min}}$ is approximately -12 kV/m, which is in good agreement with previous investigations on E_r. However, this value is found not to be a universal number and deviations are found in plasmas in which $v_i \times B$ becomes an important contribution to

E_r, e.g. at low density. A comparison with local neoclassical theory shows that close to the position of $E_{r,\mathrm{min}}$ the poloidal main ion flows are at the neoclassical level, but the experimentally measured inner E_r gradient is regularly underestimated if neoclassical main ion flows are imposed in the radial force balance. This indicates that the main ion flow is not at the neoclassical level in the entire edge region of L-mode plasmas. However, also the application of local neoclassical theory might be already invalid in this plasma region, which will be investigated in more detail in the future.

In the SOL the L-mode E_r profiles are well described by $-\nabla_r T_{e,\mathrm{OMP}}/e$, which is in agreement with theoretical predictions of the upstream E_r in the SOL in conduction-limited plasmas.

Comparisons of L-modes with matched parameters in favourable and unfavourable drift configuration show that the gradients of E_r are consistently lower in unfavourable compared to favourable drift configuration. This finding is in line with the observation of a higher P_{LH} in unfavourable drift configuration. The difference in E_r is due to a less negative $E_{r,\mathrm{min}}$ in unfavourable drift configuration in the edge of the confined plasma. A systematic difference of SOL-E_r profiles between favourable and unfavourable drift configuration, as suggested by SOL modelling, has not been observed. The reason for the difference in the E_r profiles between favourable and unfavourable drift configuration are not clear as of yet. No differences in the edge kinetic profiles, which could explain the modifications in E_r, were observed between the two drift configurations. Also neoclassical predictions can not resolve this discrepancy, because it predicts equally strong plasma flows and, thus, the same E_r.

The development of E_r during the L-I-H transition in unfavourable drift configuration points to an important role of E_r in the I-H, but not in the L-I transition. A constant outer E_r gradient is found at the I-H transition for a wide range of densities and for both NBI and ECRH heated plasmas. Together with the paradigm of a critical $v_{E\times B}$ needed to access H-mode, this finding is in agreement with the observation that P_{LI} shows only a weak dependence on B_ϕ, whereas P_{IH} increases linearly with B_ϕ. On the other hand the E_r gradients at the L-H transition in favourable drift configuration are lower than at the I-H transition in unfavourable drift configuration, making the observation of a constant outer E_r gradient at the H-mode access not universal to all drift configurations.

A comparison between NBI and ECRH heated plasmas shows that the toroidal rotation of the main ions $v_{\phi,i}$ strongly influences the shape of E_r. Therefore, $E_{r,\mathrm{min}}$ is not always a valid proxy for the gradient of E_r as even positive $E_{r,\mathrm{min}}$ values are observed in certain plasma conditions. During ECRH heating ramps it is found that the E_r gradients do not necessarily steepen with heating power. $\nabla_r p_i/(en_i)$ and $v_i \times B$ can have competing roles in the formation of E_r in L-mode. In certain conditions, e.g. at low density, an increase of the ECRH power can even lead to a decrease of the edge E_r gradient due to a strong increase of $v_{\phi,i}$.

Measurements of the intrinsic impurity toroidal edge rotation together with neoclassical predictions show that $v_{\phi,i}$ is co-current in all drift configurations for a wide range of collisionalities. However, with increasing collisionality $|v_{\phi,i}|$ decreases and flips sign, when the ion edge collisionality is in the Pfirsch-Schlüter regime. The outer E_r gradient is constant over the complete collisionality range, but the absolute values shift downwards with increasing collisionality. This points to a correlation between SOL flows and the intrinsic edge rotation, where the intrinsic edge rotation in the confined plasma follows the direction of the Pfirsch-Schlüter flows in the SOL of the HFS.

Experiments in pure H and D plasmas have shown that their respective E_r profiles show no significant differences in the confined plasma as well as in the SOL for matched plasma parameters and at the L-H transition. This contradicts SOL modelling results which predict a higher SOL-E_r for D plasmas. Power balance calculations show that the increased P_{LH} in H compared to D can be related to an increased ion heat transport in hydrogen L-mode edge plasmas. Furthermore, it is found that P_{LH} is lower in ECRH than in NBI heated H plasmas. Power balance calculations reveal that $Q_{i,\mathrm{edge}}$ is the same at the L-H transition for both heating methods, supporting its critical role in the L-H transition physics. Measurements of the inner E_r gradient at the L-H transition show that it is steeper in NBI than in ECRH heated plasmas, whereas the outer E_r gradient is the same. Experiments in mixed hydrogen-deuterium plasmas exhibit a non-linear dependence of P_{LH} on the relative hydrogen content f_{H}, whereas E_r is constant at the L-H transition independent of the relative hydrogen content.

In low-density ECRH powered hydrogen-deuterium plasmas an I-mode-like confinement regime was found which exhibits improved heat confinement, but L-mode-like particle confinement. It also features a weakly-coherent mode. Since this confinement regime was found in favourable drift configuration, but at low density and a relative hydrogen content of $f_{\mathrm{H}} = 0.6 - 0.8$, it is concluded that the I-mode is not restricted to plasma operation in unfavourable drift configuration, but can occur in conditions in which P_{LH} is high.

The obtained results show that the interaction of SOL flows, edge rotation and kinetic pressure gradients are important to understand the formation of E_r in the plasma edge and its development towards the L-H transition. Several of the presented observations support the paradigm that a shear in the $v_{E\times B}$ flow leads to the H-mode access. Especially, strong differences in P_{LH} can be explained by clear differences in the L-mode E_r gradients. However, not all obtained results are conclusive and support directly the theory that the condition $\gamma_{E\times B} > \gamma_{\mathrm{turb}}$ triggers the L-H transition. This suggests that possibly additional effects are at play for some of the conditions. In particular it could not be clarified whether the inner or the outer E_r gradient gives the dominant contribution to the shear flow, and, thus, is responsible for the H-mode onset.

The experiments in mixed ion species plasmas can help to improve predictions for next-step fusion devices like ITER. The critical role of the edge ion heat flux in the L-H transition physics could be confirmed, giving more confidence in applying the existing scaling of the $\bar{n}_{e,\mathrm{min}}$ to ITER. Furthermore, it could be shown that in pure ECRH heated plasmas the conditions for the H-mode onset are influenced by the plasma core physics. Although it was found that the high P_{LH} in H plasmas can not be sensitively reduced by He doping as suggested by other work, the observations that the scaling law overestimates P_{LH} by a factor of two close to the density minimum is favourable for ITER.

9.2 Outlook

The development of the new spectroscopy-based diagnostics (HES) to measure the E_r gradient across the separatrix has given new insights in the structure of E_r in different confinement regimes and magnetic configurations. However, the temporal resolution of HES is a limiting factor in its usage for experimental studies focusing on fast and transient events. For example, it could not be experimentally ruled out whether the steepening of the $(\nabla_r p_i)/(en_i)$ and E_r gradients is the cause or a consequence of the L-H transition. For this reason it is foreseen to upgrade the diagnostics such that a time resolution of a few tenth of µs can be obtained. Since the read-out frequency of the CCD-chip of the spectrometer camera is the main limiting factor, the idea is to use a different read-out mode. This other read-out mode has been already successfully tested on beam-based CXRS measurements. Usually, the increase in temporal resolution is accompanied by a reduction of signal amplitude. However, the amount of puffed He and, thus, the signal amplitude can easily be increased while not being perturbative. Another improvement which is foreseen is to combine the HES diagnostics with the He-beam diagnostics. Both systems have similar working principles, and, thus, can employ the same in-vessel components (piezo valve, optical heads). Sharing these components will enable simultaneous measurements of the $n_{e,\mathrm{edge}}$-, $T_{e,\mathrm{edge}}$-, and E_r-profiles on the same plasma volume. This will help to improve the alignment of the E_r profiles with respect to the separatrix and other E_r diagnostics. Thus, a detailed study on systematic dependences of the radial position of E_r can be performed. Ultimately it will help to better define the region of turbulence suppression in the plasma edge and, thus, help to clarify the roles of the inner and outer E_r gradient in the L-H transition physics.

The obtained experimental data and observations will be used as input for interpretive modelling and for comparison to predictive simulations. In a first step it is foreseen to calculate the main ion edge flows with a global neoclassical code and compare it to the local predictions as well as to the experimental data. In a second step it is planned to run gyro-kinetic simulations on selected cases in order to understand the edge turbulence behaviour of L-modes in favourable and unfavourable drift configuration close to the L-H transition. Also, the formation of the I-mode regime in favourable drift configuration at high relative hydrogen content f_{H} can be investigated with models of increasing complexity. SOL modelling of the different drift configuration plasmas, including full drift effects, could help to better understand the interaction of the SOL flows with the confined plasma and, thus, help to understand the formation of E_r across the separatrix.

Further experiments are planned focusing on the comparison of L-mode edge parameters in low- and high-density plasmas in the different drift configurations. Moreover, it is foreseen to determine the nature of the SOL flows experimentally by means of Mach probes. The studies can be extended to other plasma and divertor conditions for which it is known that P_{LH} differs, for example L-H transition experiments in a closed divertor compared to an open divertor as well as having the strike line on the horizontal target compared to vertical target. Such experiments would also enable more inter-machine comparisons.

Bibliography

[1] ITER Organization. https://www.iter.org/ (latest date accessed: 29/09/2021).

[2] Ralph Dux. Plasmaphysik und Fusionsforschung Teil II: Fusionsforschung. Lecture notes (in German), Universität Augsburg, 2002.

[3] J. P. Freidberg. Plasma Physics and Fusion Energy. Cambridge University Press, New York, 2007.

[4] John Wesson. Tokamaks. Oxford University Press, New York, 3rd edition, 2004.

[5] D. Reiter, G.H. Wolf, and H. Kever. Stationary burning: Analysis of profile effects on the required exhaust efficiency and the permitted helium particle confinement time. J. Nucl. Mater., 176-177(C):756–762, dec 1990.

[6] M. Keilhacker, et al. High fusion performance from deuterium-tritium plasmas in JET. Nucl. Fusion, 39(2):209, 1999.

[7] V. S. Mukhovatov and V. D. Shafranov. Plasma equilibrium in a Tokamak. Nucl. Fusion, 11(6):605, 1971.

[8] Institute for Plasmaphysics Garching. ASDEX Upgrade.

[9] V. Yu. Sergeev, et al. Conceptual design of divertor and first wall for DEMO-FNS. Nucl. Fusion, 55(12):123013, 2015.

[10] G. Federici, et al. Plasma-material interactions in current tokamaks and their implications for next step fusion reactors. Nucl. Fusion, 41(12):1967, 2001.

[11] V. Rohde, et al. Wall conditioning in ASDEX Upgrade. J. Nucl. Mater., 365:1369–1374, 2007.

[12] A. Kallenbach, et al. Non-boronized compared with boronized operation of ASDEX Upgrade with full-tungsten plasma facing components. Nucl. Fusion, 49(4):045007, 2009.

[13] B. Lipschultz, Y. Lin, E. S. Marmar, D. G. Whyte, and S. Wukitch. Influence of boronization on operation with high- Z plasma facing components in Alcator C-Mod. J. Nucl. Mater., 365:1110–1118, 2007.

[14] ASDEX Team. The H-mode of ASDEX. Nucl. Fusion, 29(11):1959–2040, 1989.

[15] H. Biglari, P. H. Diamond, and P. W. Terry. Influence of sheared poloidal rotation on edge turbulence. Phys. Fluids B Plasma Phys., 2(1), 1990.

[16] J. W. Connor and H. R. Wilson. A review of theories of the L-H transition. Plasma Phys. Control. Fusion, 42:R1–R74, 2000.

[17] Clemente Angioni. Turbulent Transport. Presentation at the European Joint PhD Network in Fusion Science., 2017.

[18] Hartmut Zohm. Plasmaphysik. Lecture notes (in German), Ludwig-Maximilians-Universität München, 2010.

[19] Per Helander and Dieter J. Sigmar. Collisional Transport in Magnetized Plasmas. Cambridge University Press, Cambridge, 2002.

[20] Ulrich Stroth. Plasmaphysik. Springer Spektrum, Berlin, 2 edition, 2018.

[21] E. Viezzer, et al. Collisionality dependence of edge rotation and in-out impurity asymmetries in ASDEX Upgrade H-mode plasmas. Nucl. Fusion, 55(12):123002, 2015.

[22] Ralph Dux. Neoclassical Transport. Presentation at the European Joint PhD Network in Fusion Science, 2017.

[23] L. Hinton and R. D. Hazeltine. Theory of plasma transport in toroidal confinement systems. Rev. Mod. Phys., 48(2):239, 1976.

[24] A. G. Peeters, et al. Influence of the centrifugal force and parallel dynamics on the toroidal momentum transport due to small scale turbulence in a tokamak. Phys. Plasmas, 16(4):042310, 2009.

[25] S. I. Braginskii. Transport Processes in a Plasma. Rev. Plasma Phys., 1:205, 1965.

[26] G. Dif-Pradalier, V. Grandgirard, Y. Sarazin, X. Garbet, and Ph. Ghendrih. Interplay between Gyrokinetic Turbulence , Flows , and Collisions : Perspectives on Transport and Poloidal Rotation. Phys. Rev. Lett., 103:065002, 2009.

[27] Y. Sarazin, et al. Large scale dynamics in flux driven gyrokinetic turbulence. Nucl. Fusion, 50(5):054004, 2010.

[28] V. D. Shafranov, V. Rozhansky, and O. G. Bakunin. Reviews of Plasma Physics. Springer Verlag, Berlin Heidelberg, 2008.

[29] U. Stroth, P. Manz, and M. Ramisch. On the interaction of turbulence and flows in toroidal plasmas. Plasma Phys. Control. Fusion, 53(2):024006, 2011.

[30] P. H. Diamond, S-I. Itoh, K. Itoh, and T. S. Hahm. Zonal flows in plasma — a review. Plasma Phys. Control. Fusion, 47(5):R35–R161, 2005.

[31] C. S. Chang, K. Seunghoe, and H. Weitzner. X-transport : A baseline nonambipolar transport in a diverted tokamak plasma edge. Phys. Plasmas, 9:3884, 2002.

[32] R. W. Brzozowski, F. Jenko, R. Bilato, M. Cavedon, and the ASDEX Upgrade Team. A geometric model of ion orbit loss under the influence of a radial electric field. Phys. Plasmas, 26:042511, 2019.

[33] Ralph Dux. Private communication.

[34] Alexander Lebschy. Experimental characterization of the core plasma flow at the ASDEX Upgrade tokamak. Phd thesis, Technical University Munich, 2018.

[35] S. P. Hirshman and D. J. Sigmar. Neoclassical transport of impurities in tokamak plasmas. Nucl. Fusion, 21(9):1079, 1981.

[36] Y. B. Kim, P. H. Diamond, and R. J. Groebner. Neoclassical poloidal and toroidal rotation in tokamaks. Phys. Plasmas, 3:2050, 1991.

[37] Peter C. Stangeby. The Plasma Boundary of Magnetic Fusion Devices. IOP Publishing Ltd., London, 2000.

[38] A. V. Chankin, et al. Fluid code simulations of radial electric field in the scrape-off layer of JET. Plasma Phys. Control. Fusion, 51(6):065022, 2009.

[39] P. C. Stangeby and A. V. Chankin. Simple models for the radial and poloidal E × B drifts in the scrape-off layer of a divertor tokamak : Effects on in / out asymmetries. Nucl. Fusion, 36(7):839, 1996.

[40] Harold Grad and Hanan Rubin. Hydromagnetic equilibria and force-free fields. In Proc. 2nd UN Conf. Peac. Uses At. Energy, volume 31, page 190, Geneva, 1958. IAEA.

[41] V. D. Shafranov. Equilibrium of a toroidal plasma in a magnetic field. J. Nucl. Energy. Part C, Plasma Physics, Accel. Thermonucl. Res., 5(4):251–258, 1963.

[42] ITER Physics Expert Groups on Confinement and Transport. Chapter 2 : Plasma confinement and transport. Nucl. Fusion, 39(12):2175, 1999.

[43] Eleonora Viezzer. Radial electric field studies in the plasma edge of ASDEX Upgrade. PhD Thesis, Ludwig Maximilian University, Munich, 2012.

[44] E. Viezzer, et al. Evidence for the neoclassical nature of the radial electric field in the edge transport barrier of ASDEX Upgrade. Nucl. Fusion, 54(1):012003, 2014.

[45] E. Viezzer, et al. High-accuracy characterization of the edge radial electric field at ASDEX Upgrade. Nucl. Fusion, 53(5):053005, 2013.

[46] H. Zohm. Edge localized modes (ELMs). Plasma Phys. Control. Fusion, 38(2):105–128, 1996.

[47] G. F. Harrer, et al. Parameter dependence of small Edge Localized Modes. Nucl. Fusion, 58(11):112001, 2018.

[48] F. Ryter, et al. H-mode power threshold and transition in ASDEX Upgrade. Plasma Phys. Control. Fusion, 40(5):725–729, 1998.

[49] D. G. Whyte. I-Mode: An H-Mode Energy Confinement Regime with L-Mode Particle Transport in Alcator C-Mod. Technical report, Plasma Science and Fusion Center Massachusetts Institute of Technology, Cambridge, 2010.

[50] T. Happel, et al. Approaching detachment in I-mode - Response of core confinement and the edge pedestal in the ASDEX Upgrade tokamak. Nucl. Fusion, 61(3):036026, 2021.

[51] T. Happel, et al. Turbulence intermittency linked to the weakly coherent mode in ASDEX Upgrade I-mode plasmas. Nucl. Fusion, 56(6):064004, 2016.

[52] T. Happel, et al. The I-mode confinement regime at ASDEX Upgrade : global properties and characterization of strongly intermittent density fluctuations. Plasma Phys. Control. Fusion, 59(1):014004, 2017.

[53] F. Ryter, et al. I-mode studies at ASDEX Upgrade: L-I and I-H transitions, pedestal and confinement properties. Nucl. Fusion, 57(1):016004, 2017.

[54] D. Silvagni, et al. I-mode pedestal relaxation events at ASDEX Upgrade. Nucl. Fusion, 60(12):126028, 2020.

[55] F. Ryter, et al. H-mode threshold and confinement in helium and deuterium in ASDEX Upgrade. Nucl. Fusion, 49(6):062003, 2009.

[56] F. Ryter, et al. L-H transition physics in hydrogen and deuterium: key role of the edge radial electric field and ion heat flux. Plasma Phys. Control. Fusion, 58(1):014007, 2016.

[57] Y. R. Martin, T. Takizuka, and the ITPA CDBM H-mode Threshold Data Group. Power requirement for accessing the H-mode in ITER. J. Phys. Conf. Ser., 123:012033, 2008.

[58] F. Ryter, et al. Experimental evidence for the key role of the ion heat channel in the physics of the L-H transition. Nucl. Fusion, 54(8):083003, 2014.

[59] M. Schmidtmayr, et al. Investigation of the critical edge ion heat flux for L-H transitions in Alcator C-Mod and its dependence on BT. Nucl. Fusion, 58(5):56003, 2018.

[60] A. E. Hubbard, et al. Threshold conditions for transitions to I-mode and H-mode with unfavourable. Nucl. Fusion, 52(11):114009, 2012.

[61] T. N. Carlstrom, et al. Experimental survey of the L-H transition conditions in the DIII-D tokamak. Plasma Phys. Control. Fusion, 36:A147, 1994.

[62] X. Bonnin, et al. Modelling and consequences of drift effects in the edge plasma of Alcator C-Mod. J. Nucl. Mater., 337-339(1-3 SPEC. ISS.):301–304, 2005.

[63] A. V. Chankin, et al. Possible influence of near SOL plasma on the H-mode power threshold. Nucl. Mater. Energy, 12:273–277, 2017.

[64] E. Righi, et al. Isotope scaling of the H-mode power threshold on JET. Nucl. Fusion, 39(3):309–319, 1999.

[65] N. Bonanomi, et al. Effect of the isotope mass on the turbulent transport at the edge of L-mode plasmas in ASDEX Upgrade and JET-ILW. Nucl. Fusion, 59(12):126025, 2019.

[66] E. A. Belli, J. Candy, and R. E. Waltz. Reversal of turbulent gyroBohm isotope scaling due to nonadiabatic electron drive. Phys. Plasmas, 26(8):082305, 2019.

[67] E. A. Belli, J. Candy, and R. E. Waltz. Reversal of Simple Hydrogenic Isotope Scaling Laws in Tokamak Edge Turbulence. Phys. Rev. Lett., 125(1):15001, 2020.

[68] A. V. Chankin, G. Corrigan, and C. F. Maggi. EDGE2D-EIRENE simulations of the influence of isotope effects and anomalous transport coefficients on near scrape-off layer radial electric field. Plasma Phys. Control. Fusion, 61(7):075010, 2019.

[69] J. Hillesheim, et al. Implications of JET-ILW L-H Transition Studies for ITER. In 27th IAEA Fusion Energy Conf., 2018.

[70] P. Gohil, T. C. Jernigan, T. H. Osborne, J. T. Scoville, and E. J. Strait. The torque dependence of the H-mode power threshold in hydrogen, deuterium and helium plasmas in DIII-D. Nucl. Fusion, 50(6):064011, 2010.

[71] E. R. Solano, JET L-H transition team, and JET Contributors. L-H transition studies at JET: tritium, helium and deuterium . In 28th IAEA Fusion Energy Conf., 2021.

[72] D. Moulton, G. Corrigan, J. R. Harrison, B. Lipschultz, and JET Contributors. vertical- and horizontal-target EDGE2D- EIRENE simulations of JET. Nucl. Fusion, 58(9):096029, 2018.

[73] F. Ryter, et al. Survey of the H-mode power threshold and transition physics studies in ASDEX Upgrade. Nucl. Fusion, 53(11):113003, 2013.

[74] Marco Cavedon, et al. Connecting the global H-mode power threshold to the local radial electric field at ASDEX Upgrade. Nucl. Fusion, 60(6):066026, 2020.

[75] M. Cavedon, et al. Inner versus outer E×B shear layer: An attempt to radially localize the L-H transition. In 46th EPS Conf. Plasma Phys. Proc., page P5.1069, Milan, 2019.

[76] T. Kobayashi, et al. Spatiotemporal structures of edge limit-cycle oscillation before L-to-H transition in the JFT-2M tokamak. Phys. Rev. Lett., 111(3):1–5, 2013.

[77] M. Cavedon, et al. Interplay between turbulence, neoclassical and zonal flows during the transition from low to high confinement mode at ASDEX Upgrade. Nucl. Fusion, 57(1):014002, 2017.

[78] O. Sauter and S .Yu. Medvedev. Tokamak coordinate conventions: COCOS. Comput. Phys. Commun., 184:293–302, 2013.

[79] Michael Griener. Active line ratio spectroscopy on thermal helium at ASDEX Upgrade. Phd, Technical University Munich, 2018.

[80] R Fischer, et al. Integrated Data Analysis of Profile Diagnostics at ASDEX Upgrade. Fusion Sci. Technol., 58(2):675–684, 2010.

[81] M Griener, et al. Qualification and implementation of line ratio spectroscopy on helium as plasma edge diagnostic at ASDEX Upgrade. Plasma Phys. Control. Fusion, 60(2):025008, feb 2018.

[82] R. J. Fonck, D. S. Darrow, and K. P. Jaehnig. Determination of plasma-ion velocity distribution via charge-exchange recombination spectroscopy. Phys. Rev. A, 29(6):3288–3309, 1984.

[83] R. M. McDermott, et al. Evaluation of impurity densities from charge exchange recombination spectroscopy measurements at ASDEX Upgrade. Plasma Phys. Control. Fusion, 60(9):095007, 2018.

[84] E. Poli, A. G. Peeters, and G. V. Pereverzev. TORBEAM, a beam tracing code for electron-cyclotron waves in tokamak plasmas. Comput. Phys. Commun., 136(1):90 – 104, 2001.

[85] D. Brida, D. Silvagni, T. Eich, M. Faitsch, and P. McCarthy. Role of electric currents for the SOL and divertor target heat fluxes in ASDEX Upgrade. Plasma Phys. Control. Fusion, 62(10):105014, 2020.

[86] P. J. McCarthy, P. Martin, and W. Schneider. The CLISTE Interpretive Equilibrium Code, IPP Report 5/85, 1999.

[87] P. J. Mc Carthy. Analytical solutions to the Grad – Shafranov equation for tokamak equilibrium with dissimilar source functions. Phys. Plasmas, 6:3554, 1999.

[88] R. Fischer, et al. Upgraded equilibrium reconstruction by coupling of an extended set of measurements with current diffusion modelling at ASDEX Upgrade. In 43rd Eur. Phys. Soc. Conf. Plasma Phys., 2016.

[89] G. D. Conway, et al. Mean and Oscillating Plasma Flows and Turbulence Interactions across the L-H Confinement Transition. Phys. Rev. Lett., 106(6):065001, 2011.

[90] G. Birkenmeier, et al. Magnetic structure and frequency scaling of limit-cycle oscillations close to L- to H-mode transitions. Nucl. Fusion, 56(8):086009, 2016.

[91] M. Cavedon, et al. On the ion and electron temperature recovery after the ELM-crash at ASDEX upgrade. Nucl. Mater. Energy, 18:275–280, 2019.

[92] P. David, et al. Optimization of the computation of total and local radiated power at ASDEX Upgrade. Nucl. Fusion, 61(6):066025, 2021.

[93] G. V. Pereverzev and P. N. Yushmanov. ASTRA - Automated System for TRansport Analysis. Technical Report IPP5/98, Max Planck Institute for Plasma Physics, 2002.

[94] M. Weiland, et al. RABBIT: Real-time simulation of the NBI fast-ion distribution. Nucl. Fusion, 58(8):082032, 2018.

[95] M. Griener, et al. Fast piezoelectric valve offering controlled gas injection in magnetically confined fusion plasmas for diagnostic and fuelling purposes, 2017.

[96] Bundesministerium für Arbeit und Soziales. Vermeidung oder Einschränkung gefährlicher explosionsfähiger Atmosphäre, 2012.

[97] Technetics Group. HELICOFLEX DELTA.

[98] Piezosystemjena. Long Distance Linear Actuator PX 500, 2014.

[99] CKD Dichtungstechnik. Fluorelastomere, 2019.

[100] Piezosystemjena. 30V300 OEM Piezo Controller, 2015.

[101] Swagelok. Swagelok sealings, 2015.

[102] DEKRA EXAM GmbH. DEKRA Munich, 2016.

[103] Christian Bürkert GmbH. Pressure measuring device.

[104] Pfeiffer Vacuum GmbH. Duo 11 ATEX, 2016.

[105] Wolfgang Demtröder. Experimentalphysik 1 - Mechanik und Wärme. Springer Spektrum, New York, 8 edition, 2018.

[106] P.B. Parks and W. Wu. Limitations of extended gas delivery tubes used for fuelling mitigated plasma disruptions, and a unique injection concept for prompt gas delivery. Nucl. Fusion, 51(7):073014, jul 2011.

[107] Vision Research. Phantom v711.

[108] Marco Cavedon. The role of the radial electric field in the development of the edge transport barrier in the ASDEX Upgrade tokamak. Phd thesis, Technical University Munich, 2016.

[109] Leica Camera AG. Objectives.

[110] Ronald E. Bell. Exploiting a transmission grating spectrometer. Rev. Sci. Instrum., 75(10):4158–4161, 2004.

[111] Princeton Instruments. CCD camera.

[112] Princeton Instruments. ProEM+ System Manual, 2012.

[113] Princeton Instruments. On-chip Multiplication Gain, 2016.

[114] M. Cavedon, et al. A fast edge charge exchange recombination spectroscopy system at the ASDEX Upgrade tokamak. Rev. Sci. Instrum., 88(4):043103, apr 2017.

[115] FARO. http://ww.faro.com/.

[116] Labsphere Incorporation. Labsphere.

[117] H. Zhu and P. Blackborow. Etendue and Optical Throughput Calculations, 2011.

[118] J. M Lerner and A. Thevenon. The Optics of Spectroscopy.

[119] Fiber optic tutorial. Fiber Optics Losses, 2016.

[120] Andor. Optical Etaloning in Charge Coupled Devices.

[121] J. Kramida, A., Ralchenko, Yu., Reader and NIST ASD Team. NIST Atomic Spectra Database (version 5.7.1), 2019.

[122] Marco Cavedon. Private Communication.

[123] Erdmann Unger. Untersuchungen zur Absolutkalibration eines Grazing-Incidence-Spektrometers für Verunreinigungsbestimmungen an einem Fusionsexperiment. Diploma, Max Planck Institute for Plasma Physics, Garching, Germany, 1992.

[124] R. M. Churchill, et al. Development of the gas puff charge exchange recombination spectroscopy (GP-CXRS) technique for ion measurements in the plasma edge. Rev. Sci. Instrum., 84(9):093505, sep 2013.

[125] R. Hoekstra, et al. Charge exchange from D(n = 2) atoms to low- Z receiver ions. Plasma Phys. Control. Fusion, 40(8):1541–1550, 1998.

[126] P. H. Goldston, R. J., Rutherford. Introduction to Plasma Physics. IOP Publishing, Bristol and Philadelphia, 1995.

[127] W. W. Heidbrink, D. Liu, Y. Luo, E. Ruskov, and B. Geiger. A Code that Simulates Fast-Ion Dα and Neutral Particle Measurements. Commun. Comput. Phys., 10(3):716–741, 2011.

[128] Benedikt Geiger. Fast-ion transport studies using FIDA spectroscopy at the ASDEX Upgrade tokamak. Phd thesis, Ludwig-Maximilian University Munich, 2012.

[129] D.J. Cruz-Zabala, et al. Upgrade of the edge Charge Exchange Recombination Spectroscopy system at the High Field Side of ASDEX Upgrade. J. Instrum., 14(11):C11006, 2019.

[130] OPEN-ADAS. https://open.adas.ac.uk/.

[131] E. Viezzer, T. Pütterich, R. Dux, and A. Kallenbach. Investigation of passive edge emission in charge exchange spectra at the ASDEX Upgrade tokamak. Plasma Phys. Control. Fusion, 53(3), 2011.

[132] A. Blom and C. Jupén. Parametrization of the Zeeman effect for hydrogen-like spectra in high-temperature plasmas. Plasma Phys. Control. Fusion, 44(7):1229–1241, 2002.

[133] Rachael Marie McDermott. Edge Radial Electric Field Studies Via Charge Exchange Recombination Spectroscopy on the Alcator C-mod Tokamak. PhD thesis, Saint Louis University, 2009.

[134] R. M. McDermott, et al. Extensions to the charge exchange recombination spectroscopy diagnostic suite at ASDEX Upgrade. Rev. Sci. Instrum., 88(7):73508, 2017.

[135] M. Von Hellermann, et al. Analytical approximation of cross-section effects on charge exchange spectra observed in hot fusion plasmas. Plasma Phys. Control. Fusion, 37(2):71–94, 1995.

[136] W. M. Solomon, K. H. Burrell, P. Gohil, R. J. Groebner, and L. R. Baylor. Extraction of poloidal velocity from charge exchange recombination spectroscopy measurements. In Rev. Sci. Instrum., volume 75, pages 3481–3486. American Institute of PhysicsAIP, 2004.

[137] Kristel Crombé. Spectroscopische studies van de dynamica van onzuiverheidsionen in de tokamaks JET en TEXTOR Spectroscopic Studies of Impurity Ion Dynamics on the JET and TEXTOR Tokamaks. PhD thesis, Gent University, 2005.

[138] R. S. Freund, J. A. Schiavone, and H. M. Crosswhite. The Electronic Spectrum and Energy Levels of the Deuterium Molecule. J. Phys. Chem. Ref. Data, 14:235, 1985.

[139] B. Cao, et al. Comparison of gas puff imaging data in NSTX with degas 2 simulations. Fusion Sci. Technol., 64(1):29–38, 2013.

[140] Ralph Dux. STRAHL User Manual. Technical report, Max Planck Institute for Plasma Physics, 2006.

[141] Bernd Wieland. Investigations on radial electric fields in the edge transport barrier of H-mode discharges. Phd thesis, Technical University Munich, 2011.

[142] J. M. Muñoz Burgos, et al. Evaluation of thermal helium beam and line-ratio fast diagnostic on the National Spherical Torus Experiment-Upgrade. Phys. Plasmas, 23(5):053302, may 2016.

[143] H. Meyer, et al. The structure, evolution and role of the radial edge electric field in H-mode and L-mode on MAST. J. Phys. Conf. Ser., 123:012005, jul 2008.

[144] Darren Temple. Experimental Investigations into the radial electric field of MAST. PhD thesis, Imperial College London, 2011.

[145] Daniel Wendler. Influence of the Reabsorption on the Temperature and Density Evaluation with the Thermal Helium Beam Diagnostic at ASDEX Upgrade. Master thesis, Technical University Munich, 2019.

[146] A. A. Galeev, S. S. Moiseev, and R. Z. Sagdeev. The theory of the stability of non-uniform plasma and anomalous diffusion. Plasma Phys. (Journal Nucl. Energy Part C), 6:645–669, 1964.

[147] M. Hirsch, E. Holzhauer, J. Baldzuhn, B. Kurzan, and B. Scott. Doppler reflectometry for the investigation of propagating density perturbations. Plasma Phys. Control. Fusion, 43(12):1641–1660, 2001.

[148] N. Bonanomi, et al. Edge turbulent transport toward the L-H transition in ASDEX Upgrade and JET-ILW. Phys. Plasmas, 28(5):052504, 2021.

[149] P. Manz, et al. Physical mechanism behind and access to the I-mode confinement regime in tokamaks. Nucl. Fusion, 60(9):096011, 2020.

[150] Thomas Pütterich. Private Communication.

[151] Gregor Birkenmeier. Private Communication.

[152] L. M. Shao, et al. On the role of the edge density profile for the L-H transition power threshold in ASDEX Upgrade. Plasma Phys. Control. Fusion, 58(2):025004, 2016.

[153] R. M. McDermott, et al. Core momentum and particle transport studies in the ASDEX Upgrade tokamak. Plasma Phys. Control. Fusion, 53(12):124013, 2011.

[154] G. D. Conway, J. Schirmer, S. Klenge, W. Suttrop, and E. Holzhauer. Plasma rotation profile measurements using Doppler reflectometry. Plasma Phys. Control. Fusion, 46(6):951–970, 2004.

[155] A. V. Chankin. Classical drifts in the tokamak SOL and divertor: Models and experiment. J. Nucl. Mater., 241-243:199–213, 1997.

[156] Dominik Brida. Private Communication.

[157] T. Eich, et al. Inter-ELM Power Decay Length for JET and ASDEX Upgrade: Measurement and Comparison with Heuristic Drift-Based Model. Phys. Rev. Lett., 107:215001, 2011.

[158] A. V. Chankin, et al. EDGE2D-EIRENE modelling of near SOL e r: Possible impact on the H-mode power threshold. Plasma Phys. Control. Fusion, 59(4):045012, 2017.

[159] R. Bilato, C. Angioni, G. Birkenmeier, F. Ryter, and The ASDEX Upgrade Team. Heuristic model for the power threshold of the L-H transition. Nucl. Fusion, 60(12):124003, 2020.

[160] A. G. Peeters. Reduced charge state equations that describe Pfirsch Schlüter impurity transport in tokamak plasma. Phys. Plasmas, 7(1):268–275, 2000.

[161] M. Landreman and D. R. Ernst. Local and global Fokker - Planck neoclassical calculations showing flow and bootstrap current modification in a pedestal. Plasma Phys. Control. Fusion, 54(11):115006, 2012.

[162] S. Buller, I. Pusztai, S. L. Newton, and J. T. Omotani. Neoclassical flows in deuterium - helium plasma density pedestals. Plasma Phys. Control. Fusion, 59(5):055019, 2017.

[163] M. Landreman, F. I. Parra, P. J. Catto, D. R. Ernst, and I. Pusztai. Radially global δ f computation of neoclassical phenomena in a tokamak pedestal. Plasma Phys. Control. Fusion, 56(4):045005, 2014.

[164] Garrard Conway. Private Communication.

[165] V. Rozhansky, et al. Modelling of radial electric field profile for different divertor configurations. Plasma Phys. Control. Fusion, 48(9):1425–1435, 2006.

[166] P. Sauter, et al. L- to H-mode transitions at low density in ASDEX Upgrade. Nucl. Fusion, 52(1):012001, 2012.

[167] B. LaBombard, et al. Transport-driven scrape-off layer flows and the x-point dependence L-H power threshold in Alcator C-Mod. Phys. Plasmas, 12(5):056111, 2005.

[168] L. Aho-Mantila, et al. Assessment of SOLPS5.0 divertor solutions with drifts and currents against L-mode experiments in ASDEX Upgrade and JET. Plasma Phys. Control. Fusion, 59(3):035003, 2017.

[169] P.A. Schneider, et al. Overview of the isotope effects in the ASDEX Upgrade tokamak. Plasma Phys. Control. Fusion, 63:064006, 2021.

[170] Arne Kallenbach. Scrape-off layer (SOL) and divertor physics. Presentation at the European Joint PhD Network in Fusion Science, 2017.

[171] R. Bartiromo, et al. Design and calibration of the JET neutral particle analyzer. Rev. Sci. Instrum., 58(5):788–795, 1987.

[172] Johannes Illerhaus. Estimation , Validation and Uncertainty of the Position of the Separatrix Contour at ASDEX Upgrade. Diploma thesis, Technichal University, Munich, 2018.

[173] U. Plank, et al. H-mode power threshold studies at ASDEX Upgrade in mixed ion species plasmas. Nucl. Fusion, 60(7):074001, 2020.

[174] A. Kappatou, et al. A forward model for the helium plume effect and the interpretation of helium charge exchange measurements at ASDEX Upgrade. Plasma Phys. Control. Fusion, 60(5):055006, 2018.

[175] R. Fischer, et al. Effective ion charge Zeff from integrated analysis of multiple diagnostics at ASDEX Upgrade. In 37th EPS Conf. Plasma Phys., page P5.107, 2010.

[176] P. A. Schneider, et al. Explaining the isotope effect on heat transport in L-mode with the collisional electron-ion energy exchange. Nucl. Fusion, 57(6):066003, 2017.

[177] ITER Organization. ITER Research Plan within the Staged Approach (Level III – Provisional Version). Technical Report ITR-18-003, ITER, 2018.

[178] C. F. Maggi, et al. L-H power threshold studies in JET with Be/W and C wall. Nucl. Fusion, 54(2):023007, 2014.

[179] C. F. Maggi, et al. Isotope effects on L-H threshold and confinement in tokamak plasmas. Plasma Phys. Control. Fusion, 60(1):014045, 2018.

[180] M. Willensdorfer, et al. Electron density evolution after L-H transitions and the L-H/H-L cycle in ASDEX Upgrade. Nucl. Fusion, 52(11):114026, 2012.

[181] D. G. Whyte, et al. I-mode: An H-mode energy confinement regime with L-mode particle transport in Alcator C-Mod. Nucl. Fusion, 50(10):105005, 2010.

[182] Davide Silvagni. Private Communication.

[183] N. Bonanomi, et al. I-mode in non-deuterium plasmas in ASDEX Upgrade. Nucl. Fusion, 61(5):054001, 2021.

[184] A. E. Hubbard, et al. Edge energy transport barrier and turbulence in the I-mode regime on Alcator C-Mod. Phys. Plasmas, 18(5):056115, 2011.

Acknowledgements

Finally I come to the point where I write this part. This work would have not been possible without the help of really many, many people. Therefore, I would like to thank the entire ASDEX Upgrade Team for their support, good collaboration and pleasant working atmosphere. However, there are of course a few people who deserve special acknowledgement.

First of all I would like to express my deep appreciation to PD Dr. Thomas Pütterich, my academic supervisor and supervisor at IPP. You guided my studies, but at the same time gave me enough freedom to develop my own ideas. Your willingness of giving last minute support was highly appreciated.

Further I would like to thank to Dr. Marco Cavedon who introduced me into the topic of CXRS and showed me the measurement systems at ASDEX Upgrade. You always gave a helping hand if one of the systems was not running as it should have and I would also like to thank you for very helpful python routines for calibration and spectra analysis.

I would like to offer my special thanks to Dr. Ralph Dux, the spectroscopy group leader at IPP. Your lecture on neoclassical transport is a reference for me and discussions about the topic plasma spectroscopy were always helpful and enlightening.

I owe my debt of gratitude to Prof. Dr. Ulrich Stroth, the director of the E2M department, for giving me the possibility to pursue a PhD at IPP. Maybe you were not aware of it, but you gave me the right hint in the right moment, so thank you for this.

I would like to thank Dr. Clemente Angioni, whom I felt I could ask everything about tokamak physics, because he knows everything about it. You not only introduced me into the world of ASTRA, but also performed plasma discharges at AUG which turned out to be very useful for my PhD.

I have greatly benefited from the knowledge of Dr. Dominik Brida on SOL physics. I would like to also thank you for providing me with helpful Langmuir probe data.

I am very grateful to Dr. Garrard Conway, Dr. Tim Happel and Dr. Pascale Hennequin, who all provided me quickly and reliably with E_r profiles from Doppler reflectometry. Your door was also always open for me regarding questions about the profiles and Doppler reflectometry in general.

I am indebted to Dr. Michael Griener who helped me setting up the piezo gas valve in the plasma vessel and the gas supply system in the torus hall. I could profit from your expertise and your precise calibration and characterization of the piezo gas valve.

I received generous support from Dr. Amanda Hubbard and Dr. Hendrik Meyer on the topic of my PhD. They both performed experiments which were also very useful for me.

I very much appreciate the Dr. Athina Kappatou, Dr. Rachael McDermott and Dr. Rainer Fischer providing me with precise and reliable kinetic plasma and equilibrium profiles. You always processed my various requests promptly, thank you for this.

I would like to thank Dr. Otto Kardaun, who always showed special interest in my work. Thank you for the fruitful discussions. I am still impressed by the fact that you foresaw some properties of the thermal He gas cloud, which turned out to be the case.

I would like to express special gratitude to Dr. Philip Schneider, with whom I could have interesting discussions on the topic of the isotope effect and I could count on his expertise in running discharges at AUG in different main ion species plasmas. I would also like to thank you for pleasant off-topic chats.

I highly appreciate the support of the other members of the spectroscopy group, mainly Diego, Eli and Pilar, during long-lasting in-vessel-calibrations and task-sharing in equally long control room sessions.

I would like to thank several other colleagues and fellow doctoral researchers for five enjoyable years as a PhD candidate at IPP. I could spend great time in the office with you, at conferences or after work. For this I thank amongst many others: Monika, Barbara W., Maxi, Georg H., Georg H., Davide, Pierre, Nicola, Teo, Markus and Thomas H.-S..

It is also important to have some life outside work. For distraction from work I would like to thank in particular Alex, Barbara E., Christian M., Claudia E., Claudia R., László, Niklas, Thomas M., Tobi, the Alps and my violin.

The best and most important support I have received all along my life comes from my parents and Richard. I am so happy that you are my family and not someone else's!